BIOLOGICAL MEMBRANES

MECHANICAL PROPERTIERS OF BIOLOGICAL PRACTICALLY TWO DIMENSIONAL MATERIALS

Translated by John Morton.
The authors wish to express their appreciation to Dr. John Morton for his helpful collaboration on the translation.

ISBN: ?????
Depósito legal: M-?????-2019

Design and layout: Albatros Comunicación, S.L.

Index

1 CHAPTER General concepts

1.1. INTRODUCTION

The objective of this section is to outline the particular properties of biological materials which have two preponderant dimensions –those which characterise the surface rather than the thickness–. In the previous section, dedicated to fibres, there was only one relevant dimension –the length of the fibre– which greatly simplified the mathematical treatment in order to understand mechanical tests and to model their behaviour. Bidimensional materials can be grouped into two families; *membranes* and *laminas*. Laminas, due to their small thickness, have a certain flexural rigidity while in membranes this can be considered negligible. This is the case with soft biological materials, which are always very flexible.

The analysis of bidimensional materials is more complicated than that of fibres because, with the presence of the additional dimension, there is often *anisotropy*; the material behaves differently in different directions in the surface.

The structure of these materials is essentially that of a material composed of fibres embedded in an organic matrix. P*olysaccharide* fibres form the leaves of plants (if the fibres are cellulose) or the cuticles of insects (when chitin fibres are used). The epithelia are constructed from *polypeptide* fibres as are blood vessels, (with elastin and collagen fibres). Therefore, the **first chapter** focuses on two important biological materials; the skin of mammals and blood vessels. A detour into the membranes of marines creatures is made, because of their growing importance in the field of biomimetics.

An additional difficulty when materials are very flexible is the mathematical treatment of the tensile state, because the Hookean approximation is no longer valid and it is necessary to define stress and strain tensors within the framework of the theory of finite deformations. In order to familiarise the reader with these new concepts, the **second chapter** outlines the most important aspects of the kinematics and stress state which are used to characterise the mechanical behaviour of biological membranes. These concepts are necessary for the understanding of the most common mechanical tests used to characterise bidimensional biological materials, which will be described below. Some tests, are special cases of more general tests developed for three dimensional materials (such as fracture or indentation tests) and for this reason they are only mentioned in passing, since they will be covered in more detail in a later section.

In the **third chapter** two important bidimensional biological materials in biomedical engineering are discussed in detail; the pericardium and blood vessels.

1.2. THE SKIN OF MAMMALS

Skin is the coating which totally covers the body of animals. It is a tissue with multiple functions; it is the first defensive barrier, it has sensors and excretory organs, and plays a critical role in regulating body temperature and in containing fluids. Furthermore, it is the source of several symptoms, some corresponding to specific skin diseases and others to internal maladies which appear on the skin.

Skin is the defensive element that protects traumas, from ultraviolet radiation, toxic agents and micro-organisms. Skin plays a part in regulating body temperature by increasing or decreasing the flow of blood reaching it. Sweat can also be involved the thermoregulation, since when it evaporates it takes away heat from the organism. Some nerve ends reach the skin, terminating in tactile corpuscles which capture heat or cold, or pressure or pain, information and transmit it through the nervous system to the brain. The production of keratin (keratinisation) hardens the outer layers of the skin and contributes to replacement of its cells.

"The skin –despite being our largest and most visible organ, despite us seeing and touching it, indeed living in it, every moment in our lives– is the organ most overlooked by the medical profession. Weighing nine kilograms and covering two square meters, skin wasn't even recognized as an organ until the eighteenth century." (Lyman M. 2019).

1.2.1 Structure

In the skin of mammals it is possible to distinguish three superimposed layers which, from outside to inside, are: the *epidermis*, the *dermis* and the *hypodermis* (figure 1).

The **epidermis** is the outermost part. It is a thin epithelium (in humans of a similar thickness to a sheet of paper) composed of cells, keratinocytes, which are in a state of continuous renewal. Dispersed between these are the melanocytes, cells which produce melanin and the Langerhans cells which have a defensive function. The epidermis has neither blood vessels nor lymphatics, but does have nerve endings. In the epidermis it is possible to observe four strata (see the detail in figure 1): corneum, granulosum, spinosum and basale or germinative.

The **dermis** is rich in blood vessels and lymphatics, and has nerve endings which collect tactile sensitivities (Meissner corpuscles), the sense of cold (Kraus corpuscles) or pressure (Pacini corpuscles). Sweat glands are situated in this layer, the sebaceous glands and hair roots. The dermis also contains collagen and elastin fibres which confer its strength and elasticity, and defence cells.

The **hypodermis** is the deepest part of the skin. It is a zone rich in fat tissue and acts like a cushion to protect the organs beneath it.

The skin which covers the natural orifices of the organism (mouth, nasal passages, *etc.)* changes its structure a little when it passes into the interior and is called the *mucosa*. The most notable difference between the structure of ordinary skin and the mucosa is that these, under normal conditions, lack keratinised layers, that is to say, its epidermis lacks the corneum stratum and the granulosum.

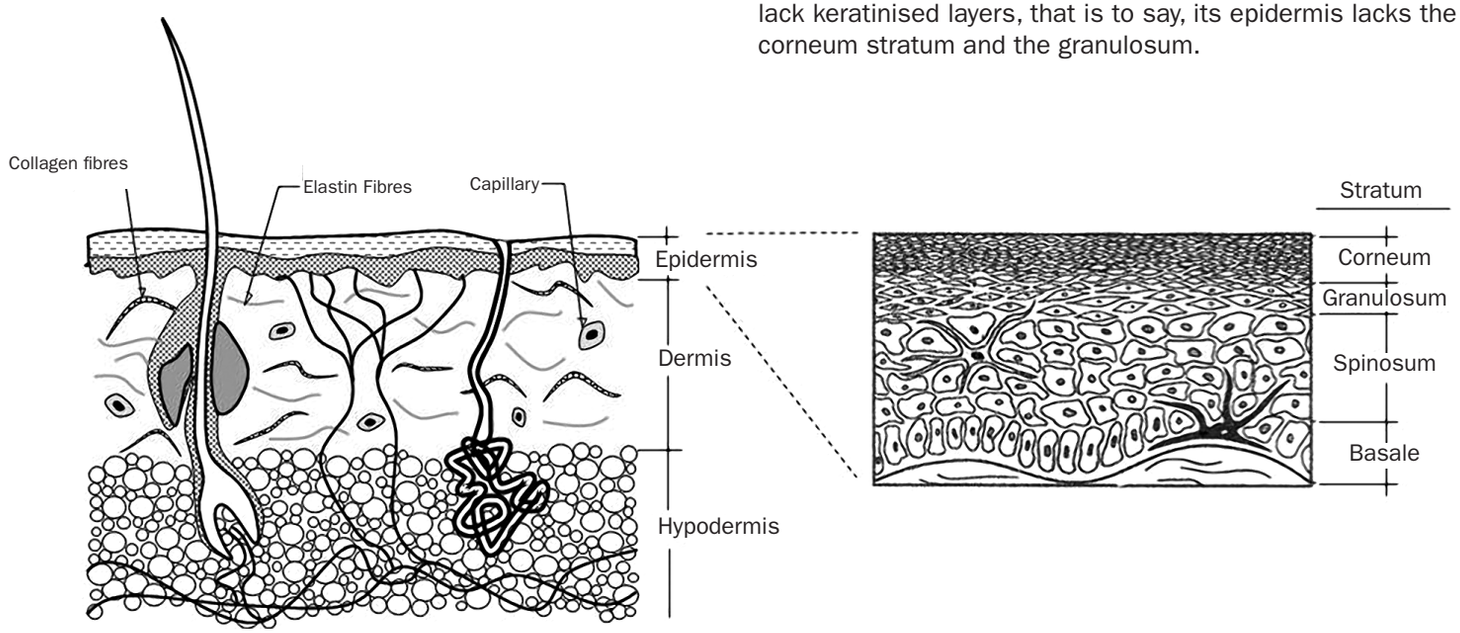

Fig. 1. *Structure of the skin of mammals..*

1.2.2 Mechanical properties

The study of the mechanical properties of skin has centred around the first two layers; the epidermis and the dermis which, in a simplified form, can be modelled as follows: In the epidermis, the superficial layer –the corneum stratum– is a keratin membrane and the rest, the raw material of leather, an amorphous material. The dermis is, roughly, a mat composed of collagen and elastin fibres in a protein and polysaccharide matrix (principally hyaluronic acid).

Later, some notable aspects of the mechanical behaviour of human skin (epidermis and dermis) will be summarised in relation to age; the variation of thickness and elasticity (Escoffier *et al*. 1989). Both properties are illustrated in figure 2. The experiments were performed *in vivo,* on the ventral forearms. The thickness is measured with ultrasonic techniques and the elasticity determined from a torsion test, described in the cited reference, which evaluates the recovery of skin once the applied stress is removed. The elasticity was estimated by means of the quotient of the instantaneous strain after unloading, ε_R, and the initial instantaneous strain, ε_o, as indicated schematically in figure 2b. The results show that skin maintains its thickness up to the 70s, while the elasticity decreases progressively with age.

A study of the mechanical behaviour of the human epidermis is interesting not only for a knowledge of its resistance to abrasion and penetration by foreign objects, but also due to the increasing use of patches and adhesives for the administration of transdermal medication. For these reasons it is important to know mechanical properties, in particular the effect of temperature and humidity on the adhesion strength of the exterior layer of the epidermis; the *stratum corneum*. The appropriate tests for this are delamination tests (which are described in detail below). Figure 3 shows the delamination energies and the stress necessary to separate the skin (from *in vitro* tests performed by Wu *et al*. in 2006). The adhesion strength (or delamination) (measured as the work required to separate an area of 1 m^2) decreases with temperature from 8 to 1 J/m^2 in totally hydrated specimens, while in those with a relative humidity of 45% it is practically constant at about 3 J/m^2 (figure 3a). The adhesion stress falls with temperature and hydration (figure 3b). The cited article also contains a study of the influence of lipids on the mechanical properties, finding that specimens in which the lipids have been partially removed are more resistant.

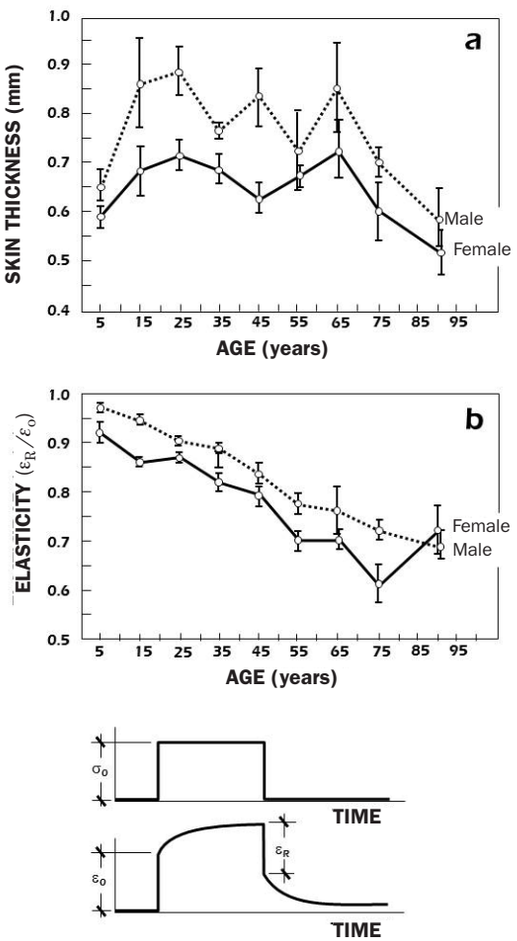

Fig. 2. *Variation of thickness and elasticity of human skin with age (Escoffier et al. 1989).*

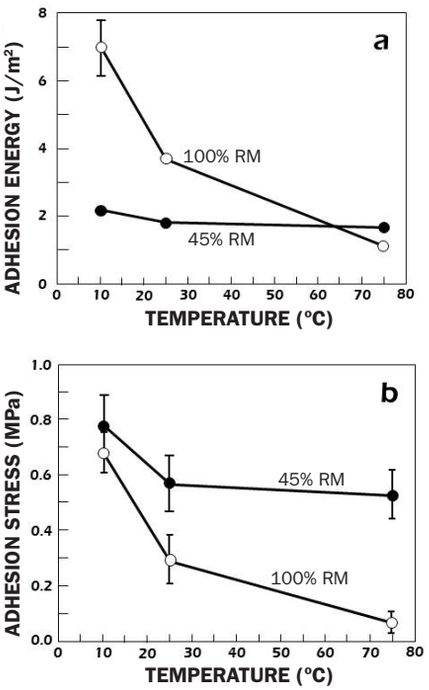

Fig. 3. *Variation of the energy and adhesion stress with temperature and humidity in the human epidermis (Wu et al. 2006).*

The effect of loading rate on the mechanical response of skin is another issue that deserves attention. H.G. Vogel studied the influence of the rate at which load was applied to the skin of rats; the speeds went from very slow movement ($5 \cdot 10^{-3}$ cm/minute) the those which corresponded to free fall from about 1 metre high (~$3 \cdot 10^4$ cm/minute) (Vogel 1972). The results of this study showed that the failure load and the elastic modulus increased almost linearly with the log of the strain rate, while the strain to failure was practically constant. Vogel also investigated the effect of age and corticosteroids, which were known to be two parameters that influenced the mechanical properties.

The situation of the skin, in this case the dorsal or ventral parts, also influences the mechanical properties. In particular, many large herbivores have very thick areas of skin for defensive purposes. R. Shadwick performed a detailed study of the mechanical properties of rhinoceros skin, one of the mammals with the thickest skin (Shadwick *et al*. 1992). Skin from the back and sides of the white rhinoceros has a very high rupture stress, 30 MPa, and a small failure strain of about 0.24. As a result, the stress-strain curve is quite steep, unlike curves for the epithelia discussed above, and its average elastic modulus can reach 240 MPa. The fracture toughness is of the order of 70 kJ/m^2. On the other hand, the ventral skin, on the stomach, is weaker, less stiff and more deformable; the average rupture stress is about 14 MPa and the corresponding strain is about 0.33. The elastic modulus lies at around 100 MPa.

Although rhinoceros skin is stronger and stiffer than that of other mammals, it should be noted that the tear resistance of the skin is small, or at least, it is not in keeping with the tensile or compressive strengths. This observation can be related to an adaptive advantage: In fights between rhinoceroses, the horns can puncture or tear (scratch) the skin, while the most frequent wounds produced are scratches, which are less dangerous because punctures could cause damage to internal organs. The design of the skin of these animals improves survival by favouring tear breaks, and lead to the end of the fight before more serious harm is caused.

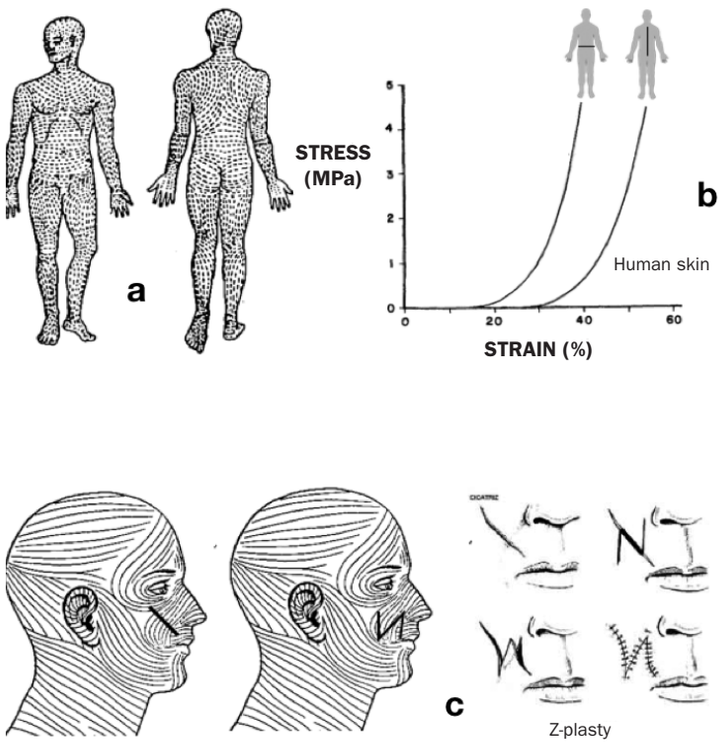

Fig. 4. *a) Langer lines*
b) Traction curves. Greater stiffnesses are observed in the Langer directions
c) Z-plasty, a surgical technique to conceal scars

1.2.3 Comentarios

In a very simplified form, and in order to understand the mechanical behaviour, it is possible to assume that the principal components of the *dermis* of mammals are collagen fibres, which are embedded into a soft tissue matrix. Collagen fibres are naturally arranged in preferential directions in the skin, which in the case of human beings are known as Langer lines (figure 4a). The greater density of collagen fibres and their alignment make the skin more rigid when subjected to tension in the direction of the Langer lines, generating a pronounced anisotropy (figure 4b). Scar formation induces an accumulation of collagen fibre points and produces, as experience confirms, a zone of much more rigid skin. Some surgical techniques take advantage of the Langer lines in order to conceal, as far as possible, the scars produced by surgery, orienting the position of the suture (that is, the scar) along the length of one of these lines. In this way the increase in the stiffness due to the presence of the scar is masked by the grater overall stiffness of the Langer lines. When it is not possible, and the line of the suture crosses the Langer lines, a technique known as z-plasty is used (figure 4c) in which a Z-shaped scar is created, which is accommodated in a possible Langer network.

When embedded in a highly deformable matrix, the position and orientation of collagen fibres change with the deformation of the tissue. The gradual take up of load in these fibres is responsible for the J-shaped stress-strain curves. As a result, the mechanical properties of the skin depend essentially on the structural arrangement –on the architecture– of these fibres. In figure 5 the various stress-strain curves show distinct behaviour depending upon the orientation of the collagen fibres in different tissues: Tendons and ligaments are tissues with a high collagen content and fibres that are already highly aligned before load introduction. Therefore, these structures are already very stiff from the beginning and, although very strong, the strain to failure is very low. The dermis of the rhinoceros is probably the mammal epithelium with collagen fibres having the greatest degree of alignment. This does not demonstrate such a marked J-curve as that of the epithelium of a cat, in which the collagen fibres are initially quite disordered, as shown schematically in the figure.

Disturbance of the network of collagen fibres and elastin can have serious consequences; some diseases are due to breaking the crosslinks between them. One of these cases is lathyrism, which can be caused by ingestion of grass pea seeds (*Lathyrus sativus*), or its principal agent β-aminopropionitrile, which reduces the formation of crosslinks in the collagen by inhibiting the enzyme lysyl oxidase. Another serious illness is scurvy, caused by vitamin C deficiency. Vitamin C is essential for the synthesis of the hydroxyproline and hydroxylysine amino acids, which form the collagen chain. Human beings and some higher primates lack the capacity to synthesise vitamin C, which they must obtain from their diet. This was a very common sickness among sailors in previous centuries. Their diets often excluded perishable products, rich in vitamin C, such as fruit and vegetables. Defective fabrication of collagen weakens the structures of all organisms, producing haemorrhages and, in extreme cases, leading to death.

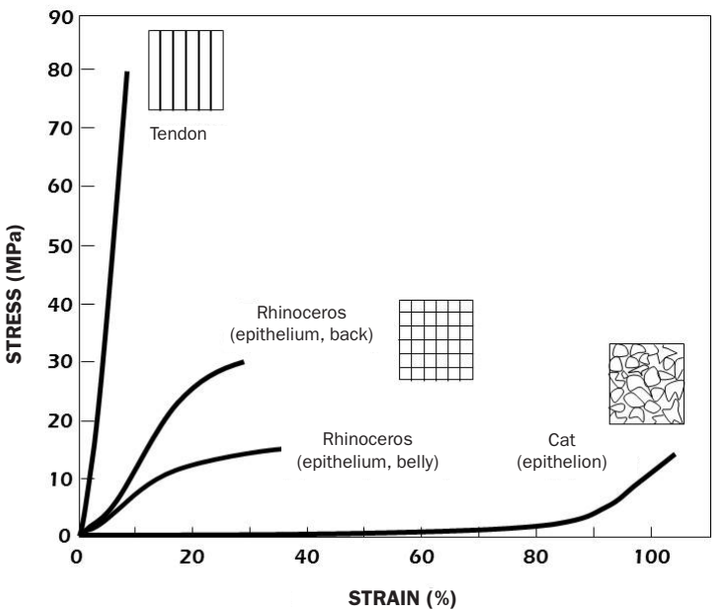

Fig. 5. *Schematic stress-strain curves as a function of the orientation of collagen fibres.*

In concluding this introduction to the epithelium it is worth elucidating some aspects of the structure of the *stratum corneum* because, although it is an excellent barrier for avoiding water loss, it is also a superb biosensor capable of initiating a series of biological processes to repair wounds and restore a homeostatic barrier.

The structure of the stratum corneum can be likened, in a simplified form, to a brick wall, in which the bricks are keratinocytes (cells which produce keratin) and the mortar a matrix of lipids. The keratinocytes play the role of protector against abrasion from external agents and the lipids are essential barrier elements which avoid water loss. The understanding of the biochemistry of the stratum corneum was facilitated by the diagnosis and treatment of various skin diseases which range from cosmetic problems –dryness, peeling– to more serious conditions, such as psoriasis or atopic dermatitis (Harding 2004).

Tissue engineering has achieved major success in the production of epithelia and has commercialised several products. One of the first, in 1997, was *TransCyte*, based on a degradable polymer scaffold on which skin keratinocytes grow. This product was a temporary protection until the skin regenerates. Nowadays, the fabrication of skin from a few donor cells is a reality. In the Unidad de Biomedicina Epitelial Ciemat Madrid, a team led by Dr. Jorcano produces skin for severe burns by cultivating epithelial cells on a fibrin matrix. This technique has been perfected in recent years, and the ultimate objective is to try to regenerate skin; which is functional and with all of its components, including glands and capillary follicles. The new technique of 3D bioimpression allows the design of structural scaffolds which, as well as being biocompatible and dissolvible, can be functionalised so that the cells that are seeded on them grow and differentiate properly (Cubo et al. 2016).

1.3. BLOOD VESSELS

This section is focused on the human cardiovascular system, although reference will also be made the blood vessels of other mammals.

The cardiovascular system is the means by which blood runs throughout an organism. The heart is the engine; it acts like a pump that pushes the blood through the arterial system and sucks through the venous system.

The arterial system is composed of a network of blood vessels called arteries which start in the heart and extend throughout the organism carrying oxygen and essential nutrients for the functioning of the cell, by means of the arterial blood. Moving further from the heart the calibre of the vessels become smaller; initially called arteries, then arterioles and, finally arterial capillaries.

The venous system consists of a network of vessels which, following a path parallel to the arterial network but in the opposite direction, carries de-oxygenated blood loaded with waste products –venous blood– back to the right cavities of the heart from which it will pass to the lungs to be oxygenated and converted to arterial blood. The veins gradually run together, progressively forming vessels of larger calibre, called capillary veins, venules and, finally, veins.

1.3.1 Structure

The structures of arteries and veins are shown, schematically, in figure 6. The arteries must support greater pressures and pressure fluctuations than veins due to the way in which the cardiovascular system works, and this is reflected in the their structure. Veins have less elastic and muscular walls because the blood circulates along their length due to the suction effect of the thorax and the pumping muscles in which they are embedded. Inside the veins there are valves which restrict the return of blood. In figure 6 it is shown that the structure of arteries and veins is formed of three layers or tunica; the *intima*, the *media* and the *adventitia* or exterior.

The *intima* layer is principally formed by endothelial cells, the *media* layer contains smooth muscular tissue cells, collagen fibrils and elastin, and the *adventitia* includes collagen fibres, fibroblasts, nerves and capillaries (except in the finest veins).

The composition and structure of blood vessels varies with size and type of vessel. The thickness of veins is, approximately, one tenth of its diameter, while the thickness of arteries is usually double that, about one fifth of their diameter. Thicker arteries, such as the aorta, contain elastic tissue that allows them to stretch during the systole (contraction of the heart, which launches blood into the arterial system) and contracts during the diastole (relaxation of the heart, during which it is filled with the venous blood). The arteiole walls contain less elastic tissue and deform less. The capillary walls are formed by a layer of endothelial cells and their diameter is so small that red blood cells can only just pass through them.

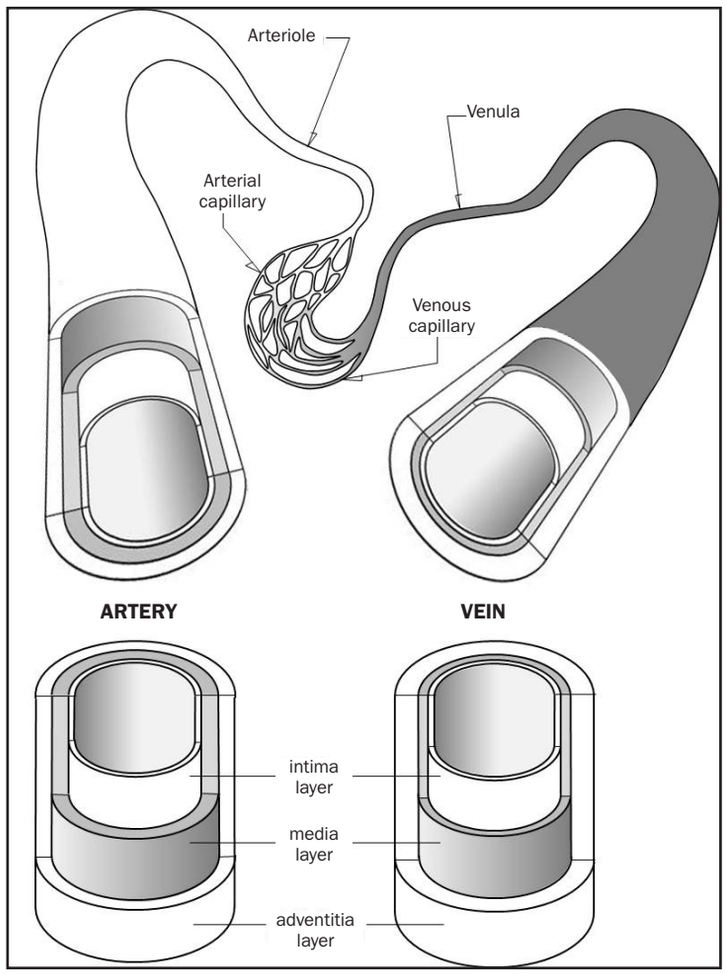

Fig. 6. *The structure of arteries and veins.*

The walls of arteries and veins consist of, approximately, 70% water, 15% collagen and elastin and the rest is smooth muscle fibre. In the aorta there is more elastin than collagen (more than 50%), and less elastin than collagen in the arterioles and veins (the proportions can be 50% in the arterioles and 30% in the veins). Veins always contain less elastin than the arteries. The percentage of smooth muscle is less in the aorta and increases in the more peripheral arteries and arterioles.

1.3.2 Mechanical properties

Knowledge of the mechanical properties of blood vessels should provide an understanding of their function and help prevent any dysfunction. Techniques for measuring the mechanical properties, modelling behaviour and describing the performance of the vessels will be discussed as this section progresses. For the moment, in order to pave the way, the itinerary that will be followed is indicated in the paragraphs below.

Due to the difficulties in testing blood vessels *in vivo* almost all experiments have been performed *in vitro*, with specimens extracted during surgical interventions or from cadavers, aiming to reproduce physiological loadings, a task that is not always straight forward because the vessels are subjected simultaneously to axial tension and internal pressure (which varies as shown in figure 7), and, in addition, having residual stresses in their walls.

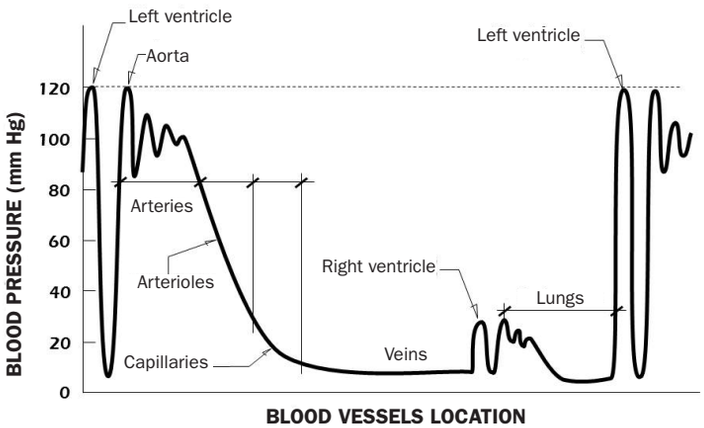

Fig. 7. *Pressure (mm Hg) in blood vessels as a function of their location.*

In order to understand the mechanical behaviour, to a first approximation, it can be assumed that blood vessels behave like a *membrane*; with no bending stiffness. Tensile tests, with specimens extracted in the longitudinal and circumferential directions (as indicated in figure 8), are the simplest. Stress-strain curves are obtained from these tests, and from relaxation or creep tests, as a function of time. Dynamic tests have also been performed on these types of specimens. For example, a study of the mechanical behaviour of the aorta of a dog, following these procedures, can be found in the article by Tanaka and Fung (1974). This information is note completely satisfactory because, in reality, the vessel tissue is subjected to biaxial loading, due to the blood pressure and the longitudinal tension, so it would be worth performing more representative tests. To this end various devices have been used to apply traction to the vessels and, at the same time, introducing internal pressure (see, for example, Froneck *et al*. 1976, or Guinea *et al*. 2005). Other devices, as well as loading the tube in tension and subjecting it to pressure can simultaneously twist it (Fung 1993, page 337). Biaxial tests performed on a coronary artery subjected to traction and internal pressure are shown in figure 8b in which the development of the diameter is shown as a function of the pressure.

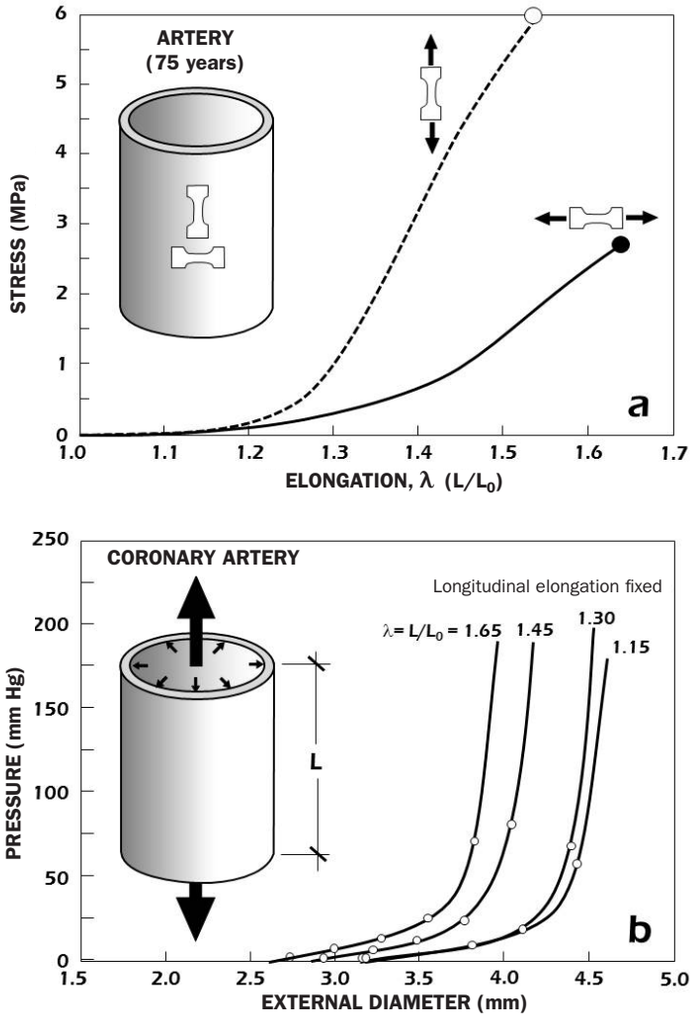

Fig. 8. *a) Engineering stress-elongation curves for an arterial blood vessel, in the radial and longitudinal directions.*
b) Internal pressure-external diameter curves for a coronary artery pulled to different values of λ, where $\lambda = L/L_0$ and L_0 is the initial length of the vessel. Note the dog-bone specimen geometry. (Claes, 2010)

More refined studies can be performed if the thickness and flexibility of the vessels need to be taken into account, that is to say they can be modelled as *laminas* subjected to traction, internal pressure and torsion. For these cases, experiments have been proposed that simulate a beam (the lamina) between on two supports or bending tests on a cantilevered beam (lamina) with an end load (Fung 1993, page 352, 355).

1.3.3 Final comments

All of this information is very useful for the diagnosis and treatment of diseases of the cardiovascular system. It is also helpful for modelling the mechanical behaviour of blood vessels and formulating the constitutive equations that allow reliable predictions of their functioning.

There are two types of accident that occur, unfortunately frequently, in human blood vessels. These will be reviewed and discussed in more detail below: *Ruptures* by longitudinal tearing and *aneurysms*, a biological degeneration which leads to a mechanical instability. The information derived from experiments indicates that the vessels possess a structure and are made of materials which are especially adapted to withstand these accidents thanks to the non-linear nature of the stress-strain curve, and the presence of residual stresses.

If blood vessels had a mechanical response in which the stiffness (slope of the curve), within the physiological range of pressures, decreases with increasing diameter, any local changes in the diameter of the vessel would provoke an instability, which gives rise to an increase in the diameter and the appearance of widening zone known as *aneurysm*.

Indeed, if the tube is not perfectly uniform, in a region in which the diameter was a little larger than those nearby a swelling will be formed—an aneurysm— because it is easier to dilate locally than become less stiff, leaving the adjacent regions (of smaller diameter, stiffer) unaltered. This is the behaviour of **elastomers** such as rubber, which is shown in figure 9, in which the phenomenon is clearly visible, for example the swelling of a cylindrical rubber balloon. On the other hand, if an increase in diameter of the tube increases its stiffness, as happens in arteries, instability will not be produced. The design of blood vessels, unlike that of rubber, protects it from that eventuality.

The shape of the stress-strain curve (or pressure-diameter, as will be discussed in detail later) is due to the structure of the vessels, formed of three layers of different mechanical properties, and the characteristics of their constituent materials; fundamentally elastin and collagen fibres. At very low pressures, of the order of 70 mmHg, only the elastin fibres work. The collagen fibres come into play little by little, and are those that carry the greater part of the load at high pressures.

Residual stresses in blood vessels make the stress in the wall more uniform, and allow support of greater pressures with less risk of rupture. The presence of residual stresses becomes apparent through a lateral cut in a circular section (as shown in figure 10) because the section opens spontaneously to a certain angle α, – known as the *angle of aperture*– being greater for greater residual stresses.

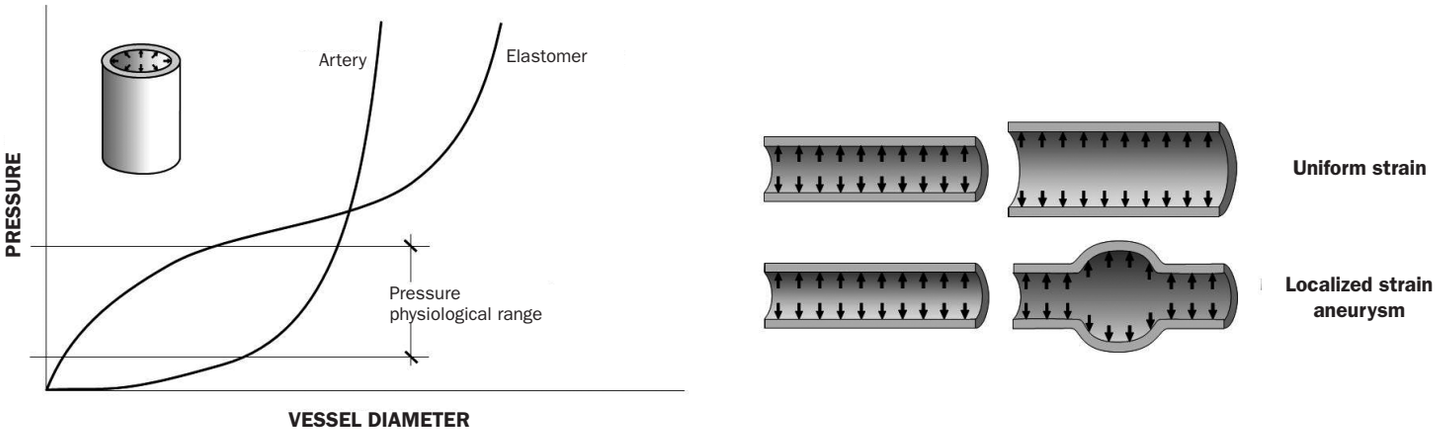

Fig. 9. *Schematic pressure-diameter curves for tubes of different materials; an elastomer and an artery. Inside the pressure physiological range, stiffness* ***(slope of the curve)*** *increases with the diameter of the artery whereas dicreases for elastomers.*

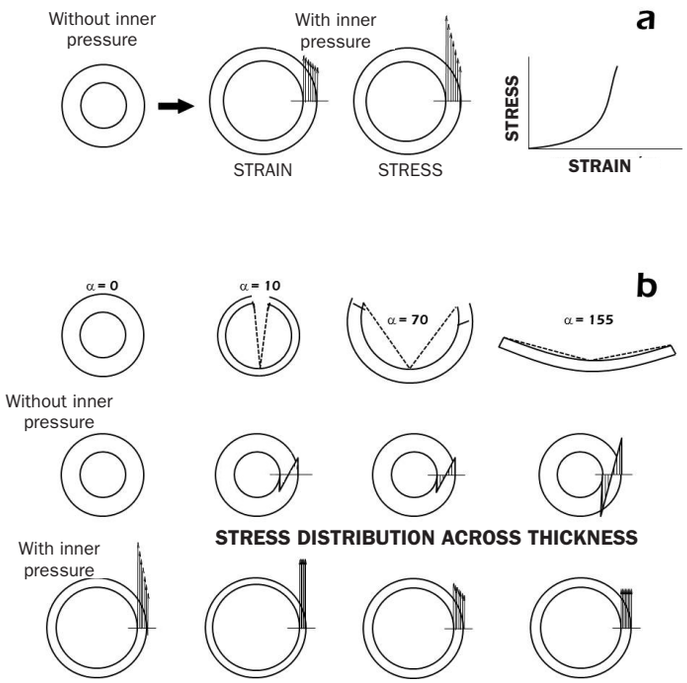

Fig. 10. *Distribution of through-the-thickness stresses in a blood vessel.*
a) Without residual stresses.
b) With residual stresses (which increase with the value of α).

The beneficial role of these stresses can be appreciated, using the following reasoning due to Fung (1993). Initially the occurrence of the residual stresses is due to the fact that the arteries have an appreciable thickness (the ratio of the radius to thickness is between 2 and 4) and the stress-strain relationship for the tissue walls is not linear, the stress increases much more rapidly than the strain (see the curve in figure 10a). When the arteries support the blood pressure (between 110 and 130 mmHg), the radius increases and the thickness decreases. In these circumstances the strain in the internal layers of the aorta is greater than that in the external ones (see figure 10a) and, since the stresses grow more rapidly than the strains, this effect is more marked in the distribution of stresses through the thickness. The beneficial role of residual stresses is shown in figure 10b, in which it can be seen that the distribution of stresses through the thickness becomes more uniform as the angle α increases. Depending upon the presence of the residual stresses (first column, figure 10b), the stress distribution through the thickness is quite ununiform when there is internal pressure, reaching very high values in the internal layers. Due to the increasing residual stresses (with increasing α) the superposition of the residual stresses and those due to internal pressure renders the total distribution more uniform through the thickness and the maximum values are reduced, so that the risk of rupture also reduces.

Pressure changes in the cardiovascular system can cause changes in the geometry, structure and mechanical properties of blood vessels, a phenomenon known as continuous structural adaption or *remodelling*. The causes of this process can be many; diseases, drugs, surgery, high salt diet, lack of oxygen (hypoxia), overpressure, lack of gravity, etc. An example of remodelling of the pulmonary artery of a rat due to increased blood pressure is described in Fung and Lin (1991). The authors observed that, initially (up to 12 hours), the *media* grew thicker while the *adventitia* hardly changed. After 95 hours, the *adventitia* had achieved the same thickness as the *media*, its thickening continuing over the next few days (between 10 and 20). Remodelling was also observed in the walls of the arterioles. In summary, they found that remodelling of the vessels is not uniform and proceeds quite rapidly; histological changes can be detected after a few hours and most of the remodelling had taken place after a couple of days. They also observed the variation of the α angle (and as a consequence the residual wall stresses) with change of pressure.

Tissue remodelling adds new parameters to the prediction of mechanical behaviour. Everything seems to indicate that the tissue cells live under stresses which modify their metabolism, internal structure, and the production or reabsorption of extracellular structures. Under normal conditions the organisms exist in dynamic equilibrium, called a *homeostatic state*. When there are changes in the external pressure the homeostatic state must re-balance through remodelling, that is to say by means of changes in the mass, structure and mechanical properties of the tissue.

Surgical repair of blood vessels consists of replacing the blocked or deteriorated section with an implant, or diverting the blood flow using a bypass. The grafted tissue may be natural, such as a piece of saphenous vein or internal mammary artery, from the actual patient or a donor, or artificial, such as Dacron. In both cases a knowledge of the mechanical properties is fundamental. Tissue engineering offers the possibility of constructing blood vessels *to-measure* for each patient, aiming to reproduce the mechanical and biological behaviour of the original material. This requires a scaffold which is biocompatible, biodegradable and functionalisable, to seed it with the appropriate cells of the patient and to allow them to grow and proliferate. Some success has already been achieved in the fabrication of blood vessels using this technique (Pashneh-Tala *et al.* 2016).

1.4. ANEMONES AND MEDUSAS

The apparent simplicity of the tissue of medusas and other marine animals has encouraged their study, with the aim of unravelling the relationships between structure and mechanical properties. The resistance of anemones and medusas to the ravages of the sea, despite their apparent fragility, has also motivated the study and the attempts to create fabrics with new features inspired by them.

1.4.1 Structure

Medusas and anemones are *cnidarians* –or flower animals– and, although they exist in different forms (figure 11), their organism has the same general arrangement. The body, with axial symmetry, has a wall formed of three layers: the external or ectoderm, the intermediate or *mesoglea*, and the internal or endoderm. In its interior, there is a gastric cavity with only one opening which functions as a mouth and an anus. This aperture is surrounded by a series of stinging tentacles (hence the name of the *cnidaria* phylum, from the Greek κνιδη, nettle).

Two forms can be observed inside the phylum: the *polyp*, which is adapted to the sessile, and the *medusa,* to the free pelagic life. Some aspects of the mechanical behaviour of the mesoglea of the polyp *Metridium senile* (a common anemone off the coasts of northeast Europe) and of the mesoglea *Rhopilema esculenta* (an edible medusa abundant in the Pacific Ocean) are discussed in this section.

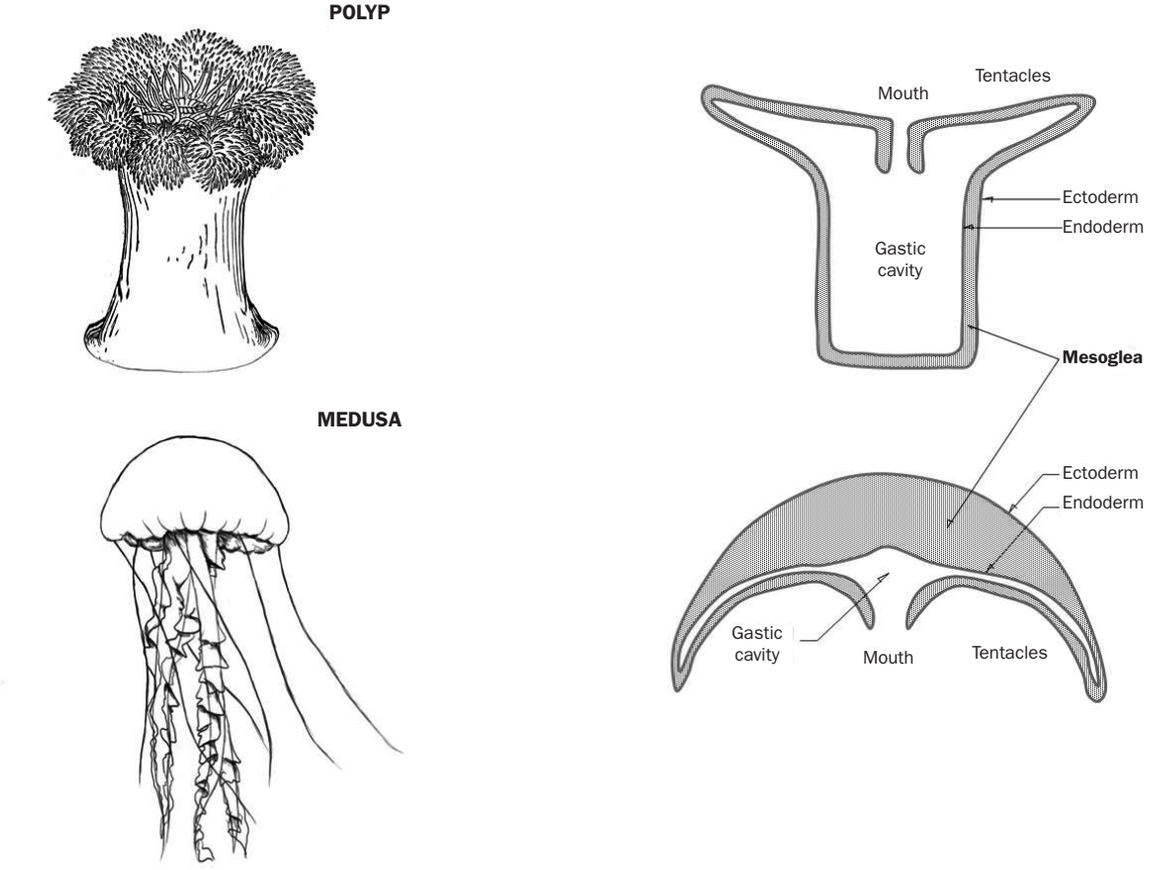

Fig. 11. *Transverse sections of an actinia and a jellyfish, in which the same general organisation is apparent. The mesoglea is show in both cases.*

1.4.2 Mechanical properties

Chapman (1953) observed that the mechanical properties of the body of anemones can be attributed only to the mesoglea, barely depend upon the muscle fibres. Alexander (1962) performed creep experiments on the mesoglea of the actinia *Metridium* and observed that under small loads the material deformed up to two or three times the initial length, and that it took about 15 hours to stabilise. On unloading the test specimen, and after a similar period of time, the material returned to its original length. Gosline (1971) continued these studies seeking a relationship between the structure and composition of the mesoglea and its mechanical properties. The following commentary has been extracted from the work of Gosline.

The mesoglea of *Metridium* can be considered as a composite of collagen fibres embedded in a matrix of polysaccharides and proteins (a gel with 2.4% solid contents). The composition of the mesoglea is, approximately; 6.7% collagen, 2% matrix, 5% salt and the rest, 86%, water. In terms of structure, (see figure 12) it is possible to distinguish two layers; an exterior in which the fibres are intertwined and another in which the fibres are more ordered radially and circumferentially. This structure suggests that the mechanical behaviour may be anisotropic, indeed this is observed in the tests discussed below.

Figure 12, shows the results of relaxation tests, at 23˚C, performed in different directions; longitudinal and circumferential. In both cases the stresses decrease with time reaching stability after about 15 hours. The previously mentioned anisotropy is clearly apparent in the experimental results.

Gosline has proposed a model for the mesoglea in which the intertwined (but not transversely connected) collagen fibres are embedded in an elastomeric matrix formed of a high molecular weight amorphous polymer. The matrix is responsible for the deformation and the elasticity of the mesoglea. The collagen fibres, whose role is to reinforce the matrix, are responsible for the initial stiffness, but the large deformability and the elastic recovery are due to the changes in the configurational entropy of the matrix polymer network. According to Gosline (1971), if the collagen fibres were transversely joined, the mesoglea could not deform more than 30% strain in the longitudinal and 55% in the circumferential direction. Alexander (1962) recorded strains of 200% in creep tests.

Another notable aspect of the mesoglea of the polyp *Metridium* is its scratch resistance; 1.2 kJ/m^2 (similar to that of bone, 1.7 kJ/m^2, or of the pig's aorta 1.0 kJ/m^2, but much lower than that of the epithelium of a mouse, 20 kJ/m^2). The measurements were made by Purslow (1983) by means of rupture by tear experiments which are described in detail in 2.2.2. The rupture strength of the mesoglea, like other highly deformable materials, is small, due in part to the elastic energy stored by deformation –which can cause rupture–.

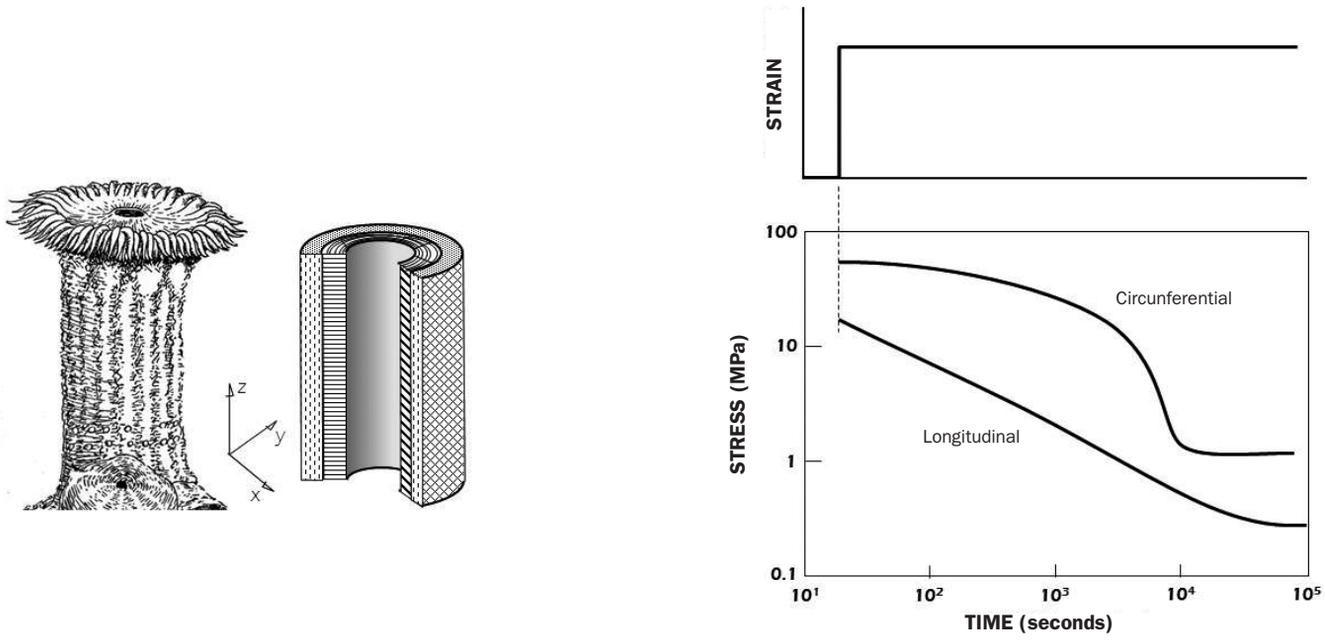

Fig. 12. *Relaxation experiments on the mesoglea of the polyp* Metridum s., *which illustrates the anisotropic character of the material. (Gosline, 1971).*

Another biological material with these characteristics –simple soft membranes– is the mesoglea of medusa. It is curious that this material –which is 97% water– has mechanical properties that withstand the ravages of the sea without suffering harm. Once again, with this type of relatively simple gel, the challenge is to study the relationship between the structure and properties, and to design and fabricate hydrogels with better mechanical properties.

For this purpose, Zhu *et al*. (2012) investigated the mesoglea of the edible medusa *Rhopilema esculentum*, of the rhizostomatidae family. The bell –or umbrella– of the medusa is composed of three layers, as shown in figure 11; the exterior or ectoderm, the intermediate or *mesoglea,* and the interior or endoderm.

The structure of the mesoglea is outlined in figure 13. It is formed of fine laminas, stacked parallel to the surface of the bell, connected by nanofibers whose diameters range from 20 to 50 nm. In terms of chemical composition, it is 97% water and the rest is composed of (type II) collagen fibres and unsaturated fatty acids.

The mechanical properties of the mesoglea were obtained from uniaxial tensile and compression tests, whose details can be found in the cited reference. A schematic representation of the specimens used in each case is shown in figure 13, as are the direction of loading and the results obtained. It can be seen that the tensile rupture load is around 0.20 MPa and the corresponding strain is about 100%. In the compression test, the rupture load approaches 2.0 MPa and the strain is around 86%. These results are better than those for most synthetic hydrogels with similar water content, and even less. Despite its apparently simple microstructure –thin sheets of interlocked fibres– there is no satisfactory model for prediction of the mechanical properties of the mesoglea. On the other hand, and bearing in mind the considerations made in previous sections, it would be very useful to have biaxial experiments for a more reliable database.

1.4.3 Final comments

Hydrogels are networks of three-dimensional hydrophilic polymers which can retain considerable amounts of water. Synthetic hydrogels have numerous applications in biomedicine and pharmacy, but their mechanical properties are poor and seldom appropriate for applications that involve support of mechanical forces. To this end it would be desirable to develop more resistant hydrogels inspired by the structure of the mesoglea of medusas.

The locomotion of medusas is quite unique; it is based on successive contractions and expansions of the bell, produced by striated muscles similar to those of vertebrates. Even though it has not yet been possible to fabricate a synthetic mesoglea, it has been possible to make an artificial medusa capable of replicating its movements (Nawroth *et al*. 2012). For that, a sheet of cells from the heart muscle of a rat was grown –which contracts under the stimulus of an electric current– combined with a silicone polymer layer –which is elastic and allows the recovery of the initial geometry when the current stops–. On applying an electric field to the *artificial medusa*, it contracts imitating the impulse of real medusas. It even creates a stream of water which could attract food near where the mouth would be.

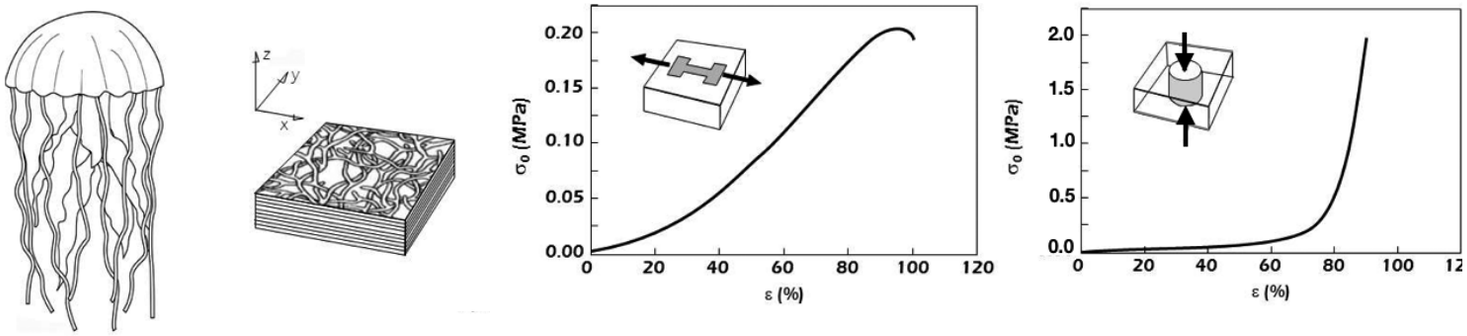

Fig. 13. *Stress-strain curves of the mesoglea of the medusa* Rhopilema esculentum, *in the radial and transverse directions, which illustrate their anisotropic character (Zhu et al., 2012).*

1.5. NATURAL ARMOURS

1.5.1 Evolution of armours

Natural armours are another type of biological membranes and laminas. Not as flexible as those mentioned above, natural armours have evolved over time to provide living beings with protection against external threats.

Fossils of fish covered in hard plates (*placodermos*) have been found. These creatures lived in, and dominated, the seas 420 million years ago, and became extinct towards the end of the Devonian period. These creatures had large plates which were juxtaposed and, although they provided a protective shell, the plates impeded mobility and locomotion. Fossils of these fish of more than eight metres long have been found.

Armour plates have evolved to improve mobility while maintaining their protective qualities. Within the gnathostomata (jawed mouth) there are two classes; the chondrichthyes (with cartilaginous endoskeleton) and osteichthyes (with skeletal bone) (figure 14).

The chondrichthyes (sharks and rays) appeared 400 million years ago and have bodies covered in *placoid* scales partially embedded in the skin. As well as the protective function, placoid scales reduce the drag resistance and accommodate various cutaneous and light organ sensor systems.

Osteichthye fish appeared in the late Silurian period, also around 400 million years ago. Osteichthyes are divided into two subclasses; sarcopterygians (lobe-finned) and actinopterygians (ray-finned) (figure 14).

Most fish are now actinopterigii and their scales differ from those mentioned above. Primitive ones, called *ganoids*, are typical of the most basal bony fish, such as sturgeons. They are composed of bone and enamel (ganoine), they look like rhomboidal shields and are arranged in the skin like pavement slabs. The other bony fish have *elasmoid* scales (due to the presence of elasmoidine) of two types; *cycloid* and *ctenoid.* The former have smooth edges and the latter jagged, which gives them a rough texture. These two types of scales are not arranged like mosaic tiles but are imbricated, like roof tiles. The free edge is directed towards the rear of the fish to reduce water resistance during swimming.

In the past sarcopterigii occupied every aquatic ecosystem on the planet, but they now are restricted to the freshwaters of Africa, South America and Australia, as well as the marine waters of the Indian Ocean, where there are only two species. The coelacanth, the famous “living fossil”, belongs to one of them. One group derived from the sarcopterigii, the tetrapods, (figure 14), has colonised all terrestrial environments of the planet; these are amphibians, reptiles, birds and mammals. These, also, have developed natural armours.

Turtle are reptiles; more accurately, chelonia. Mammals which appeared towards the end of the Triassic period, about 200 million years ago. The shell of turtles is formed of hard bony plates which protects them against the attacks of predators; cats, crocodiles, sharks and, even, birds which can scratch, bite or peck them. They must also withstand hard impacts, when eagles seize them and drop them on rocks to break their shells. This armour is very strong but not very flexible.

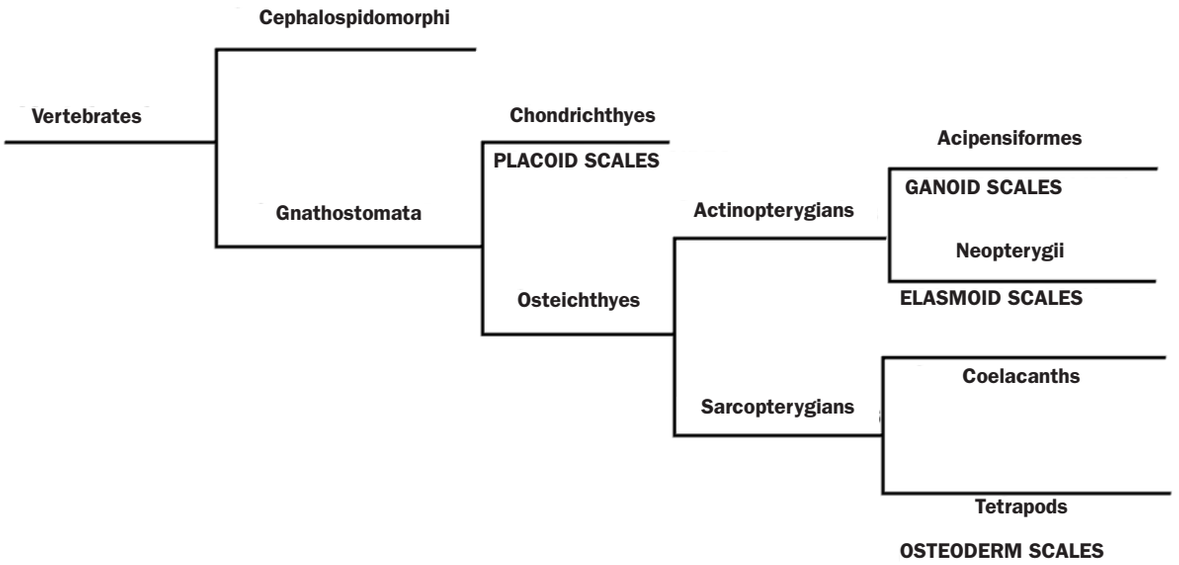

Fig. 14. *Types of scales and their position in evolution.*

Other reptiles which are coated in armour are crocodiles, whose ancestors appeared in the Triassic period, about 180 million years ago, and who lived alongside the dinosaurs. This long lineage has now been reduced to just three families; gavials, crocodiles and alligators. They all have armoured skin. Although they rarely encounter dangerous enemies, they need their armour to defend their territory from members of their own species because their bites can be fatal. Compared to turtles, their armour is more flexible and it gives them greater agility to capture prey. In former times, some warriors created armoured breastplates from crocodiles to protect themselves from arrows and pointed objects.

Mammals have also developed natural armour during their evolution. In particular, within the order of edentata, a group of armadillos (whose name is spanish, already indicates that function) and pangolins. Some edentates in the relatively recent past were much more impressive than current ones. Glyptodonts, which became extinct about 10,000 years ago, were a mammalian version of land turtles and reached weights of several tons. They were equipped with a golf ball like shell, made of dermal bones. They achieved great success and diversity; originating in South America, they spread into southern North America.

Pangolins are one of the few remaining representatives of armoured edentates. They live in tropical and subtropical regions of Africa and Asia. Their scales are *imbricated* and cover the major part of their skin. This arrangement provides great flexibility than other reptiles whose plates are *juxtaposed* and connected by collagen fibres. When threatened the pangolin curls up into a ball and it sticks out its exterior scales, like a half-open pine cone, protecting it and hurting the attacker. The distribution of the scales on the pangolin has inspired the design of armour since ancient times. In 1820, the United Kingdom's King George III was presented with a coat made of pangolin scales.

Armadillos are another living group of armoured edentates. They live in South America and the lower part of North America. Armadillos are covered in bony plates, called *osteoderm*, which protect them from predators, in particular, when the animal rolls up into a ball.

1.5.2 Composition and structure

The ingredients available for living species to fabricate armours have been limited; cell secretions (which provide collagen fibres) and minerals (principally calcium, in the form of carbonates and phosphates).

To a large extent, the elements of natural shields are formed of two layers; the very hard exterior provides protection against impact and the tougher interior provides strength. However, the strength of the plates is provided, to a large extent, by the hierarchical structure of the components.

The exterior layer is formed of highly mineralised tissues, which are hard, avascular and with little or no collagen. The most common tissue is *enamel* and another is *ganoin* which covers the scales of some bony fish. The enamel which covers the teeth is the same as that which we share with other tetrapod animals and fish. A recent study (Qu *et al*. 2015) suggests that enamel may have its origin in primitive fish scales, because a genetic analysis identified a link between *ganoin* and *enamel* matrices .

The interior layer is formed of mineralised collagen fibres within a mineral matrix. Depending on the grade of mineralisation and the distribution of the collagen fibres several types of structures have been identified; *dentin, elasmoidine,* and *lamellar bone*, among others (Sire et al. 2009).

The microstructure and composition of the plates vary according to the species considered. The three examples selected –*ganoid* scales*, elasmoid* scales, and *osteodermal* plates– give an idea of the structures which nature has developed to protect animals (Yang *et al.* 2013a)

The fish *Atractosteus spatula* provides an example of the structure of *ganoid* scales. It is one of the largest fresh water fishes in North America, reaching a length of three metres and weighing 100kg when fully grown. The scales are formed of two layers (figure 15a). The external layer, called *ganoine*, which has a thickness of 0.5 mm in adults, is hard and composed of hydroxyapatite crystals. The internal layer is thicker, about 3.5 mm, and formed of sheets of dentine, elasmodine and bone tissue. Native Americans value these scales and use them as adornments.

The *Arapaima gigas* is another large freshwater fish, reaching lengths of 2.5 metres and weighing 150 kg, it inhabits the Amazon river, and has elasmoid scales. In the adult, the scales can approach a length of 100mm and width of 40 mm. They are also formed of two layers, (figure 15b). The external layer can have a thickness of 0.6 mm and the internal one 1.0 mm. The external layer is highly mineralised and rough. The internal layer contains collagen fibres which are arranged in parallel planes. The planes can be stacked in a helical

form, creating a structure called *Bouligand* (Bouligand, 1972) which confers great rigidity. The scales can be considered as a multifunctional protector; the external layers provides hardness and wear resistance and the internal layer flexibility and toughness.

A mammal, the armadillo *Dasypus novemcintus* is covered with hexagonal plates called *osteoderms*, which can be translated as "bone skin". It is the same protection used by some reptiles (crocodiles and turtles). O*steoderms* in turtles form part of their skeleton, in other animals they form part of the skin and are vascular. Once again, two layers can be identified in these plates: The exterior or epidermis, is of α-keratin which provides stiffness and sealing. In the interior layer three regions can be observed; the first is dense and bony, the middle is porous bone and the inner is, again, dense bone (figure 15c). This structure– dense bone, porous bone, dense bone– is frequently seen in animals which need strength and energy absorbing capability combined with lightness, that is to say low density.

It is interesting to compare the similarities between the structure and properties of armours of turtles and armadillos because they fulfil a common function –both provide protection against predators– despite important differences, in turtles the dorsal plates include vertebrae and ribs, and in armadillos both are inside and separate from the plate. Even so, the connections between the plate and its structure are very similar. In both creatures the plates are interconnected by collagen fibres to provide a degree of flexibility to the shell, although the arrangement of the sutures in turtles is more complicated than that of armadillos. The structure is similar in both cases; dense bone, porous bone, dense bone. Since turtles and armadillos belong to the different families –reptiles and mammals– it is interesting to note that their evolutions converged on similar solutions to the problem of protecting these animals from predators.

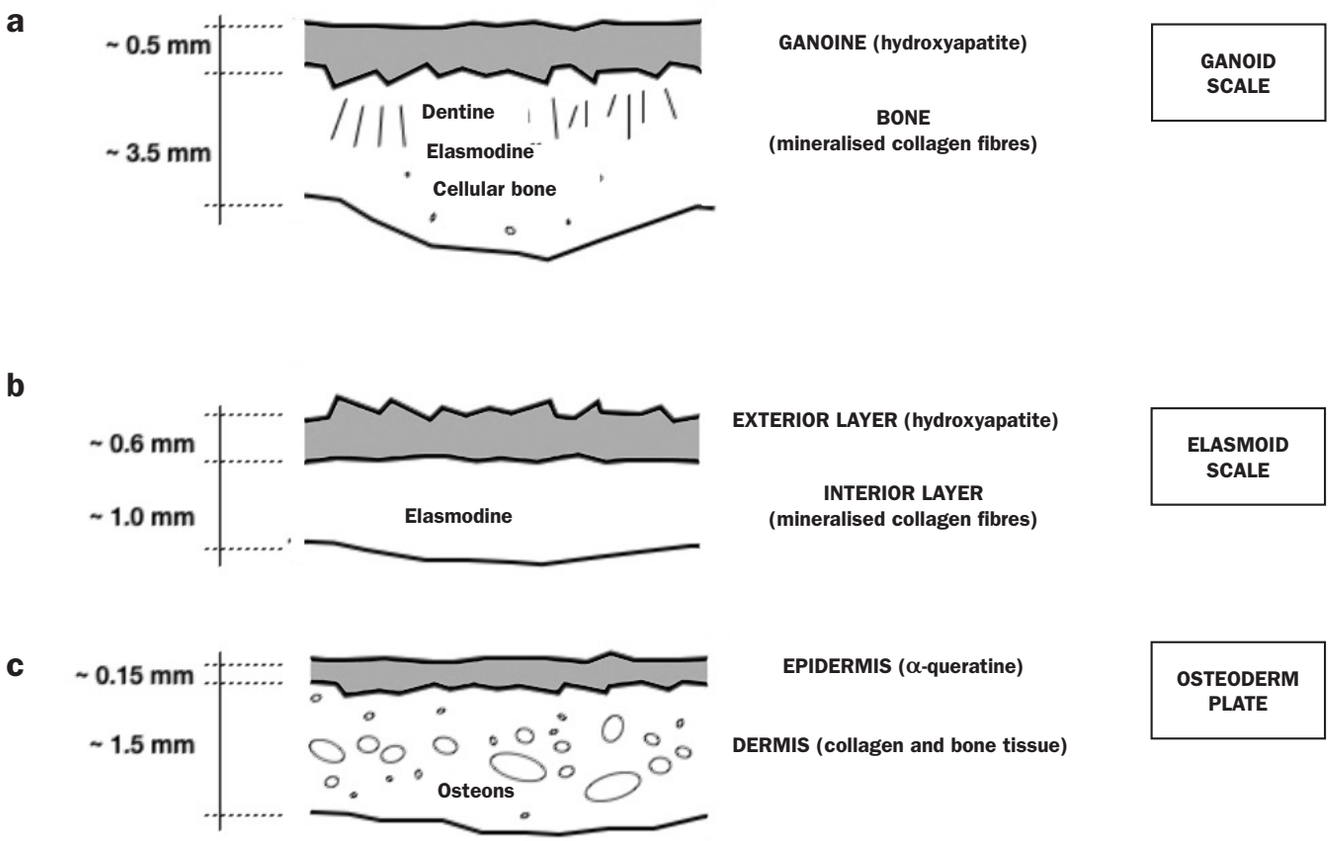

Fig. 15. *Greatly simplified schematic sections of two types of scales (ganoid and elasmoid) and a bony plate*

1.5.3 Mechanical properties

Living beings have developed materials for protection against external threats over millions of years. These materials – which form plates and scales– have excellent mechanical properties, even though their components are soft and brittle (Hydroxyapatite and collagen, for example).

The function of natural armours is two-fold; to provide protection and, at the same time, sufficient flexibility to allow the movement. In particular, the components of the armour are materials which possess high hardness, resistance to indentation and tenacity. It is difficult to characterise these properties because the plates and scales are small, thin, and heterogeneous. All this means that the traditional techniques for measuring strength, fracture toughness or resistance to indentation provide results that are difficult to interpret.

The tensile strengths of scales or bony plates have been measured by extracting dog-bone specimens in the longitudinal (direction of movement of the fish, for example) and transverse directions, with the aim of detecting anisotropy. Humidity affects the results; tensile tests with dry specimens produce higher rupture values and lower strains. Temperature also has its influence on the test results.

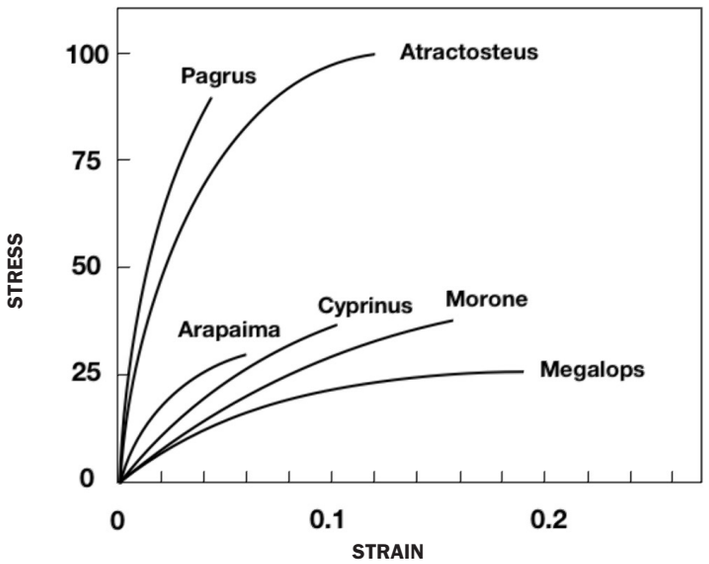

Fig. 16. *Tensile tests on fish scales, in a humid environment, at ambient temperature and in a direction parallel to the body. Approximate mean values due to the large spread in results. Engineering stresses and strains. Pagrus (Ikoma, 2003). Atractosteus (Yang, 2013b). Arapaima (Yang, 2014). Cyprinus (Cugno, 2012). Morone (Zhu, 2012), Megalops (Murcia, 2018).*

Figure 16 contains the tensile test results for various scales, performed in a humid environment and at ambient temperature. The aim of the graph is to provide an idea of the values but these should be treated with caution, since the tests produce results with a great deal of scatter (consult the cited references for details). Tensile test with specimens taken from bony plate provide different values according to the degree of humidity, for example; in a humid environment; 40 MPa (pangolin) or 13 MPa (turtles and armadillos), in a dry medium 70 MPa (pangolin) or 23 MPa (turtles and armadillos). Once again these are only indicative values.

The resistance to penetration and the toughness of scales has caught the attention of researchers. For example, M A Meyers and co-workers studied the protection capacity of the scales of *Arapaima gigas* against bites from the piranha *Sarrasalmus manueli*, because both fish live in the Amazon basin and coexist in harmony (Meyers *et al.* 2012). The aforementioned investigators performed penetration experiments with the teeth of the piranha on the scales of the arapaima. The results showed that the teeth of the piranha were not capable of penetrating the exposed part of the scales; the teeth broke and remained embedded in the scales without the power to penetrate further. The external layer of the highly mineralised and very hard scales played a fundamental role in protecting the arapaima from the bites of the piranha. In some cases, the external layer could break, owing to its hardness and the pointed form of the teeth, leaving the collagen laminae exposed. If the teeth continued to penetrate, they would separate the collagen fibres in the layer but meet the next layer with collagen fibres in another direction (the Bouligand structure, mentioned above) which slow down further progress. This is the basic mechanism which provides toughness to ctenoid scales.

Attempts have been made to estimate the toughness of some scales using standard tests with pre-cracked specimens (these tests will be discussed later in this book). As these are anisotropic, heterogeneous and hierarchical materials, it has only been possible to obtain indicative values which are difficult to interpret.

Microhardness tests suffer from the same difficulties mentioned above, but provide comparative values for various types of scales and predator teeth, such as in the example cited for the piranha and the arapaima.

1.5.4 Artificial armours

Since ancient times, hardness of scales and their distribution over the skin –imbricated or juxtaposed, providing some degree of flexibility to movement– have inspired the fabrication of body armour for human beings.

The origins of the these artificial armours go back more than four thousand years; remains were found in the tomb of Kenamon, who lived in Egypt during the reign of Amenotep II (1436-1411 BC). The Seythians had coats with iron or bronze scales stitched onto leather vests. The best documented ancient armours are those of the Roman Empire (Bishop and Coulston, 2006). Armour scales (*lorica squamata*) were formed from small metal plates sewn into a supporting fabric. The scales, fabricated from a copper alloy, had dimensions of about 15 mm long by 13 mm wide, joined together by wires and then sewn to a linen cloth using threads of the same material. While being less flexible than a chain mail, they were, however, popular throughout the roman period. In the Far East, fish scales also inspired a means of protection; Japanese armours (*gyorin kozane* or *kozane do*) were similar to those described above although the laminas were made of leather, *kozane* means scale, and their early versions date to the Fujiwara period (XI century). In these cases, the scales were fabricated from materials which were more available; copper alloys, iron, leather (raw or boiled), horn, seeds or pangolin scales.

Nowadays, the strategies developed by nature for making armours continue to inspire the fabrication of artificial armours. Armours based on polymers have the advantage of flexibility and lightness but lack the required hardness for some situations (Rudykh *et al*. 2015, Funk *et al*. 2015). When hard elements are incorporated, such as in *Dragon Skin* armour with ceramic plates, mobility is reduced. Other armours can be found which are more flexible, imitating armadillo shell (Chintapalli *et al*. 2014). In that case, hexagonal glass is used on a rubber base. The mechanical properties of the skin of fish continues being an attractive model for developing more flexible light armour, particularly when scales with greater resistance to penetration, a good linking system and tough elastic substrate are available.

2 CHAPTER Mechanical properties

2.1. INTRODUCTION

In order to use a biological material for structural purposes, it is ideal is to have its constitutive equation. This equation allows a knowledge of the mechanical response of the material (the strain as well as the stress state) under external loading (forces, pressure, displacements, temperature, humidity etc.).

This objective is not easy due to the complexity involved, and to achieve it requires experimentation. For that it is essential to define precisely the relevant variables, design the experiment properly, and to know how to interpret the results correctly.

The bi-dimensionality further complicates the study and interpretation of experiments on biological materials in the form of membranes. Familiarisation with the basic concepts outlined below requires considerable effort, but this is necessary for when the reader comes across specialist articles which take for granted, for example, a knowledge of the *Green-Lagrange* strain tensor or the *Piola-Kirchhoff* stress tensors.

To this end the structure of this chapter is: In the first place, the concepts required to describe the stress-strain behaviour of the material. Then, some experiments are described, which provide data for the characterisation of the material, attempting to accompany the exposition with simple examples that can facilitate the assimilation of the basic concepts of continuum mechanics. In this book there is no room to expand upon these notions, and the interested reader may consult, for example, the books of Y.C. Fung (1993), J.D. Humphrey (2002), G. A. Holzapfel or F.M. Capaldi (2012).

The exposition is completed by presenting the most common experiments used to characterise these materials; biaxial tension, rupture by tearing, and simple peeling or by pressurisation tests. The information obtained from these is essential for the formulation of the constitutive equations that define the mechanical behaviour of soft materials, and very valuable for understanding the relationships between their microstructure and mechanical properties. It is also very useful in the field of medicine; for regenerative surgery, for transplants and to feed into computer programmes in robotic surgery.

2.2. MECHANICAL BEHAVIOUR

2.2.1. Pseudo-elastic materials

The mechanical behaviour of soft biological materials is far from being elastic; the deformations depend upon the loading history, do not usually recover, and when they do they depend upon time. All of this makes it very difficult to establish a one-to-one relationship between stress and strain; when subjected to cyclic loading and unloading they exhibit **hysteresis** (the unloading curve does not coincide with that of loading, and for the same value of strain there are two possible values of stress), if the strain is held constant the stress **relaxes** with time, and if the stress is kept constant the strain increases (**flows**) with time. If, in addition to these difficulties we add, among other inconveniences, anisotropy, heterogeneity and the influence of the age of the tissue, the mathematical formulation of a model of mechanical behaviour is greatly complicated.

However, under cyclic testing a soft biological tissue exhibits a phenomenon known as *accommodation* which often allows the proposition of an approximate constitutive equation. Accommodation means that, after several loading and unloading cycles, the hysteresis loop does not change, and the stresses and strains always follow the same path. When that happens and the hysteresis cycle (for a given strain rate) is stabilised, it is said that the specimen has been *preconditioned*. In these cases, the relationship between stress and strain is unique, repeatable and predictable. The relationship between the stress and strain is **unique** –both for the *rising load* branch and the *unloading branch*– if the branches are considered separately.

As the stress and strain have a one-to-one relationship in each branch of the hysteresis loop it is possible to treat the material as if they were two different *elastic* materials; one for the loading process and the other for that of unloading. This idea, due to Y. C. Fung, allows use of the tools of elasticity to model the behaviour of *preconditioned* materials. In order to avoid possible confusion with truly elastic materials, Fung has proposed calling them **pseudo-elastic.**

Bear in mind that pseudo-elasticity is not an intrinsic property of the material, it is merely a convenient description of the relationship between the stress and strain in a cyclic loading process, which is valid only up to the level of the maximum load reached in a preconditioning cycle and, most often, for a given strain rate.

The key kinematic concepts and the state of stress used for characterising the mechanical behaviour of membranes subjected to biaxial loads are summarised below. The aim of this exposition is to delve a little into the concepts and definitions that the reader will meet when they analyse experimental results or constitutive equations. A rigorous development of these concepts would take us beyond the purpose of this book. Interested readers can usefully consult the already quoted books as well as the article of M. Sacks (2003). The following definitions are intended only as a guide to assist the reader of works related to this topic.

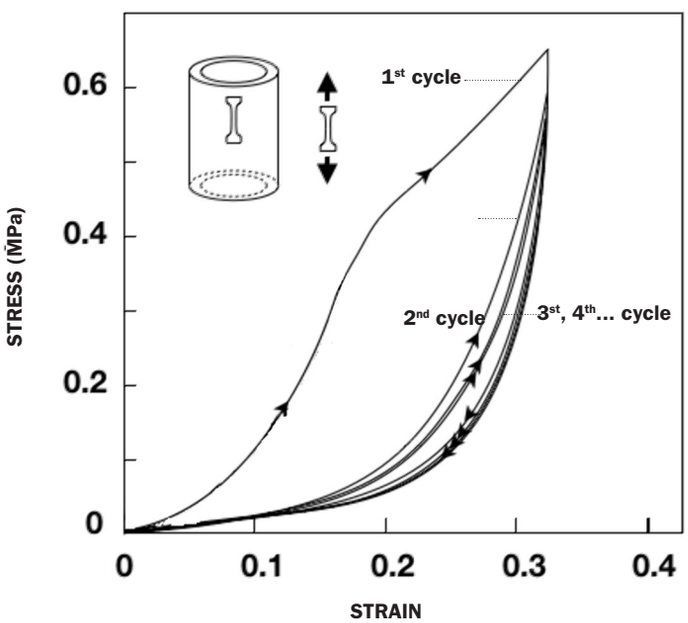

Fig. 17. *Cyclic true stress-strain curves from human thoracic aorta specimens (adapted from Horry et al. 2010). The material shows a very important hysteresis loop which reduces notably after a few cycles, attaining a stable repeatable behaviour.*

2.2.2. Strain and stress

Strains and strain tensor

Consider a *two-dimensional* continuous body formed by a set of particles. The simultaneous position of all the particles is called the *configuration,* and the position $\mathbf{X}$ of all the particles which occupy a space Ω_0 at a certain time (see figure 18) is the *reference* configuration. In what follows, capital letters $\mathbf{X}$ are used to denote the position vectors of points in the reference configuration, which is the configuration with respect to which displacements or strains are measured.

When an external load or displacement is applied to the body, it may deform and the positions of the particles change. The *deformed* configuration, which now occupies a space Ω, is the set of the new positions $\mathbf{x}$ of the points, and lower case letters are used for this situation (as indicated in figure 18).

The relationship between the values of the points in the deformed configuration $\mathbf{x}$ and the values of the reference configuration $\mathbf{X}$, is provided through the equation of motion

$$\mathbf{x} = \boldsymbol{\kappa}(\mathbf{X},t) \tag{1}$$

Each point in the reference configuration must have a corresponding point in the deformed configuration and vice versa. This implies that there must be an inverse function

$$\mathbf{X} = \boldsymbol{\kappa}^{-1}(\mathbf{x},t) \tag{2}$$

which allows us to obtain the position of a point in the reference configuration when its position in the deformed configuration is known.

The *displacement,* **u**, de un punto material, *P*, is the difference between the deformed position $\mathbf{x}(\mathbf{X}_p,t)$ and the reference position $\mathbf{X}_p$, that is to say:

$$u(\mathbf{X}_P,t) = \mathbf{x}(\mathbf{X}_P,t) - \mathbf{X}_P \tag{3}$$

This is the *material* (or Lagrangian) description of displacement, where the independent variables are the coordinates of the reference configuration and time.

It is also possible to write the displacement as a function of the variables in the deformed configuration and time, which is known as the *spatial* (or Euclidian) description in the form:

$$u(\mathbf{x}_P,t) = \mathbf{x}_P - \mathbf{X}(\mathbf{x}_P,t) \tag{4}$$

Figure 18 illustrates these concepts and allows us to advance a little further into the ideas related to the deformation of a body.

Suppose that the points P(X_1, X_2) and P'(X_1 + dX_1, X_2 + dX_2) (in Ω_0) are very close to each other, if the body is continuous, after deformation the corresponding points Q(x_1, x_2) and Q'(x_1 + dx_1, x_2 + dx_2) (in Ω) will also be close. The vector $d\mathbf{X}$ =(dX_1, dX_2) in the initial (or reference) configuration will be transformed into the vector $d\mathbf{x}$=(dx_1, dx_2) of the deformed (or instantaneous) configuration. We can calculate the vector $d\mathbf{x}$ from $d\mathbf{X}$ by means of equation (1):

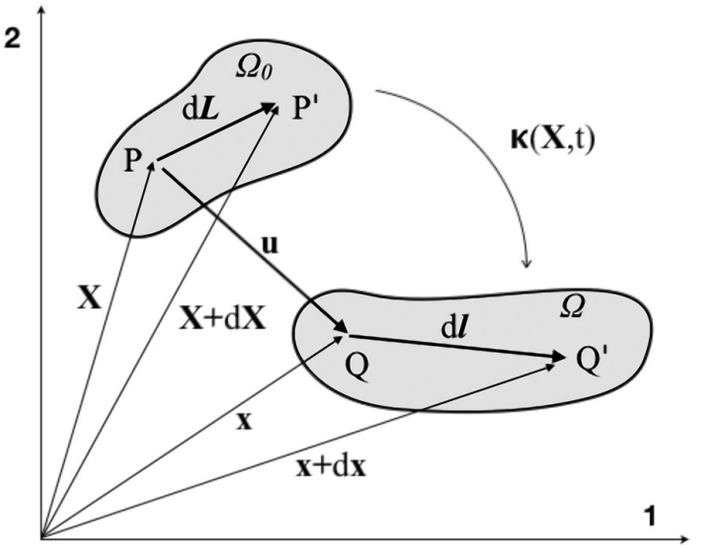

Fig. 18. *Notation used in the reference Ω_0, and the deformed Ω configurations.*

$$d\mathbf{x} = \frac{\partial \boldsymbol{\kappa}(\mathbf{X},t)}{\partial \mathbf{X}} d\mathbf{X} = \mathbf{F} d\mathbf{X} \tag{5a}$$

Expression (5a) defines the *deformation gradient tensor* $\mathbf{F}$, which contains all of the information needed to determine the relative position $d\mathbf{x}$=(dx_1, dx_2) of the material particles from their initial separation $d\mathbf{X}$=(dX_1, dX_2):

$$\begin{bmatrix} dx_1 \\ dx_2 \end{bmatrix} = \begin{bmatrix} \frac{\partial \kappa_1}{\partial X_1} & \frac{\partial \kappa_1}{\partial X_2} \\ \frac{\partial \kappa_2}{\partial X_1} & \frac{\partial \kappa_2}{\partial X_2} \end{bmatrix} \begin{bmatrix} dX_1 \\ dX_2 \end{bmatrix} \quad \text{or} \quad dx_i = \frac{\partial \kappa_i}{\partial X_j} dX_j = \frac{\partial x_i}{\partial X_j} dX_j \tag{5b}$$

in which we have assumed a cartesian coordinate system. To simplify writing, and in what follows, we will use the Einstein summation convention in which a repeated index indicates the sum of the terms over all of its possible values.

In a similar manner, we can obtain $d\mathbf{X}$ from $d\mathbf{x}$ using equation (2)

$$d\mathbf{X} = \frac{\partial \boldsymbol{\kappa}^{-1}(\mathbf{x},t)}{\partial \mathbf{x}} d\mathbf{x} = \mathbf{F}^{-1} d\mathbf{x} \quad \text{or} \quad dX_i = \frac{\partial X_i}{\partial x_j} dx_j \tag{6}$$

It is useful to know, for reasons which will become apparent later, how an infinitesimal length between two infinitely close points, such as *P* and *P'* in figure 18 deforms. For that we look for a relationship between the *reference* dL and the deformed dl segments, whose magnitudes are given by:

$$(dL)^2 = d\mathbf{X} \cdot d\mathbf{X} = dX_1^2 + dX_2^2 \tag{7}$$

and

$$(dl)^2 = d\mathbf{x} \cdot d\mathbf{x} = dx_1^2 + dx_2^2 \tag{8}$$

Taking into account equation (6) we obtain

$$\left(dL\right)^2 = \frac{\partial \boldsymbol{\kappa}^{-1}}{\partial \mathbf{x}} d\mathbf{x} \cdot \frac{\partial \boldsymbol{\kappa}^{-1}}{\partial \mathbf{x}} d\mathbf{x} = \left(\frac{\partial \boldsymbol{\kappa}^{-1}}{\partial \mathbf{x}}\right)^T \frac{\partial \boldsymbol{\kappa}^{-1}}{\partial \mathbf{x}} d\mathbf{x} \cdot d\mathbf{x} \tag{9}$$

where the superscript $(^T)$ indicates the transposed tensor. The above expression becomes, in cartesian coordinates,

$$(dL)^2 = \delta_{ij} \cdot dX_i \cdot dX_j = \delta_{ij} \frac{\partial X_i}{\partial x_l} \frac{\partial X_j}{\partial x_m} dx_l dx_m =$$

$$= \frac{\partial X_i}{\partial x_l} \frac{\partial X_i}{\partial x_m} dx_l dx_m \tag{10}$$

where δ_{ij} equals 1 if $i=j$, and 0 if $i \neq j$. From equation (5) we also have

$$\left(dl\right)^2 = \left(\frac{\partial \boldsymbol{\kappa}}{\partial \mathbf{X}}\right)^T \frac{\partial \boldsymbol{\kappa}}{\partial \mathbf{X}} d\mathbf{X} \cdot d\mathbf{X}$$

and

$$\left(dl\right)^2 = \frac{\partial x_i}{\partial X_l} \frac{\partial x_i}{\partial X_m} dX_l dX_m \tag{11}$$

The difference between the squares of the deformed segment dl and the reference segment dL, can be written as:

$$\left(dl\right)^2 - \left(dL\right)^2 = 2\mathbf{E} d\mathbf{X} \cdot d\mathbf{X} \quad \text{ó} \quad \left(dl\right)^2 - \left(dL\right)^2 = 2E_{ij} dX_i \cdot dX_j \tag{12}$$

or,

$$\left(dl\right)^2 - \left(dL\right)^2 = 2\eta d\mathbf{x} \cdot d\mathbf{x} \quad \text{ó} \quad \left(dl\right)^2 - \left(dL\right)^2 = 2\eta_{ij} dx_i \cdot dx_j \tag{13}$$

where $\mathbf{E}$ is the *Green-Lagrange strain tensor* (introduced by Green and St. Venant) and η is the *Almansi strain tensor* (introduced by Almansi and Hamel[3]), efined as

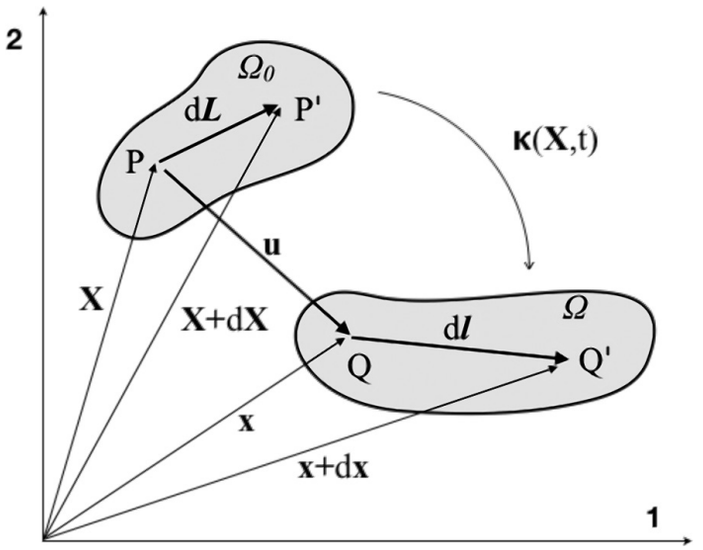

Fig. 18. *Notation used in the reference* Ω_0, *and the deformed* Ω *configurations.*

$$\mathbf{E} = \frac{1}{2}\left[\left(\frac{\partial \boldsymbol{\kappa}}{\partial \mathbf{X}}\right)^T \frac{\partial \boldsymbol{\kappa}}{\partial \mathbf{X}} - \mathbf{1}\right] \quad \text{or} \quad E_{ij} = \frac{1}{2}\left[\frac{\partial x_\alpha}{\partial X_i}\frac{\partial x_\alpha}{\partial X_j} - \delta_{ij}\right] \tag{14}$$

and

$$\eta = \frac{1}{2}\left[\mathbf{1} - \left(\frac{\partial \boldsymbol{\kappa}^{-1}}{\partial \mathbf{x}}\right)^T \frac{\partial \boldsymbol{\kappa}^{-1}}{\partial \mathbf{x}}\right] \quad \text{or} \quad \eta_{ij} = \frac{1}{2}\left[\delta_{ij} - \frac{\partial X_\alpha}{\partial x_i}\frac{\partial X_\alpha}{\partial x_j}\right] \tag{15}$$

Expressions (14) and (15) obtained for the Green-Lagrange and Almansi tensors can be written in term of the displacement **u** taking into account equations (3) and (4):

$$\mathbf{E} = \frac{1}{2}\left[\left(\frac{\partial \mathbf{u}}{\partial \mathbf{X}}\right)^T + \frac{\partial \mathbf{u}}{\partial \mathbf{X}} + \left(\frac{\partial \mathbf{u}}{\partial \mathbf{X}}\right)^T \frac{\partial \mathbf{u}}{\partial \mathbf{X}}\right]$$

or

$$E_{ij} = \frac{1}{2}\left[\frac{\partial u_j}{\partial X_i} + \frac{\partial u_i}{\partial X_j} + \frac{\partial u_\alpha}{\partial X_i}\frac{\partial u_\alpha}{\partial X_j}\right] \tag{16}$$

$$\eta = \frac{1}{2}\left[\left(\frac{\partial \mathbf{u}}{\partial \mathbf{x}}\right)^T + \frac{\partial \mathbf{u}}{\partial \mathbf{x}} - \left(\frac{\partial \mathbf{u}}{\partial \mathbf{x}}\right)^T \frac{\partial \mathbf{u}}{\partial \mathbf{x}}\right]$$

or

$$\eta_{ij} = \frac{1}{2}\left[\frac{\partial u_j}{\partial x_i} + \frac{\partial u_i}{\partial x_j} - \frac{\partial u_\alpha}{\partial x_i}\frac{\partial u_\alpha}{\partial x_j}\right] \tag{17}$$

[3] Emilio Almansi (1869-1948) was an Italian physicist and mathematician famed for his work on the theory of elasticity and the solution of non-linear problems. Georg Karl Wilhelm Hamel (1877-1954) was a German mathematician and author of several treatises on mechanics.

The following example may help to cement the ideas and concepts mentioned above. In what that follows the effect of time is ignored.

EXERCISE 0

Consider the homogeneous membrane represented in the figure, loaded uniformly by forces $\mathbf{f}_1 = \mathrm{f}_1 \mathbf{e}_1$ and $\mathbf{f}_2 = \mathrm{f}_2 \mathbf{e}_2$. The dimensions and the coordinate system are also shown in the figure.

It is assumed that the deformation is homogeneous, that is, the same at every point, and the thickness h changes during the deformation but the volume remains constant. Consequently the density r will be constant. It is further assumed that there are no angular deformations, and, therefore, the membrane maintains a rectangular shape during the deformation. This is the case if the material is isotropic and also if, being anisotropic, there is a material symmetry with respect to the 1 and 2-axes (since the deformation must respect that symmetry and, therefore, also the rectangular form of the plate, which is symmetric with respect to said axes).

In the *reference* configuration, the initial values are: L_1, L_2 and H.

In the *deformed* configuration, these values will be $l_1 = \lambda_1 L_1$, $l_2 = \lambda_2 L_2$ and h, where by conservation of volume, $l_1\, l_2\, h = L_1\, L_2\, H$.

Assume, for convenience, that the origin of the coordinates does not change its position with the deformation.

Under these conditions, apply expressions (1) to (15) to the deformation of the membrane.

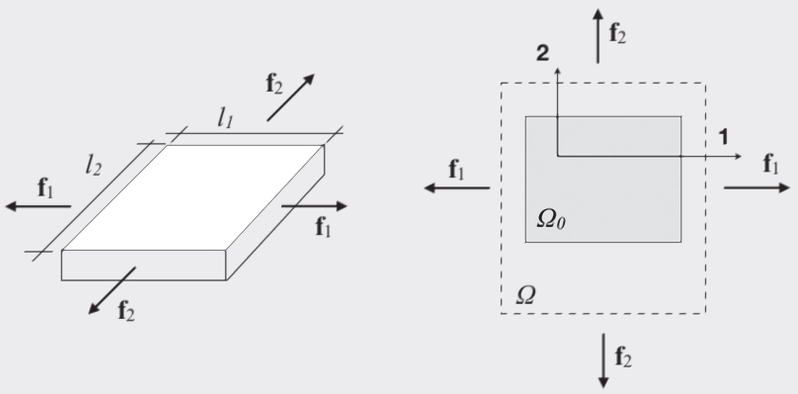

SOLUTION:

Equations (1) and (2) provide a knowledge of the *position* of a point in the membrane after the deformation. A point in the reference configuration (initial) with position $(\mathrm{X}_1, \mathrm{X}_2)$ is displaced to point $(\mathrm{x}_1, \mathrm{x}_2)$ in the deformed configuration according to equation (1):

$\mathbf{x} = \boldsymbol{\kappa}(\mathbf{X})$ vector notation

$(x_1, x_2) = (\lambda_1 X_1,\ \lambda_2 X_2)$ coordinate notation

$$\begin{bmatrix} x_1 \\ x_2 \end{bmatrix} = \begin{bmatrix} \lambda_1 & 0 \\ 0 & \lambda_2 \end{bmatrix} \begin{bmatrix} X_1 \\ X_2 \end{bmatrix}$$ matrix notation

The position of a point in the reference configuration, when its position in the deformed configuration is known, is given by equation (2)

$\mathbf{X} = \boldsymbol{\kappa}^{-1}(\mathbf{x})$ vector notation

$(X_1, X_2) = (x_1/\lambda_1, x_2/\lambda_2)$ coordinate notation

$$\begin{bmatrix} X_1 \\ X_2 \end{bmatrix} = \begin{bmatrix} 1/\lambda_1 & 0 \\ 0 & 1/\lambda_2 \end{bmatrix} \begin{bmatrix} x_1 \\ x_2 \end{bmatrix}$$ matrix notation

The value of the *displacement,* **u**, of a point P (see figure 18) as a function of the coordinates (X_1, X_2) of the reference configuration is given by equation (3)

$u(\mathbf{X}_P) = \mathbf{x}(\mathbf{X}_P) - \mathbf{X}_P$ vector notation

$[u_1(X_1, X_2), u_2(X_1, X_2)] = [(\lambda_1 - 1)\, X_1,\ (\lambda_2 - 1)\, X_2]$ coordinate notation

$$\begin{bmatrix} u_1 \\ u_2 \end{bmatrix} = \begin{bmatrix} \lambda_1 - 1 & 0 \\ 0 & \lambda_2 - 1 \end{bmatrix} \begin{bmatrix} X_1 \\ X_2 \end{bmatrix}$$ notación matricial

Similarly, the displacement **u** as a function of the coordinates (x_1, x_2) in the deformed configuration is given by equation (4)

$u(\mathbf{x}_P) = \mathbf{x}_P - \mathbf{X}(\mathbf{x}_P)$ vector notation

$[u_1(x_1, x_2),\ u_1(x_1, x_2)] = [(1 - 1/\lambda_1)\, x_1,\ (1 - 1/\lambda_2)\, x_2]$ coordinate notation

$$\begin{bmatrix} u_1 \\ u_2 \end{bmatrix} = \begin{bmatrix} 1 - 1/\lambda_1 & 0 \\ 0 & 1 - 1/\lambda_2 \end{bmatrix} \begin{bmatrix} x_1 \\ x_2 \end{bmatrix}$$ matrix notation

The *deformation gradient tensor,* $\mathbf{F}$, defined by equations (5a,b) becomes

$$\mathbf{F} = \frac{\partial \boldsymbol{\kappa}(\mathbf{X})}{\partial \mathbf{X}} \quad \text{or} \quad F_{ij} = \frac{\partial x_i}{\partial X_j}$$

which, for this example, is $\mathbf{F} = \begin{bmatrix} \lambda_1 & 0 \\ 0 & \lambda_2 \end{bmatrix}$

for this problem $\mathbf{F}$ is symmetrical so that $\mathbf{F} = \mathbf{F}^{\mathrm{T}}$. We can also obtain the inverse tensor $\mathbf{F}^{-1}$ from equation (6)

$$\mathbf{F}^{-1} = \frac{\partial \boldsymbol{\kappa}^{-1}(\mathbf{x})}{\partial \mathbf{x}} \qquad \text{or} \quad F_{ij}^{-1} = \frac{\partial X_i}{\partial x_j}$$

which for this example becomes,

$$\mathbf{F}^{-1} = \begin{bmatrix} 1/\lambda_1 & 0 \\ 0 & 1/\lambda_2 \end{bmatrix}$$

which is also symmetric, so that $\mathbf{F}^{-1} = \mathbf{F}^{-\mathrm{T}}$.

If we need to know the relationship between the infinitesimal length dL between two infinitely close points (for example P and P' in figure 18) and its value after deformation, dl, we use expressions (9) and (11)

$$(dL)^2 = \mathbf{F}^{-T}\mathbf{F}^{-1}d\mathbf{x}\cdot d\mathbf{x} = \begin{bmatrix} 1/\lambda_1^2 & 0 \\ 0 & 1/\lambda_2^2 \end{bmatrix} d\mathbf{x}\cdot d\mathbf{x}$$

$$(dl)^2 = \mathbf{F}^T\mathbf{F}\ d\mathbf{X}\cdot d\mathbf{X} = \begin{bmatrix} \lambda_1^2 & 0 \\ 0 & \lambda_2^2 \end{bmatrix} d\mathbf{X}\cdot d\mathbf{X}$$

Thus, using equation (7)

$$(dl)^2 - (dL)^2 = \begin{bmatrix} \lambda_1^2 & 0 \\ 0 & \lambda_2^2 \end{bmatrix} d\mathbf{X}\cdot d\mathbf{X} - d\mathbf{X}\cdot d\mathbf{X} = \begin{bmatrix} \lambda_1^2 - 1 & 0 \\ 0 & \lambda_2^2 - 1 \end{bmatrix} d\mathbf{X}\cdot d\mathbf{X}$$

and also, using (8)

$$(dl)^2 - (dL)^2 = d\mathbf{x}\cdot d\mathbf{x} - \begin{bmatrix} 1/\lambda_1^2 & 0 \\ 0 & 1/\lambda_2^2 \end{bmatrix} d\mathbf{x}\cdot d\mathbf{x} = \begin{bmatrix} 1-1/\lambda_1^2 & 0 \\ 0 & 1-1/\lambda_2^2 \end{bmatrix} d\mathbf{x}\cdot d\mathbf{x}$$

which can be identified as the *Green-Lagrange strain tensor* expression (12)

$$\mathbf{E} = \frac{1}{2}\begin{bmatrix} \lambda_1^2 - 1 & 0 \\ 0 & \lambda_2^2 - 1 \end{bmatrix}$$

and the *Almansi strain tensor* expression (13) is

$$\eta = \frac{1}{2}\begin{bmatrix} 1-1/\lambda_1^2 & 0 \\ 0 & 1-1/\lambda_2^2 \end{bmatrix}$$

which can also be expressed using equations (14)

$$\mathbf{E} = \frac{1}{2}\left[\mathbf{F}^T\mathbf{F} - \mathbf{1}\right] = \frac{1}{2}\left\{\begin{bmatrix} \lambda_1^2 & 0 \\ 0 & \lambda_2^2 \end{bmatrix} - \begin{bmatrix} 1 & 0 \\ 0 & 1 \end{bmatrix}\right\}$$

and equation (15)

$$\eta = \frac{1}{2}[\mathbf{1} - \mathbf{F}^{-T}\mathbf{F}^{-1}] = \frac{1}{2}\left\{\begin{bmatrix} 1 & 0 \\ 0 & 1 \end{bmatrix} - \begin{bmatrix} 1/\lambda_1^2 & 0 \\ 0 & 1/\lambda_2^2 \end{bmatrix}\right\}$$

The diagonal components of the *Green* tensor measure the change in length of fibres orientated parallel to the reference axes, relative to the *initial* length. It can be shown that

$$E_{11} = \frac{1}{2}(\lambda_1^2 - 1) \quad \text{and} \quad E_{22} = \frac{1}{2}(\lambda_2^2 - 1) \tag{18}$$

where $\lambda_i = dl_i/dL_i = 1 + \Delta(dL_i)/dL_i$ is the unit elongation (or more simply, elongation) in the i-direction $(i=1, 2)$. λ_i measures the relationship between final length and the initial length of an element *initially* lying parallel to the i-direction. Note that $\Delta(dL_i)/dL_i$ is the nominal or engineering strain in the i-direction.

In the same manner it can be seen that the diagonal components of the *Almansi* tensor provide a measure of the relative change in length of linear elements relative to the *deformed* length:

$$\eta_{11} = \frac{1}{2}\left(1 - \frac{1}{\tilde{\lambda}_1^2}\right) \quad \text{and} \quad \eta_{22} = \frac{1}{2}\left(1 - \frac{1}{\tilde{\lambda}_2^2}\right) \tag{19}$$

now $\tilde{\lambda}_i$ is the elongation of an element which *after strain* stays parallel to the i-direction. Note that dl and dL don't have to be parallel, and in general they are not (figure 18).

EXERCISE 1
Derive equations (18) and (19)

SOLUTION:
If we apply equation (12) to an element dL_i *lying initially* (in the reference configuration) in the i-direction we see that:

$$(dl_i)^2 - (dL_i)^2 = (dl_i)^2 - (dX_i)^2 = 2E_{ii}(dX_i)^2$$

since $dL_i = dX_i$. The square of the elongation is given by

$$\lambda_i^2 = \frac{(dl_i)^2}{(dX_i)^2} = \frac{(dX_i)^2 + 2E_{ii}(dX_i)^2}{(dX_i)^2} = 1 + 2E_{ii}$$

from which equation (18) is immediately deduced. Note that an element initially parallel to the i-direction does not have to remain parallel to this direction after deformation.

In order to derive equation (19) we now consider an element in the deformed configuration, in the i-direction, and for that $dl_i = dx_i$. We have:

$$(dl_i)^2 - (dL_i)^2 = (dx_i)^2 - (dL_i)^2 = 2\eta_{ii}(dx_i)^2$$

the square of the elongation is

$$\tilde{\lambda}_i^2 = \frac{(dx_i)^2}{(dL_i)^2} = \frac{(dx_i)^2}{(dx_i)^2 - 2\eta_{ii}(dx_i)^2}$$

From which equation (19) is deduced. Just as above, note that although dl_i is parallel to the i-direction in the deformed configuration, dL_i does not have to have been parallel to this direction in the initial configuration.

Other relationships which are convenient to quantify in straining are:

- The value of the strain which is produced in a segment which is initially orientated in any direction
- The value of the angle created in the deformed configuration by two directions which initially form an arbitrary angle
- The change suffered by an elemental area once deformed relative to the initial area in the reference configuration
- The change in volume of the membrane once deformed relative to the initial volume in the reference configuration

All of these relationships, as will be seen, can be expressed as functions of the Green-Lagrange, or Almansi strain tensors.

If dA is the area of an enclosure in the reference configuration and da is the corresponding area in the deformed configuration, their values are related by :

$$\frac{da}{dA} = \det\left[\frac{\partial \kappa(\mathbf{X},t)}{\partial \mathbf{X}}\right] = \det \mathbf{F} = \det\left[\frac{\partial x_i}{\partial X_j}\right] \tag{20}$$

In order to demonstrate this expression without loss of generality let us consider the area $dA=d\boldsymbol{X}\cdot d\boldsymbol{Y}$ defined by the elemental vectors $d\boldsymbol{X}$ and $d\boldsymbol{Y}$ aligned with the axes 1 and 2 in the reference configuration. The deformed values will be $d\boldsymbol{x}$ and $d\boldsymbol{y}$, so that the deformed area $da = dx\,dy\,sin\,\theta_{12}$ from which we can write

$$\left(\frac{da}{dA}\right)^2 = \left(\frac{dx}{dX}\right)^2\left(\frac{dy}{dY}\right)^2(1-\cos^2\theta_{12}) = \left(2E_{11}+1\right)\left(2E_{22}+1\right) - 4E_{12}^2$$

in which equation (18) has been used along with the value of the angle θ_{12} obtained from EXERCISE 3. Given that the Cauchy-Lagrange strain tensor is symmetrical and $E_{12}=E_{21}$, we can write

$$\left(\frac{da}{dA}\right)^2 = \left(2E_{11}+1\right)\left(2E_{22}+1\right) - 4E_{12}E_{21} =$$

$$= \det\left[2E_{ij}+\delta_{ij}\right] = \det\left[\frac{\partial x_\alpha}{\partial X_i}\frac{\partial x_\alpha}{\partial X_j}\right] = \det^2\left[\frac{\partial x_i}{\partial X_j}\right] \tag{21}$$

and, making use of equation (14), we arrive at equation (20). Observe that equation (21) –like equation (20)– is independent of the choice of the coordinate system, since the determinant is a tensorial invariant. Note that in this example $da/dA = \lambda_1\,\lambda_2$

From equation (20) we can calculate the change in volume of the membrane, letting its thickness be H in initial (reference) configuration and h in the deformed configuration. The deformed volume will be $dv=hda$ and the initial volume $dV=HdA$. Using equation (20) we see that

$$\frac{dv}{dV} = \frac{hda}{HdA} = \frac{h}{H}\det\left[\frac{\partial \kappa(\mathbf{X},t)}{\partial \mathbf{X}}\right] = \frac{h}{H}\det \mathbf{F} \tag{22}$$

Again, for this example $dv/dV = h\lambda_1\lambda_2/H$

When the displacement and gradient of the displacements $(\partial u/\partial X$ ó $\partial u/\partial x)$ are small, it can be seen that the second order terms in equations (16) and (17) can be ignored. In these circumstances the Green and Almansi tensors coincide

$$\varepsilon = \frac{1}{2}\left[\frac{\partial \mathbf{u}}{\partial \mathbf{X}} + \left(\frac{\partial \mathbf{u}}{\partial \mathbf{X}}\right)^T\right] \quad \text{or} \quad \varepsilon_{ij} = \frac{1}{2}\left[\frac{\partial u_i}{\partial X_j} + \frac{\partial u_j}{\partial X_i}\right] \tag{23}$$

called the *infinitesimal strain tensor.*

Even though the membranes have a small thickness, the bodies are not strictly bi-dimensional, and in order to analyse their behaviour adequately it is necessary to develop a hypothesis about the deformation in the thickness direction. Since soft biological materials have a high water content, and this is nearly incompressible for most ordinary load levels, it is often assumed that the membrane itself is incompressible or, which is the same, that its density is constant.

It is also assumed that the movement of points in the plane of the membrane (axes 1 and 2) is independent of their position through the thickness (axis 3) or, in other words, the function $\mathbf{x} = \boldsymbol{\kappa}(\mathbf{X}, t)$, equation (1), does not depend upon the coordinate X_3 for the point considered ($x_1=\kappa_1(X_1,X_2)$; $x_2=\kappa_2(X_1,X_2)$). In this way the problem can be treated as purely two-dimensional (with only the dimensions 1 and 2), adjusting, for each point, the value of the thickness required to conserve the volume.

EXERCISE 2

Determine as a function of the Green-Lagrange tensor the value of the elongation $\lambda_{\boldsymbol{N}}$ in an arbitrary direction $\boldsymbol{N}$ in the reference configuration $\boldsymbol{N}$ is a unit vector.

Apply the result to the deformation of the membrane in EXERCISE 0.

SOLUTION:

Let $d\boldsymbol{X} = dL\boldsymbol{N}$ an elemental vector along direction $\boldsymbol{N}$ in the reference configuration. Its deformed value is $d\boldsymbol{x} = dl\,\boldsymbol{n}$ ($\boldsymbol{n}$ is a unit vector). From equation (5)

$$d\mathbf{x} = dl\ \mathbf{n} = dL\frac{\partial \boldsymbol{\kappa}(\mathbf{X},t)}{\partial \mathbf{X}}\ \mathbf{N} \quad \text{or} \quad dl\ n_i = dL\frac{\partial x_i}{\partial X_j}\ N_j$$

performing the scalar multiple of this with itself, we obtain

$$(dl)^2 = (dL)^2\,\delta_{ij}\frac{\partial x_i}{\partial X_l}\frac{\partial x_j}{\partial X_m}\ N_l N_m$$

and, using equation (14), the elongation becomes

$$\lambda_N^2 = \frac{(dl)^2}{(dL)^2} = \delta_{ij}\frac{\partial x_i}{\partial X_l}\frac{\partial x_j}{\partial X_m}\ N_l N_m = (2E_{lm} + \delta_{lm})\ N_l N_m$$

or $\lambda_N^2 = (2E_{11}+1)\ \cos^2\alpha + 2(E_{12}+E_{21})\ \cos\alpha\ \sin\alpha + (2E_{22}+1)\ \sin^2\alpha$

where α is the angle which the unit vector $\boldsymbol{N}$ form with the 1-axis, so $\boldsymbol{N}_1 = \cos\alpha$ and $N_2 = \sin\alpha$.

When $\boldsymbol{N}$ is the unit vector in the 1-direction 1 ($\alpha = 0$) we recover the expressions in equations (18).

If we apply the above result to the membrane in EXERCISE 0 we find that the elongation in the 1-direction is

$$\lambda_{N\equiv\vec{1}}^2 = 2E_{11} + 1 = 2\frac{1}{2}(\lambda_1^2 - 1) + 1 = \lambda_1^2$$

since $dl_1/dL_1 = \lambda_1$, and the deformation is homogeneous (the same at every point) then $l_1/L_1 = \lambda_1$ as well.

Equally, in the 2-direction

$$\lambda_{N\equiv\vec{2}}^2 = 2E_{22} + 1 = 2\frac{1}{2}(\lambda_2^2 - 1) + 1 = \lambda_2^2$$

and

$dl_2/dL_2 = l_2/L_2 = \lambda_2$.

EXERCISE 3

As a function of the Green-Lagrange strain tensor, determine the angle θ_{NM} formed in the deformed configuration by two arbitrary directions $\boldsymbol{N}$ and $\boldsymbol{M}$ in the reference configuration. $\boldsymbol{N}$ and $\boldsymbol{M}$ are unit vectors.

Apply the result to the deformation of the angle formed by the 1 and 2-axes in the membrane in EXERCISE 0.

SOLUTION:

Let $d\boldsymbol{X}=dX\boldsymbol{N}$ and $d\boldsymbol{Y}=dY\boldsymbol{M}$ be elemental vectors along directions $\boldsymbol{N}$ and $\boldsymbol{M}$ ein the reference configuration. Their deformed values will be $d\boldsymbol{x}=dx\boldsymbol{n}$ and $d\boldsymbol{y}=dy\,\boldsymbol{m}$ ($\boldsymbol{n}$ and $\boldsymbol{m}$ are unit vectors). In order to calculate the angle subtended by $d\boldsymbol{x}$ and $d\boldsymbol{y}$ we perform their scalar product:

$$\cos\theta_{NM}=\frac{d\mathbf{x}\cdot d\mathbf{y}}{dxdy}=\frac{\delta_{ij}\dfrac{\partial x_i}{\partial X_l}\dfrac{\partial x_j}{\partial X_m}dX\,N_l\,dY\,M_m}{dxdy}=\frac{\left(2E_{lm}+\delta_{lm}\right)N_lM_m}{\left(dx/dX\right)\left(dy/dY\right)}$$

in which we have made use of equations (5) and (14).

However, and from EXERCISE 2, we know that $\lambda_N^2=\left(2E_{lm}+\delta_{lm}\right)N_lN_m$ and $\lambda_M^2=\left(2E_{lm}+\delta_{lm}\right)M_lM_m$

so that $\cos\theta_{NM}=\dfrac{\left(2E_{lm}+\delta_{lm}\right)N_lM_m}{\sqrt{\left(2E_{ij}+\delta_{ij}\right)N_iN_j}\sqrt{\left(2E_{sr}+\delta_{sr}\right)M_sM_r}}$

In particular, if $\boldsymbol{N}$ and $\boldsymbol{M}$ are the 1 and 2-axes, then: $\cos\theta_{12}=\dfrac{2E_{12}}{\sqrt{2E_{11}+1}\sqrt{2E_{22}+1}}$

In EXERCISE 0, if we take directions $\boldsymbol{N}$ and $\boldsymbol{M}$ as the 1 and 2-axes, since E_{12} = 0 we obtain the previous expressions $\cos\theta_{12}=0$ and $\theta_{12}=90°$. That is to say, the deformed angle corresponding to the right angle formed by the 1 and 2-axes remains a right angle.

EXERCISE 3bis

Determine the relative change in the area and volume of the membrane in EXERCISE 0.

SOLUTION:

Using equation (21): $\left(\dfrac{da}{dA}\right)^2=\left(2E_{11}+1\right)\left(2E_{22}+1\right)-4E_{12}E_{21}=\lambda_1^2\lambda_2^2$

from which we obtain the relative change in area $da/dA=\lambda_1\lambda_2$, where λ_1, λ_2 are the elongations of the 1 and 2-axes, respectively.

Given the homogeneity of the deformation we can see that this result coincides with the relationship between the total areas of the membrane after and before the deformation:

$(l_1\,l_2)/(L_1\,L_2)=(l_1/L_1)\,(l_2/L_2)=\lambda_1\,\lambda_2$ since $l_1/L_1=\lambda_1$ y $l_2/L_2=\lambda_2$, as was seen in EXERCISE 2.

On the other hand, from equation (22) we obtain the relationship between the volumes dv/dV

$$\frac{dv}{dV}=\frac{hda}{HdA}=\frac{h}{H}\lambda_1\lambda_2$$

where H and h are the thicknesses of the reference configuration and that of the deformed configuration, respectively.

Conservation of volume, established in the statement of EXERCISE 0, implies that the dimensions of the initial and deformed configurations satisfy the relationship: $l_1\,l_2\,h=L_1\,L_2\,H$ and bearing in mind that $l_1/L_1=\lambda_1$ and $l_2/L_2=\lambda_2$, we obtain $\lambda_1\,\lambda_2\,h=H$, an expression which if introduced into the equation for the relationship between the volumes dv/dV leads to

$$\frac{dv}{dV}=\frac{h}{H}\lambda_1\lambda_2=\frac{1}{\lambda_1\lambda_2}\lambda_1\lambda_2=1$$ conforming with the statement made in EXERCISE 0.

Stresses and the stress tensor

Consider the two-dimensional body represented in figure 19a, subjected to forces on its boundary, and the action of gravity. Imagine a small segment of length Δl, located in its interior, together with the unit vector normal to it, $\mathbf{n}$. This vector allows us to distinguish space on either side of the segment Δl; the positive side, which is where $\mathbf{n}$ points and the negative side, which is opposite. Furthermore, we assume that the body has a thickness h, which is very small compared to the other dimensions.

Examine closely the part of the material which is on the positive side (the shaded area in figure 19a). This part exerts a force $\Delta \boldsymbol{F}$ on the other part. The force $\Delta \boldsymbol{F}$ will depend upon the location of the element Δl considered, and its size and orientation.

If the hypothesis is made that the quotient $\Delta \boldsymbol{F}/(h\Delta l)$, when Δl tends to zero, has a definite limit, the resulting vector

$$\boldsymbol{t} = \lim_{\Delta l \to 0} \frac{\Delta F}{\mathrm{h}\Delta l} = \frac{d\boldsymbol{F}}{h dl} \tag{24}$$

is known the *stress vector* at that point, which acts on dl (due to the material on the positive part) defined by the normal $\mathbf{n}$. Observe that $\Delta \boldsymbol{F}$ does not have to be parallel to $\mathbf{n}$, and in general it is not.

With the aim of explaining the notation used, consider a small square of side dl orientated along the axes 1 and 2, as shown in figure 19b, and the stresses acting on its faces. On each one of them, the stress vector can be decomposed into two vectors; one *normal* to the face and the other *tangent* to it. In figure 19b this decomposition is shown on one of the two faces perpendicular to the 1-axis. The stress vector $\boldsymbol{t}$ is decomposed into the *normal stress vector* σ_{11}, and the *tangential stress vector* σ_{12}. The other faces can be treated in an analogous manner. The set of four stresses (σ_{11}, σ_{12}, σ_{21}, σ_{22}) is the *stress tensor* σ_{ij}(i, j=1, 2), which characterises the forces which act a point in the body.

The stress tensor σ_{ij} is symmetric and σ_{12}=σ_{21}, so that there are only three independent components (σ_{11}, σ_{12}, σ_{22}). If this tensor is known then the stress $\boldsymbol{t}$ which acts on some inclined segment dl*, characterised by its normal $\boldsymbol{n}$ (figure 19c) is also known, through the expression:

$$\mathbf{t} = \sigma \mathbf{n} \quad \text{or} \quad t_i = \sigma_{ij} n_j \tag{25}$$

where n_j is the component of the vector $\mathbf{n}$ in the j-direction.

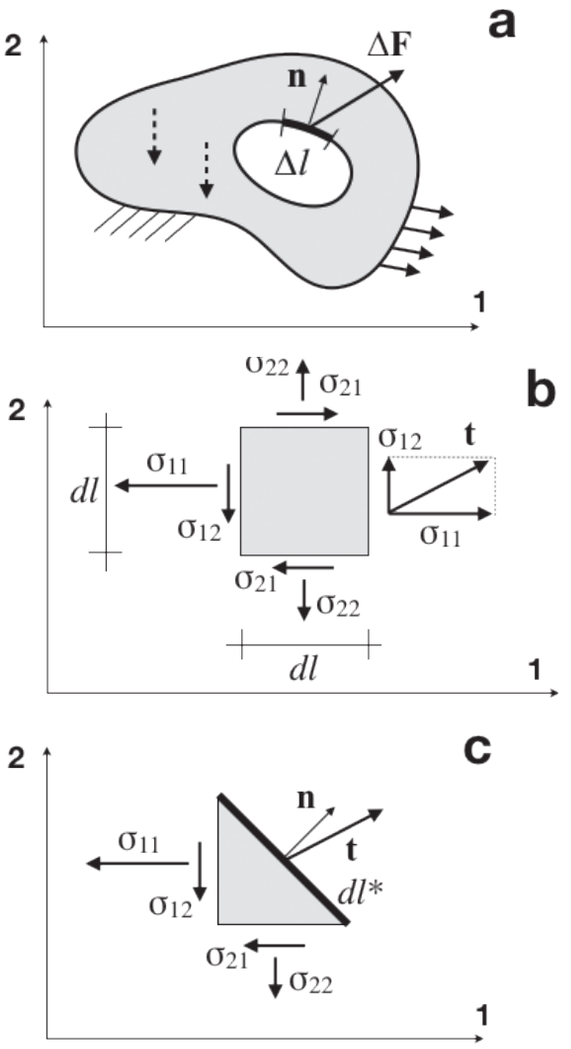

Fig. 19.*a) Definition of stress*
b) Stress tensor notation
c) Equilibrium of an infinitesimal element

Equilibrium of the element represented in figure 19b requires that the following equations must be satisfied,

$$\begin{aligned} \frac{\partial \sigma_{11}}{\partial x_1} + \frac{\partial \sigma_{21}}{\partial x_2} + \rho g_1 = 0 \\ \frac{\partial \sigma_{12}}{\partial x_1} + \frac{\partial \sigma_{22}}{\partial x_2} + \rho g_2 = 0 \end{aligned} \tag{26}$$

where g_1 and g_2 are the components of the gravitational acceleration along the 1 and 2-axes, and ρ is the density. The equilibrium equations (26) are none other than the statement that the sum of all of the forces on the element is zero.

The following exercises are intended to help the reader gain familiarity the above concepts.

EXERCISE 4
Show that the stress tensor is symmetric.

SOLUTION:
If we consider equilibrium of moments about lower right corner for the square dl x dl of figure 19b, (and taking the thickness of the element to be h) we obtain:

$\sigma_{12} h\,(dl)^2 - \sigma_{21} h\,(dl)^2 - \rho g_1 h (dl)^3/2 - \rho g_2 h\,(dl)^3/2 = 0$

In the limit as $dl \to 0$ it is concluded that $\sigma_{12} = \sigma_{21}$.

EXERCISE 5
Prove the equation (25)

SOLUTION:
Considering figure 19c, equilibrium of the elements along the 1 and 2-axes gives:

$t_1 h\,dl^* - \sigma_{11} h\,dl^* n_1 - \sigma_{21} h\,dl^* n_2 + \rho\, g_1 h\,(dl^*)^2 n_1 n_2 / 2 = 0$

$t_2 h\,dl^* - \sigma_{12} h\,dl^* n_1 - \sigma_{22} h\,dl^* n_2 + \rho\, g_2 h\,(dl^*)^2 n_1 n_2 / 2 = 0$

since $(h dl^* n_1)$ and $(h dl^* n_2)$ are the projections of the area $(h dl^*)$ along the 1 and 2-axes, respectively and $\rho h (dl^*)^2 n_1 n_2 / 2$ is the mass of the element. g_1 and g_2 are the components of the gravitational acceleration along the 1 and 2-axes.

In the limit as $dl^* \to 0$ for the above expressions, and exploiting the symmetry of the stress tensor we arrive directly at

$$\begin{bmatrix} t_1 \\ t_2 \end{bmatrix} = \begin{bmatrix} \sigma_{11} n_1 + \sigma_{12} n_2 \\ \sigma_{21} n_1 + \sigma_{22} n_2 \end{bmatrix} = \begin{bmatrix} \sigma_{11} \sigma_{12} \\ \sigma_{21} \sigma_{22} \end{bmatrix} \begin{bmatrix} n_1 \\ n_2 \end{bmatrix}$$ matrix notation

which can be written as

$t_i = \sigma_{ij} n_j$ coordinate notation

or also

$\mathbf{t} = \sigma \mathbf{n}$ vector notation

which are the two forms of equation (25).

EXERCISE 6
Derive the equilibrium equations (26).

SOLUTION:
In order to obtain the equilibrium equation, we must consider the changes in the in the stresses acting on the differential element in figure 19b, along the 1 and 2-directions. The stresses acting on the left and lower faces will be σ_{11}, σ_{22}, σ_{12} and σ_{21}, while the stresses on the right and upper faces, which are displaced by distances $dx_1(= dl)$ and $dx_2(= dl)$ respectively, will be

$\sigma_{11}+ (\partial\sigma_{11}/\partial x_1)\, dx_1$ y $\sigma_{12}+ (\partial\sigma_{12}/\partial x_1)\, dx_1$ on the right face
$\sigma_{21}+ (\partial\sigma_{21}/\partial x_2)\, dx_2$ y $\sigma_{22}+ (\partial\sigma_{22}/\partial x_2)\, dx_2$ on the upper face

The equilibrium equations corresponding for the element will then be:

$$-\sigma_{11}\, h dx_2 - \sigma_{21}\, h dx_1 + (\sigma_{11}+ (\partial\sigma_{11}/\partial x_1)\, dx_1)\, h dx_2 + (\sigma_{21}+ (\partial\sigma_{21}/\partial x_2)\, dx_2)\, h dx_1 + \rho\, g_1 h\, dx_1\, dx_2 = 0$$

$$-\sigma_{22}\, h dx_1 - \sigma_{12}\, h dx_2 + (\sigma_{22}+ (\partial\sigma_{22}/\partial x_2)\, dx_2)\, h dx_1 + (\sigma_{12}+ (\partial\sigma_{12}/\partial x_1)\, dx_1)\, h dx_2 + \rho\, g_2 h\, dx_1\, dx_2 = 0$$

cancelling terms and eliminating $h\, dx_1\, dx_2$ we obtain the equations

$$\begin{bmatrix} \partial\sigma_{11}/\partial x_1 + \partial\sigma_{21}/\partial x_2 + \rho g_1 \\ \partial\sigma_{12}/\partial x_1 + \partial\sigma_{22}/\partial x_2 + \rho g_2 \end{bmatrix} = \begin{bmatrix} 0 \\ 0 \end{bmatrix}$$ matrix notation

which are equation (26), and which can also be written as

$$\frac{\partial\sigma_{ij}}{\partial x_i} + \rho g_j = 0$$ coordinate notation

or

$$div\boldsymbol{\sigma} + \rho\boldsymbol{g} = \boldsymbol{0}$$ in vector notation..

Observe that the use of the updated stresses (that is, considering their variations along the 1 and 2-axes) on the right and upper faces in figure 19b for the calculations performed in EXERCISE 5, does not change the result since the terms added to the moment equilibrium equation $-((\partial\sigma_{11}/\partial x_1)dl)h(dl)^2/2$, $-((\partial\sigma_{22}/\partial x_2)dl)h(dl)^2$ and $-((\partial\sigma_{22}/\partial x_2)dl)h(dl)^2/2$ are higher order infinitesimals.

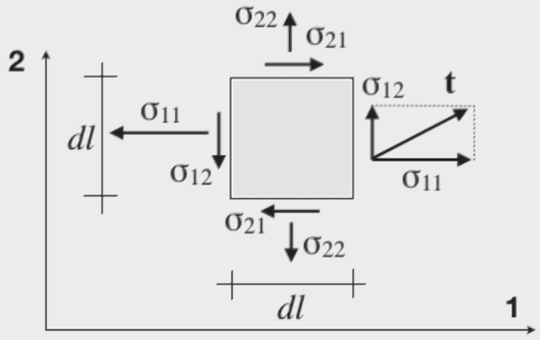

Up to now we have only considered stresses generated by forces acting in the plane of the body. However, there can also be forces acting perpendicular to the plane, such as when the membrane of a balloon is subjected to pressure. Figure 20 illustrates such a situation. In this case the membrane must be curved in order to balance the pressures exerted on its faces, and an equation of equilibrium in the thickness direction must be added to the set of equations (26):

$$p = h\left(\frac{\sigma_{11}}{R_1} + \frac{\sigma_{22}}{R_2}\right) \tag{27}$$

in which R_i is the radius of curvature in the i-direction. Equation (27) is known as Laplace's law.

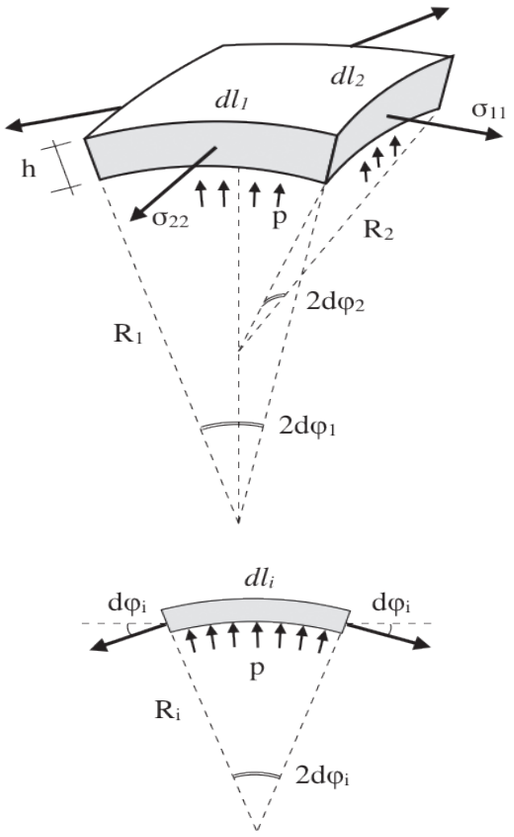

Fig. 20. *Equilibrium of a curved membrane element subjected to pressurec.*

EXERCISE 7
Prove equation (27).

SOLUTION:
Equation (27) is obtained assuming equilibrium along the normal to the element $dl_1\, x\, dl_2$. Considering the forces shown in figure 20 we have

$$p\, dl_1\, dl_2 - 2\, \sigma_{22}\, h\, dl_1\, d\varphi_2 - 2\, \sigma_{11}\, h\, dl_2\, d\varphi_1 - \rho\, g_n\, h\, dl_1 dl_2 = 0$$

where g_n is the component of the gravitational acceleration along the normal to the element. In the above equation we have used the approximation $\sin(d\varphi_2) \approx d\varphi_2$. Also since $2\, d\varphi_1 = dl_1 / R_1$ and $2\, d\varphi_2 = dl_2 / R_2$ then

$$p\, dl_1\, dl_2 - \sigma_{22}\, h\, dl_1\, dl_2 / R_2 - \sigma_{11}\, h\, dl_2\, dl_1 / R_{12} - \rho\, g_n\, h\, dl_1 dl_2 = 0$$

which leads directly to equation (27), if the self-weight of the element is ignored. This last assumption is reasonable given that for thicknesses of less than a millimetre the term $h\rho g_n$ is less than 10 Pa. This value is several orders of magnitude less than the usual physiological pressures such as the pressure measured in blood vessels (100mmHg ≈ 13kPa) or the eyeball (14mmHg ≈ 2kPa).

The fact that biological membranes undergo large deformations, and as a result the initial and deformed configurations may be very different, makes it necessary to clarify in which configuration (initial or deformed) the force and areas are expressed for use in equation (24) which defines the tension vector $\boldsymbol{t}$.

Depending upon the choice of one or the other it is possible to make the following definitions:

- *Cauchy stress vector* $\boldsymbol{t}$ or true stress vector, defined as the force acting in the deformed configuration per unit area in the deformed configuration. That is to say

$$\mathbf{t} = \frac{d\mathbf{f}}{h dl} \tag{28}$$

in which dl and h are the values of length and thickness in the deformed configuration.

- *First Piola-Kirchhoff stress vector,* $\boldsymbol{p}$, nominal (or engineering) stress vector defined as the force acting in the deformed configuration per unit area in the initial configuration. That is to say:

$$\mathbf{p} = \frac{d\mathbf{f}}{H dL} \tag{29}$$

in which now dL and H are the values of the length and thickness in the initial configuration, corresponding to dl and h. Note that in equations (28) and (29), the force vector $\mathbf{f}$ is the same.

- *Second Piola-Kirchhoff stress vector,* $\boldsymbol{s}$, also defined in terms of the unit area in the initial configuration, and using the force referred to the initial configuration

$$\mathbf{s} = \frac{d\mathbf{T}}{H dL} \tag{30}$$

$\mathbf{T}$ *is the vector corresponding to vector* $\mathbf{f}$ (=the force acting in the deformed configuration) according to the relationship which connects the vectors $d\boldsymbol{X}$ and $d\boldsymbol{x}$, equation (6), that is to say:

$$\mathbf{T} = \frac{\partial \boldsymbol{\kappa}^{-1}(\mathbf{x},t)}{\partial \mathbf{x}} \mathbf{f} = \mathbf{F}^{-1}\ \mathbf{f} \quad \text{or} \quad T_i = \frac{\partial X_i}{\partial x_j} \mathrm{f}_j \tag{31}$$

Vector $\boldsymbol{s}$ has no obvious physical meaning but it is introduced, as will be explained later, because the corresponding stress tensor is symmetric, and also is the conjugate[4] of the Green-Lagrange strain tensor.

From these different stresses, and following the development in the previous paragraphs, it is possible to find the corresponding stress tensors. Therefore, we will define the *stress vectors of Cauchy* σ, and of the *first Piola-Kirchoff,* $\boldsymbol{P}$, and the *second*, $\mathbf{S}$.

We have that:

$$\begin{aligned} &\mathbf{t} = \sigma \mathbf{n} && t_i = \sigma_{ij} n_j \\ &\mathbf{p} = \mathbf{P}\mathbf{N} && p_i = P_{ij} N_j \\ &\mathbf{s} = \mathbf{S}\mathbf{N} && s_i = S_{ij} N_j \end{aligned} \tag{32}$$

which correspond to equations (25), and which provide knowledge of the stress vectors in the deformed ($\mathbf{t}$) or the reference configuration ($\mathbf{p}$, $\mathbf{s}$) from the stress tensor and the direction normal to the segment on which the stress acts.

The *first Piola-Kirchhoff stress tensor* $\mathbf{P}$ is a function of the *Cauchy stress tensor* $\mathbf{s}$ and given by:

$$\mathbf{P} = \frac{h}{H} \det\left[\frac{\partial \boldsymbol{\kappa}(\mathbf{X},t)}{\partial \mathbf{X}}\right] \sigma \left[\frac{\partial \boldsymbol{\kappa}^{-1}(\mathbf{x},t)}{\partial \mathbf{x}}\right]^T = \frac{h}{H} \det \mathbf{F}\ \ \sigma \mathbf{F}^{-T} \tag{33a}$$

$$P_{ij} = \frac{h}{H} \det\left[\frac{\partial x_\alpha}{\partial X_\beta}\right] \sigma_{im} \frac{\partial X_j}{\partial x_m} \tag{33b}$$

which is not, in general, symmetric, even though σ_{ij} is.

The *second Piola-Kirchhoff stress tensor* $\mathbf{S}$ is also a function of the *Cauchy stress tensor* σ and given by:

$$\mathbf{S} = \frac{h}{H} \det\left[\frac{\partial \boldsymbol{\kappa}(\mathbf{X},t)}{\partial \mathbf{X}}\right] \left[\frac{\partial \boldsymbol{\kappa}^{-1}(\mathbf{x},t)}{\partial \mathbf{x}}\right] \sigma \left[\frac{\partial \boldsymbol{\kappa}^{-1}(\mathbf{x},t)}{\partial \mathbf{x}}\right]^T =$$

$$= \frac{h}{H} \det \mathbf{F}\ \ \mathbf{F}^{-1} \sigma \mathbf{F}^{-T} \tag{34a}$$

$$S_{ij} = \frac{h}{H} \det\left[\frac{\partial x_\alpha}{\partial X_\beta}\right] \frac{\partial X_i}{\partial x_l} \frac{\partial X_j}{\partial x_m} \sigma_{lm} \tag{34b}$$

[4] In mechanics, it is said that two quantities are conjugate when their product permits calculation of the work done.

Alternatively, we can write

$$\sigma = \frac{H}{h}\frac{1}{\det \mathbf{F}}\,\mathbf{P}\mathbf{F}^T \quad \text{or} \quad \sigma_{ij} = \frac{H}{h}\frac{1}{\det\left[\partial x_\alpha/\partial X_\beta\right]} P_{im}\frac{\partial x_j}{\partial X_m} \quad (35)$$

$$\sigma = \frac{H}{h}\frac{1}{\det \mathbf{F}}\,\mathbf{F}\mathbf{S}\mathbf{F}^T \quad \text{or} \quad \sigma_{ij} = \frac{H}{h}\frac{1}{\det\left[\partial x_\alpha/\partial X_\beta\right]}\frac{\partial x_i}{\partial X_l}\frac{\partial x_j}{\partial X_m} S_{lm} \quad (36)$$

which is no more than the solution for σ in equations (33) and (34). As can be seen, S_{ij} is symmetric, since σ_{ij} is, and also the product of the derivatives. The proofs of the previous equations can be can be found in the reference texts.

EXERCISE8

Calculate the Cauchy and Piola-Kirchoff stress tensors for the deformed membrane of EXERCISE 0.

SOLUTION:

The *Cauchy stress tensor* follows from equations (28) and (32)

$$\sigma_{11} = \frac{\mathrm{f}_1}{l_2 h} \qquad \sigma_{22} = \frac{\mathrm{f}_2}{l_1 h} \qquad \text{and} \qquad \sigma_{12} = \sigma_{21} = 0$$

Similarly, the *first Piola-Kirchhoff tensor* follows from equations (29) and (32):

$$P_{11} = \frac{\mathrm{f}_1}{L_2 H} \qquad \mathrm{P}_{22} = \frac{\mathrm{f}_2}{L_1 H} \qquad \text{and} \qquad \mathrm{P}_{12} = P_{21} = 0$$

The same result can be achieved by applying equations (33) and bearing in mind that for this problem

and that $l_1/\lambda_1 = L_1$ and $l_2/\lambda_2 = L_2$, as was seen in EXERCISES 0 and 2.

The *second Piola-Kirchhoff* tensor follows from equations (30) and (32)

in which we have calculated the forces in the reference configuration according to equation (31):

$$S_{11} = \frac{1}{\lambda_1}\frac{\mathrm{f}_1}{L_2 H} \qquad \mathrm{S}_{22} = \frac{1}{\lambda_2}\frac{\mathrm{f}_2}{L_1 H} \qquad \text{and} \qquad \mathrm{S}_{12} = S_{21} = 0$$

The equivalent result for $\mathbf{S}$ is obtained from equations (34).

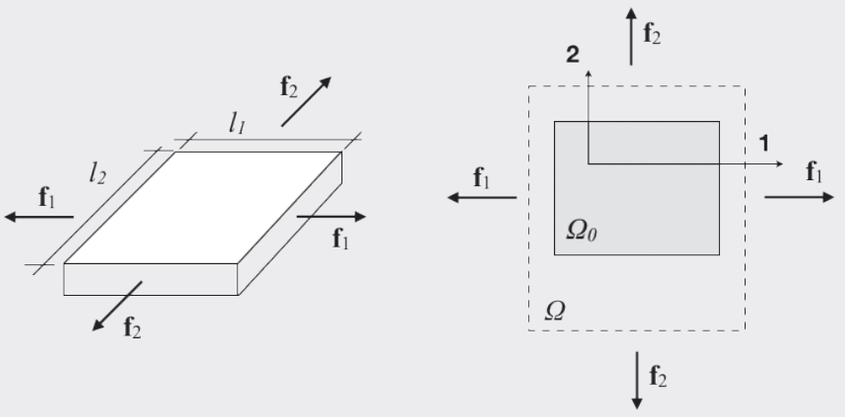

2.2.3. Example: Homogeneous biaxial test

The biaxial tensile test (figure 21) was illustrated in EXERCISE 0, and analysed in the subsequent exercises. The conclusions reached are summarised in this section, grouping the results obtained, for greater clarity and use in other examples.

The experiment consists of subjecting a homogeneous isotropic membrane to a uniform load under orthogonal forces $\mathbf{f}_1$, $\mathbf{f}_2$, which produce the same strain at every point (homogeneous). Furthermore, it is assumed that during deformation the volume remains constant.

In the *reference* configuration, the initial values (length, width and thickness) are: L_1, L_2, H.

In the *deformed* configuration, the values will be $l_1=\lambda_1 L_1$, $l_2=\lambda_2 L_2$ and h, to satisfy conservation of volume, requires that $l_1 l_2 h = L_1 L_2 H$.

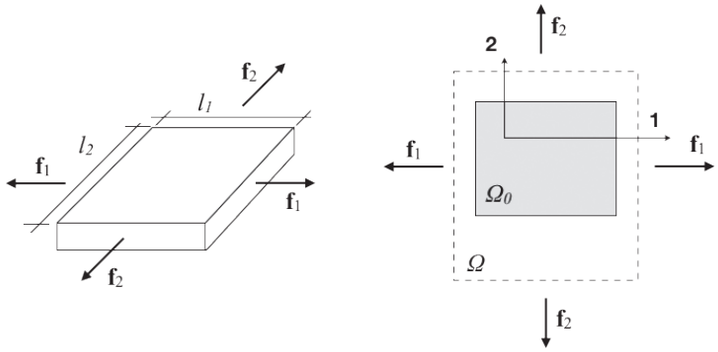

Fig. 21. *Homogenous biaxial test. Geometric and loading notation.*

The displacement equations for directions 1 and 2 are, respectively,

$$x_1 = \lambda_1 X_1 \qquad x_2 = \lambda_2 X_2 \tag{37}$$

and,

$$X_1 = x_1/\lambda_1 \qquad X_2 = x_2/\lambda_2 \tag{38}$$

In which it has been assumed, for convenience, that the origin of the coordinates does not change its position with the deformation.

The *displacement* vector $\mathbf{u}_i$ is given by equation (3)

$$u_1 = (\lambda_1 - 1)X_1 \qquad u_2 = (\lambda_2 - 1)X_2 \tag{39}$$

or, equation (4)

$$u_1 = (1 - \lambda_1^{-1})x_1 \qquad u_2 = (1 - \lambda_2^{-1})x_2 \tag{40}$$

The *Green-Lagrange strain tensor* E_{ij}, (14) equation (14), in this simple example, is reduced the diagonal (E_{11}, E_{22}) whose values become:

$$E_{11} = \frac{1}{2}\left(\lambda_1^2 - 1\right) = \frac{1}{2}\left(\frac{x_1^2}{X_1^2} - 1\right) \text{ and } E_{22} = \frac{1}{2}\left(\lambda_2^2 - 1\right) = \frac{1}{2}\left(\frac{x_2^2}{X_2^2} - 1\right) \tag{41}$$

Similarly, *Almansi strain tensor,* η_{ij}, (15) equation (15) is also reduced to the diagonal (η_{11}, η_{22}), and given by

$$\eta_{11} = \frac{1}{2}\left(1 - \frac{1}{\lambda_1^2}\right) = \frac{1}{2}\left(1 - \frac{X_1^2}{x_1^2}\right) \quad \text{and} \quad \eta_{22} = \frac{1}{2}\left(1 - \frac{1}{\lambda_2^2}\right) = \frac{1}{2}\left(1 - \frac{X_2^2}{x_2^2}\right) \tag{42}$$

In both cases, for small deformations ($\lambda \approx 1+\varepsilon$, with ε being very small), the two tensors coincide with the tensor ε_{ij} in equation (23) which, for this example, become:

$$E_{11} = \eta_{11} = \varepsilon_{11} = \lambda_1 - 1 \qquad E_{22} = \eta_{22} = \varepsilon_{22} = \lambda_2 - 1 \tag{43}$$

The *Cauchy stress tensor* is, following equations (28) and (32),

$$\sigma_{11} = \frac{\mathrm{f}_1}{l_2 h} \qquad \sigma_{22} = \frac{\mathrm{f}_2}{l_1 h} \qquad \text{and} \qquad \sigma_{12} = \sigma_{21} = 0 \tag{44}$$

The *first Piola-Kirchhoff tensor* is given, from equations (29) and (32), or alternatively, equation (33), by

$$P_{11} = \frac{\mathrm{f}_1}{L_2 H} \qquad \mathrm{P}_{22} = \frac{\mathrm{f}_2}{L_1 H} \qquad \text{and} \qquad \mathrm{P}_{12} = P_{21} = 0 \tag{45}$$

The *second Piola-Kirchhoff tensor* is, according to equations (30) and (32), or alternatively equation (34)

$$S_{11} = \frac{1}{\lambda_1}\frac{\mathrm{f}_1}{L_2 H} \qquad \mathrm{S}_{22} = \frac{1}{\lambda_2}\frac{\mathrm{f}_2}{L_1 H} \qquad \text{and} \qquad \mathrm{S}_{12} = S_{21} = 0 \tag{46}$$

with the forces in the reference configuration equation (31):

$$\mathbf{T}_1 = \frac{\mathrm{f}_1}{\lambda_1}\mathbf{e}_1 \qquad \text{and} \qquad \mathbf{T}_2 = \frac{\mathrm{f}_2}{\lambda_1}\mathbf{e}_2 \tag{47}$$

2.2.4. Example: Extension and inflation of a thin tube

The extension and inflation of a homogeneous thin-walled tube made from an isotropic material is now considered. The process is represented in figure 22a.

The tube is taken to be right and infinitely long, loaded uniformly by axial forces $\mathbf{f}$ y and an internal pressure p.

We assume that the tube remains right and maintains a circular cross section, undergoing an affine deformation process. This is the case for an isotropic material, and also for an anisotropic material provided it has material symmetry with respect to the 3-axis[3].

In this development two different coordinate systems will be used, the cartesian formed of the 1,2 and 3-axes (figure 22b) and the cylindrical (r, θ, z) (figure 22c), both centred on the axis of the tube. In this way, as well as familiarising the reader with the representation of both systems, we will take advantage, as the occasion arises, of the symmetry of the problem.

In the *reference* configuration we assume that the tube has a thickness H, radius R and length L. In the *deformed* configuration, the values will be h, r and l.

If ($\mathbf{e}_1$, $\mathbf{e}_2$, $\mathbf{e}_3$) is the standard basis for the *cartesian coordinate system* (figure 22b), the position of a point $\mathbf{X}=X_1\mathbf{e}_1+X_2\mathbf{e}_2+X_3\mathbf{e}_3$ in reference configuration after deformation will be:

$$\mathbf{x} = \lambda_\theta X_1\mathbf{e}_1 + \lambda_\theta X_2\mathbf{e}_2 + \lambda_3 X_3\mathbf{e}_3 \tag{48}$$

which we can recognise as the set of equations (1). The non-dimensional parameters λ_θ and λ_3 define the state of deformation of the tube at a particular instant, and reflect the fact that the tube is homogeneous. Observe also that, by the symmetry of the problem, the deformation along the axes $\mathbf{e}_1$ and $\mathbf{e}_2$ at any point, must be equal. In equation (48) we call λ_θ –for reasons that will become apparent shortly– the unit elongation in both directions. The dimensions of the tube will then be $r=\lambda_\theta R$ and $l=\lambda_3 L$,

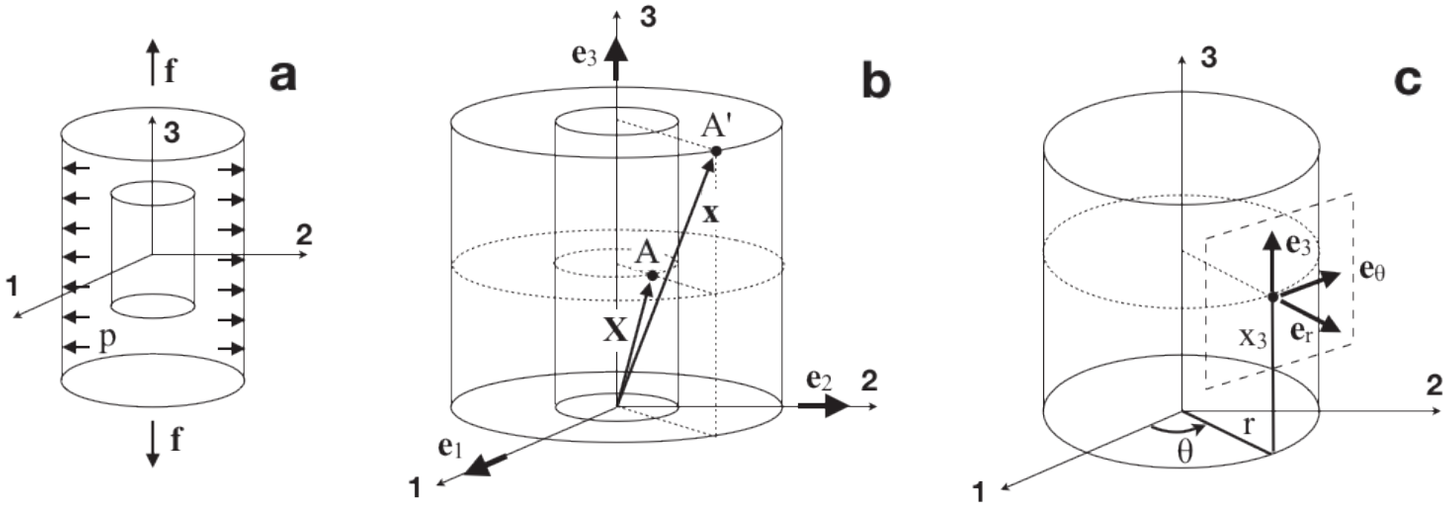

Fig. 22. *Extension and inflation of a thin tube*
a) Loading
b) Cartesian coordinates
c) Cylindrical coordinates

[3] This material is termed transversely isotropic, and its behaviour is the same in all directions situated in planes perpendicular to its axis of symmetry.

From equations (5), (14) and (15), it is possible to obtain the strain tensors. In our case, and given that we are using a three-dimensional coordinate system, the indices (i,j) take on the values 1, 2 and 3. A simple calculation leads to

$$\frac{\partial \kappa}{\partial \mathbf{X}} = \mathbf{F} = \begin{bmatrix} \lambda_\theta & & \\ & \lambda_\theta & \\ & & \lambda_3 \end{bmatrix} \tag{49}$$

and Green and Almansi strain tensors

$$\mathbf{E} = \frac{1}{2}\begin{bmatrix} \lambda_\theta^2 - 1 & & \\ & \lambda_\theta^2 - 1 & \\ & & \lambda_3^2 - 1 \end{bmatrix} \quad \eta = \frac{1}{2}\begin{bmatrix} 1 - 1/\lambda_\theta^2 & & \\ & 1 - 1/\lambda_\theta^2 & \\ & & 1 - 1/\lambda_3^2 \end{bmatrix} \tag{50}$$

The three-dimensional approach here is different from the two-dimensional situation considered previously for the membranes represented in figure 21, since due to the curvature of the tube no pair of coordinate axes is contained within the surface of the membrane. The strains obtained using equations (50) are referred to cartesian axes which are not parallel to the membrane, and the values will not be directly comparable to the results of other tests such as –for example– the biaxial tensile test discussed in the examples above.

Given that the tensors in equation (50) are diagonal, and also have the same values for axes 1 and 2, any other orthonormal reference system which contains the 3-axis will provide the same values, since any line perpendicular to the 3-axis is a principal axis of strain. In other words, if we rotate the 1 and 2-axes together by an arbitrary angle about the 3-axis, in order to obtain the axes 1', 2' and 3, the value of the tensors represented in the new coordinate system will be exactly the same as with the 1, 2 and 3-axes[4].

In particular, if we consider the cylindrical axes represented in figure 22c, the above rationale leads to the unit elongation in the circumferential (defined as $\mathbf{e}_\theta$) and the radial (defined as $\mathbf{e}_r$) directions –directions rotated from the 1 and 2-axes– being the same for the two axes, equal to λ_θ, (that is to say, $\lambda_r = \lambda_\theta$), and

$$h = \lambda_r H = \lambda_\theta H \tag{51}$$

If, in addition, conservation of volume is considered

$$2\pi\, r\, l\, h = 2\pi\, R\, L\, H \tag{52}$$

so

$$h = \frac{H}{\lambda_\theta \lambda_3} \tag{53}$$

which only agrees with equation (50) in the particular case that $\lambda_3 = 1/\lambda_\theta^2$.

If we set out the problem using the *cylindrical coordinates* shown in figure 22c, we define the points $\mathbf{X}$ in the reference configuration by their coordinates $(\mathrm{R},\Theta,\mathrm{X}_3)$ and those of the deformed configuration $\mathbf{x}$ by $(\mathrm{r},\theta,\ \mathrm{x}_3)$. The relationship between the coordinates of the corresponding points, according to the assumptions made, are

$$\begin{aligned} r &= \lambda_\theta R \\ \theta &= \Theta \\ x_3 &= \lambda_3 X_3 \end{aligned} \tag{54}$$

Expressed in terms of the axes $(\mathbf{e}_\mathrm{r}, \mathbf{e}_\theta, \mathbf{e}_3)$, the position vectors are

$$\mathbf{X}(R,\Theta,Z) = R\mathbf{e}_r + X_3\mathbf{e}_3 \tag{55}$$

for the reference configuration, and for the deformed

$$\mathbf{x}(r,\theta,z) = r\mathbf{e}_r + x_3\mathbf{e}_3 = \lambda_\theta R\mathbf{e}_r + \lambda_3 X_3\mathbf{e}_3 \tag{56}$$

The *deformation gradient tensor* $\mathbf{F} = \partial\kappa(\mathbf{X})/\partial\mathbf{X}$ is obtained from equation (5), expressed in cylindrical coordinates (Humphrey, 2002, Appendix II), yielding:

$$\mathbf{F} = \begin{bmatrix} \dfrac{\partial r}{\partial R} & \dfrac{1}{R}\dfrac{\partial r}{\partial \Theta} & \dfrac{\partial r}{\partial X_3} \\ r\dfrac{\partial \theta}{\partial R} & \dfrac{r}{R}\dfrac{\partial \theta}{\partial \Theta} & r\dfrac{\partial \theta}{\partial X_3} \\ \dfrac{\partial x_3}{\partial R} & \dfrac{1}{R}\dfrac{\partial x_3}{\partial \Theta} & \dfrac{\partial x_3}{\partial X_3} \end{bmatrix} = \begin{bmatrix} \lambda_r = \lambda_\theta & & \\ & \lambda_\theta & \\ & & \lambda_3 \end{bmatrix} \tag{57}$$

which, as we now know, results in the strains in equation (52).

---

[4] This result can be proved by applying to the tensors in equation (52) $\mathbf{Q}_\beta$ about the 3-axis by an angle β, $\mathbf{Q}_\beta = \begin{bmatrix} \cos\beta & sen\beta & \\ -sen\beta & \cos\beta & \\ & & 1 \end{bmatrix}$ and bearing in mind that a tensor $\mathbf{A}$ transforms under rotation as $\mathbf{A'}=\mathbf{QAQ}^\mathrm{T}$

We see once again –this time in cylindrical coordinates– that if we consider the three-dimensional problem with the movement of equation (54) the conservation of volume hypothesis is not satisfied. However now, given that the plane $(\mathbf{e}_\theta, \mathbf{e}_3)$ is always parallel to the surface of the tube, we can decouple the dimensions of the study and force the conservation of volume condition of equation (52). With this approach, the deformation of the tube can be analysed by decomposing the movement into that of the tangent plane $(\mathbf{e}_\theta, \mathbf{e}_3)$ (= two-dimensional movement) together with a deformation in the thickness direction of the tube $(\mathbf{e}_r)$ which is given by the unit elongation λ_r. We can then force the condition that the unit elongation λ_r need, not be equal to λ_θ s was obtained from equation (57), without requiring satisfaction of the condition.

$$\frac{h}{H} = \lambda_r = \frac{1}{\lambda_\theta \lambda_3} \tag{58}$$

which is a sufficient approximation for thin tubes.

Under these conditions, the deformation gradient tensor in the tangent plane ($\mathbf{e}_\theta$, $\mathbf{e}_3$) will be

$$\frac{\partial \kappa}{\partial \mathbf{X}} = \mathbf{F} = \begin{bmatrix} \frac{r}{R}\frac{\partial \theta}{\partial \Theta} & r\frac{\partial \theta}{\partial X_3} \\ \frac{1}{R}\frac{\partial x_3}{\partial \Theta} & \frac{\partial x_3}{\partial X_3} \end{bmatrix} = \begin{bmatrix} \lambda_\theta & \\ & \lambda_3 \end{bmatrix} \tag{59}$$

and the Green and Almansi tensors

$$\mathbf{E} = \frac{1}{2}\begin{bmatrix} \lambda_\theta^2 - 1 & \\ & \lambda_3^2 - 1 \end{bmatrix} \quad \text{and} \quad \eta = \frac{1}{2}\begin{bmatrix} 1 - 1/\lambda_\theta^2 & \\ & 1 - 1/\lambda_3^2 \end{bmatrix} \tag{60}$$

which indicate that the circumferential ($\mathbf{e}_\theta$) and axial ($\mathbf{e}_3$) directions are stretched, with elongations λ_θ and λ_3 respectively. The deformed thickness h is obtained from equation (58).

The displacement vector $\mathbf{u} = \mathbf{x} - \mathbf{X}$ becomes

$$\mathbf{u} = (\lambda_\theta - 1)R\mathbf{e}_r + (\lambda_3 - 1)X_3\mathbf{e}_3 \tag{61}$$

and the small strain tensor –equation (23)– is equal to

$$\varepsilon = \begin{bmatrix} \lambda_\theta - 1 & \\ & \lambda_3 - 1 \end{bmatrix} \tag{62}$$

which coincides with the value of $\mathbf{E}$ and η for small values of λ_θ and λ_3.

The Cauchy stress in the *axial direction* σ_{33} can be calculated directly from its definition in equation (28)

$$\sigma_{33} = \frac{\mathrm{f}}{2\pi r h} = \frac{\mathrm{f}\lambda_3}{2\pi R H} \tag{63}$$

in which we have used equations (54) and (58).

The Cauchy stresses in the *circumferential direction* $\sigma_{\theta\theta}$ can be deduced from the Laplace law, equation (27) taking into account the fact that the radius of curvature in the circumferential direction is r and its value in the axial direction tends to infinity (for a right tube)

$$\sigma_{\theta\theta} = \frac{pr}{h} = p\frac{\lambda_\theta^2 \lambda_3 R}{H} \tag{64}$$

From the symmetry of the problem $\sigma_{\theta 3} = 0$, so that the Cauchy stress tensor is

$$\sigma = \begin{bmatrix} p\frac{\lambda_\theta^2 \lambda_3 R}{H} & \\ & \mathrm{f}\frac{\lambda_3}{2\pi R H} \end{bmatrix} \tag{65}$$

and the Piola-Kirchoff tensors, deduced from equations (33) and (34) become

$$\mathbf{P} = \begin{bmatrix} p\frac{\lambda_\theta \lambda_3 R}{H} & \\ & \frac{\mathrm{f}}{2\pi R H} \end{bmatrix} \qquad \mathbf{S} = \begin{bmatrix} p\frac{\lambda_3 R}{H} & \\ & \frac{\mathrm{f}}{2\pi\lambda_3 R H} \end{bmatrix} \tag{66}$$

The stress in the *radial direction* σ_{rr} is not defined in the two-dimensional approximation that we have used. However, we can narrow down its value given that on the internal surface of the tube it must be equal to the internal applied pressure (– *p*) and zero on the exterior surface. Given the small value of the thickness of the tube, it is usually considered in the stress analysis that the radial stress does not diverge much from these two values, and frequently its value is ignored compared to the much higher values of $\sigma_{\theta\theta}$ and σ_{33}.

2.2.5. Constitutive equations

So far we have considered the mathematical description of the deformation of a solid, the definition of the state of stress, and have derived the equilibrium equations for a differential element, but said nothing about the nature of the material. It seems obvious that the mechanical behaviour will be very different if we examine the deformation of the mesoglea of an anemone or the dilation of an aorta, differences which come from the distinct natures of these materials.

On the other hand, the information provided by the three equilibrium equations and the conservation of mass equation are not sufficient to provide a knowledge at every point in the body of the seven variables necessary to solve the problem; the three components of the stress tensor, the two components of the displacement vector, the thickness and the density (which can be depend upon position). The equations must be supplemented by other relationships which characterise the physical properties of the material in question; these equations are known as the *constitutive equations*.

In general, the theory for the development and application of constitutive equations are quite complex, and beyond the scope of this book. Sufficient to say that the constitutive equation describes a physical property of the material and must, therefore, be independent of the reference coordinate system. Consequently, it has to be a tensorial equation.

In this book we will only consider some very simple examples of constitutive equations, in order to give the reader an idea of how to proceeded in other cases. Bear in mind that, in general, the deformations in soft biological materials will be large, (not small, as in hard structural materials), possibly depend upon loading history, temperature, humidity and the loading rate and, in some cases, may produce rupture of the material.

Constitutive equations are significantly simplified when there is no residual deformation (when the stress is removed the strain is also zero). Even so, its dependency on the *time* variable through the loading history (as in the viscoelastic examples discussed in our earlier study of fibres) makes them complicated because, in the stress-strain curves, the loading curve does not usually coincide with that of unloading. In these cases, the concept of *pseudo-elasticity* can be useful.

Another step towards the simplification of these equations is when they don't depend upon time, and the loading and unloading branches of the stress-strain curve coincide, that is to say, there is a one-to one correspondence between stresses and strains. In these circumstances the material behaves e*lastically* and it can be shown that the stresses can be derived from a potential, either the internal energy U, or the free energy $F = U - TS$ per unit volume. (Capaldi, 2012, for example).

In the particular case in which the strains depend only upon mechanical causes (when there is a function for the energy which only depends upon the deformation), the constitutive equations are simplified even further. Such materials are usually called *hyperelastic*.

Until recently, the constitutive equations for soft biological materials were hardly known. This lack of information has impeded the development of this branch of Materials Science; unable to model these materials, devise experiments, or interpret their results and make predictions. Experience with the continuum mechanics of metallic materials, ceramics and elastomers has not been sufficient to address the study of tissue and blood vessels. Later we shall briefly describe some of the simpler experiments and their results, which can help model the mechanical behaviour of these complex materials.

Hyperelastic constitutive equation

If W_m is the energy, per unit mass, due to the deformation of the body and ρ_0 the density of the body in the reference configuration, $\mathcal{W}=\rho_0 W_m$ will be the energy due to the deformation per unit volume of the body in the reference configuration. This energy coincides with the internal energy per unit volume in isentropic processes and with the free energy per unit volume in isothermal processes.

If $\mathcal{W}=f(E_{ij})$ is expressed as a function of the components of the Green-Lagrange strain tensor E_{ij} equation (14) (recall that in this case the strains are taken with respect to the reference configuration), it can be shown (see, for example, Y. Fung 1993) that:

$$\mathbf{S} = \frac{\partial \mathcal{W}}{\partial \mathbf{E}} \quad \text{or} \quad S_{ij} = \frac{\partial \mathcal{W}}{\partial E_{ij}} \tag{68}$$

which indicates that the second Piola-Kirchoff stress tensor is the thermodynamic conjugate of the Green-Lagrange strain tensor[5]. From this result it is possible to obtain the compo-

[5] When this expression is used care must be taken when writing the non-diagonal terms E_{ij} and E_{ji} inside the W function, since even though $E_{ij} = E_{ji}$ in each case W must be differentiated with respect to a different argument.

nents of the Cauchy tensor using equation (36) below.

$$\sigma = \frac{H}{h}\frac{1}{\det \mathbf{F}}\mathbf{F}\mathbf{S}\mathbf{F}^T \quad \text{or} \quad \sigma_{ij} = \frac{H}{h}\frac{1}{\det\left[\partial x_\alpha/\partial X_\beta\right]}\frac{\partial x_i}{\partial X_l}\frac{\partial x_j}{\partial X_m}S_{lm}$$

In the previous paragraphs, we have assumed that the analysis is two dimensional, and that the indices i, j, α, β, etc... take on the values 1 and 2, which define the axes in the plane of the membrane. The only deformation considered in the 3-direction –perpendicular to the plane of the membrane– is the change of thickness h/H. If the membrane is incompressible, the change in the thickness h/H will compensate for the change of volume produced by the deformation (= change in area) in the plane of the membrane.

It is important to note that if the strain defined by $\mathbf{F}$ does not change the area ($\det\mathbf{F}=1$, equation (20)) and the function $\mathcal{W}$ does not depend upon the area of the membrane, any hydrostatic stress $q\mathbf{1}$ defined in the plane of the membrane[6] added to the result of equation 36 will satisfy the constitutive equation, since it produces no work because the area of the membrane remains constant. In this case the correct expression for calculating the Cauchy stress tensor σ at a given point will be

$$\sigma = \frac{H}{h}\mathbf{F}\mathbf{S}\mathbf{F}^T + q\mathbf{1} \quad \text{or} \quad \sigma_{ij} = \frac{H}{h}\frac{\partial x_i}{\partial X_l}\frac{\partial x_j}{\partial X_m}S_{lm} + q\delta_{ij} \qquad (68a)$$

where the value of the parameter q must be determined from the boundary or equilibrium conditions.

The stresses through-the-thickness (σ_{13}, σ_{23}, σ_{33}) are not considered in the two-dimensional calculation and must be estimated separately (or neglected), as was shown in example 2.2.4.

A frequent alternative, mostly in non-planar membranes such as the walls of blood vessels, is to develop directly the three-dimensional problem in three spatial coordinates in the deformed and reference configuration $\mathbf{x}(x_1, x_2, x_3)=\kappa[\mathbf{X}(X_1, X_2, X_3)]$, and using equation (5a) to obtain the three-dimensional deformation gradient tensor $\mathbf{F}$. This process was already used in example 2.2.4 to obtain equation (52).

The three-dimensional analysis leads again to equation (68a), which remains valid but with the indices taking on the values 1, 2 and 3, and the stresses and strains obeying the same conventions and notation as those used in the two-dimensional case. Thus, the components of the second Piola-Kirchhoff tensor $\mathbf{S}$ will be (S_{11}, S_{12}, S_{22}) in the plane of the membrane and (S_{13}, S_{23}, S_{33}) through-the-thickness. Note that now $det\mathbf{F}$ becomes the membrane volumetric strain dv/dV, qwhich incorporates the variation due to the thickness (included in an independent form) by means of the term h/H in equation (36). Then the Cauchy stress tensor is given by

$$\sigma = \frac{1}{\det \mathbf{F}}\mathbf{F}\mathbf{S}\mathbf{F}^T \quad \text{or} \quad \sigma_{ij} = \frac{1}{\det\left[\partial x_\alpha/\partial X_\beta\right]}\frac{\partial x_i}{\partial X_l}\frac{\partial x_j}{\partial X_m}S_{lm} \qquad (68b)$$

with components (σ_{11}, σ_{12}, σ_{22}) in the plane of the membrane and (σ_{13}, σ_{23}, σ_{33}) through the thickness.

In a parallel manner to that in the two-dimensional situation, when a deformation which conserves volume –and therefore $det\mathbf{F}=1$– and also when an energy deformation function $\mathcal{W}$ is not sensitive to the volume change of the membrane, each stress given by the expression

$$\sigma = \mathbf{F}\mathbf{S}\mathbf{F}^T + q\mathbf{1} \quad \text{or} \quad \sigma_{ij} = \frac{\partial x_i}{\partial X_l}\frac{\partial x_j}{\partial X_m}S_{lm} + q\delta_{ij} \qquad (68c)$$

will be a solution to the constitutive equation, since an arbitrary three-dimensional hydrostatic stress[7] $q\mathbf{1}$ will produce no work on the membrane while its volume is conserved. The value of the parameter q is determined, as mentioned above, using the boundary or equilibrium conditions of the problem. In this case it is not necessary to make any estimate of, or hypotheses about, the through-the-thickness stresses, since these are all obtained directly from equation (68c).

Not all elastic materials can be described by means of a strain energy function, those in which it is possible are called *hyperelastic*s, as already noted above. Observe that equation (68) is biunivocal: for every state of stress there is a corresponding strain state and vice versa.

Biological materials, and in particular tissues, are not perfectly elastic. However, in some circumstances, when it is possible to precondition them they can be treated as *pseudo-elastic*, in the sense discussed previously. In these cases, it is possible to propose a *pseudo-strain energy* function, valid for the increasing strain branch and another for the decreasing strain of the stress-strain response.

[6] $\mathbf{1}$ is the two-dimensional unity tensor in the plane of the membrane. The parameter q may be a function of position.

[7] Observe that here 1 is the three-dimension unit tensor.

In order to illustrate and cement these ideas we will summarise, below, the development of a *pseudo-constitutive equation* for the epithelium of a rabbit, as obtained by Tong and Fung (1976) using data from Lanir and Fung (1974).

The authors began by proposing the following empirical expression for $\mathcal{W}=\rho_0 W_m$:

$$\mathcal{W}=\frac{1}{2}\left\{f(\alpha,\mathbf{E})+c\exp\left[F(a,\mathbf{E})\right]\right\} \tag{69}$$

where

$$f(\alpha,\mathbf{E})=\alpha_1E_{11}^2+\alpha_2E_{22}^2+\alpha_3E_{12}^2+\alpha_3E_{21}^2+2\alpha_4E_{11}E_{22} \tag{70}$$

$$F(a,\mathbf{E})=a_1E_{11}^2+a_2E_{22}^2+a_3E_{12}^2+a_3E_{21}^2+2a_4E_{11}E_{22} \tag{71}$$

From equations (67) and (69), the components of the second Piola-Kirchhoff tensor, S_{ij}, are given by

$$S_{11}=\alpha_1E_{11}+\alpha_4E_{22}+cA_1B$$

$$S_{22}=\alpha_4E_{11}+\alpha_2E_{22}+cA_2B$$

$$S_{12}=\alpha_3E_{12}+ca_3E_{12}B \tag{72}$$

where

$$A_1=a_1E_{11}+a_4E_{22}\quad A_2=a_4E_{11}+a_2E_{22}$$

and

$$B=\exp\left[F(a,\mathbf{E})\right] \tag{73}$$

Calculation of the constants α_1, α_2, α_3, α_4, a_1, a_2, a_3, a_4 and c is achieved from experimental results in the biaxial tests discussed above. In this case $S_{12}=0$, since $E_{12}=0$.

Two experimental curves (preconditioned, as discussed previously) are shown in figure 23a; one in which λ_2 is held constant (λ_2 = 1) and λ_1 varies, and the other in which λ_2 varies while keeping λ_1 constant (λ_1 = 1).

In order to calculate the constants, two points have been selected in each test; one where the force varies rapidly with the elongation (points A and C) and the other where the force varies slowly with the elongation (points B and D). At each point the values of the coordinates and slope were measured and equated to the values of S_{11} and S_{22} and their corresponding derivatives with respect to E_{11} and E_{22}. (See Tong and Fung (1976) for details. Here, the aim is only to outline the way forward).

With the values obtained, the function $\mathcal{W}(\mathbf{E};\alpha_i,a_i,c)$ for the rising part of the force-elongation curve is now known, and from it good agreement with the two experiments is achieved, as shown in figure 23b. Authors, Tong and Fung, noted that it is not surprising that the agreement was good, since four points on the curve were used, but it is remarkable that the *whole* curve was reproduced quite well given the nonlinear behaviour of the epithelium.

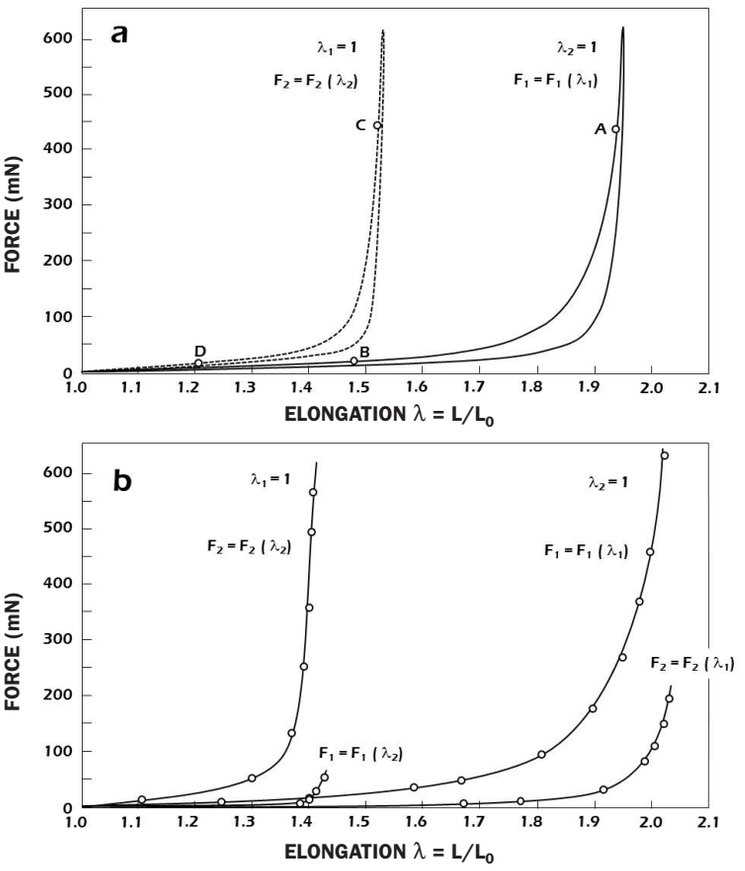

Fig. 23. *a) Force-elongation curves, for rabbit epithelium, corresponding to two preconditioned biaxial tests (Lanir and Fung, 1974).*
b) Numerical results (o) obtained from the data in figure 23a (see the explanation in the text) (Tong and Fung, 1976).

Pseudo-constitutive equations, similar to but even simpler than equation (69), have been developed for other tissues, by ignoring the first term, that is:

$$\mathcal{W} = c\exp\left[F(a,\mathbf{E})\right] \tag{74}$$

For artery walls and for pulmonary tissue Fung and co-workers have developed equations like (74) and which work reasonably well (Fung 1975, Fung et al. 1978, Vawter et al. 1979).

An ambitious objective, when constitutive equations need to be formulated, is to relate the structure of the material to its properties. In general, the aim is to go from bottom to top; starting with the properties of the molecules and microscopic structure to deduce the macroscopic behaviour. Or, starting with the macroscopic behaviour, to try to understand the role played by the microscopic constituents of the material. In either case, the intention is to enhance knowledge of the relationship between the structure and mechanical behaviour.

To cite some examples along these lines, Viidik (1968, 1990) developed a tissue model based on collagen fibres which are progressively loaded by increasing the deformation. Lanir (1979) improved Viidik's first model by assuming that tissue is a material composed of elastin and collagen fibres, which come under load at different stages in the deformation process. Shoemaker and Fung (1986) have developed a similar model for human skin and the pericardium of a dog. Despite obtaining good results the authors recognised that there was a lack of information on the microstructure of these materials and their fibres.

Following another approach, not based on microstructural data, Kwan and Woo (1989) developed models which reproduce the nonlinear relationships between stresses and strains for tendons and ligaments. With an undulating form of collagen fibres, they proposed a model in which each fibre is formed of two components; a very flexible one, which reproduces the initial part of the stress-strain curve and the other, more rigid, which captures the final, stiffer, part of the response. The model consists of a judiciously chosen bundle of fibres which is capable of reproducing the experimental results reasonably well.

EXERCISE 9

For pulmonary tissue, Y. C. Fung proposed the following equation for the internal energy, based on previously expressed ideas (Fung 1975).

$$U = c\ \exp(a_1E_{11}^2 + a_2E_{22}^2 + 2a_4E_{11}E_{22})$$

in which it was assumed that the through-the-thickness strain could be ignored, compared to E_{11} and E_{22} and behaviour practically bidimensional.

The strain energy, as already mentioned, coincides with the internal energy U ein an isentropic process, and with the free energy in an isothermal process.

Under these conditions, calculate the corresponding stress tensor as a function of the material constants (a_1, a_2, a_4 and c).

SOLUTION:

From equation (66) we obtain the stresses in the second Piola-Kirchoff tensor

$$S_{11} = 2c(a_1E_{11} + a_4E_{22})\exp(a_1E_{11}^2 + a_2E_{22}^2 + 2a_4E_{11}E_{22})$$
$$S_{12} = 0$$
$$S_{22} = 2c(a_2E_{22} + a_4E_{11})\exp(a_1E_{11}^2 + a_2E_{22}^2 + 2a_4E_{11}E_{22})$$

In order to obtain the Cauchy stresses from equation (36) we need to know the deformation gradient tensor, $\mathbf{F} = \partial\kappa/\partial\mathbf{X}$, qwhich depends upon the type of deformation $\mathbf{x} = \kappa(\mathbf{X},t)$ to which the solid is subjected.

EXERCISE 10

Calculate directly the value of the strain energy in a tensile test on an elastic material as a function of both the engineering and true stresses and strains in the test. Compare its value with that obtained from equation (68). Hint: use the results of example 2.2.3.

SOLUTION:

The example analyses the case of a state of biaxial tension. For a uniaxial tensile test $f_1 = F$ and $f_2 = 0$.

If the material is elastic and there are no dissipative processes, the work Fdl_1 done by the tensile force F is stored entirely in the form of elastic strain energy. The value of the energy per unit volume in the reference configuration (= initial, undeformed) $\mathcal{W}$ will be the integral

$$\mathcal{W} = \frac{1}{L_1 L_2 H}\int_{L_1}^{l_1} F dl_1 = \int_{L_1}^{l_1} \frac{F}{L_2 H} d\left(\frac{l_1}{L_1}\right) = \int_1^{\lambda} s d\lambda$$

in which $L_1\ L_1\ H$ is the initial volume, $s = F/(L_2 H)$ the engineering stress and $\lambda = l_1/L_1$ the elongation of the specimen. Since, $\lambda = 1 + e$, and $e = (l_1 - L_1)/L_1$ the engineering strain, we have $d\lambda = de$ so that the resulting value is $\mathcal{W} = \int_1^{\lambda} s d\lambda = \int_0^{e} s de$ which is the area under the engineering stress-strain curve (s, e).

If we refer to the elastic strain energy in the instantaneous configuration the result is

$$\omega = \frac{1}{l_1 l_2 h}\int_{L_1}^{l_1} F dl_1 = \int_{L_1}^{l_1} \frac{F}{l_2 h}\frac{dl_1}{l_1} = \int_0^{\varepsilon} \sigma d\varepsilon$$

where $\sigma = F/(l_2 h)$ is the true stress and $d\varepsilon = dl_1/l_1$ the differential of the true strain (see the section dedicated to the tensile test in the biological fibres volume). Now we recognise the value of ω, the elastic strain energy per unit volume in the instantaneous configuration, as the area under the true stress-strain curve (σ, ε).

In order to apply equation (68) $S_{ij} = \partial \mathcal{W}/\partial E_{ij}$ which relates the energy per unit volume in the reference configuration and the second Piola-Kirchoff stresses, we will use equations (46) which lead to

$$S_{11} = \frac{1}{\lambda_1}\frac{F}{L_2 H} = \frac{s}{\lambda} \qquad S_{22} = S_{12} = S_{21} = 0$$

A partir de la ecuación (68) obtenemos From equation (68) we obtain

$$d\mathcal{W} = \frac{\partial \mathcal{W}}{\partial E_{ij}} dE_{ij} = S_{ij} dE_{ij} = S_{11} dE_{11} = \frac{s}{\lambda} dE_{11}$$

since S_{11} is the only non zero term. The Green-Lagrange strain is obtained from the value just calculated

$$E_{11} = \frac{1}{2}\left(\lambda_1^2 - 1\right)$$

and differentiating it we see $dE_{11} = \lambda_1 d\lambda_1 = \lambda d\lambda$, which leads to $\mathcal{W} = \int d\mathcal{W} = \int_1^{\lambda} s\, d\lambda$

coincident with the result obtained directly.

If $J = l_1 l_1 h/(L_1 L_2 H)$ is the ratio of the deformed and undeformed volumes, the strain energy per unit volume in the deformed configuration will be simply
$\omega = \mathcal{W}/J$, given by

$$\omega = \frac{\mathcal{W}}{J} = \frac{1}{J}\int_1^{\lambda} s\, d\lambda = \int_1^{\lambda} \frac{L_1 L_2 H}{l_1 l_2 h}\frac{F}{L_2 H} d\lambda = \int_1^{\lambda} \frac{\sigma}{\lambda} d\lambda = \int_{L_1}^{l_1} \sigma \frac{dl_1}{l_1} = \int_0^{\varepsilon} \sigma\, d\varepsilon$$

Note that when $J = 1$ both specific energies coincide.

2.3. EXPERIMENTAL AND CHARATERISATION TECHNIQUES

The objective of this section is the summary description of the most common two-dimensional mechanical tests used to characterise biological membranes.

The essential aspects upon which the experiments are based are emphasised, without going into details of the experimental equipment, which can be found in the cited references. Besides, there is not much point in delving into these details because data acquisition and reduction techniques evolve rapidly and soon become obsolete.

The experiments discussed below are specific to bidimensional materials. This does not meant to exclude other types of tests, such as tensile tests (already mentioned in the first volume) or, tests developed for three-dimensional materials, such as indentation or fracture (which will be presented in the following volume).

To begin with, tensile tests in two perpendicular directions are described. Experiments on tubes are also discussed, when these are subjected to combined traction and internal pressure, and even torsion.

Several fracture tests are also outlined: The *tear* resistance is an interesting property of tissue, in particular of the epithelium. Another rupture test –the *peel* test– provides knowledge of the adhesion energy between the membrane and the substrate. To this end, two experiments are discussed; simple peeling and the tympanum test.

2.3.1. Biaxial tensile tests

Biaxial tensile tests on soft biological material tissue are difficult to perform and analyse. To begin with, gripping the specimens is complicated if damage to the material is to be avoided and the application of forces to the edges is not easy. Measurement of the deformations must be made using optical processes (contact extensometers could disturb the measurement due to the flexibility of the specimen and the reaction of the sample, if it is alive). The anisotropy, which is almost always present in these tissues, also makes the interpretation of data a complex task.

For these experiments thin specimens are used –less than 3 mm thick and often less than 1 mm– loaded with forces acting in the plane of the specimen. The general arrangement of the biaxial test on a membrane is shown schematically in figure 24. In practice the sample is almost always immersed in a saline solution and tested at a controlled temperature.

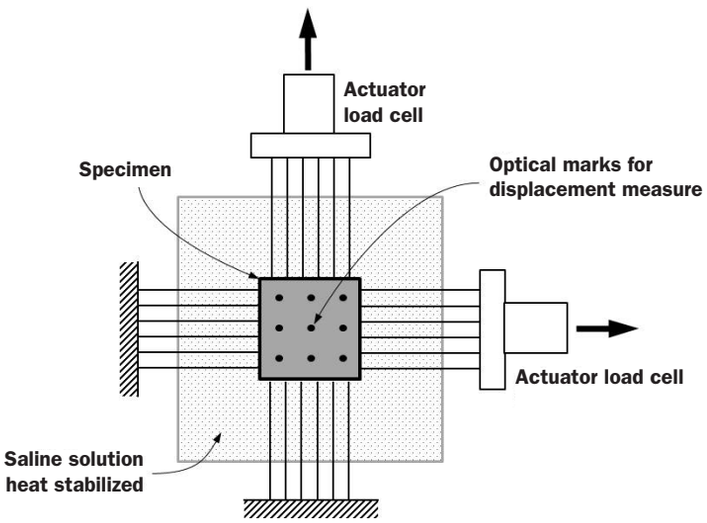

Fig. 24. *Schematic arrangement of a biaxial tension test.*

The loads are applied in the directions indicated in the figure and displacements measured optically using marks drawn in the centre of the membrane, in a region in which it is assumed that the loading constraints have no influence, and in which it is assumed that that the strains and stresses are uniform.

With this arrangement it is possible to perform a range of tests; uniaxial tension, biaxial, creep or relations, and dynamic. For more details, see for example, Sacks (1999, 2003).

Several curves obtained from uniaxial tests on cat epithelium (Veronda and Westmann 1970), donkey and rhinoceros (Shadwick *et al*. 1992) are shown in figure 25. Epithelia can be modelled as if they were materials composed of elastin and collagen fibres embedded in a protein and polysaccharide matrix. In these tissues forces are resisted primarily by the elastin and collagen fibres. The elastin fibres are much more flexible than those of collagen; they have an initial elastic modulus of about 0.6 MPa and can be strained up to 200%. The collagen fibres form a plushy mass which gradually align with the loading direction as the tissue deforms. Consequently, at the start of the deformation the elastin fibres are the ones that support the load but as the deformation increases it is the stiffer collagen fibres that come under load. This behaviour is responsible for the “J-form” of the curves obtained from tensile tests.

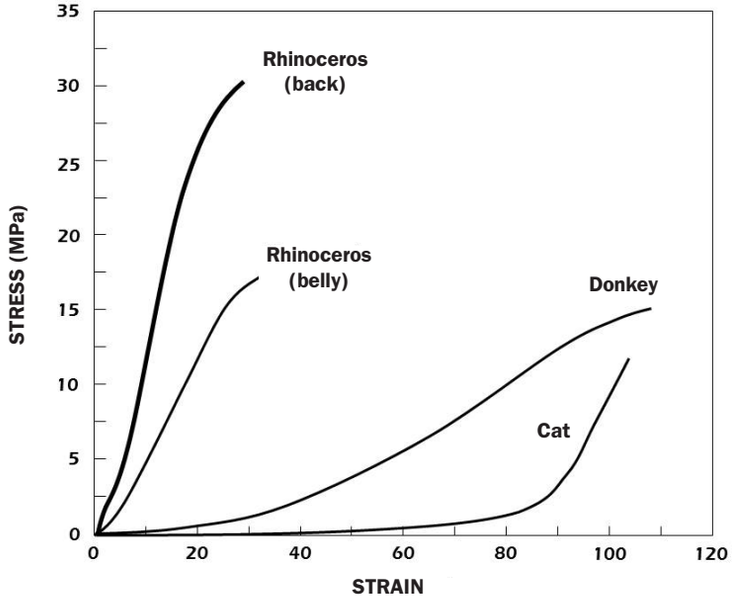

Fig. 25. *Typical stress-strain curves for various epithelia.*

EXAMPLE: RABBIT EPITHELIUM

An understanding of the mechanical behaviour of epithelia is of great interest to plastic surgeons, and for interpreting many pathological situations. As will be seen below, traditional tensile tests do not provide the required information, so it is necessary to resort to more complex test, such as the biaxial ones mentioned above.

To a first approximation, skin can be considered as an incompressible material. This allows the construction of three-dimensional models –closer to reality– based on data from two dimensional tests, in which variations in the third dimension can be deduced from the changes in the other two dimensions.

In this example, some results of Lanir and Fung's (1974), now classic, two-dimensional experiments on rabbit epithelia are summarised. Details of the equipment and specimen preparation can be found in the cited reference.

Skin specimens, measuring 35 mm by 35 mm, cut such that two edges were parallel to the axis of the body and the other two, perpendicular to it, were tested. Tensile and relaxation tests were performed, uniaxial as well as biaxial, and the influence of the rate of loading and temperature on the data were recorded.

Figure 26, contains the data from several tensile tests; uniaxial tests in the direction of the *x*-axis (Scheme A), biaxial tests with the applied load increasing in the x-direction and while keeping the displacement along the *y*-axis constant (Scheme B) and similar experiments with the traction in the *y*-direction (Schemes C and D). The direction of the *x*-axis is parallel to axis of the body of the rabbit.

The experiments clearly show that the epithelium is *anisotropic* since its behaviour varies with the loading direction (compare the figures corresponding to the A and C loadings, for example) The mechanical response is *nonlinear* and shows a degree of *hysteresis*. Another relevant result is that the response of the tissue depends upon the mode of loading; that under uniaxial tension (test A, for example) is not the same as in biaxial tension (test B). These results provide a warning against using uniaxial tensile tests to predict the behaviour of the epithelium, since in practice this tissue is subjected to biaxial loading.

The referenced article also includes biaxial relaxation tests, as shown schematically in figure 27. In this figure the relaxation force in the *x*-direction is reported, after the tissue was stretched in the *x*-direction (by a quantity denoted by $\lambda = l/l_0$) and keeping the strain in the perpendicular *y*-direction constant. Here, again, it was found that the stress relaxation is different when the loading is in the *y*-direction (these values are not shown in the figure); it is not the same if the sides are constrained or free, in which a contraction is produced in the test. All this indicates that uniaxial relaxation tests are not truly representative because in reality the sides are always restrained, and the tissue adapts itself to the loading, reorienting the collagen fibres in order to reduce both the stress in the loading direction and the strain in the transverse direction.

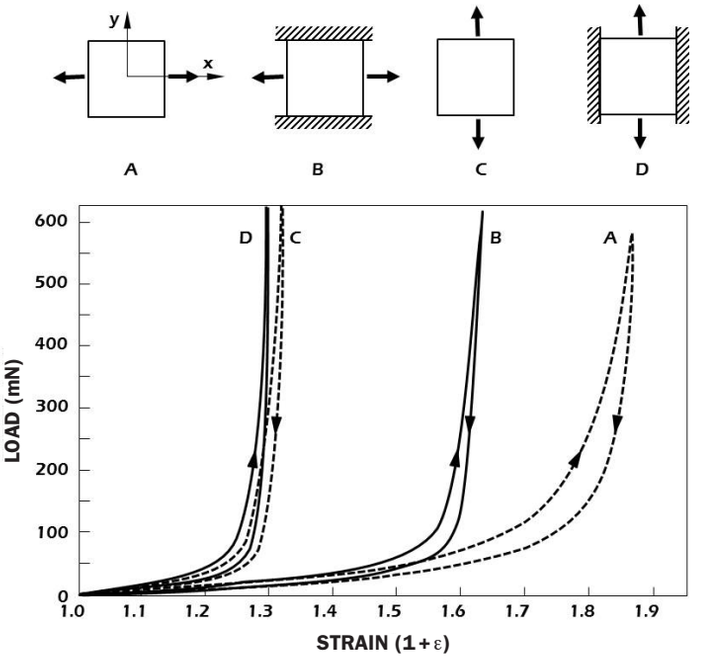

Fig. 26. *Uniaxial tensile (A and C) and biaxial (B and D) test on the rabbit epithelia (Lanir and Fung, 1974).*

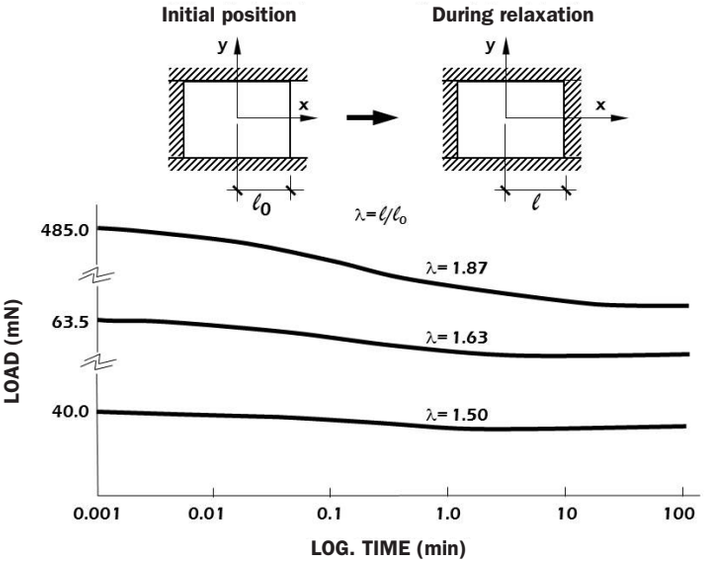

Fig. 27. *Biaxial relaxation tests (Lanir and Fung, 1974).*

2.3.2. Pressure test

Bulge test

An alternative means of performing biaxial tests on biological membranes consists of clamping a circular piece around its edge, subjecting it to a pressure, and measuring the displacements produced on the surface (bulge test), as shown in figure 28a. This is a very simple experimental technique which is, however, difficult to interpret if the membrane is not isotropic (which is almost always the case), since the anisotropy of the materials requires the application of numerical modelling (Tonge *et al*. 2013a,b). Therefore, this method is almost exclusively used to compare biomaterials, and perform fatigue strength studies.

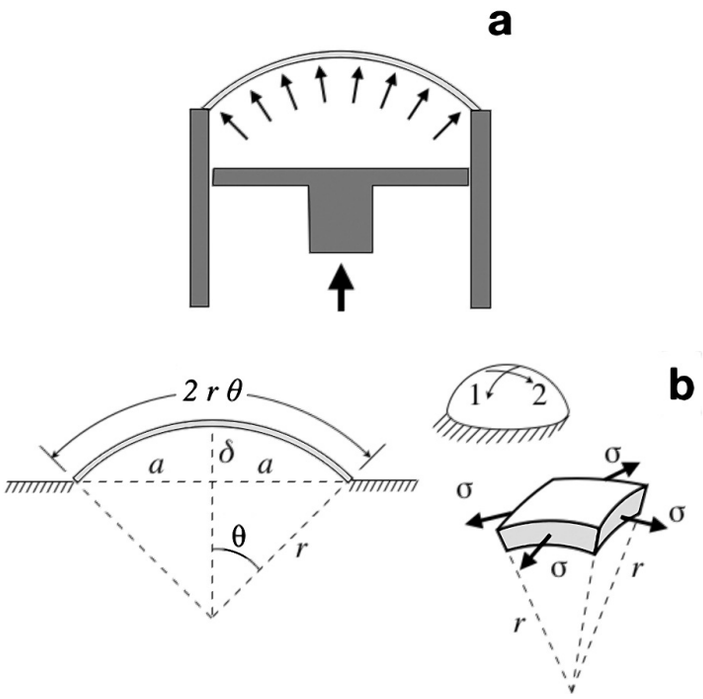

Fig. 28. *a) Membrane pressure test (bulge test). The membrane is subjected to a state of biaxial tension induced by the applied pressure in the interior of the apparatus.*
b) Simplified analysis assuming spherical deformation.

A simplified analysis of this experiment, valid for small displacements of the membrane, which is assumed thin homogeneous and isotropic, can be performed by assuming that the deforming membrane takes on a spherical shape, as indicated in figure 28b. With the notation of the figure we see that $sin(\theta) = a/(r-\delta) \approx a/r$ and $r\,cos(\theta) + \delta = r$, from which we can obtain the radius of curvature as a function of the displacement of the apex δ and the radius a of the membrane in its initial state

$$r = \frac{a^2 + \delta^2}{2\delta} \tag{75}$$

With this value, we can estimate the elongations of the deformed membrane at its apex that, because of the assumed spherical deformation, will be the same in any direction. It is sufficient to refer to the initial membrane diameter *(2a)* which, in the deformed configuration, extends to an arc length equal to $2r\theta$ (figure 28b). Therefore

$$\lambda = \frac{2r\theta}{2a} = \frac{a^2 + \delta^2}{2a\delta} arcsin\left(\frac{2a\delta}{a^2 + \delta^2}\right) \simeq 1 + \frac{2}{3}\frac{\delta^2}{a^2} \tag{76}$$

Taking into account equations (18) and (19) and that all of the directions on the surface of the membrane are equivalent, the strain tensor at the apex of the deformed membrane will be

$$\mathbf{E} = \eta \simeq \frac{2}{3}\frac{\delta^2}{a^2}\begin{bmatrix} 1 & \\ & 1 \end{bmatrix} \tag{77}$$

in which we have ignored terms of higher order than δ^2.

If we assume, as is common in biological materials, that the membrane is incompressible and volume is conserved during the deformation, we can calculate the deformed thickness h near the central apex from the initial thickness H using equation (22). If we equate this expression to 1 and solve for h taking into account that $da/dA = \lambda^2$

$$h = \frac{H}{\lambda^2} \simeq H\left(1 - \frac{4}{3}\frac{\delta^2}{a^2}\right) \tag{78}$$

The Cauchy stresses σ can be obtained from the applied pressure p using Laplace's law (equation 27), since the radius of curvature is known and equal to r in every direction. The resulting value is

$$\sigma = \frac{pr}{2h} = \frac{p(a^2 + \delta^2)}{4h\delta} \simeq \frac{p}{H}\left(\frac{a^2}{4\delta} + \frac{7\delta}{12}\right) \tag{79}$$

Equations (75), (76), (77), (78) and (79) provide the stress-strain state of the apex of the membrane as a function of its dimensions a and H, and the displacement δ produced under the pressure p.

Pressure-diameter test

Pressure-diameter tests on blood vessels and other biological ducts are also biaxial experiments which aim to reproduce the workings of these tissues inside the body. In essence, during the test the change in diameter of the duct is measured as a function of the internal pressure. The test can be complemented by subjecting the duct to traction and, in some experiments, simultaneously to traction and torsion.

The equipment necessary for traction and internal pressure applied to blood vessels is shown, in schematic form, in figure 29. For more details, see (Guinea *et al.* 2005). The blood vessels are tested immersed in a physiological serum at a controlled temperature. The vessel is placed in a transparent cell which allows visualisation and measurement of the diameter by optical methods. The ends of the vessel are held in the grips of a mechanical testing machine and the internal pressure is applied to the vessel by means of an auxiliary physiological serum circuit at the temperature of the experiment, driven by a compressed air pump. Pressure regulators control and stabilise the air pressure.

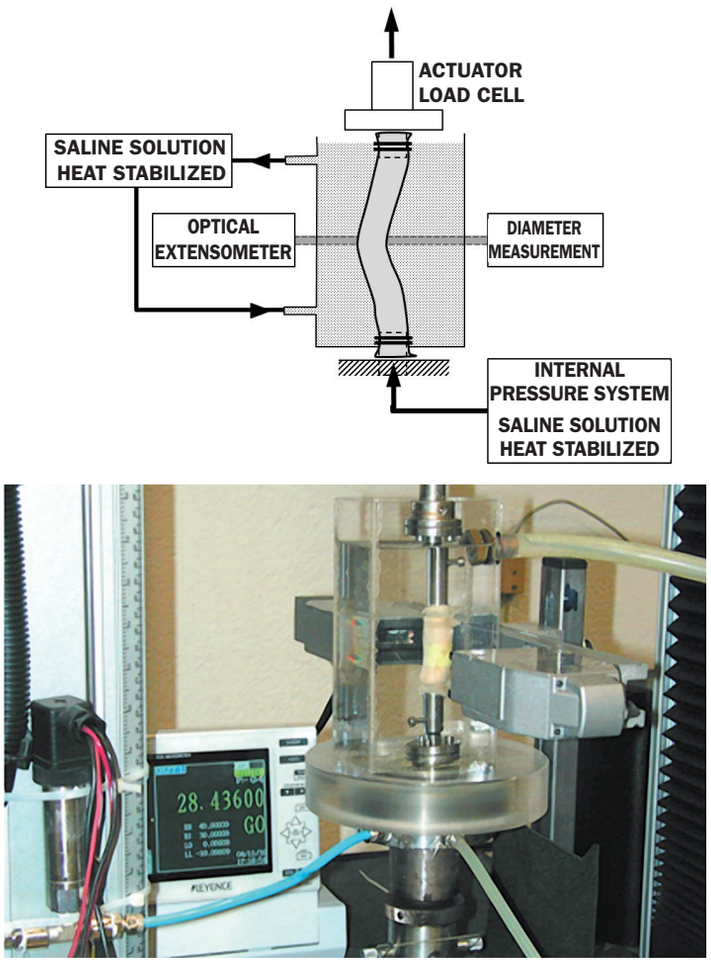

Fig. 29. *a) Schematic representation of an experiment for tubes subjected to traction and internal pressure. b) Experiment on an arterial aorta.*

In Fung's (1993) book, and the reference cited in it, similar equipment is described for recording the variation in diameter as a function of the internal pressure, traction and torsion to which the vessel is subjected.

The process of stretching and inflation of a thin tube –which was analysed in a previous section (2.2.4)– can be applied to these experiments. If the duct wall is thick, or when residual stresses have to be considered, a complete three-dimensional analysis must be performed. This can be found in Humphrey (2002).

Two challenges in testing pressurised ducts are due to instabilities such as *buckling* or the *formation of protuberances* (known as *aneurisms* in the case of blood vessels) which change the geometry and invalidate the test. Because of their practical interest, both cases are discussed briefly below.

Buckling or the collapse of the wall of a tube generally appears at the beginning of the test, at small pressures and under axial traction. This situation is shown in figure 30 in a test on a carotid artery. Although buckling of the tube can only be produced for negative pressures (suction), inhomogeneities in the wall and the residual stresses may provoke its occurence with positive pressures. In general, biological ducts have only reasonably circular cross sections above a certain minimum pressure, of around kPa (~10mmHg) in the case of blood vessels. Figure 30b contains pressure-diameter curves corresponding to different values of applied axial elongation. We see that axial traction produces a stabilising effect which reduces the buckling propensity.

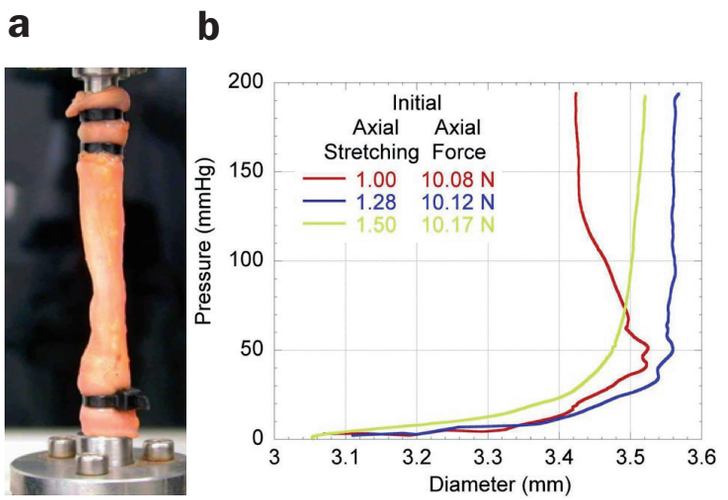

Fig. 30. *a) Buckling of an artery during a pressure-diameter test. b) Effect of the axial load on the response of the vessel.*

The formation of **protuberances** in the wall is a phenomenon which is the inverse of that of buckling, because a section of the duct is dilated abnormally with relative to the rest, figure 31a. In arterial vessels this dilatation is known as an aneurism and is a very serious complication which can lead to incapacitation or even death. Mechanically, the formation of protuberances usually occurs because of a local weakening of the wall, which dilates due to the pressure. This is the situation of keratoconus, figure 31b, in which a protrusion of the cornea causes a severe loss of vision, and many aneurisms. However, it can also produce an abnormal dilatation without the presence of inhomogeneities, exclusively due to the mechanical behaviour of the material of the duct as will be seen below.

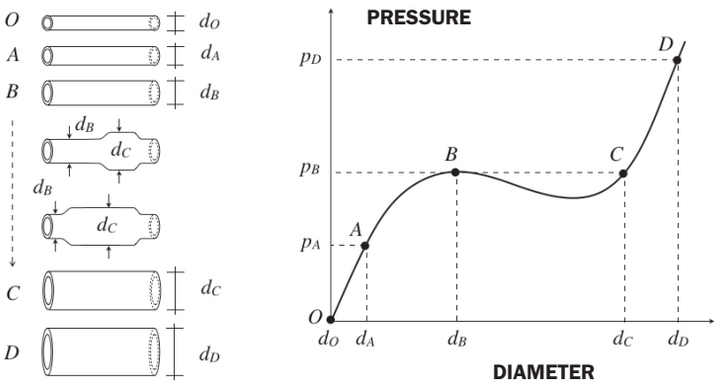

Fig. 32. *a) Deformation process and the appearance of protuberances in a duct. b) Pressure-diameter curve.*

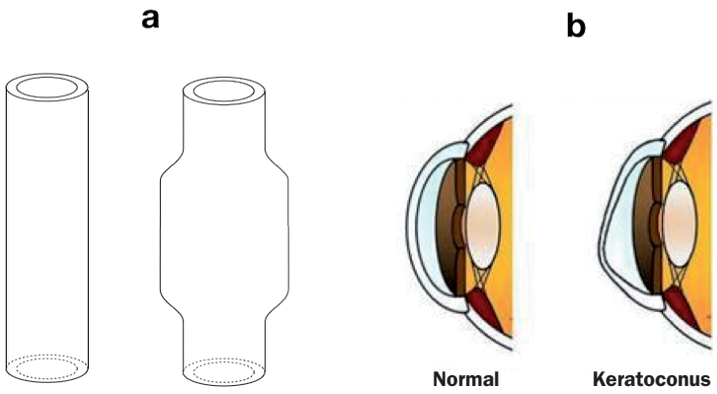

Fig. 31. *a) Inhomogeneous dilatation of a duct. b) Local dilatation of the cornea, known as keratoconus.*

Figure 32 shows the case of a duct whose pressure-diameter curve has a local minimum. When the tube is at rest its diameter is d_{O} and its geometry uniform. If we apply pressure in the range $(0, p_{\mathrm{B}})$ the tube diameter increases uniformly d_{B}, which is the diameter corresponding to a unique mechanical equilibrium state. The situation changes at the moment p_{B}, is reached, since there are now two solutions to the mechanical problem, each one with a different value of the diameter: d_{B} and d_{C}. The points between B and C on the pressure-diameter curve are unreachable since each section of the duct has two possible diameters for a given value of pressure, and the situation is unstable.

From the instant at which a p_{B} is reached two zones of different diameter are generated in the duct, each one corresponding to points B and C. If we try to increase the pressure in the tube, it will not exceed the value of p_{B} until all of the duct has transformed to the diameter d_{C}, corresponding to point C, after which the deformation process returns to being uniform.

We see, then, that the cause of the instability lies in the appearance of a local minimum in the pressure-diameter curve, and which, if it were to increase monotonically, the phenomenon would not occur. Certain constitutive equations, such as those of some elastomers, can give rise to this behaviour and it is instructive to determine the pressure-diameter curve from a stretching and inflation test on these materials.

Yeoh's hyperelastic model[8] de Yeoh (1993) is often used to model incompressible, isotropic elastomers. The strain energy per unit volume function $\mathcal{W}$ in three-dimensions is

$$\mathcal{W} = \alpha tr\mathbf{E} + \beta\left(tr\mathbf{E}\right)^2 + \gamma\left(tr\mathbf{E}\right)^3 =$$

$$= \alpha\left(E_{11}+E_{22}+E_{33}\right) + \beta\left(E_{11}+E_{22}+E_{33}\right)^2 + \gamma\left(E_{11}+E_{22}+E_{33}\right)^3 \quad (80)$$

where tr is the trace operator and α, β, γ model constants..

[8] Recall that for a hyper-elastic material there is a one-to-one relationship between stress and strain, which depends on neither time nor temperature.

In this example a three-dimensional analysis of the problem was performed, using expression (66) in order to obtain the second Piola Kirchoff stress tensor $\mathbf{S}$, since it was a hyperelastic material:

$$\mathbf{S}=\left(\alpha+2\beta tr\mathbf{E}+3\gamma\left(tr\mathbf{E}\right)^2\right)\begin{bmatrix}1&&\\&1&\\&&1\end{bmatrix}=$$

$$=\left(\alpha+2\beta\left(E_{11}+E_{22}+E_{33}\right)+3\gamma\left(E_{11}+E_{22}+E_{33}\right)^2\right)\begin{bmatrix}1&&\\&1&\\&&1\end{bmatrix} \quad (81)$$

and from equation (68c)

$$\sigma=\mathbf{FSF}^T+q\mathbf{1} \quad \text{or} \quad \sigma_{ij}=\frac{\partial x_i}{\partial X_l}\frac{\partial x_j}{\partial X_m}S_{lm}+q\delta_{ij}$$

for calculation of the Cauchy stresses σ at any point since, as discussed in section 2.2.5, the material is incompressible (= conservation of volume) and any arbitrary hydrostatic stress tension, $q\mathbf{1}$, satisfies the constitutive equation.

Applying the above results to the tube inflation and stretching experiment in section 2.2.4 we will arrive at the Cauchy stresses deduced by means of equations (81) and (68c)

$$\sigma=\left(\alpha+2\beta tr\mathbf{E}+3\gamma\left(tr\mathbf{E}\right)^2\right)\begin{bmatrix}\lambda_r^2&&\\&\lambda_\theta^2&\\&&\lambda_3^2\end{bmatrix}+q\mathbf{1} \quad (82)$$

in which we have taken into account that fact that the value of the three-dimensional deformation gradient tensor of the problem is,

$$\mathbf{F}=\begin{bmatrix}\lambda_r&&\\&\lambda_\theta&\\&&\lambda_3\end{bmatrix} \quad (82bis)$$

obtained from the corresponding tensor in the two-dimensional problem –equation (59)– by adding the elongation in the radial direction λ_r.

The above stresses must coincide with those calculated from the equilibrium equation (65) in the circumferential and axial directions, which leads to:

$$\begin{aligned}p\frac{\lambda_\theta^2\lambda_3 R}{H}&=\left(\alpha+2\beta tr\mathbf{E}+3\gamma\left(tr\mathbf{E}\right)^2\right)\lambda_\theta^2+q\\ \mathrm{f}\frac{\lambda_3}{2\pi RH}&=\left(\alpha+2\beta tr\mathbf{E}+3\gamma\left(tr\mathbf{E}\right)^2\right)\lambda_3^2+q\end{aligned} \quad (83)$$

Assuming in the radial direction $\sigma_{rr}=0$, as discussed in section 2.2.4, we will have the third equation, which allows us to obtain q

$$0=\left(\alpha+2\beta tr\mathbf{E}+3\gamma\left(tr\mathbf{E}\right)^2\right)\lambda_r^2+q \quad (84)$$

Finally, substituting into Equation (83) the values of $\mathbf{E}$ obtained from equation (82b) using equation (14), and the value $\lambda_r=1/(\lambda_\theta\lambda_3)$ given by the incompressibility condition (58) we arrive at

$$p=\frac{H}{R}\left(\frac{1}{\lambda_3}-\frac{1}{\lambda_\theta^4\lambda_3^3}\right)\left(\alpha+\beta\left(\lambda_\theta^2+\lambda_3^2+\frac{1}{\lambda_\theta^2\lambda_3^2}-3\right)+\frac{3}{4}\gamma\left(\lambda_\theta^2+\lambda_3^2+\frac{1}{\lambda_\theta^2\lambda_3^2}-3\right)^2\right) \quad (85)$$

This equation is represented in figure 33 which was developed for a tube of diameter D=3mm and thickness H=0.5mm without loading. These dimensions correspond, approximately, to those of the carotid artery. The ordinate in figure 33 is pressure in mmHg (1mmHg=133Pa, the usual unit of measurement in cardiovascular mechanics) and the abscissa has been drawn in terms of the ratio of the instantaneous and initial diameters $d/D=\lambda_\theta$.

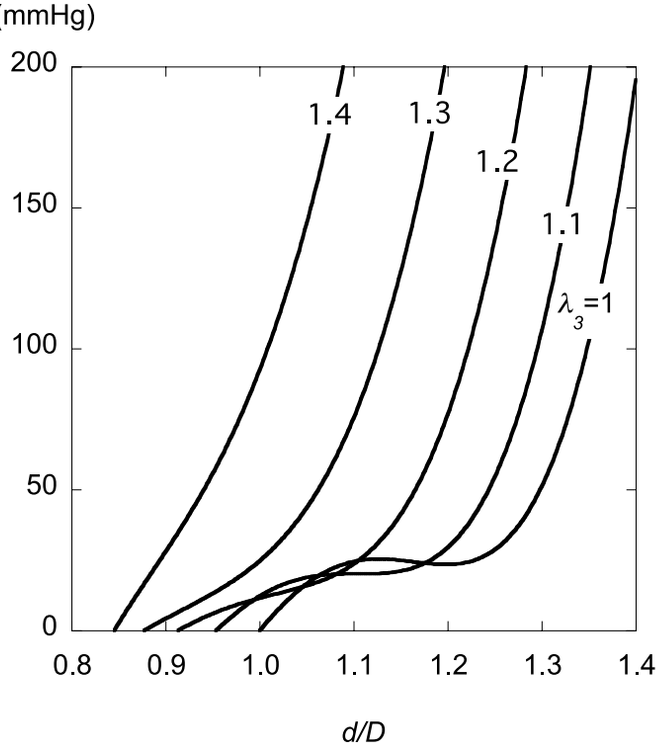

Fig. 33. *Pressure-diameter test for a tube subjected to different axial elongations. Initial diameter 3mm, initial thickness 0.5mm. Yeoh's incompressible material (α = 40 kPa, β = -142 kPa and γ = 1200 kPa).*

The parameters of the model are α = 40 kPa, β = -142 kPa and γ = 1200 kPa, reasonable values for an elastomer, and which simulate the behaviour of the artery wall. In figure 34 the uniaxial tension curve of the material is represented. This was obtained following the same process as with the tube, making use of the results of section 2.2.3.

As we can see in figure 33, for the indicated geometry and material, the pressure-diameter curve has a relative minimum when the test is performed in the absence of elongation (λ_3=1), so that on reaching a pressure of ~26mmHg an instability will appear giving rise to two sections with different diameters. When the tube is subjected to an axial elongation, the relative minimum tends to disappear, which happens in the figure, for elongations of 1.2 and greater. In this case the strain in the tube during the whole inflation process is uniform.

Blood vessels and other biological ducts avoid the occurrence of instabilities such as those mentioned by having constitutive equations which don't give rise to pressure-diameter curves with a relative minimum. Furthermore, blood vessels are natural stretched, with elongations $\lambda_3$of about 1.2, which increases their stability.

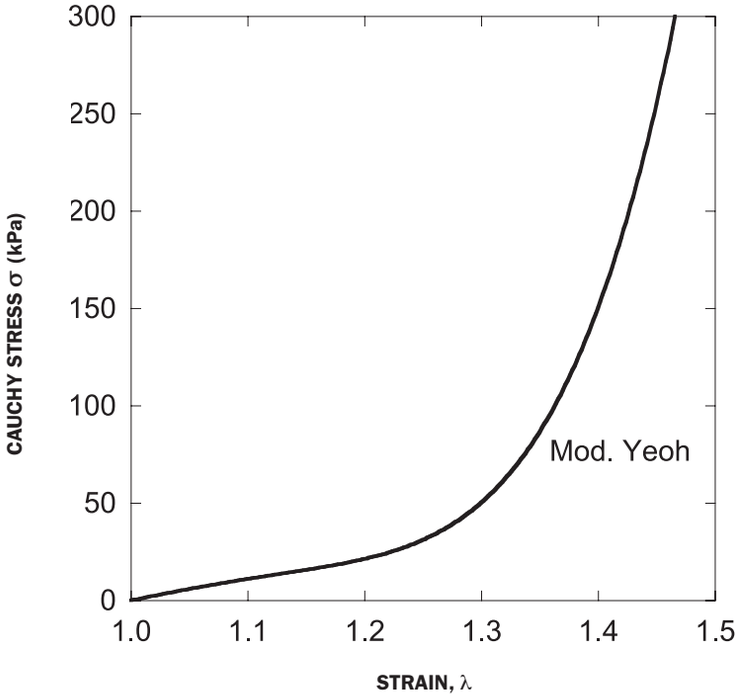

Fig. 34. *Uniaxial stress-strain curve for Yeoh's incompressible material. (α = 40 kPa, β = -142 kPa and γ = 1200 kPa).*

2.3.3. Rupture by tearing test

Figure 35a illustrates, in a schematic form, how a thin membrane can be torn. This type of test–called the Elmendorf tear test, in the paper industry– is a rupture test. During the test the force F is recorded as a function of the displacement of the point of application of the force and, from this plot, it is possible to determine the specific fracture strength R, that is, the energy expended per unit area of the tear.

The simplest model of the Elmendorf test is based up on the assumption that the material behaviour is *linear elastic* (characterised by an elastic modulus E) up to rupture, and that the elastic energy due to flexure is negligible compared to that of traction. It is also postulated that the work done by the external forces is converted exclusively into elastic deformation of the material and in tearing (consuming a constant energy per unit tear surface R).

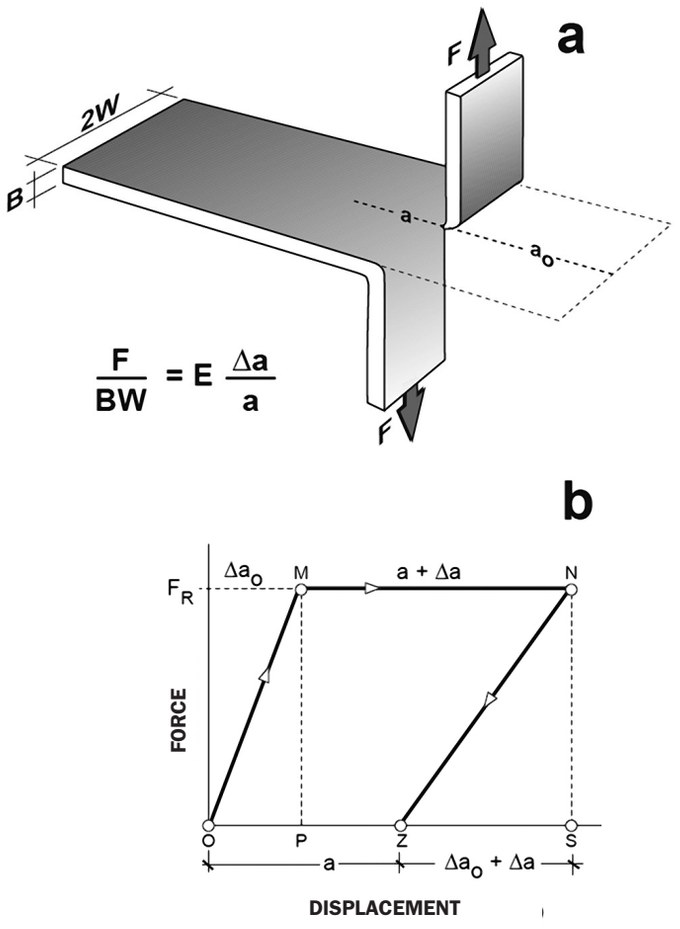

Fig. 35. *Schematic of the Elmendorf tear test on a lamina, along with the corresponding force-displacement diagram. The displacement corresponds to one of the forces, considering that the plane of the untorn the membrane remains immobile.*

Bearing in mind this hypothesis, the diagram in figure 35, represents an elementary process of loading, rupture and unloading: along the section *OM* the band, of length a_0 and the cross section *BW*, deforms elastically until the force reaches the value F_R, ewhen rupture is initiated by tearing the membrane. (In these types of test, tearing starts at a force F_R, but almost always continues to progress under the action of the same force). If the force is held constant failure progresses in a stable manner and the crack grows to a length a. On reaching point *N*, at which the elastic displacement is $\Delta a_0 + \Delta a$, the membrane is unloaded and the path *NZ* is followed The membrane is unstressed and has a residual displacement *OZ* = a.

The work done in the process *OMNZ* will be the energy expended in tearing, that is to say:

$$2F_R\left(a+\frac{\Delta a}{2}\right)=R\cdot Ba \tag{86}$$

in which the left hand side represents the work done by the two forces (the double of the area of the trapezium OMNZ) and the term on the right is the tear resistance; the specific strength, R, per unit area of tear Ba.

The value of Δa can be calculated from the hypothesis made at the beginning; that the deformation is linear and elastic, assuming that each one of the torn pieces is subjected to a state of uniaxial tension under the force F, from which:

$$\Delta a=\frac{F}{EBW}a \tag{87}$$

Introducing this result into equation (86) yields the specific tearing strength R, given by:

$$R=\frac{2F_R}{B}+\frac{F_R^2}{B^2WE} \tag{88}$$

Often, when the elastic modulus is high, the second term in this expression is negligible compared to the first, producing a very simple expression for estimating the tear strength of a membrane from the force obtained in an Elmendorf test:

$$R=\frac{2F_R}{B} \tag{89}$$

This procedure remains valid for *nonlinear elastic* materials –elastomers and biological materials in particular– provided that the work done by the external forces is distributed only between the tearing of the material and elastic deformation. Measuring the area, *A*, enclosed by the *force-displacement* diagram results in:

$$R = \frac{2A}{Ba} \tag{90}$$

Note that the number 2 appears because there are two forces doing work.

For Elmendorf tear tests on *elastomers*, which exhibit a nonlinear *force-displacement* curve F-, Rivlin and Thomas (1953) Rivlin and Thomas (1953) derived an expression similar to equation (88), (see also Atkins and Mai (1985) section. 2.10):

$$R = \frac{2F_R\lambda_R}{B} - 2W_R \tag{91}$$

where $\lambda = l/l_0 = 1 + e$, and e is the engineering strain remote from the tear and W the elastic energy density referred to the volume in the undeformed configuration, also remote from the torn region.

Equation (91) can be written in a more compact form as

$$R = 2W\int_0^{s_R} \lambda\, ds = \frac{2}{B}\int_0^{F_R} \lambda\, dF \tag{91bis}$$

since $s = F/(BW)$.

These results are proved in the following exercises.

Values of the specific fracture resistance R obtained from tear tests on the epithelia of several animals are presented in Table 1.

TABLA 1. TENACITY OF ANIMAL EPITHELIA

ANIMAL	LOCATION OF EPITHELIA	R (KJ/M^2)	REFERENCE
Rat	back (longitudinal)	25	Purslow (1983)
	back (transversal)	20	Purslow (1983)
	belly (longitudinal)	17	Purslow (1983)
	belly (transversal)	11	Purslow (1983)
Rabbit		20	Atkins, Mai (1985)
Rhinoceros	back (deep)	43	Shadwick et al (1992)
	back (shallow)	78	Shadwick et al (1992)

For the tearing of a small crack subjected to remote traction, either in the centre of the membrane or on one of the sides, as shown in figure 36, the following expression, valid for *elastic* materials (linear and nonlinear), can be used for the tear resistance R:

$$R = 2ka\mathcal{W}_R \tag{92}$$

where a is the crack length, $\mathcal{W}$ the elastic energy density (as discussed) remote from the crack and k a parameter which depends upon λ and which can be approximated by $\pi/\lambda^{1/2}$. (Atkins and Mai, 1985).

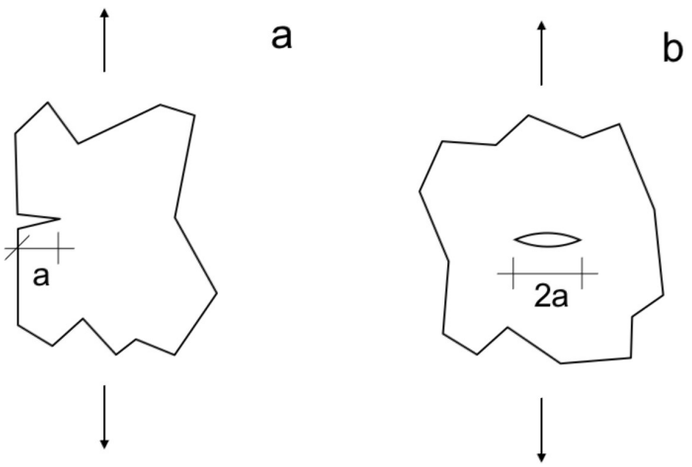

Fig. 36. *Tearing of a large membrane subjected to remote traction.*

Equation (92) can be derived from a nondimensional analysis of the fracture process (see EXERCISE 13). The value of the parameter $k(\lambda)$ can be approximated using the empirical relationship $k = \pi/\lambda$, due to Lakes (see Linley 1972). For a linear elastic material, where $\mathcal{W}_R = \sigma^2/2E$, and for small deformations when $\lambda \approx 1$, the value of the paramete k becomes equal to π.

An interesting aspect of the tear resistance of epithelia is the shape of the stress-strain curve; materials with a J-form curve are less sensitive to cracks than those with a linear shape (that is to say, whose stress-strain curve is a continuation of the tangent at the origin).

The *critical value* of the crack length can be deduced from equation (92), as a function of the strain, as shown in figure 37, in which the behaviour of the epithelium of a cat in a test like that shown in figure 36 is presented. It is assumed that the stress-strain curve is that shown in figure 24 and the tear strength is 25 kJ/m^2, a value similar to that of the rat (see table 1).

Note that if the behaviour of the epithelium were linear elastic (with an elastic modulus equal to the tangent at the origin) the corresponding curve would be that indicated by the dashed line in figure 37. This would imply that the epithelium would be much more sensitive to defects; a tiny fissure under small strains would be enough to tear the skin. The epithelium of cats can withstand large strains –up to 80%– with little risk. In general, epithelia can support large deformations without storing much elastic energy, which would have induced fracture, and for this reason they are difficult to tear. Another consideration is why it is difficult to initiate crack propagation. This is due to the deformability of epithelia at the tip of the crack which blunts very quickly and, as a result, the stress concentration is not very high.

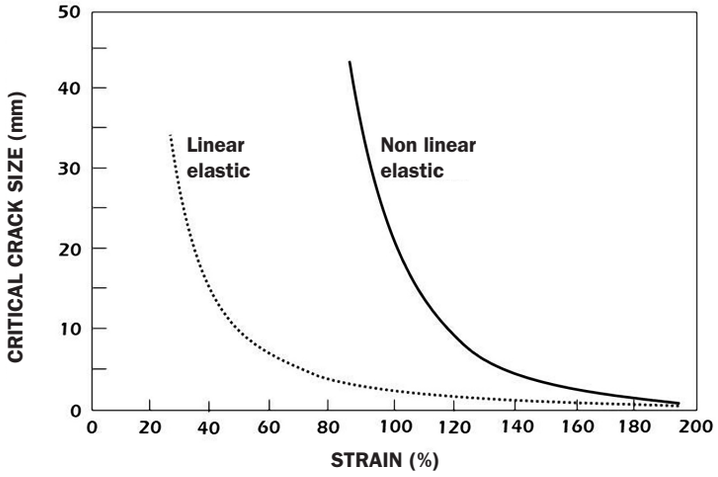

Fig. 37. *Critical crack size (in a tear test using the configuration shown in figure 36) as a function of the strain in the lamina for the epithelium of a cat. The solid stress-strain curve was obtained from a uniaxial tensile test. The dashed curve was obtained by assuming the curve is linear elastic, with the modulus of elasticity equal to the tangent at the origin of the previous curve.*

EXERCISE 11

Derive equation (91) and show that this coincides with equation (89) if the material is assumed rigid, or if the material is linear elastic. Ignore the elastic energy outside the two tear zones and assume that these are subjected to uniaxial tension under a force F.

SOLUTION:

The Elmendorf tear test is shown in the figure. Let x be the length of the tear, and B and W the dimensions of the unloaded specimen. Under the action of the force F the length of each piece becomes λx, where λ is the elastic elongation.

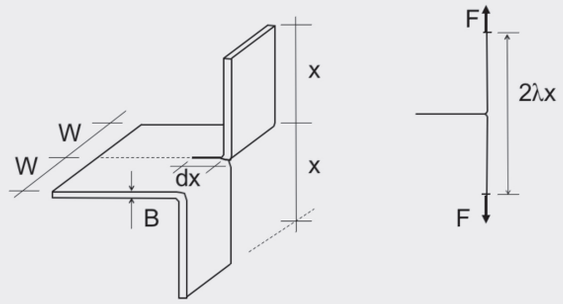

If the crack grows by dx the work done by the applied forces will be

$$2F\, d(\lambda x) = 2F\, \lambda dx + 2F\, x\, d\lambda$$

in which we see that the length of the tear zones in the specimen can grow either because they deform by $(d\lambda)$, or they tear by (dx). Since the body is elastic (linear or otherwise) work is only done in changing the elastic energy or in the fracture process, since no energy has been consumed through plastic deformation or other dissipative mechanisms.

Assuming that the two torn pieces are under a state of uniaxial tension, their elastic energy will be the product of their initial volume $2BWx$ and the energy density $W(\lambda)$, which will be the same at every point and will not depend upon the level of strain reached, which we characterise by the elongation λ. The change in energy will be

$$d(2BWx\, \mathcal{W}) = 2BW\, \mathcal{W} dx + 2BW\, (d\mathcal{W}/d\lambda)\, x\, d\lambda$$

We will then have $2F\, d(\lambda x) = 2F\, \lambda dx + 2F\, x\, d\lambda = 2BW\, \mathcal{W} dx + 2BW\, x\, (d\mathcal{W}/d\lambda)\, d\lambda + RB\, dx$
where $RB\, dx$ is the energy expended in tearing the material. This expression can be written as

$$(2F\, \lambda - 2BW\, \mathcal{W} - RB)\, dx = (2BW\, x\, (d\mathcal{W}/d\lambda) - 2F\, x)\, d\lambda$$

which must be true for any conceivable process $(dx, d\lambda)$, since x and λ sare independent variables. This condition requires that the coefficients of dx, $d\lambda$ are identically zero, and therefore that

$$R = 2F\, \lambda / B - 2W\, \mathcal{W}$$

which is equation (91), and $F = BW\, (d\mathcal{W}/d\lambda)$ or $\sigma = d\mathcal{W}/d\lambda$

which is none other than equation (67) applied to a uniaxial tension test (see EXERCISE 10).

For a *rigid material* the strains are very small (≈ 0) and the value of λ will be close to unity. Furthermore, for the same reason, the energy density W is also very small, and the term $2W\mathcal{W}_R$ in equation (91) can be neglected. With these approximations equation (89) is recovered.

In the case of a nonlinear elastic material with engineering stress and strains s and e (see the exercise in section 2.2.5)

$$\mathcal{W} = \frac{1}{2} se = \frac{F_R}{2BW} e_R$$

whereby equation (91) becomes $R = \dfrac{2F_R(1+e_R)}{B} - \dfrac{F_R}{B} e_R = \dfrac{2F_R}{B} + \dfrac{F_R}{B} e_R$

since $\lambda = 1 + e$, and then $e_R = \dfrac{s_R}{E} = \dfrac{F_R}{BWE}$

substituting in the expression for R we recover equation (88). Note that linear elastic materials are only defined in the small deformation range where $s \approx \sigma$ and $e \approx \varepsilon$.

EXERCISE 12
Show that equation (91) can never be negative and that it can be rewritten as equation (91b).

SOLUTION:
The strain energy is equal to (see the exercise in section 2.2.5)

$$\mathcal{W} = \int_0^e s\,de$$

which can be written as $R = \dfrac{2F_R\lambda_R}{B} - 2W\mathcal{W}_R = 2W\left[s_R\lambda_R - \int_0^{e_R} s\,de\right]$ since $s_R = F_R/(BW)$.

The value of the integral can be bounded, since the stress will always be $s < s_R$

$$\int_0^{e_R} s\,de < s_R\int_0^{e_R} de = s_R e_R = s_R(\lambda_R - 1)$$

and we conclude that $s_R\lambda_R - \int_0^{e_R} s\,de > s_R\lambda_R - s_R(\lambda_R - 1) = s_R > 0$

so that $R > 0$ always. On the other hand, since $de = d(\lambda - 1) = d\lambda$

$$R = 2W\left[s_R\lambda_R - \int_0^{e_R} s\,de\right] = 2W\left[s_R\lambda_R - \int_0^{\lambda_R} s\,d\lambda\right]$$

and integrating by parts we recover equation (94).

$$R = 2W\left[s_R\lambda_R - \int_0^{\lambda_R} s\,d\lambda\right] = 2W\left[s_R\lambda_R - s_R\lambda_R + \int_0^{s_R} \lambda\,ds\right] = 2W\int_0^{s_R} \lambda\,ds$$

EXERCISE 13
Derive equation (92) $R = 2k\,a\,W_R$.

SOLUTION:
If we examine either of the two cases shown in figure 36, we can see that the only relevant geometrical variable is the size of the crack a, since the dimensions of the plates are infinite in both cases.

Therefore, for the problem posed, each equation for R must be able to be written as a function of:
- R
- the geometric parameter a
- the stress-strain level, which we can characterise by the strain energy per unit volume W_R, at points remote from the crack
- the response of the material, characterised by the elongation λ in the direction of loading, evaluated at points remote from the crack

Considering the possible nondimensional groups that can be assembled from these parameters, we see that the required equation must have the form:

$$f\left(\frac{R}{a\mathcal{W}_R},\ \lambda\right) = 0$$

since $R/(a\,W_R)$ and λ are the two monomials that can be formed. The previous equation can be rewritten to express one monomial as a function of the other

$$R/a\mathcal{W}_R = g(\lambda)$$

which we can easily recognise as a form of equation (92) by making $g(\lambda) = 2k(\lambda)$

EXERCISE 14

Examine how the membrane material influences the value of the critical crack length when it is subjected to a traction as illustrated in figure 36. Use equation (92) to obtain the critical crack length. For this consider the following forms of the uniaxial stress-strain curves for the material:

- linear: $s = e\,E$
- concave: $s = eE + e^m E\,;\ m>1$
- convex: $e = s/E + s^m/E^m;\ m>1$

SOLUTION:

The three stress-strain curves are shown in figure (a) for $m=3$.

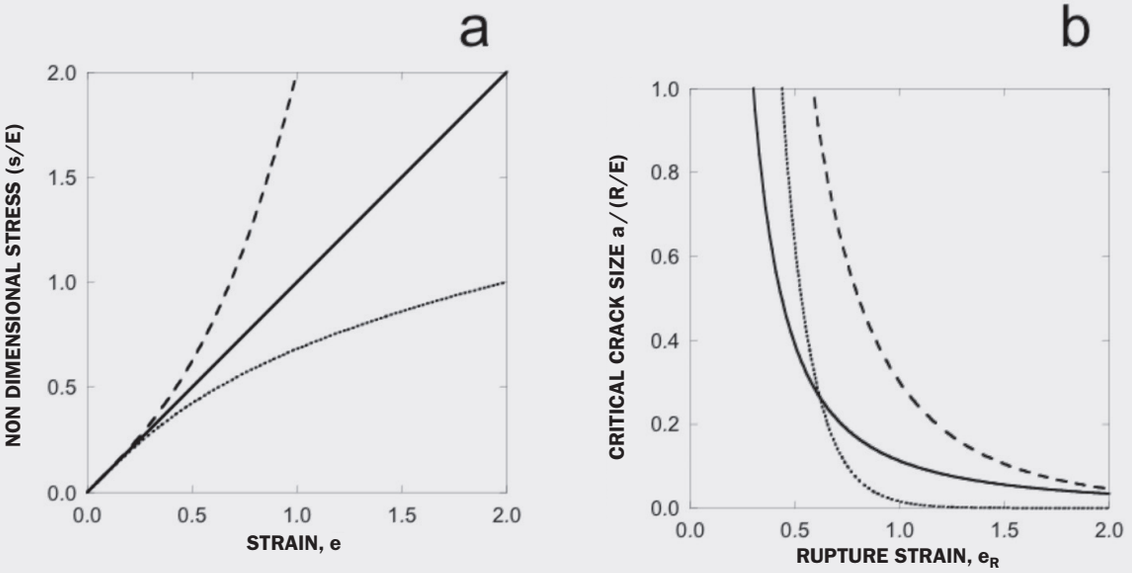

In order to calculate the critical crack size, isolate a in equation (92) and write it in the nondimensional form

$$\frac{a}{R/E} = \frac{\sqrt{\lambda}}{2\pi}\frac{1}{\mathcal{W}_R/E} = \frac{\sqrt{1+e}}{2\pi}\frac{1}{\mathcal{W}_R/E}$$ and we calculate $\mathcal{W}_R/E$ by integration.

In the case of the **concave** curve s-e this will be $$\mathcal{W}_R/E = \int_0^{e_R}(s/E)\,de = \int_0^{e_R}\left(e+e^m\right)de = \frac{e_R^2}{2} + \frac{e_R^{m+1}}{m+1}$$

For **linear** behaviour $$\mathcal{W}_R/E = \int_0^{e_R}(s/E)\,de = \int_0^{e_R} e\,de = \frac{e_R^2}{2}$$

and for the **convex** case, we integrate by part to obtain $$\mathcal{W}_R/E = \frac{1}{E}\int_0^{e_R} s\,de = \frac{1}{E}\left(s_R e_R - \int_0^{s_R} e\,ds\right) = \left(s_R/E\right)^2\frac{1}{2} + \left(s_R/E\right)^{m+1}\frac{m}{m+1}$$

in which we have used the equation of the curve $e = s/E + s^m/E^m$. From these we can relate each value of the strain e_R with the stress s_R, and with the last one obtain W_R/E.

The values of the critical crack size are shown in figure (b) as a function of the failure strain. In this it is noted that the most beneficial form (the largest critical value for a given rupture strain) is always the concave curve, as exemplified in the text with the cat epithelium.

Observe also that there is a certain value of the strain at rupture below which a convex curve is more favourable than that of linear behaviour.

EXAMPLE: RAT EPITHELIUM

During the preparation of his doctoral theses at the end of the 1970s, P. Purslow experimented with soft tissue and measured the specific tear strength of a rat epithelium using the tear test. A summary of these results is discussed below. Details can be found in Purslow (1983).

The epithelium, of approximately 1 mm thickness, is represented schematically in figure 38. Sixteen specimens were cut from the epithelium: half were tested in the longitudinal and the other half in the transverse direction, in order to investigate possible anisotropy in the tissue, as shown in figure 38a.

The force displacement curves, representative of the tear tests, are reproduced in figure 38b. The specific fracture energy, R, was calculated, initially, from equation (91), but Purslow argued that, in this case, the following simplifications could be made:

Since the applied forces were small, about 5 N, when the skin tears, the deformation remote from the crack could also be considered small and the value of λ approximated to 1. For this reason, he neglected the elastic energy density *W* far from the region of the crack. (Paradoxically it is as if the material were rigid, see the exercise 11).

After these simplifications, the specific strength is given by

$$R \backsimeq \frac{2F_R}{B}$$

The average values of R (from 8 tests) obtained by Purslow in the longitudinal and transverse directions were, respectively, 17 ± 1 kJ/m^2 and 11 ± 2 kJ/m^2, results which showed an appreciable anisotropy in the specific fracture energy.

Purslow also studied, the influence of the load rate and temperature on the values of R. Increasing the deformation rate (from 5 to 500 mm/minute) doubled the value of R. As far as temperature was concerned, experiments were performed between 7 and 23˚C but no clear trend was observed, perhaps only a small increase with temperature.

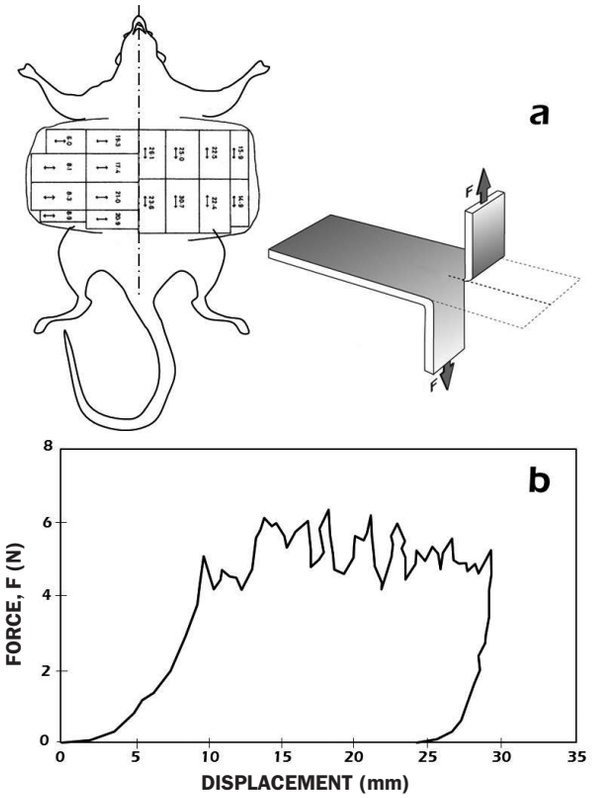

Fig. 38. *Tear test on the epithelium of a rat (Purslow, 1983). a) Schematic illustration of the extraction of the test pieces. b) Typical result of the tear test.*

2.3.4. Separation tests

Simple peeling test

The peeling of a thin membrane from a substrate is shown in figure 39a. This type of test –attributed to Dannenberg (1961) by some authors– is a rupture test which provides knowledge of the specific adhesion energy between a lamina and substrate. During such a test the force F is recorded as a function of the displacement of the point of application of the force. The specific adhesion strength can be calculated from a plot of this data following the same steps outlined in the previous section.

The simplest way to model this test is to assume that the membrane behaves as a *linear elastic* material (small deformations, and elastic modulus E) and that the elastic energy due to flexure is negligible compared to that of traction. Furthermore, it is postulated that the work done by the external force is converted only into elastic deformation of the membrane and in separating it (while consuming constant specific energy R). In this simple model any viscoelastic effects are ignored. Again, as happened in the case of tearing, separation is usually produced under the action of a constant force F_R.

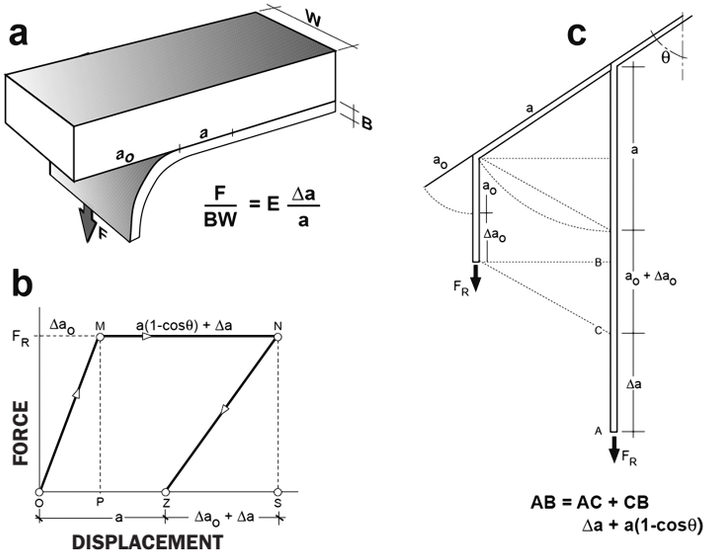

Fig. 39. *Schematic diagram of a simple separation test on a lamina, together with the corresponding force-displacement plot.*

Incorporating these assumptions, the diagram in figure 39b outlines the basic loading, separation, and unloading process: In the process represented by the line *OM* the membrane, of length a_0 and cross section *BW*, deforms elastically until the force reaches a value F_R, at which point separation starts. If the force is held constant, separation progresses in a stable manner, increasing up to a length a. On reaching point *N*, the membrane is unloaded and the path *NZ* is followed. The membrane is left stress-free but with a residual displacement *OZ*=a.

An energy balance performed for the OMNZ process, in a similar manner to that carried out in the previous section, results in the expression:

$$F_R\left[a(1-\cos\theta)+\frac{\Delta a}{2}\right]=R\cdot Wa \tag{93}$$

which the term on the left hand side represents the work done by the force F (the area under the trapezium *OMNZ*) and the term on the right the separation strength; the separated area, Wa, multiplied by the specific strength, R. The diagram in figure 39c is drawn to help explain the calculation.

The value of Δa is calculated bearing in mind the hypothesis that the membrane behaves linear elastically, so that:

$$\Delta a=\frac{F}{EBW}a \tag{94}$$

Substituting this result into equation (93), the specific separation (or adhesive) strength R is obtained:

$$R=\frac{F_R}{W}\left(1-\cos\theta+\frac{F_R}{2EBW}\right)=\frac{F_R}{W}\left(1-\cos\theta+\frac{\varepsilon}{2}\right) \tag{95}$$

Note that $F_R/2EBW$ is $\varepsilon/2$, half of the elastic strain in the membrane.

When the modulus of elasticity is high, the last term inside the bracket is usually negligible compared to the others, (analogous to the previous case of rupture by tearing). In these circumstances, a very simple expression is obtained for estimating the specific adhesive strength between the membrane and substrate. If the membrane separation is perpendicular to the substrate, the $R \approx F_R/W$.

This procedure is also valid if the membrane exhibits *nonlinear elastic* behaviour. The specific strength is obtained by dividing the area under the F-u diagram by the separated area: aW.

There are two relatively simple arrangements which create a separation zone in a membrane, one like that just discussed –subjected to a state of uniaxial tension– and the other a separation in a tympanum object, described in the following section–which is a membrane subjected to a state of biaxial stresses–.

The first arrangement is shown in figure 40a, in which the lamina is separated using a bracket. The same hypotheses are made as before; linear elasticity, small deformations, and ignoring the elastic energy due to flexure compared to that stored in traction. It is also assumed that initially an are $a_0 W$ is separated and the initial strain is zero.

The problem can be solved following the procedures described above; from the area under the F-u diagram. The result can also be written directly if it is observed this problem is analogous to the previous one, but in this case the force F is replaced by $F/2 \sin\theta$. The final result is then:

$$R = \frac{F_R}{2W\sin\theta}\left(1 - \cos\theta + \frac{\varepsilon}{2}\right) = \\ = \frac{F_R}{2W\sin\theta}\,\frac{1 + \cos\theta - 2\cos^2\theta}{2\cos\theta} \tag{96}$$

in which the strain ε has be written as:

$$\varepsilon = \frac{1-\cos\theta}{\cos\theta} \tag{97}$$

It is sometimes convenient to write the specific strength as a function of the height H nd the pressure that causes separation *p*. (In this case we can define an average pressure equivalent to that obtained from the quotient of the force *F* and the area *2aW*). That is to say:

$$R = \frac{FH}{2aW}\,\frac{1 + \cos\theta - 2\cos^2\theta}{2\sin^2\theta} \equiv f_1(\theta)\cdot Hp \tag{98}$$

For small values of $\theta, f_1(\theta)$ tends to ¾ and the separation strength can be approximated by:

$$R \simeq \frac{3}{4}\,Hp \tag{99}$$

A second configuration, referred to previously and shown in figure 40b, involves a lamina which is separated under the action of an internal pressure p. The same hypotheses are made as before; linear elasticity, small deformations and consider lamina as a membrane. Under these conditions it can be assumed that the deformation is a cylindrical surface, of radius ρ, and the separating force becomes,$F = p \cdot 2\rho\, sin\,\theta \cdot W$.

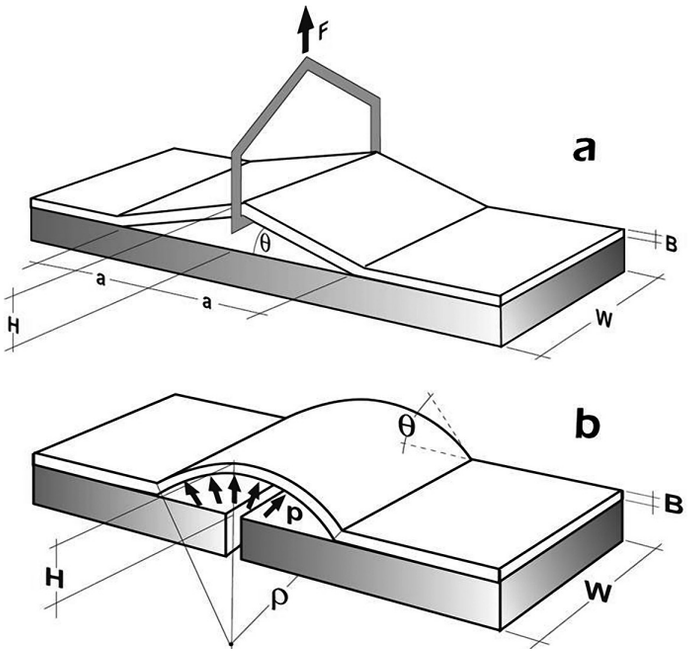

Fig. 40. *Schematic representations of two lamina separation tests.*
a) Using a bracket.
b) Using internal pressure.

Using similar reasoning that in the previous example, the specific adhesion will be given by equation (95)

$$R = \rho p\left(1 - \cos\theta + \frac{\varepsilon}{2}\right) = \rho p\left(1 - \cos\theta + \frac{\theta - \sin\theta}{2\sin\theta}\right) \tag{100}$$

where, now, the strain ε can be approximated by

$$\varepsilon = (\theta - \sin\theta)/\sin\theta$$

This result can also be written as a function of H and p, in the following form

$$R = Hp\left[1 + \frac{\theta - \sin\theta}{2\sin\theta\,(1 - \cos\theta)}\right] \equiv f_2(\theta)\cdot Hp \tag{101}$$

which, for small values of θ, reduces to

$$R \simeq \frac{7}{6}\,Hp \tag{102}$$

Once again, if the lamina exhibits *nonlinear elastic* behaviour, the specific separation strength can be found by measuring the work done and dividing it by the area of the separated surface.

Separation test on a tympanum

In order to measure the adhesion of thin laminas (or films) it is sometimes helpful to use a technique based on the formation of a blister or vesicle from a tympanum. This test, proposed by Dannenberg (1961) and modified by Wan and Mai (1995), has the advantage of not requiring jaws or grips which could cause plastic deformation and the necessary measurements –pressure and height of the blister– are not difficult to obtain.

The test is shown schematically in figure 41. When a pressure p is introduced through a hole in the substrate, the film (of thickness *B*) can separate and form a blister, (with a cross section which is assumed to be circular, of radiu a and height H). To model this test several distinct hypotheses can be made about the behaviour of the film, which range from considering it as a thin plate, with a certain flexural stiffness, to considering its behaviour to be like a membrane with no flexural rigidity. Later, both situations will be analysed in order to obtain bounds to the solution of the problem.

If it is supposed that the film behaves like a **plate**, the displacements of the tympanum due to the pressure p can be calculated by assuming that the deformations are small and the behaviour *linear elastic* (see, for example, Timoshenko and Woinowsky, 1959). The result is:

$$h(r) = \frac{p}{64D}\,(a^2 - r^2)^2 \tag{103}$$

where a, h and r are shown in la figure 41, D is the flexural rigidity of the plate, given by $D = EB^3/12\,(1-\nu^2)$, E is the modulus of elasticity and ν is the Poisson ratio. The maximum displacement, H, is produced at the centre *(*r = 0*)* and is:

$$H = \frac{pa^4}{64D} \tag{104}$$

The specific adhesive strength can be calculated from the elastic energy (see, for example Elices 1998, page 90) yielding:

$$R = \frac{p^2a^4}{128D} = 0.5Hp \tag{105}$$

This is a very simple result that depends only upon the pressure p and the blister height H.

If it the hypothesis is that the film behaves like a **membrane**, the displacements can also be calculated by assuming small deformations and *linear elastic* behaviour. The maximum displacement is produced at $r = 0$ and has a value:

$$H = c_1 \left(\frac{pa^4}{EB}\right)^{1/3} \tag{106}$$

where c_1 v is approximately 0.6 and varies weakly with the Poisson ratio ν (Williams 1997).

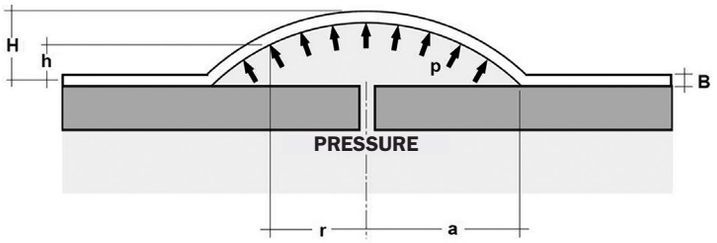

Fig. 41. *Schematic representation of the biaxial separation of a film. (Tympanum or blister test).*

The specific adhesive strength, calculated from the elastic energy (Elices 1998) becomes:

$$R = \frac{5}{4}\,\frac{c_1c_2}{(EB)^{1/3}}\,(pa)^{4/3} = \frac{5}{4}\,c_2Hp \tag{107}$$

where c_2 is approximately 0.52 (Elices, 1998).

This simple result is very similar to that obtained with the hypothesis that the film behaves like a thin plate, that is to say $R = 0.5Hp$. Assuming that it behaves like a membrane $R \approx 0.65\,Hp$ (again, this last result changes very little with the value of ν).

These two hypotheses represent two extreme cases and they suggest that a lamina tested in this way will exhibit an intermediate behaviour. In reality, the two solutions are similar and the error in adopting one or the other is not great. The specific adhesive strength can then be written as:

$$R = \lambda\,Hp \tag{108}$$

where p is the pressure that produces the separation, H is the height of the blister formed and λ is a nondimensional coefficient which lies between 0.5 and 0.65, depending upon the hypothesis made.

It might be imagined that if the film is very flexible the small deformation approximation, on which the previous formulae were based, is not valid. This was examined by J.G. Williams (1997) who concluded that, even in such cases, the approximation was reasonably good. To be more precise, he obtained

$$R = Hp\left[\frac{5}{8} + \frac{(H/a)^2}{8\,[(H/a)^4 + 3\,(H/a)^2 + 1]}\right] \tag{109}$$

This result indicates that R is almost insensitive to (H/a); for $H/a = 0$,

$$R = \frac{5}{8}Hp = 0{,}625\,Hp \tag{110}$$

and the that maximum value of $R\,/\,Hp$ is 0.644 qhen $H/a = 3^{0.25} \approx 1.31$.

EXERCISE 15

The figure shows data obtained by Kita and co-workers (1990) who used an ocular micro-injection device to determine the bonding of the retina to the back of the eye. The investigators measured simultaneously the radius of the separation zone *a* and the subretinal pressure Δp which induces detachment of the retina.

From the data provided, evaluate which separation model of the tympanum –plate or membrane– is more appropriate for analysing the experiment, and estimate the value of the specific adhesive strength of the retina. Assume that the displacements and deformations are very small and that the retina behaves linear elastically with E = 0.43 MPa, ν = 0.42 and thickness B = 0.3 mm. For the membrane analysis, model the separated area as a spherical shell.

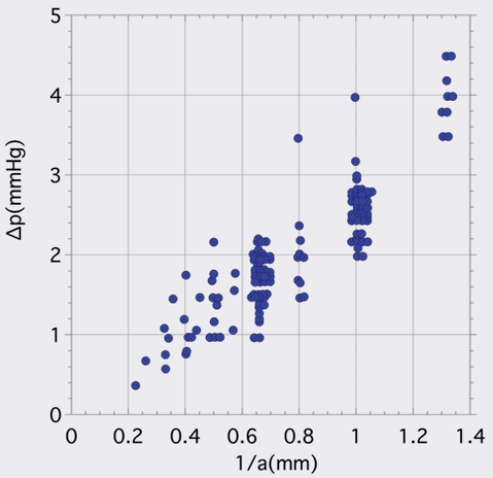

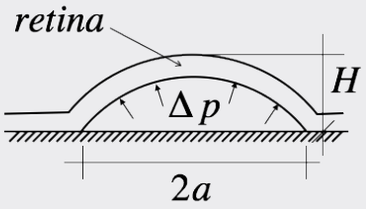

SOLUTION:

For the **plate** model, equation (105) provides the relationship between the pressure and the radius of the separated zone. This Δp - a relationship can then be written as

$$\Delta p = \sqrt{\frac{32EB^3R}{3(1-\nu^2)}}\left(\frac{1}{a}\right)^2$$

which indicates that the experimental Δp - $1/a$ curve should be parabolic.

The corresponding equation for the **membrane** model is deduced from equation (108), but it is also necessary to know the relationship between the height of the separation zone *H,* its radius *a* and the pressure Δp. For that we assume that the shape of the tympanum is spherical, as shown in figure a). Then

$$H = \frac{1-\cos\theta}{\sin\theta}a \approx \frac{\theta a}{2}$$

The value of θ is obtained by assuming that the deformation occurs under a stress σ, which we obtain from equilibrium of forces on the membrane in the vertical direction ($2\pi a B\sigma \sin\theta = \Delta p \pi a^2$):

$$\sigma = \frac{\Delta p a}{2B\sin\theta} \approx \frac{\Delta p a}{2B\theta}$$

By symmetry of the problem, the stress state in the membrane is equiaxial, and the stress which acts in two mutually perpendicular directions is equal to σ, giving rise to a strain (applying Hooke's Law)

$$\varepsilon = \frac{\sigma}{E} - \frac{\nu}{E}(\sigma + 0) = \frac{1-\nu}{E}\sigma = \frac{r\theta - a}{a} \approx \frac{\theta^2}{6}$$

since $a = r\sin\theta \approx r(\theta - \theta^3/3! + \ldots)$. From the previous two expressions we can eliminate σ to obtain $\theta = \left(\frac{3(1-\nu)\Delta p a}{EB}\right)^{1/3}$

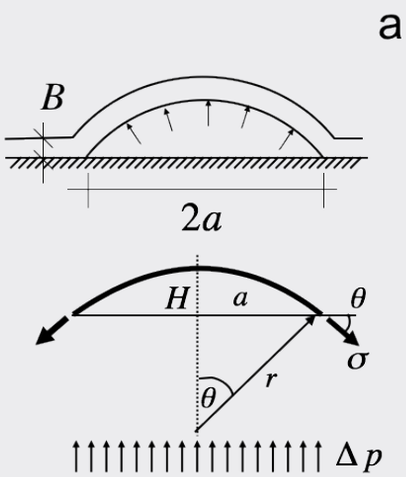

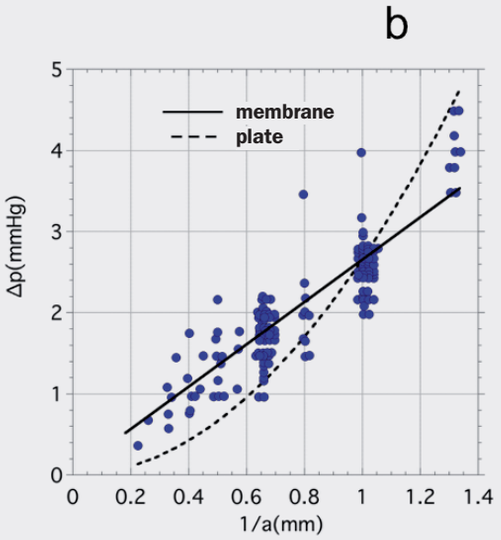

and then $H = \frac{\theta a}{2} = \left(\frac{3(1-\nu)\Delta p a^4}{8EB}\right)^{1/3}$

with which, and using equation (108), we finally obtain

$$R = \lambda p H = \lambda\left(\frac{3(1-\nu)(\Delta p)^4 a^4}{8EB}\right)^{1/3}$$

The Δp - a relationship in this case becomes:

$$\Delta p = \left(\frac{8EBR^3}{3\lambda^3(1-\nu)}\right)^{1/4}\frac{1}{a}$$

which represents a linear relationship between Δp and $1/a$.

The Δp - $1/a$ fits for both models are shown in figure b). Despite the large scatter, it seems that the membrane model provides a better fit to the experimental data (the membrane data correlation coefficient is 0.89 as opposed to 0.67 for the plate model). The values of R can be obtained from B, E and υ data, and the constants from the curve fit:

- Plate model: Δp = 2.65 mmHg mm^2 $(1/a)^2$
- Membrane model: Δp = 2.63 mmHg mm $(1/a)$

from which we deduce

- Plate model: R=8.29 10^{-4} J/m^2
- Membrane model: R=185 10^{-4} J/m^2

3 CHAPTER Examples

3.1. INTRODUCTION

The objective of this chapter is to provide some applications of the concepts developed above –the mechanical properties of biological membranes–. When dealing with practically two-dimensional materials, the mathematical treatment is rather more complex than that of the fibres considered in the first volume of this book.

In the following examples, attempts are made to characterise the mechanical behaviour of membranes using certain parameters which will need to be measured, for this reason relevant experiments are also detailed. From this information attempts will be made to predict the mechanical response of the membrane under particular external loads using constitutive models. In practice, these models often have a limited scope due to the complexity of biological structures.

The first example concerns the *pericardium*, the membrane which surrounds and protects the heart. The mechanical behaviour of the pericardium has been studied extensively because of the interest in its use as a biomaterial in bio-prosthetics for vascular grafts, repair patches on the abdominal wall and in heart valves.

The second example is the *wall of the arterial aorta*. The objective is to describe and model its biomechanical behaviour in order to understand its physiological characteristcs, the ageing process and the development of its pathologies. This information is useful in applications of particular medical interest, such as the rupture of aneurisms or the effects of arterial hypertension.

The third example will consider *elasmoid scales* of fish, a type of rigid membrane, unlike the previous ones. Interest in the study of the mechanical properties of these scales lies in understanding their tenacity, flexibility and resistance to penetration. These properties have been, and are, a source of inspiration for the design of armours.

In all of these examples, when attempting to model the mechanical behaviour, we encounter materials which possess complex structures because they are very hierarchical. In these materials there is no clear separation between *material* and *structure* because the different components are joined together without interruption across several scales of observation, from the molecular to macroscopic levels.

In order to develop models using continuum mechanics it is assumed that the material is composed of homogenous parts, a distinction which is arbitrary and made exclusively as a function of the available data and the type of information needed for the model. This implies that the stresses and strains obtained from the models will have no physical sense below a certain level.

3.2. PERICARDIUM

3.2.1. Description

The pericardium is a membrane that covers and protects the heart, separating it from the neighbouring structures while allowing its freedom of movement. It covers and extends to the roots of the great vessels.

It is an anisotropic membrane composed essentially of collagen and elastin fibres in layers of different orientation, embedded in a matrix of glycol proteins and glycosaminoglycans. Thanks to the collagen content, the pericardium exhibits good mechanical strength, and prevents the excessive dilation of the chambers of the heart, limiting hypertrophy under conditions of maximum activity.

The pericardial sac has a conical form (figure 42a). In this figure, two preferential anatomical directions are identified; the apex-caudal or *radial*, from the upper part of the heart to the apex, and the *circumferential*, in a direction orthogonal to the previous one. The pericardium contains collagen fibres grouped in bundles of micrometric thickness which, together with its small thickness, can be observed through the membrane by means of a beam of light. Low angle light scattering experiments (Sacks *et al.* 1997) revealed that the collagen fibres are arranged preferentially in the radial and circumferential directions (figure 42b).

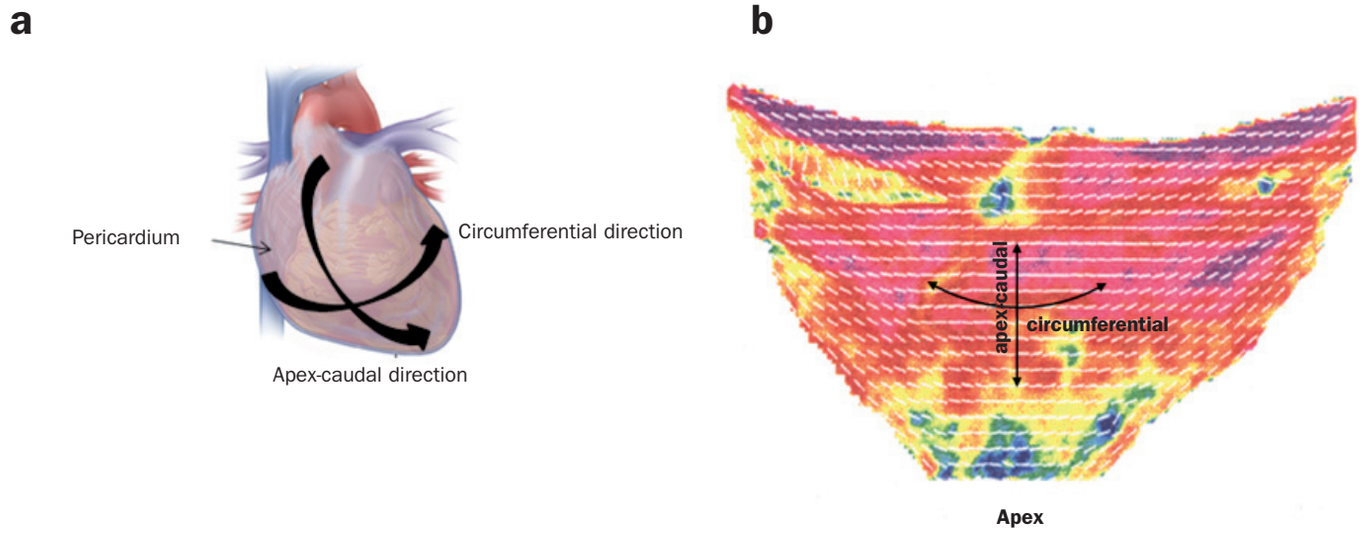

Fig. 42. *a) Anatomical arrangement of the pericardium and preferential directions. b) Collagen fibre orientation obtained by light diffraction (Sacks et al. 1997).*

The pericardium has two layers (figure 43): the fibrous pericardium and the serous pericardium. The fibrous pericardium is the outer layer and is attached to the adjacent structures (diaphragm and sternum) by ligaments. It is a strong stiff film with a high collagen content (figure 44). Its inner surface is intimately connected to the parietal layer of the serous pericardium, which is thinner and formed of mesothelial cells. The innermost layer of the serous pericardium, also called the epicardium, is attached to the heart, forming its external coating. Between the two layers of the serous pericardium is the pericardial cavity which contains a small quantity of fluid, similar to blood plasma, and which minimises the friction produced by the beating heart.

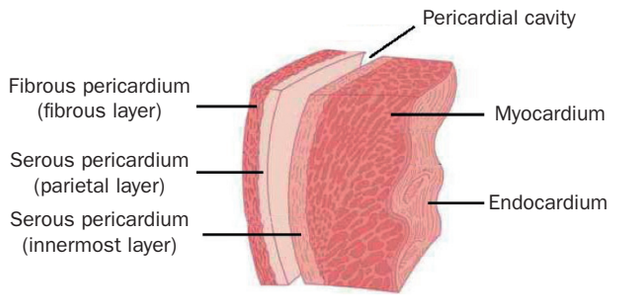

Fig. 43. *Layers of the pericardium.*

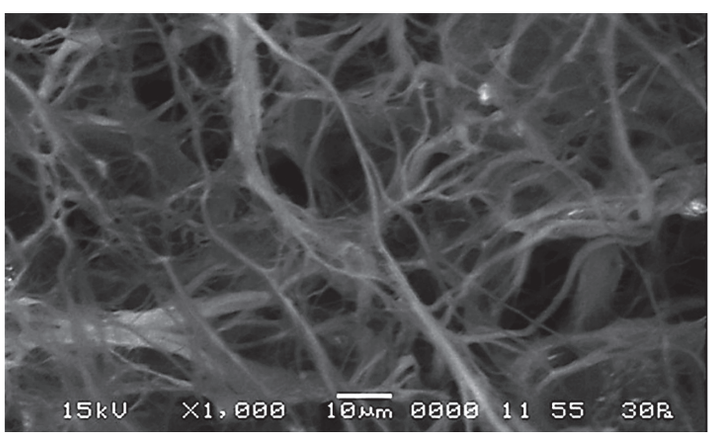

Fig. 44. *Scanning electron microscope image of the fibrous layer (Mendoza-Novelo et al., 2013).*

Due to the discontinuity produced by the pericardial cavity, the combined fibrous and serous/parietal layers is often improperly called pericardium because they form a quite distinct set that separates easily from the heart.

Animal, typically bovine, pericardium is a material often used in medicine for the repair of all sorts of structures; in cardiovascular, abdominal, ophthalmic or genitourinary surgery. It is also used as a bioprosthetic heart valve sheath (figure 45). In these cases, the fibrous layer is used –and the parietal zone of the serous layer attached to it– since, as well as being easy to acquire, it is the strongest layer.

Fig. 45. *Bio-prosthesis for replacing a heart valve. The veils are made of three crosslinked membranes of pericardium.*

In order to increase the stability of the tissue, avoid its decomposition in the interior of the body and to reduce its antigenicity, the pericardium (that is the fibrous layer) is treated by physical (heat or UV radiation) or chemical means to form irreversible crosslinks of the functional groups of the collagen molecules.

Among the chemical treatments, the most common uses glutaraldehyde at a concentration of 0.625%. This treatment provides greater strength, although it induces calcium deposits on the membrane.

3.2.2 Mechanical behaviour

The mechanical behaviour of the pericardium has been studied extensively because of its interest as a structural biomaterial, conferring mechanical strength to biological structures. The material analysed is usually pericardium (its fibrous and serous-parietal layers) with crosslinks, generally treated with glutaraldehyde. In the following, and unless indicated to the contrary, these will be the conditions of the pericardial membrane to which we refer.

Uniaxial tensile tests

Figure 46 shows representative curves of the tensile behaviour of bovine pericardium under physiological conditions along the two preferential anatomical directions. In this figure, the true stress (or Cauchy stress, as we saw above) σ, obtained by dividing the load by the instantaneous cross sectional area, is plotted against the ratio of the instantaneous and initial lengths (the elongation λ). We can observe a clear dependency on the direction (anisotropy). Furthermore, the shape of the curves reflects the process of regrouping and progressive alignment of the collagen fibres with increasing load, producing the typical J-shape.

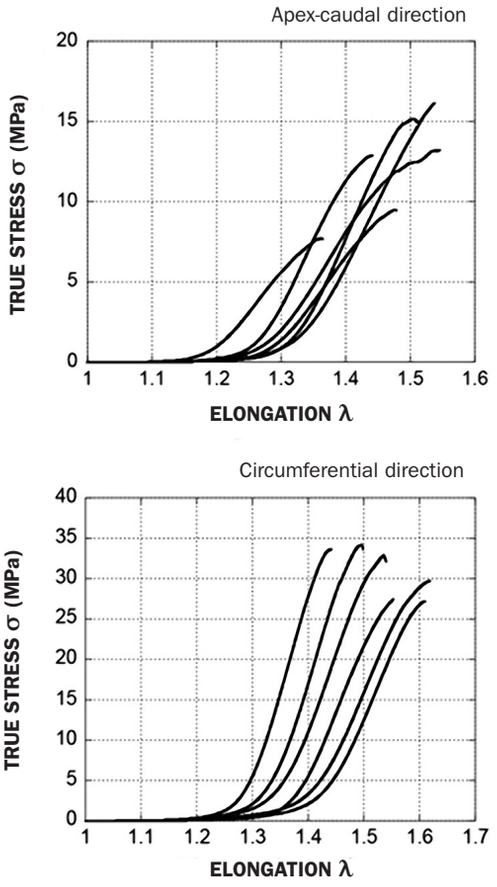

Fig. 46. *Uniaxial tensile tests on bovine pericardium specimens (18 x 2 mm) treated with glutaraldehyde. Average thickness 0.52 mm. Loading rate 0.2%/s. Specimens immersed in physiological serum at 37ºC. (Tobaruela, 2016).*

The influence of the reorientation of the fibres is more apparent if the pericardium specimens are subjected to some tensile fatigue cycles. Figure 47 shows such tests, in which 100 loading and unloading cycles were applied, up to a maximum value of 3MPa which corresponds to approximately 10% of the strength of the material in the circumferential direction and 25% of its strength in the apex-caudal direction. As we can see, almost after the first cycle of loading and unloading the response stabilises, which suggests that the structure of the membrane has essentially reached its final configuration.

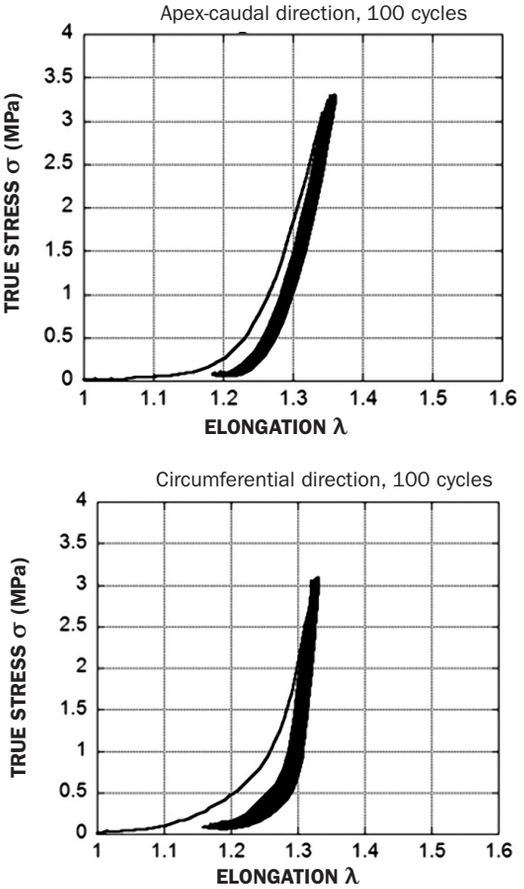

Fig. 47. *Uniaxial tensile fatigue tests on bovine pericardium specimens (18 x 2 mm) treated with glutaraldehyde. Average thickness 0.52 mm. Strain rate 2%/s. Specimens immersed in physiological serum at 37ºC. A = apex-caudal direction, Ci = circumferential direction (Tobaruela, 2016).*

In figures 48 and 49 the tensile strength is shown as a function of the number of cycles previously applied to the specimen, which, as we have seen, indicates a rearrangement of the internal structure of the material. While the tensile strength remains substantially constant (at about 10MPa for the apex-caudal direction and 30MPa in the circumferential), the value of the elongation drops significantly with increasing cyclic treatment (from ~1.5 to ~1.3). In both cases the anisotropy of the material remains unchanged.

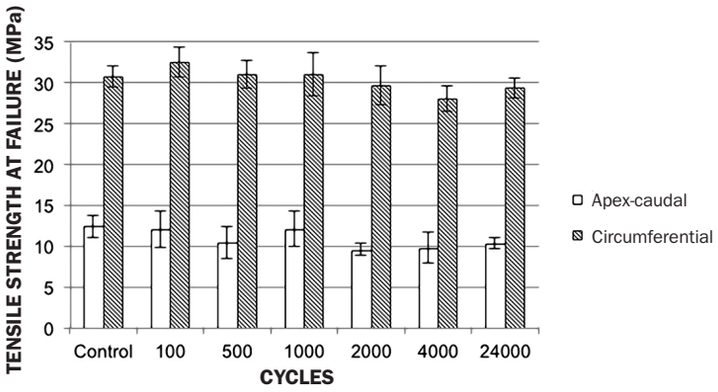

Fig. 48. *Tensile strength values (mean value ± standard error, N=33) of bovine pericardium after various uniaxial tensile fatigue cycles (maximum stress = 3MPa). Dimensions of the specimens: 18 x 2 mm. Average thickness 0.52 mm. Specimens treated with glutaraldehyde. Fatigue strain rate 2%/s. Strain rate in the tensile strength tests 0.2%/s. Specimens immersed in physiological serum at 37ºC (Tobaruela, 2016).*

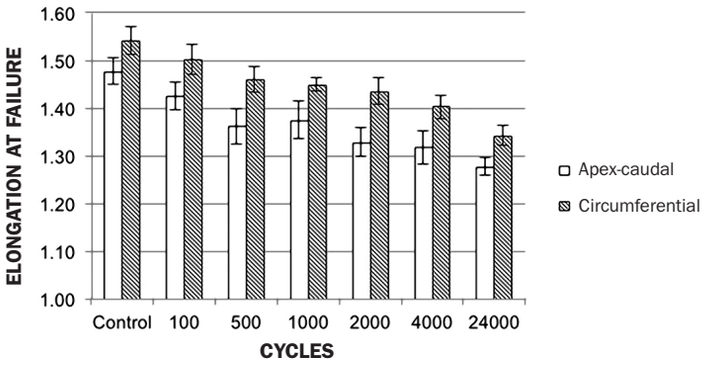

Fig. 49. *Values of the elongation at failure (mean value ± standard error, N=33) of bovine pericardium after various uniaxial tensile fatigue cycles (maximum stress = 3MPa). Dimensions of the specimens: 18 x 2 mm. Average thickness 0.52 mm. Specimens treated with glutaraldehyde. Fatigue strain rate 2%/s. Strain rate in the tensile strength tests 0.2%/s. Specimens immersed in physiological serum at 37ºC (Tobaruela, 2016).*

It is interesting to determine the slope of the linear part (tangent modulus) of the $\sigma-\lambda$ curves before rupture of the uniaxial tensile specimens, since these can provide an idea of the stiffness of the membrane when all of the fibres have attained maximum alignment. In figure 50, these values are shown both for the specimens without prior fatigue (control) and those which have been subjected to a pre-determined number of accommodation cycles. It can be seen that the stiffness remains essentially constant, which confirms that the final state, with the fibres aligned, is reached very quickly and in every case within the first 100 fatigue cycles. If it is assumed that there is a direct relationship between the fibre content and the specimen stiffness, we can estimate that the relative amount of collagen in the two anatomical directions should be about 8/3, which is the ratio of the corresponding stiffnesses (approximately 200MPa in the circumferential and 75MPa in the apex-caudal direction).

In 2001, Carrera *et al.* tested specimens which were 20 mm wide and 120 mm long, treated with 0.625% glutaraldehyde and loaded in the apex-caudal direction. Specimens were subjected to uniaxial tension in load steps of 2 MPa, 3 MPa, and 8 MPa. The values of the rupture stresses lay between 26.6 MPa and 32.6 MPa.

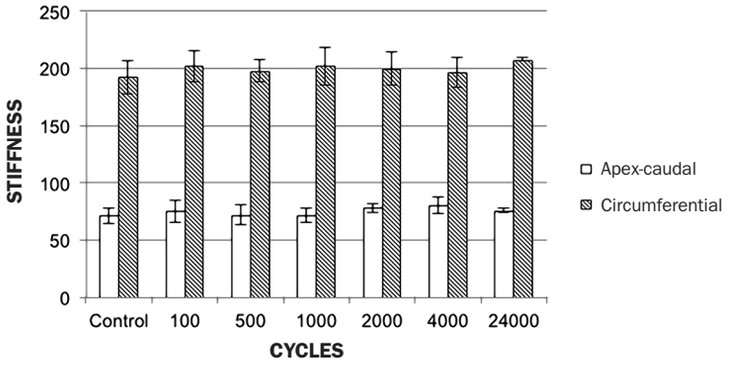

Fig. 50. *Stiffness values (slopes of the $\sigma-\lambda$ curves, or tangent modulus) (mean value ± standard error, N=33) of bovine pericardium after various numbers of fatigue cycles (maximum stress = 3MPa). Specimen dimensions: 18 x 2 mm. Average thickness 0.52mm. Specimens treated with glutaraldehyde. Strain rate in fatigue 2%/s. Strain rate in the rupture tests 0.2%/s. Specimens immersed in physiological serum at 37ºC (Tobaruela, 2016).*

Biaxial tensile tests

Biaxial tensile tests have been performed in order to obtain a constitutive equation for the pericardium. Figure 51 shows the arrangement used by Sacks and co-workers (Sacks and Chuong 1998) in which the pericardium membrane is secured using sutures on its edges, taking advantage of the good tear resistance demonstrated by this material.

The approximation, which is frequently applied to the modelling of other soft materials such as skin, tendons or blood vessels, is that the behaviour of the pericardium, once stabilised after a few fatigue loading and unloading cycles (pre-conditioning), can be represented by a hyper-elastic constitutive equation, in which the relationship between the stress and strain energy is given by equation (67):

$$S_{ij} = \frac{\partial \mathcal{W}}{\partial E_{ij}}$$

where $\mathcal{W}=\rho_0 \mathcal{W}_m$ is the strain energy per unit volume, $\mathcal{W}_m$ eis the energy per unit mass and ρ_0 the density of the body in the reference configuration.

The fact that the behaviour may be different between loading and unloading, is resolved by adopting a different strain energy function for each situation. This is the *pseudo-elastic* model proposed by Fung.

Several strain energy functions specific to the pericardium have been proposed, such as that used by Choi and Vito (1990), and also employed by Sacks and Chuong (1998):

$$\mathcal{W} = b_0[\exp(\frac{1}{2}b_1 E_{11}^2) + \exp(\frac{1}{2}b_2 E_{22}^2) + \exp(b_3 E_{11} E_{22}) - 3] \quad (111)$$

or the simplified expression of Billiar and Sacks (2000)

$$\mathcal{W} = \frac{c}{2}[\exp(a_1 E_{11}^2 + a_2 E_{22}^2) - 1] \quad (112)$$

in which a_1, a_2, b_0, b_1 , b_2 , b_3 and c are constants. In neither of these is account taken of the effect of shear strains (E_{12}), given their small experimental relevance.

Other more elaborate expressions separate the contributions to the strain energy due to collagen fibres, $\mathcal{W}^c$, elastin fibres $\mathcal{W}^e$ and the matrix $\mathcal{W}^m$

$$\mathcal{W} = \mathcal{W}^c + \mathcal{W}^e + \mathcal{W}^m$$

In this case, the values of $\mathcal{W}^e$ and $\mathcal{W}^c$ depend only on the elongation produced in the preferential direction of the fibres. More details can be obtained by consulting Humphrey (2002).

As an illustration of the process of obtaining the constitutive equation from the results of biaxial tensile tests, it is interesting to review the work of Sacks and Chuong (1998) on bovine pericardium membranes crosslinked with glutaraldehyde. The experimental arrangement is shown in figure 51.

Square, 25x25mm, specimens were cut from the pericardium membrane so that the preferential orientation of the collagen fibres is one of the axes of the test (1-axis). In this way, and by symmetry of the specimen, biaxial tension does not produce angular deformation and the situation is equivalent to that studied in section 2.2.3. The specimens were pre-conditioned with biaxial loading and unloading with equal strains along both axes. As is often the case when dealing with soft biological materials it was assumed that the volume remains constant.

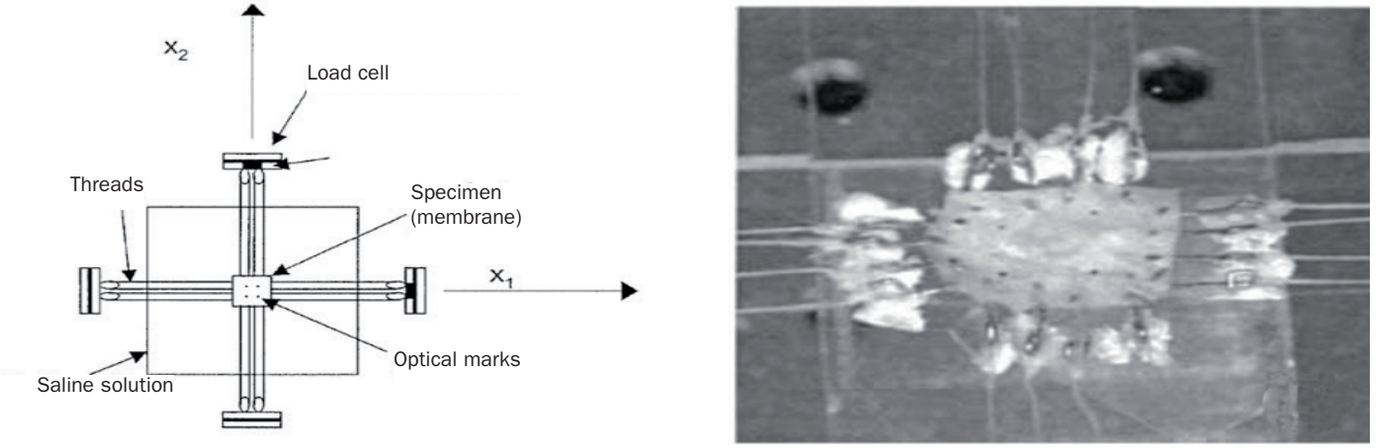

Fig. 51. *Biaxial tensile tests. The load is applied using suture threads and the strain measured from the displacement of marks drawn on the surface of the membrane (Sacks and Chuong 1998).*

The value of the strain was measured from the positions of four reference points on the specimen (figure 51), using equation (41), and the second Piola-Kirchoff stress tensor was obtained from the forces exerted on the sides of the membrane, by means of equations (47).

Biaxial tests were performed with the ratios E_{11}/E_{22}= 1/3, 1/2, 1, 2 and 3, up to a maximum strain value of 0.16, equal to that used in the pre-conditioning cycles. This is equivalent, according to equation (41), to applying an elongation of λ_2 varying with λ_1 as shown in figure 52. The maximum level of strain was chosen so that the stresses did not approach 0.16MPa, which is the upper limit of stress estimated that can be reached during the normal function of the valve veils. Note that these values are far from the rupture values of the pericardium (stresses approximately between 10 and 30MPa).

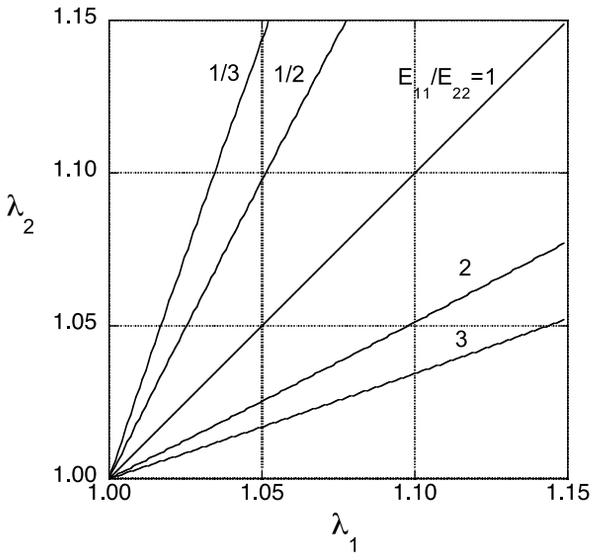

Fig. 52. *Values of the elongation in Sacks and Chuong's (1998) biaxial tensile tests.*

Figure 53 contains the results of the biaxial tensile tests performed and the stresses obtained from a fit to the constitutive equation (111):

$$\mathcal{W}(\text{kPa}) = 1.873\ [\exp(53.46E_{11}^2) + \exp(35.7E_{22}^2) + \exp(45.52E_{11}E_{22}) - 3] \tag{113}$$

which provides the stresses

$$\begin{aligned} S_{11}(\text{kPa}) &= 200.3E_{11}\exp(53.46E_{11}^2) + 85.26E_{22}\exp(45.52E_{11}E_{22}) \\ S_{22}(\text{kPa}) &= 133.7E_{22}\exp(53.46E_{22}^2) + 85.26E_{11}\exp(45.52E_{11}E_{22}) \\ S_{12} &= 0 \end{aligned} \tag{114}$$

which agree reasonably well with the experimental results (r^2=0.97).

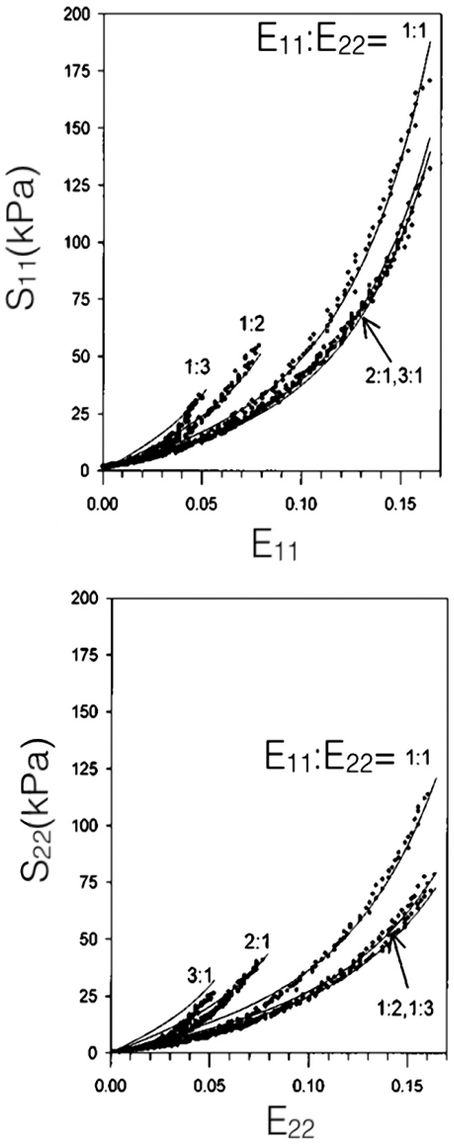

Fig. 53. *Biaxial tensile tests on bovine pericardium. Second Piola-Kirchoff stress, S, as a function of the Green-Lagrange strain, E, and fit of the model given by equation 111. Sacks and Chuong (1998)*

Sacks and Chuong (1998) also showed that the predictions from equations (117) are reasonable for simulating an experiment in which the deformation is restrained along the 1-axis (that of the collagen orientation). Figure 54 shows the experimental results and the predictions from equations (114).

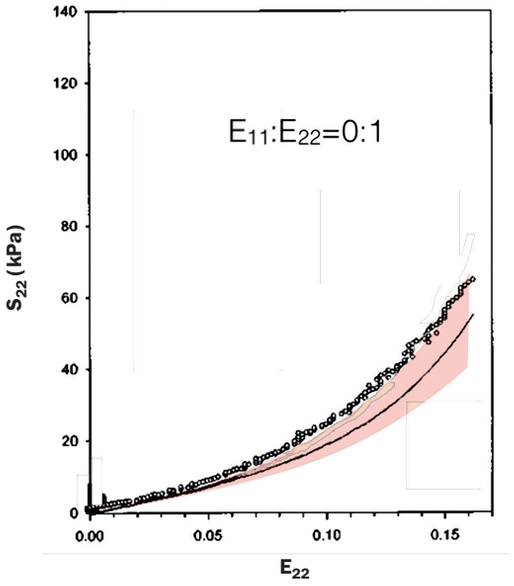

Fig. 54. *Biaxial tensile test on bovine pericardium with restrained deformation E_{11} Experimental results and predictions of the model from equation (117). The margin of error is shown shaded. S_{22}=second Piola-Kirchoff stress, E_{22}=Green-Lagrange strain. Sacks and Chuong (1998).*

It is also possible, with the aid of equations (114), to predict the results of a uniaxial tensile test, in which stress is applied in only one direction. Figure 55 shows the stress-elongation curve deduced from equations (114) for the cases S_{11}=0 (uniaxial tension along the 2-axis, perpendicular to the collagen fibres) and S_{22}=0 (uniaxial tension along the 1-axis, parallel to the collagen fibres). The second Piola-Kirchoff stresses (S_{11} or S_{22}) have been represented together with the Cauchy stresses (σ_{11} or σ_{22}) obtained by using equations (44) and (46). The elongations λ_1 and λ_2 were obtained from the Green-Lagrange strains using equation (41).

Claramunt *et al*. (2011) performed biaxial fatigue tests by pressurising membranes, adopting the arrangement shown in figure 28. This process simulates the loading of the pericardium when it is used as a veil in valve prostheses. With these it was shown that the behaviour in the first few fatigue cycles is a good indicator of the fatigue strength of the bovine pericardium.

Also using pressurisation tests, García Páez *et al*. (2001) showed that ostrich pericardium has a greater static strength than the bovine pericardium (both crosslinked with glutaraldehyde) even though its resistance to fatigue is much lower (Claramunt *et al*. 2012).

By means of biaxial fatigue tests by pressurisation at different frequencies (from 1 to 30 Hz) and average maximum stresses between 0.5 MPa and 1 MPa –which are estimated to be the maximum produced in a valve veil– it has been demonstrated that biaxial fatigue induces residual strains which can significantly alter both the geometry of the specimen (Sun *et al*. 2004) and its mechanical properties (Martin and Sun, 2014), increasing the rupture load and stiffening the pericardium membrane.

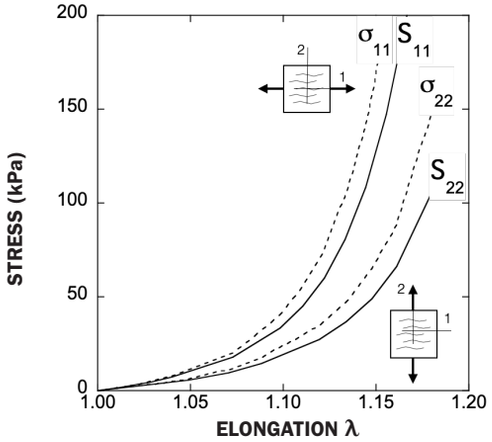

Fig. 55. *Uniaxial tensile curves deduced from the constitutive equation (117).*

In these experiments it has also been demonstrated that– just as in uniaxial fatigue– the first fatigue cycle is different from the rest, being focused primarily in permanent deformation of the membrane by alignment of the fibres in the loading direction (Sellaro *et al.* 2007). This fact plays a critical role in the mechanical response of the material, since various studies have shown that the energy dissipated in the first fatigue cycle is an indicator of damage in the material, which can be used to estimate its durability and strength, figure 56 (García Páez *et al.,* 2009; Rojo *et al.,* 2010; and Claramunt et al., 2011).

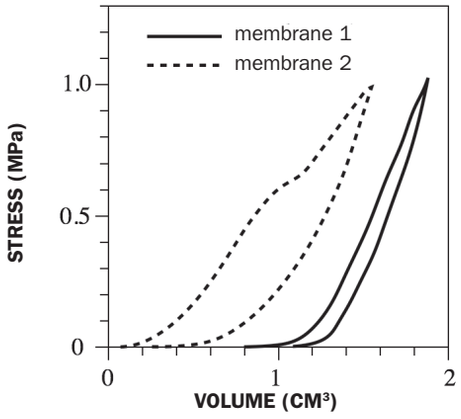

Fig. 56. *First loading-unloading cycle in pressurisation tests. The hysteresis curve of greater area indicates a lower specimen durability to fatigue (Rojo et al. 2010). Membrane 1: Hysteresis energy in the 1st cycle = 0.09J; failure after 600 cycles. Membrane 2: Hysteresis energy in the 1st cycle = 0.30J; failure after 13 cycles.*

Tear tests

The tear strength of the pericardium has been investigated by several authors, given its use as a structural biomaterial, and the need to know its strength when subjected to loading through sutures. Unfortunately, the variability of the results obtained is very large, and depends not only on the type of pericardium but also on the particular crosslinking treatment and the animal from which it was obtained, so that it is only possible to establish trends and general values of the rupture parameters.

In 1989 Trowbridge studied the sensitivity of bovine pericardium membranes to the presence of triangular notches such as that shown in figure 57. As can be seen in figure 58, the pericardium membranes are quite tolerant to the presence of this type of defect, which do not significantly affect the rupture stress or strain. In this work, it was observed that the tearing of the pericardium was always accompanied by a process of delamination between the fibrous and serous-parietal layers (see figure 43).

Using Elmendorf's tear test, the specific rupture energies of bovine and ostrich pericardium have been measured. It was observed that there is a significant variation with the length of the tear. Bovine pericardium specimens of smaller dimensions (tear 2.5mm) had an average energy of 33 N/mm compared to the 270 N/mm recorded for a tear length ten times bigger (25mm) (García Páez, *et al.,* 2006). In this work no significant differences were observed between the circumferential and apex-caudal directions.

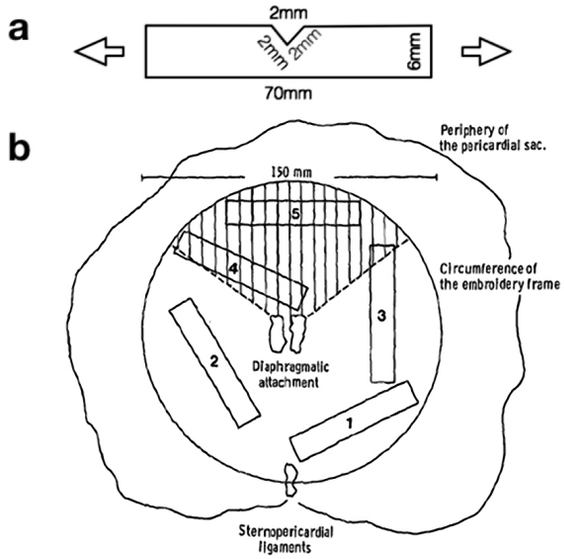

Fig. 57. T*ear tests on notched specimens. a) specimen geometry; b) anatomical position (Trowbridge 1989).*

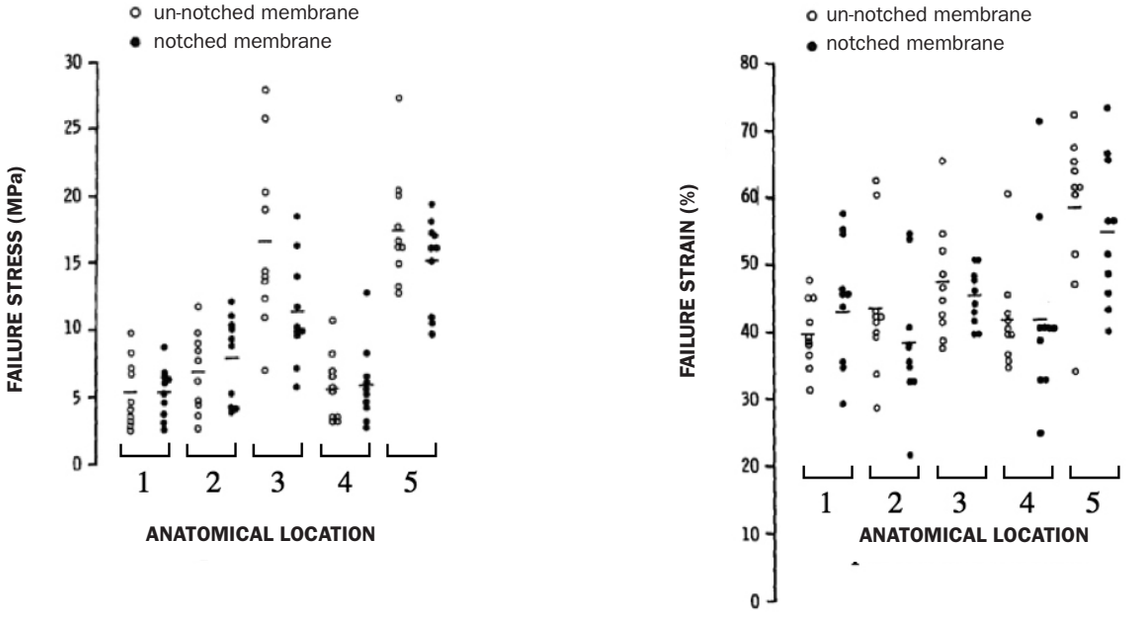

Fig. 58. *Tear stress and strain in specimens with triangular notches. There are no significant differences between the notches and un-notched specimens, nor between the different locations and orientations of the specimens (Trowbridge 1989)*

García Páez *et al.* in 2004 also measured the load which produces the tearing of sutures in bovine and ostrich pericardium (figure 59). The specimen, in the form of trousers, had dimensions of 20 mm wide and 120 mm long. The load to initiate tearing in sutured specimens was similar to, or somewhat larger than, that in the pericardium without suturing.

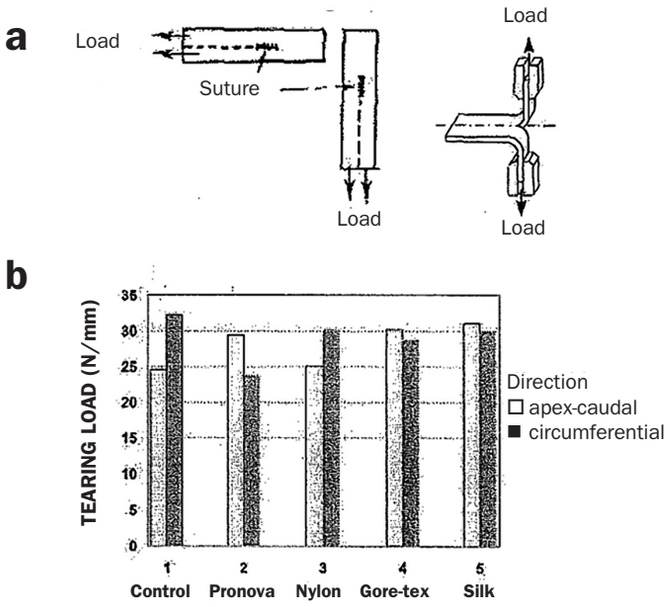

Fig. 59. *a) Specimens use to evaluate the strength of sutures in pericardium. b) Values of the tearing load (García-Páez et al. 2004)-*

However, the energy absorbed in tearing was greater in the material without the suture, as shown in some Elmendorf tests. In these, the average tear strength measured in the apex-caudal direction was 120N/mm in specimens without sutures compared to a value of 47 N/mm in 10mm sutured specimens. (García Páez *et al.,* 2010). In these cases, it was observed that tearing of the membrane produced delamination between the layers.

A detailed inspection of pericardium membrane ruptured by the tearing process shows that delamination always occurs between its layers, in the manner indicated in figure 60.

This phenomenon accounts for the increasing the rupture energy with greater length of tear (and, therefore, the greater the delamination area). In their work, Tobaruela *et al*. (2016) estimated that the "pure" tear resistance (that is to say, tearing of the pericardium layers, without producing delamination) is of the order of 30 N/mm, whether the test is performed on the apex-caudal or circumferential direction, while the delamination process –inseparable from the former– consumes about 0.5 N/mm, also nearly independent of the test direction.

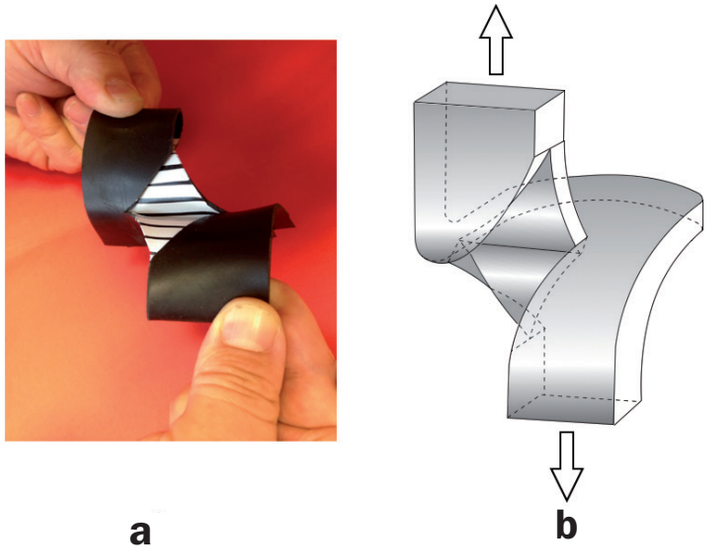

Fig. 60. *Delamination during the tearing process (Tobaruela et al. 2016).*

Effect of crosslinking

For use in bio-prostheses it is essential, as we have noted, that the pericardium is treated and crosslinked, in order to avoid it degrading in the interior of the body and to reduce its immunogenicity potential. Hence, the vast majority of studies performed have been carried out on treated membranes, as noted in previous sections.

There are several pieces of work on natural membranes which show the effect of crosslinking treatment on the mechanical properties of the pericardium. In general, the treatment with glutaraldehyde substantially increases the stiffness of the material and the elongation at rupture, but there are no conclusive results as to its effect on the tensile strength. (Trowbridge *et al*., 1989; and Mirnajafi *et al*., 2005).

It has been demonstrated that some decellularization processes with ionic detergents such as SDS (sodium dodecyl sulphate or sodium lauryl-sulphate, commonly used in biology and personal hygiene products), can produce irreversible denaturation and swelling of the collagen, which reduces the tensile strength (Courtman *et al*., 1994; García-Paéz *et al*., 2000; and Mendoza-Novelo *et al*., 2009). Therefore, it is preferred, if possible, to avoid non-ionic detergents. (Mendoza-Novelo *et al*., 2011).

3.2.3. Applications

The pericardium used as a biomaterial is commonly bovine or porcine, although on occasions other sources such as equine, canine, ostrich or kangaroo have been employed. Table 2 shows the most important biomedical applications found in the market.

TABLE 2 APPLICATIONS OF PERICARDIUM MEMBRANES (RÉMI ET AL., 2011)

SOURCE OF PERICARDIUM	SURGICAL APPLICATIONS	COMMERCIAL PRODUCT	COMPANY
Bovine or Porcine	- Repair of soft tissue - Hernias - Defects in the abdominal wall and thorax	- Implantable surgical tissue Peripatch® - TutoMesh®	Neovasc, Maverick Biosciences PTY Ltd, Tutogen medical GmbH, RTI Biologics,Med&Care, Biovascular Inc, Novomedics
	- Suture reinforcement	- Veritas Peristrips® Dry	Synovis Life Tech
	- Orbital reinforcement	- Tutopatch® - Ocugard®	Tutogen medical GmbH, RTI Biologics, Med&Care, Biovascular Inc, Novomedics
	- Dural repair	- Lyolem® All BP	National Tissue Bank Malaysia
	- Perivascular repair	- Parche vascular Peripatch®	Neovasc
	- Cardiac repair and reconstruction	- Implantable surgical tissue Peripatch®	Neovasc, Maverick Biosciences PTY Ltd
	- Heart valve replacement	- PercevalS® - Mitroflow® - Freedom solo® - Carpentier-Edwards PERIMOUNT® Magna EaseAortic Heart Valve - Carpentier-Edwards PERIMOUNT® Magna Mitral Ease Heart Valve - Carpentier-Edwards PERIMOUNT® Theon Aortic Heart Valve - Carpentier-Edwards PERIMOUNT® Theon Mitral Replacement System	Grupo Sorín Edwards Life Sciences
Equine	- Tendon repair	- OrthADAPT®	Synovis Life Tech
Human	- Valvuloplasty - Heart valve	- Autologous, homologous or heterologous grafts	

Heart valves

The most important use of the pericardium as a biomaterial, as much as for mechanical as economic reasons is found in the field of biological heart valves (figure 45). The pericardium is used as a valve veil, and must support the continuous functioning of these prostheses for millions of cycles. Currently, even though the means of selecting the biomaterial with a certified durability is not available, which would allow biological prostheses to compete for reliability with mechanical ones, the latter have the inconvenience requiring the prescription of an anticoagulant treatment for life.

The most common cause of premature rupture of the pericardium valve veils is calcification, which stiffens the membrane and promotes the propagation of cracks. This phenomenon is known to be associated with the collagen cross-linking treatments (glutaraldehyde induces calcium deposits) and, moreover, this is sensitive to the stress-strain state in the membrane. Currently, this is one of the most active areas of scientific study.

On the other hand, the introduction of, and the advances in, the techniques of valve implantation by catheter (percutaneous implantation) is driving the miniaturisation of bio-prostheses in a form that can be folded and transported through the interior of a catheter as far as its end point, where it is unfolded and attached the walls of the duct (figure 61).

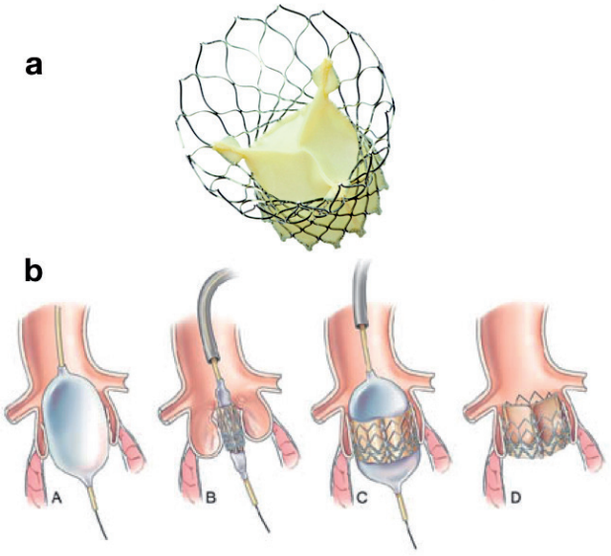

Fig. 61. *a) Valve for percutaneous implantation. b) Surgical procedure*

This type of application is very demanding in terms of the thickness and uniformity of the veils, which cannot exceed about 0.3 mm thickness. Neonatal bovine pericardium is a good candidate for these applications, being finer and more elastic that than in the adult. However, the expected duration of this type of valve, less than 10 years, imposes severe restrictions on its use, which is limited to patients whose condition is highly deteriorated, or at high risk in invasive surgery.

Repair of soft tissue

The traditional use of pericardium membranes has been in the repair of ruptured membranes of the abdominal cavities and blood vessels. In these cases, a piece of pericardium is cut into the desired shape and stitched to the adjacent tissue, in order to return the structural integrity (figure 62).

Pericardium membranes are indicated for patients with severe obesity or diabetes, where biological grafts, rather than synthetic meshes, enhance revascularisation and reduce the risk of postoperative infections.

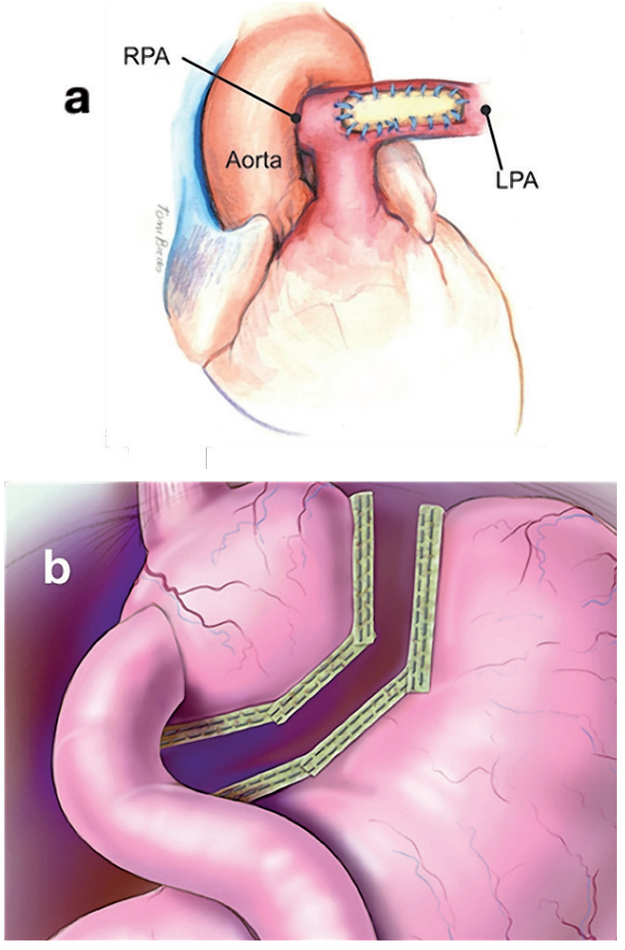

Fig. 62. *a) Pulmonary artery repair using a pericardium patch. b) Reinforcement of the suture line in a stomach reduction procedure with pericardium*

Conclusion

The pericardium, primarily that of bovine or porcine origin, is a biological tissue that is widely used as a biomaterial in bio-prostheses for vascular grafts, patches for the repair of the abdominal or vaginal wall and, more frequently, heart valves. However, despite the advances achieved over the last few years, pericardium membranes still present some important drawbacks such as the deterioration of its biological matrix and degeneration in the body, often associated with the appearance of calcification.

There are a large number of decellularisation and cross-linking protocols aimed at providing stability and durability to the pericardium to eliminate cell antigens. Of these the most common is the treatment with glutaraldehyde, which despite its undeniable advantages, changes the mechanical properties, the integrity of the extracellular matrix and increases the risk of calcification.

The problem of calcification, together with the difficulties in finding material selection procedures which guarantee uniform properties, are the principal drawbacks which limit the use and development of biological heart valves. A better understanding of the structure of the pericardium and improved selection and processing methods will improve the conception and design of pericardium bio-prostheses and increase the safety of the patients.

3.3. AORTIC ARTERIAL WALL

3.3.1. Introduction

The aorta is the human artery which distributes blood from the heart to the rest of the arteries which form the major circulation system, responsible for carrying oxygenated blood throughout the body. It is also the largest artery, with an average diameter and thickness of 25 mm and 2 mm, respectively (Burton, 1954). By means of its elastic deformation, the aortic artery smooths out the pulsating blood flow coming from the heart, facilitating the passage of blood to the other organs and tissues.

The aortic artery is prone to injury induced and/or aggravated by the blood pressure, the most common being the formation of plates, the development of aneurysms and dissections (or tears) in the wall. It has been found that such injuries, like other histopathological changes in the aortic wall, are spatially correlated with the mechanical stresses present (Bäck *et al*. 2013). The aortic artery is also sensitive to ageing, which produces important changes in its thickness, diameter and stiffness (Lanne *et al*. 1992).

There is great interest in describing and modelling the biomechanical behaviour of the aortic wall in order to better understand its physiological behaviour and ageing process, and to improve and optimise the diagnostic processes and treatment of aortic illnesses, and the development of its pathologies. There have, therefore, been a large number of expositions and constitutive equations proposed for the biomechanical study of this biological material. The task is not easy, and a satisfactory knowledge is still a long way off, since it is difficult to incorporate the complex architecture and composition of the arterial wall into biomechanical models which are robust and readily transferable to clinical practice.

In this section, a brief summary of the behaviour of the aortic arterial wall is presented, together with the current state of biomechanical modelling, beginning with a short description of its composition and structure. Its mechanical behaviour and the most important models used for its study will then be reviewed. The section is concluded with some applications of medical interest, such as rupture of aneurysms and the effect of arterial hypertension.

3.3.2. Description of the aortic wall

The aortic wall, like other blood vessels, is composed of an extracellular matrix of proteins and proteoglycans which maintain its integrity, and a set of cells which, as well as generating and preserving that a matrix, have direct mechanical action on the geometry of the vessel in order to control its physiological function.

The most principal components of the extracellular matrix are *elastin* and *collagen* proteins, which determine the passive mechanical behaviour –without muscular activation– of the artery. The smooth muscle cells present in the aortic wall are responsible for its active behaviour and, together with the fibroblasts, produce and maintain the extracellular matrix, (McDonald, 1974).

The structure of the aortic wall is also similar to that of other blood vessels, being organised in three layers: *intima, media* and *adventitia* (figure 63).

The **intima** layer is the innermost, and is formed of a monolayer of endothelial cells. These cells develop and grow on a very thin basal plate, about 80nm thick, formed of type IV collagen and adhesive molecules, fundamentally laminina 1 and fibronectin. The basal plate is supported, in turn, by a sub-endothelial lamina composed of connective tissue and smooth muscle cells aligned with the axial direction of the vessel. The endothelial cells are plane and elongated in the axial direction, the direction of the blood flow. Their dimensions are approximately 0.3μm x 12μm x 40μm (thickness x width x length) (Humphrey, 2002).

The endothelial cells are in constant contact with the blood flow and provide an anti-thrombogenic, low friction substrate, bearing the frictional shear stress with the blood whose physiological value lies between 1 and 2 Pa. These cells communicate the variations in the blood flow to the other cells in the aortic wall, so that they can adapt to the new conditions (Humphrey, 2002; Chen *et al*., 2003).

The **media** layer is primarily responsible for the mechanical behaviour of the aorta, as much because of its dimensions as its components and configuration. It is composed of sub-layers called *lamellar units* (figure 64a) which are about 14μm thick (Clark and Glagov, 1985). Each lamellar unit consists of concentric sheets of fine highly crosslinked elastin fibres (0.1 to 0.5μm) between which are inserted smooth muscle cells and some fibroblasts, all preferentially arranged in the circumferential direction (O'Connell *et al*., 2008]. The number of lamellar units varies as a function of the thickness of the aortic wall so that the circumferential force which each unit supports is, essentially, constant at about 2 ± 0.4 N/m, figure 64b (Wollensky and Glagov, 1967).

Bundles of collagen fibres lie between the lamellar units, running parallel to the muscle cells, surrounding them. These fibres are wavy and, at physiological pressures, only about 7% of them carry any stress (Armentano *et al*., 1991).

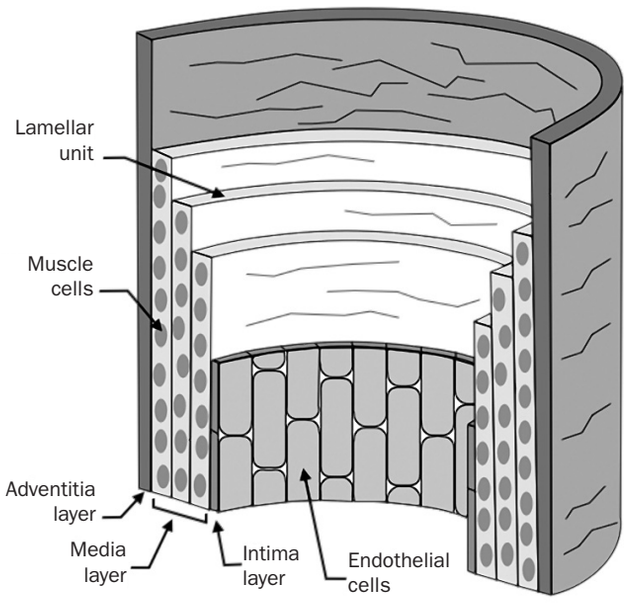

Fig. 63. *Structure of the aortic wall. For simplicity, only three lamellar units are shown.*

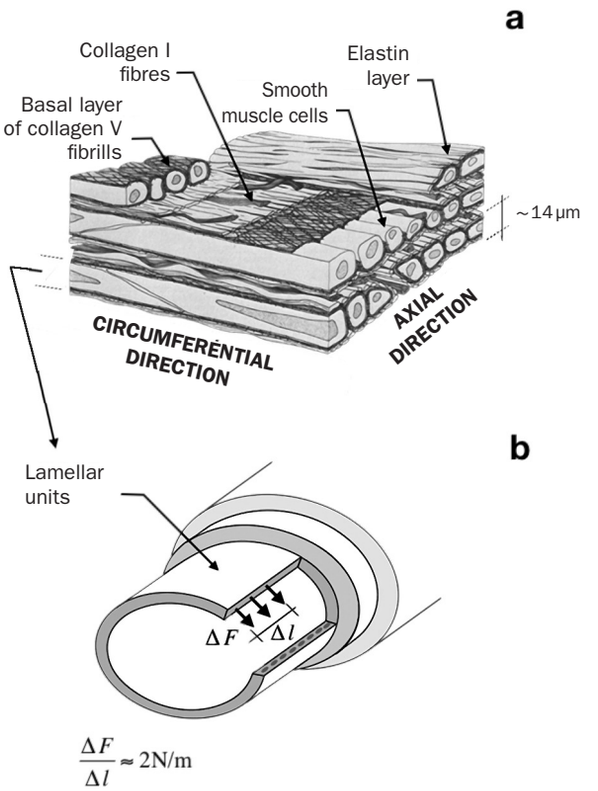

Fig. 64. *a) Schematic representation of lamellar units (Clark and Glagov 1985) b) Circumferential force carried by each lamellar unit.*

The **adventitia** is the outermost layer (figure 63), and is composed principally of bundles of micrometric-sized collagen fibres and loose connective tissue which anchors the artery to its surrounding tissue. Some soft muscle cells and, mainly, fibroblasts are responsible for its maintenance, being able to adjust the expression and synthesis of collagen in response to mechanical signals (Bishop and Lindahl, 1999).

The structure and composition of the aortic artery are not uniform, and change with position, as shown in figure 65. The elastin content, and in consequence the elastic character of the vessel, reduces significantly from the diaphragm, into the abdominal region of the aorta. The diameter and thickness also diminish monotonically away from the exit from the heart. (Sokolis, 2007).

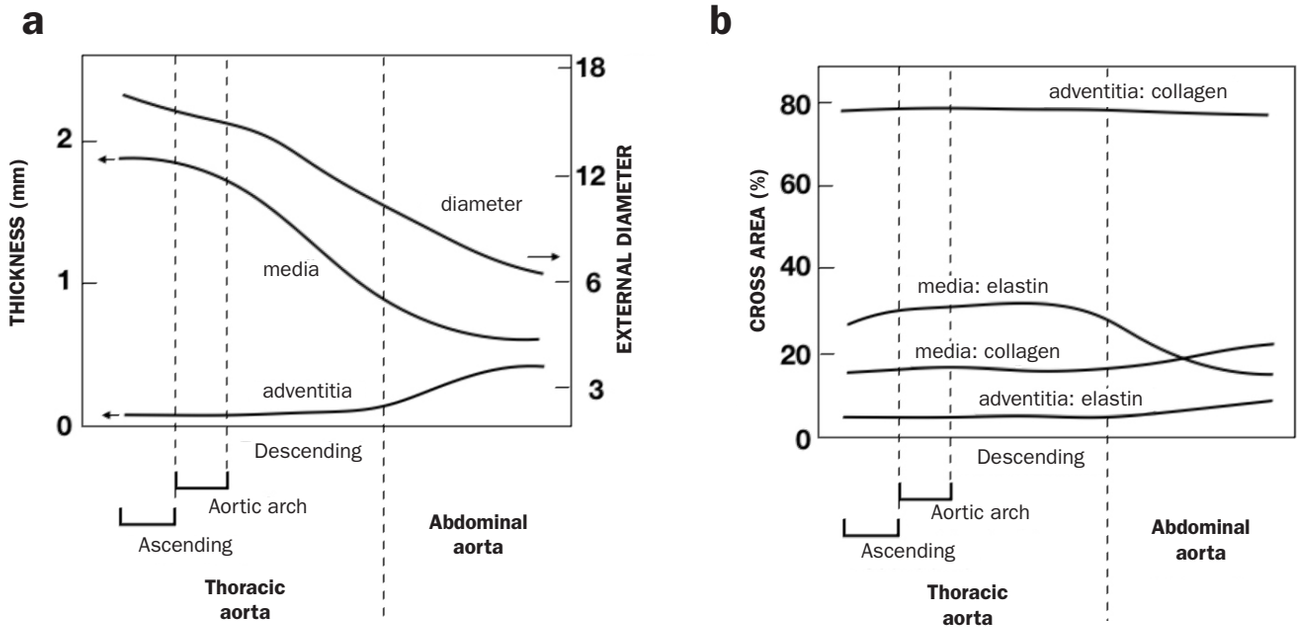

Fig. 65. *Structure of the porcine aortic wall as a function of its position.*
a) External diameter of the vessel and thickness of each layer.
b) Percentage of cross-section occupied by each component.
Note that the intima layer occupies less than 1% of the total thickness (Sokolis, 2007).

3.3.3. Mechanical behaviour

Owing to essentially mechanical functions - blood flow and pressure regulation (by deformation and elastic recovery) - and also by the number of mechanical defects which it can suffer (wall ruptures, formation of aneurysms), the aortic artery has always been at the forefront of the study of biomechanics, since the pioneering works of C. S. Roy in 1881.

In a study of the behaviour of the aorta, we must distinguish between its passive and active states. The former corresponds to the situation in which the smooth muscle cells are not contracted, while in the latter there is muscular contraction. Although, ideally, the passive state is reached when the cell population dies, some authors regard the passive as corresponding to the basal cellular state, in which there is some degree of contraction (basal muscle tone).

Figure 66 shows pressure-diameter tests carried out on rat aorta under the maximum muscle activation and in the passive state. The curves were obtained for two different values of axial elongation in the aorta, since in their *in-vivo* physiological state the arteries are always stretched. In the human aorta the average elongation *in-vivo* reaches a value of λ =1.4 in young persons, decreasing with age (Horny *et al*., 2014). Muscular activation changes the behaviour of the vessel making it stiffer, especially in low pressure zones. Note that the arterial pressure of rats is similar to that of humans, having an average value of around 100 mmHg.

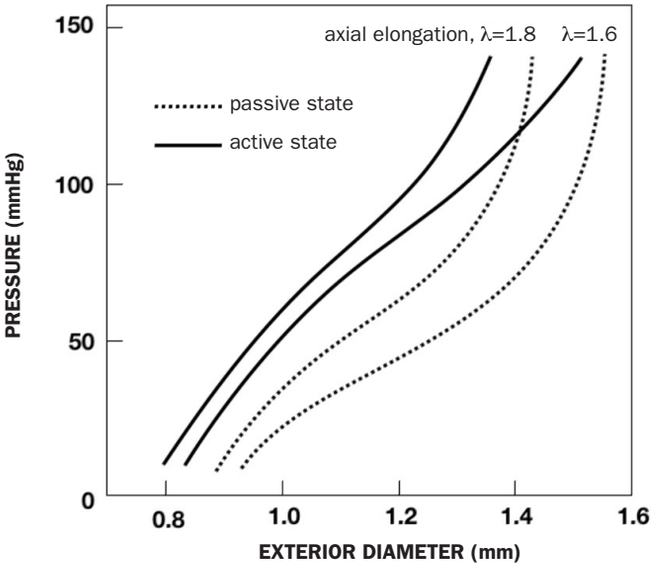

Fig. 66. *Pressure-diameter curves of rat aorta in the passive and active states. The rat aorta is subjected in-vivo to an axial elongation λ=1.76. Adapted from (Agianniotis et al., 2012).*

The results in figure 66 indicate that, if it is required to simulate correctly the *in-vivo* behaviour of the artery, muscular contraction cannot be ignored. The same is true of the other arteries, since the effect of the smooth muscle contraction on the artery wall increases as we move away from the heart, and becomes very important in the farthest arteries–called muscular– such as those originating in the celiac trunk, renal or radial arteries. The presence of the smooth muscle and its activation, not only change the elastic response of the aorta but also significantly affect its viscoelastic behaviour.

Examination of passive behaviour shows that the pressure-diameter curves of the aorta has two zones of very different stiffnesses, figure 67. The first of these zones corresponds to the region with pressures equal to, or less than, the physiological, while the second is where they are higher than the normal physiological pressure of 120 mmHg. When the vessel exceeds this value of pressure, its stiffness increase greatly–by almost an order of magnitude– due to the collagen fibres coming into play, which were initially wavy and stress-free.

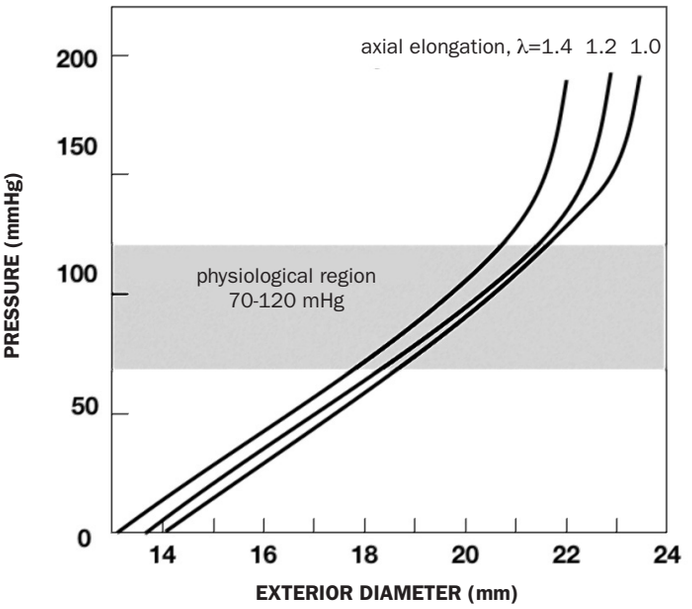

Fig. 67. *Pressure-diameter curves for human aorta (20 year old female) in the passive state. (García-Herrera, 2008).*

The functioning physiological zone, of pressures between 70 and 120 mmHg, is situated in the most flexible region of the pressure-diameter curve, immediately before the transition. In this interval, the mechanical behaviour of the aorta is almost exclusively controlled by the elastin fibres, which are very elastic (Roach and Burton, 1957). Therefore, when work-

ing in the physiological range, the aorta exercises its entire capacity to deform elastically to accommodate the volume of blood pumped by the heart, and to smooth out its delivery to the rest of the arterial system, in a phenomenon known as the Windkessel[9] effect. When the pressure rises above the physiological level, the collagen fibres are activated, as a reinforcement which prevents excessive deformations which could lead to rupture of the vessel.

The uniaxial tensile test on the arterial wall, although somewhat removed from the real mechanical situation than the pressure-diameter test on the vessel, is more frequently used due to its ease of execution and data interpretation. Figure 68 contains data from uniaxial tensile tests to rupture, performed on healthy adult (ages between 16 and 36 years) human aortas.

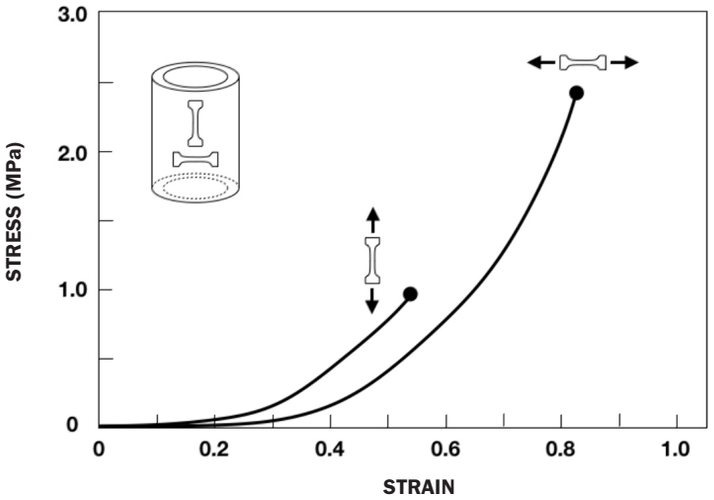

Fig. 68. *Fig. 68. True stress-strain curves for specimens from the human aorta of healthy young adults (16 and 36 years), in the passive state. (García-Herrera, 2008).*

These experiments provide a graphic illustration of the anisotropy in the aortic wall, which is much stiffer and weaker in the axial than the circumferential direction, since, as has been seen in the previous section, the collagen fibres, like those of elastin, are distributed preferentially in the circumferential direction.

Uniaxial tensile tests are also very useful in characterising the behaviour of aortic material as a function of time. Figure 69 shows loading and unloading cyclic tests performed on specimens orientated in the longitudinal and circumferential directions. The material initially shows an important hysteresis loop which is significantly reduced after a small number of cycles, attaining a repetitive and stable behaviour[10]. From a physiological point of view, the hysteresis cycle has an important damping effect which helps reduce the flow and pressure fluctuations produced by the waves generated by the heart beat.

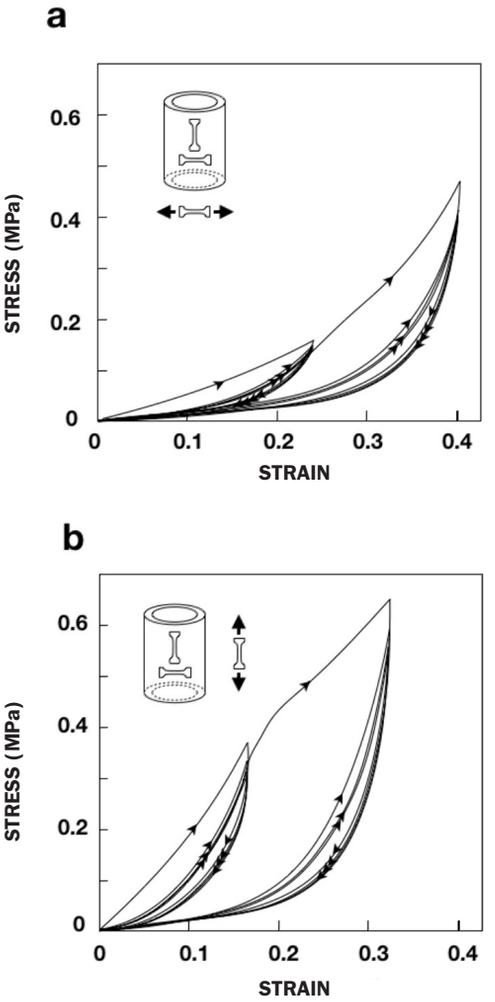

Fig. 69. *Fig. 69. Cyclic true stress-strain curves of human thoracic aorta specimens. Adapted from Horný et al. 2010.*

[9] In German *windkessel* means *air chamber*, referring to devices used in water tanks by XVIII th Century firemen to obtain a continuous flow of water, and eliminate pulsations of the pump piston. The elastic deformation of the arterial aorta and other elastic arteries store some of the blood pressure from the heart systole, and return it to the arterial system during the diastole, smoothing out the blood flow. This idea was proposed by the English scientist and cleric Stephen Hales (1677–1761), and mathematically modelled by the German physiologist Otto Frank (1865–1944).

[10] This phenomenon, known as the Mullins effect, was first described for rubbers by the English researcher Leonard Mullins (1918–1997).

Biomechanical models

The first challenge appears when considering the structure of the aortic wall. The aorta is a combination of solid components (protein, proteoglycan and cellulose fibres) and water, the great part of which have little mobility being tied by the proteoglycan and elastin macromolecules. Even so, there is a radial flux generated by pressure differences in the blood, in the interior of the artery, and the interstitial fluid in the exterior which is essential for the diffusion of nutrients and signalling molecules. On the other hand, the disposition of the solid components is very complex as we have seen, and there is not –as occurs in all biological materials– and clear distinction between material and structure, since the different components interact over a wide range of scales of observation, from the molecular to the microscopic level, without interruption.

In order to overcome this difficulty using the mechanics of continuous media it is necessary to assume that the aortic wall is a continuous solid[11] composed of homogeneous parts. Although this assumption is common, and has been made for all types of materials, in the case of biological materials, due to its internal organisation, this distinction is totally arbitrary and is made solely on the basis of the available data and/or the type of information required in the model. Therefore, we will have to consider the simplest models of the aortic wall as a single homogeneous material (for example, Hoppmann and Wan, 1970), or a homogeneous material reinforced with fibres, as in the case of Gasser *et al*. 2012. The most complex models consider the aorta as a material composed of several phases, each one with its own laws of evolution, Clearly, an increasing level of detail requires more sophisticated techniques and more refined experimental data which allow a reliable determination of the parameters of the models, which is not always possible.

It is not the aim of this test to go deeply into the biomechanical models of the aorta, so we will only provide a few simple examples, concentrating on the passive behaviour. For a deeper understanding of the topic, the interested reader can consult the bibliography at the end of the chapter.

TABLE 3: VALUES OF SOME THREE-DIMENSIONAL STRAIN ENERGY FUNCTIONS USED TO MODEL THE BEHAVIOUR OF THE AORTIC WALL IN THE PASSIVE STATE.

MATERIAL	STRAIN ENERGY $\mathcal{W}$	REFERENCE
Isotropic	$\mathcal{W} = c_0 \exp\left(c_1 I_{1E} - 1\right)$	Deimirai (1981) Polzer et al. (2013) Riveros et al. (2013)
	$\mathcal{W} = \sum_{i=1}^{N} c_i I_{1E}^i$	Yeoh (1993) N=2: Raghavan and Vorp (2000) N=5: Polzer et al. (2013)
Orthotropic	$\mathcal{W} = c_0\left(\mathrm{e}^{Q} - 1\right)$ $Q = c_1 E_{\theta\theta}^2 + c_2 E_{33}^2 + c_3 E_{rr}^2 + c_4 E_{\theta\theta} E_{33} + c_5 E_{rr} E_{33}$ $+ c_6 E_{rr} E_{\theta\theta} + c_7 E_{\theta 3} E_{3\theta} + c_8 E_{r3} E_{3r} + c_9 E_{r\theta} E_{\theta r}$	Chong and Fung (1986)
	$\mathcal{W} = c_0\left[\exp\left(c_1 E_{\theta\theta}^2\right) + \exp\left(c_2 E_{33}^2\right) + \exp\left(c_3 E_{\theta\theta} E_{33}\right) - 3\right]$	Choi and Vito (1990) Van der Geest et al. (2006)
	$\mathcal{W} = -c \ln\left(1 - Q\right)$ $Q = \frac{1}{2} c_1 E_{\theta\theta}^2 + \frac{1}{2} c_2 E_{33}^2 + c_3 E_{\theta\theta} E_{33}$	Matsumoto and Hayashi (1996)
	$\mathcal{W} = c_0 I_{1E} + \sum_{i=1}^{N} c_{1i}\left\{\exp\left[c_{2i}\left(I_{4i} - 1\right)^2\right] - 1\right\}$	Holzapfel and Gasser (2001)

$\mathcal{W}$ is the strain energy per unit volume in the reference configuration.
c_i are the appropriate constants for each models.
I_{1E} is the first invariant of the Green-Lagrange strain tensor.
I_{4i} is a parameter which takes into account the strain according to the orientation of the i-th family of fibres.

[11] We understand a continuous solid to be one which completely occupies the space over which it extends, so that it leaves no “gaps”. Therefore, a continuous solid can be subdivided infinitely, with every one of its parts keeping the properties of the original solid.

The simplest models represent the aortic wall as a continuous, elastic, incompressible material. This hypothesis is reasonable as a first approximation, since the materials can be considered continuous at the macroscopic scale (in the region of mm), which is the level at which surgical procedures are carried out (sutures, prosthetic implants and grafts, *etc*..) and also the level of precision of the common experimental measurements, both purely mechanical (forces and displacements), and flow and blood pressure. This implies that the stresses and strains obtained from the models lose their physical meaning below the millimetric scale, similar to that which occurs with homogeneous solids such as concrete, in which it is meaningless to specify stresses and strains obtained from continuous material models in regions smaller than the size of the aggregate.

On the other hand, as we have seen in figure 69, if the loading is cyclic the arterial tissue is stabilised and presents a response which does not vary with time. In this way, under the action of cyclic pressures originating in the heart, the arterial wall is found to be *preconditioned* in the sense indicated in section 2.2, so that one-to-one relationships can be established between stresses and strains, for the loading and unloading branches. This situation allows a hyper-elastic representation of the constitutive equation[12] valid (and only valid) for each branch. This is the pseudo-elastic process proposed by Fung in 1979 (Fung *et al*. 1979) and which is still used today.

Finally, as a result of its high water content, the aortic wall –like the majority of biological tissues– can be considered to be an incompressible material. This does not mean that there are no volumetric strains, but rather that these are several orders of magnitude less than the others, so they can be neglected without loss of accuracy[13].

As was observed in section 2.2.5, hyper-elastic models are defined in terms of the strain energy per unit volume in the reference configuration $\mathcal{W}=f(\mathbf{E})$. From this, employing equations (66) the second Piola-Kirchhoff stress tensor $\mathbf{S}$ can be obtained, while using equation (67) (for the two-dimensional problem) or (69) (for the three-dimensional problem) yields the Cauchy stress tensor σ.

When the material is isotropic, the strain energy function $\mathcal{W}=f(\mathbf{E})$ can be written as $\mathcal{W}=f(I_{1\mathrm{E}}, I_{2E}, I_{3\mathrm{E}})$, depending only upon the invariants[14] of the strain tensor, $\mathbf{E}$. Table 3 shows some of the more popular isotropic functions for aortic tissue, in which, normally, $\mathcal{W}$ only depends upon the first invariant. Even though the aortic wall is not isotropic, these expressions are useful for one-dimensional representations in which it is required to model a single relationship, such as the force-displacement curve in a uniaxial test, or the pressure-diameter behaviour under axial elongation *in-vivo*, without concern for the values of the other strains or forces acting.

In order to model the anisotropic behaviour of the aortic wall the anisotropy is introduced directly into the hyper-elastic constitutive equation, either by writing it as a function of the individual components of the strain tensor, or through the particular invariants that take into account the structure of the material.

From the configuration of the constituents, described in section 3.3.2, the aortic wall is considered as an orthotropic[15] material whose principal directions are the radial, circumferential and axial axes, which were defined in figure 22c. For this reason, some models define the strain energy function $\mathcal{W}$ directly in terms of the components of the Green-Lagrange strain tensor in these axes, as shown in table 3.

Alternatively, some authors model the anisotropic behaviour using an *isotropic* strain energy function to which the dependence on some specific parameters I_m is added, which account for the directions of anisotropy $\mathcal{W}=f(I_{1\mathrm{E}}, I_{2\mathrm{E}}, I_{3\mathrm{E}}, I_4, I_5, I_6...)$. In general, each parameter I_m takes into account the effect of a family of reinforcing fibres, according to their orientation in the aortic wall. One of these models is also shown in table 3. Details can be found in the references.

---

[12] As the reader will have already observed, in order to avoid confusion with the elastic behaviour under small deformations, it is usual to adopt the word hyper-elastic in order to refer to elastic behaviour in the presence of large deformations.

[13] An incompressible material does not change its volume no matter what load is applied. From a practical point of view, we can consider a material to be incompressible when its bulk modulus is much greater than its elastic modulus.

[14] In an isotropic material the strain energy does not vary with the special orientation of the strain tensor, and therefore depends only upon its invariants, defined as $I_1=tr\mathbf{E}$, $I_2=(tr^2\mathbf{E}-tr\mathbf{E}^2)/2$ and $I_2=(tr^3\mathbf{E}-3\,tr\mathbf{E}\,tr\mathbf{E}^2+2tr\mathbf{E}^3)/6$. The number of independent invariants is equal to the number of dimensions of the tensor: (I_1, I_2) for two dimensions and (I_1, I_2, I_3) for three.

[15] An orthotropic material has three planes of material symmetry.

3.3.4. Application: Arterial hypertension

Sustaining a high pressure in the arteries (typically more than 100 mmHg diastolic and 140 mmHg systolic pressures) causes remodelling and a permanent change in its geometry and mechanical properties. Later we will present, as an illustration, the study performed by Matsumoto and Hayashi (1994, 1996) who investigated the behaviour of rat aortas into which hypertension was induced over eight weeks by mechanically reducing the cross section of the renal artery.

After dispatching the animals and extracting their thoracic artery, the authors found that the thickness of the aortic wall increased considerably owing to the increased thickness of the lamellar units, while the internal radius of the artery was unchanged, or slightly increased. As a result of this change in geometry, the circumferential stress in aortas subjected to the hypertension remained essentially constant at the physiologically normal value of $\sigma_{\theta\theta}=300$ kPa. The thickening of the wall also increased the value of the residual stresses, whose angle of aperture angle α (see section 1.3, figure 10) appeared to increase linearly with the arterial pressure. The remodelling of the vessel also produced a reduction in the *in-vivo* elongation, λ_3, of 15%.

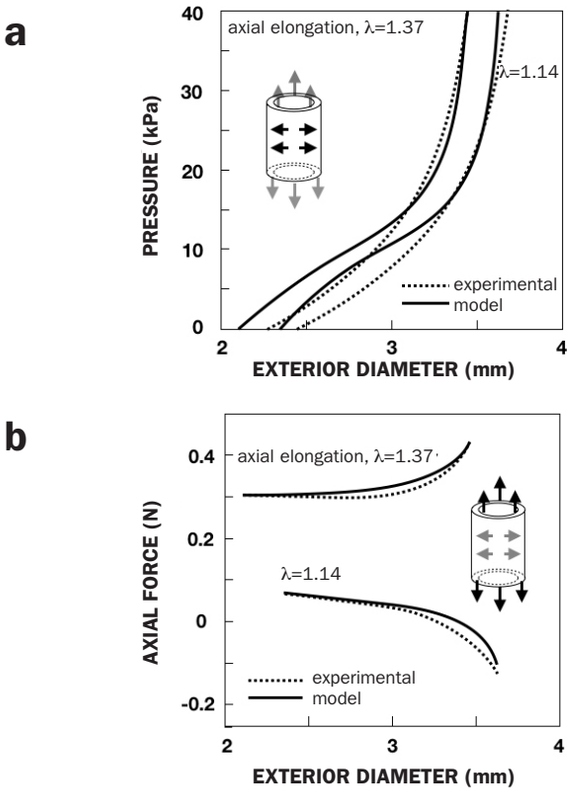

Fig. 70. *Pressure tests under axial elongation of arteries subjected to chronic hypertension.*
a) Pressure-diameter curves and fit of the biomechanical model.
b) Value of the axial force and fit of the biomechanical model.
The in-vivo elongation of the normotensive vessels is about 1.37, and that in hypertension is about 1.14. Adapted from Matsumoto and Hayashi 1996.1996.a

Figure 70 shows a comparison between Matsumoto and Hayashi's constitutive equation proposed in table 3 and experimental data from the pressure-diameter test. In this case a calculation was performed in which the vessel's internal residual stresses (measured by the angle of aperture) were incorporated.

As can be observed, the model agrees reasonably well with multiaxial load produced by the pressure and simultaneous elongation of the vessel. The values of the parameters obtained were:

c = 69.1 kPa, $c_1=1.317$, $c_2=2.001$, $c_3=0.355$
for the aorta which had suffered arterial hypertension (hypertensive aorta), and

$c=94.2$ kPa, $c_1=0.773$, $c_2=1.031$, $c_3=0.237$
for the aorta under normal pressure conditions (normotensive aorta).

Figure 71 contains the predictions of the model for uniaxial tests in the circumferential and axial directions. The model adequately reproduces the large stiffness of the vessels in the axial direction and the general stiffening produced by the hypertension.

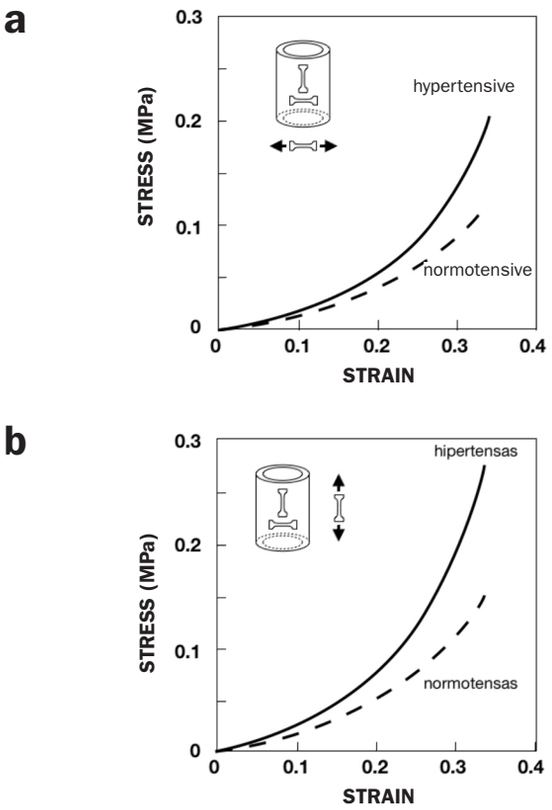

Fig. 71. *Modelling of uniaxial tensile tests on normotensive arteries and those subjected to chronic hypertension. a) Tested in the circumferential direction) and b) Tested in the axial direction. Adapted from Matsumoto and Hayashi, 1996.*

Several models developed to predict the evolution of the geometry and properties of hypertensive arterial walls have been developed. Perhaps the first and simplest –despite its complexity– was proposed by Rachev and co-workers (Rachev *et al*. 1998) which used the strain energy function suggested by Chong and Fung (1986).

The model proposes phenomenological approaches for the temporal development of the variables which control the geometry and the strain energy function W.

Predicted values of the temporal variation of the thickness and angle of aperture (as a measure of the residual stresses) are shown in figure 72 for the rabbit thoracic aorta, using the model.

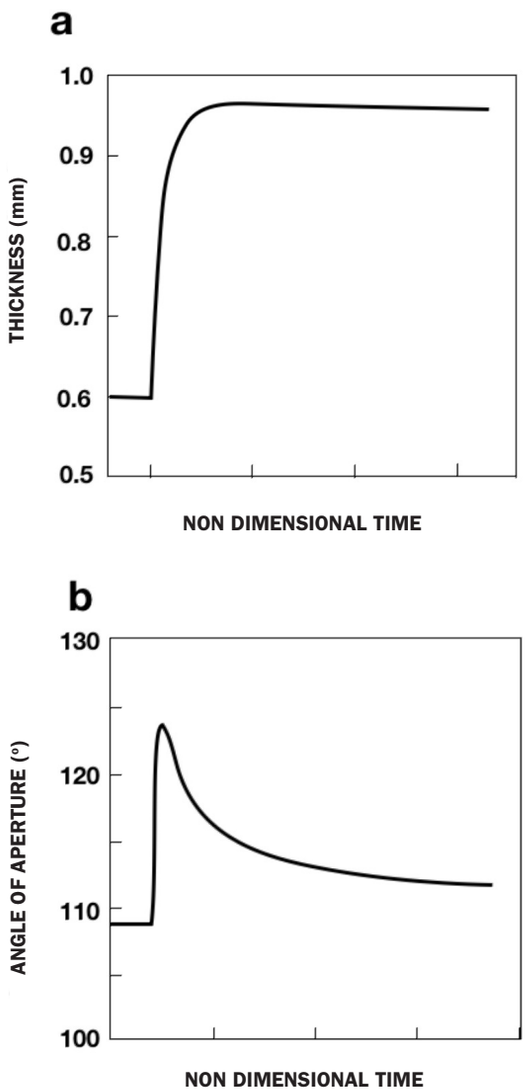

Fig. 72. *Model of the temporal variation of the hypertensive rabbit thoracic aortic. a) Variation of the aortic wall thickness and, b) Variation of the angle of aperture. Adapted from Rachev et al. 1998.*

The model correctly predicts a monotonic increase in the aortic wall, reaching an equilibrium state when the thickness is approximately 50% greater than that of the normotensive vessel. The temporal evolution of the angle of aperture presents a very rapid increase followed by a drop to an asymptotic equilibrium value which can be above or below the control value, depending upon the location of the vessel, an observation also made by several authors (Fung and Liu, 1989). A similar trend (not shown in the figure) is observed for the internal radius, which tends rapidly to its initial value.

This model also correctly predicts the evolution of the mechanical behaviour of the vessel, which reproduces the experimental observations of Matsumoto and Hayashi (1994), as shown in figure 73.

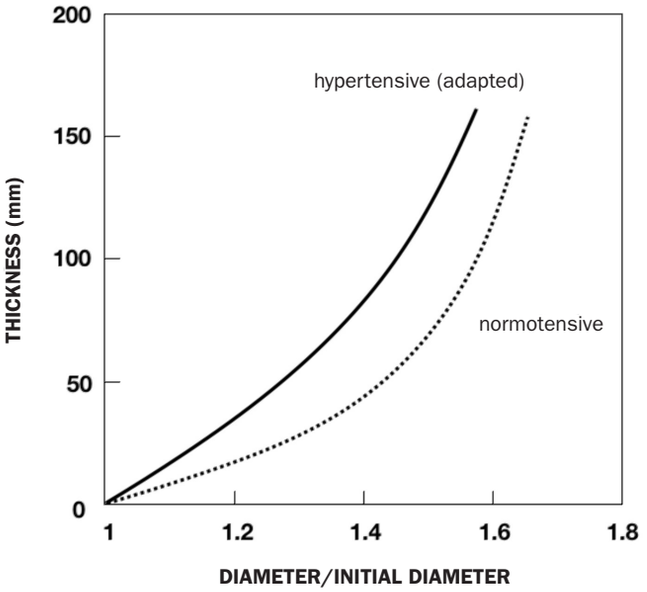

Fig. 73. *Pressure-diameter curves for the normotensive aorta, and that after reaching the equilibrium state under hypertension. Adapted from Rachev et al. 1998.*

Conclusion

Aortic tissue –and biological tissues in general– manifests a huge capacity to adapt to mechanical changes to its surroundings, so it is increasingly urgent to have accurate, experimentally validated, biomechanical models which allow a better understanding of these processes, and are useful as a guides to the design and implementation therapeutic interventions and new medical devices. In this context, the biomechanics concepts illustrated in these pages are useful for establishing a sound and objective foundation upon which to build and develop new theories which, with the aid of powerful computational techniques, can be brought to bear in their biological study and medical practice.

3.4. ELASMOID SCALES

3.4.1. Structure of elasmoid scales

The structure of *elasmoid* scales is, at first glance, simple. In a cross-section of the scales two layers can be distinguished; a hard surface layer, of collagen which is highly-mineralised (with apatite), and a soft lower layer, with less-mineralised collagen, formed by packets of superimposed fibres of different orientations. These scales, which are thinner than *ganoids* scales, are anchored to the dermis and partially overlap adjacent ones.

Two types of *elasmoid* scales are shown in figure 74: *Cycloids* (figure 74a) have a smooth exposed parts and their form is oval or almost circular, while *ctenoids* (figure 74b) have rough patches or spines on their exposed parts. Rings, corresponding to stages of growth, can be observed on the scales. The spacing and other details of these lines give clues to the life of the fish –growth, spawning, and other development events– which can be interpreted by expert biologists. Radial lines can also be seen, which appear to emanate from a focus, located at the centre of the rings.

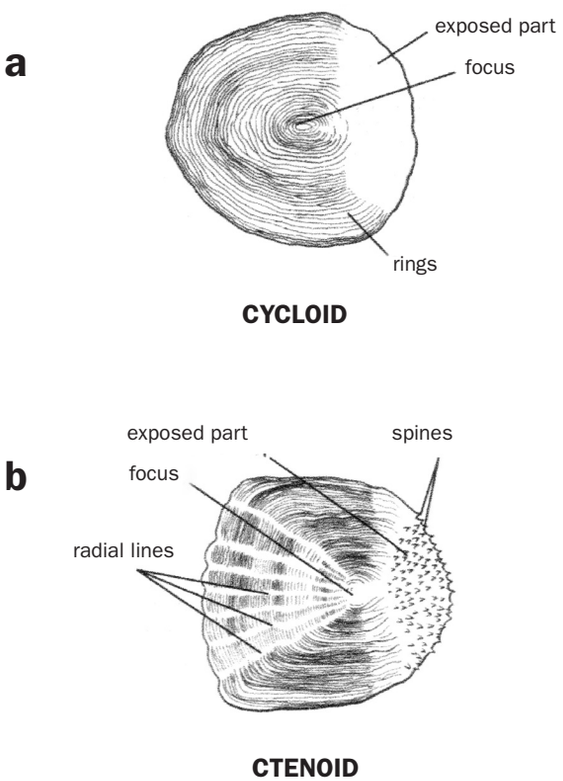

Fig. 74. *Types of elasmoid scales*

One of the scales studied in most detail is that of the fish *Arapaima gigas* (Sherman *et al*. 2017), previously mentioned in section in 1.5. The scales overlap, so that, on average, the each part of the skin is covered with three scales. Part of each scale is exposed and the other part covered by the adjacent scales.

The hierarchical structure of these scales is shown, in a simplified form, in figure 75. Note that the structures considered range from centimetres to nanometres, that is, about 7 orders of magnitude. The *exposed* part of the scale is covered with a hard corrugated, highly mineralised, layer, (inhabitants of the Amazon used these scales to file their nails) which can reach a thickness of 0.5 mm. Underneath this hard layer there is another, softer, one formed of collagen fibre sheets arranged in parallel packs, with thicknesses of about 50 μm. These sheets are stacked almost orthogonally (figure 75). The sheets themselves are formed of cylindrical bundles of fibres, with diameters of approximately 1.0 μm. Each bundle is, in turn, composed of collagen fibrils of about 100 nanometres in diameter (Yang *et al*. 2014).

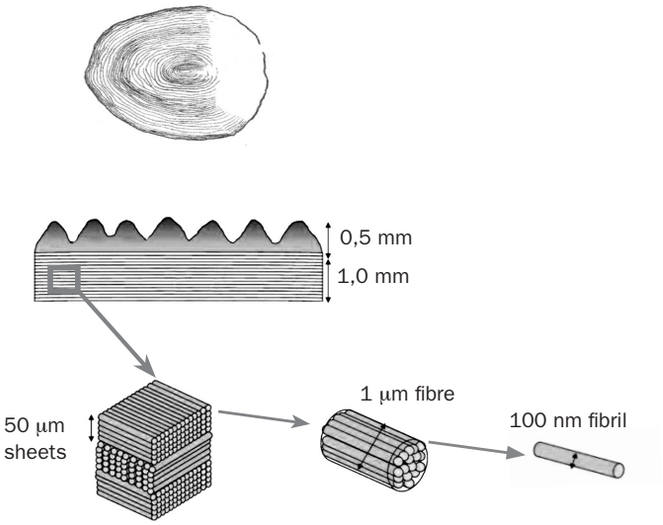

Fig. 75. *Hierarchical structure of the scale of Arapaima gigas.*

Another *elasmoid* scale which has been studied in some detail is that of the *Megalops atlanticus*, the shad or tarpon (Murcia *et* al. 2018, Gil-Duran *et al*. 2016). It is a large silver fish with a compressed fusiform body, which can reach a length of two metres. While it is a sea fish, it can survive the river waters because it can tolerate waters which lack oxygen by inhaling air directly into its swim bladder, which acts as a lung.

A simplified cross-section of these scales is shown in figure 76a in which three regions can be identified: A hard external layer formed of highly mineralised collagen, with an apatite mineral/collagen ratio greater than three, and an internal softer layer, also formed of less-mineralised collagen fibres, known as *elasmoidine.* This second region can, in turn, be subdivided in two (figure 76a); an upper layer, with a mineral/collagen ratio which varies between 3.0 and 0.5, and an inner layer of elasmoidine with a mineral/collagen ratio of less than 0.5. The collagen fibres are grouped into helically-stacked sheets, whose average thickness is about 20 µm. In this structure, called a *Bouligand structure* (Y. Bouligand, 1972), the angles between the adjacent sheets can vary from 35° to 85°.

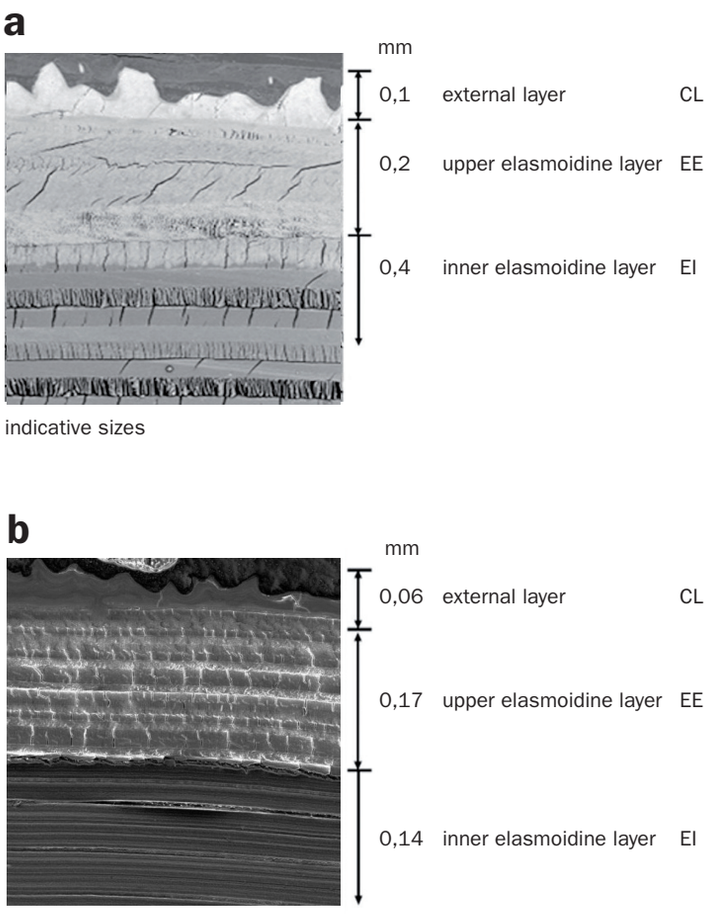

Fig. 76. *a) Cross-section of the scale of a shad*
b) Cross-section of the scale of a carp

Other types of *elasmoid* scales which are worth examining, in order to compare the structures in different circumstances, are those fish which do not have special needs, both in locomotion and in protection against predators. Carp, *Cyprinus carpio*, is a fresh water fish which serves this purpose.

A simplified cross-section of a carp scale is shown in figure 76b. The structure is very similar to that of the shad, but thinner (Murcia *et al*. 2015). Three regions can also be identified; a hard external layer, of highly mineralised collagen, and another inner layer of less mineralised collagen (elasmoidine). The collagen fibres are also grouped in sheets, whose average thickness is about 10 µm, and the sheets are helically stacked, as in the shad.

The *elasmoid* scales of other fish are similar, but differ in size and detail, depending upon their anatomical position. S Murcia *et al*. (2017) performed a comparative study between the three scales discussed, with the following results:

– The materials which form *elasmoid* scales are a combination of type I collagen and apatite. Unlike hard mineral tissues, such as bone, dentine or enamel which are highly mineralised, *elasmoid* scales have lower mineralisation, which allows the construction of an armour which may be flexible to facilitate the motion of the fish.

– In all three examples, the microstructure is similar. Three distinct zones are apparent, although the thickness of the scales varies; about 1.5 mm for the arapaima, less than 1 mm for the shad, and less than 0.5 mm for the carp.

– The thickness of the surface layer, the hard layer, is much larger in the arapaima than in the other two fish; between 500 and 300 µm for the arapaima, and less than 100 µm for the shad and carp. Perhaps this is due to the fact that the arapaima must withstand the teeth of piranhas. A curious fact is that, in both the shad and carp, this thickness is the same in the scales of the head, as those of the body and those of the caudal peduncle. This is not the case in the arapaima, in which the thickness decreases with distance from head to tail.

– The thickness of the sheets formed of collagen fibres also varies; about 50 µm for the arapaima, more than 20 µm for the shad and 10 µm for the carp. The most important difference is found in the stacking of these sheets; in the shad and the carp the stacking sequence repeats itself every five lamina, while in the arapaima it is every two.

3.4.2. Mechanical properties

The objective in studying the mechanical properties of *elasmoid* scales is to try to understand their tenacity, flexibility and resistance to penetration, for two reasons; the first, in order to determine the role each component plays in such a hierarchical structure and, secondly, to derive ideas which would allow the design of armours with the same or greater benefits than those offered by nature. To this end, conventional tensile, tearing and puncturing tests have been performed.

Tensile tests

Experiments were carried out with prismatic specimens, such as those shown in figure 77, and tested in tension, recording the force as a function of the displacement. These data reflect the response of a complex structure –this does not relate to a homogeneous isotropic material but a heterogeneous and hierarchical one– and, in consequence, represent the behaviour of the whole structure and not that of some component. In order to evaluate the contribution of the different elements, when it is not possible to test them separately, models have been developed based on the available information and, to test their validity, they are compared with the experimental results. Because of the characteristic the structure of the scales it should not be surprising that the tensile tests show that the material is anisotropic and that, moreover, the results have a large dispersion introduced by the heterogeneity of the samples.

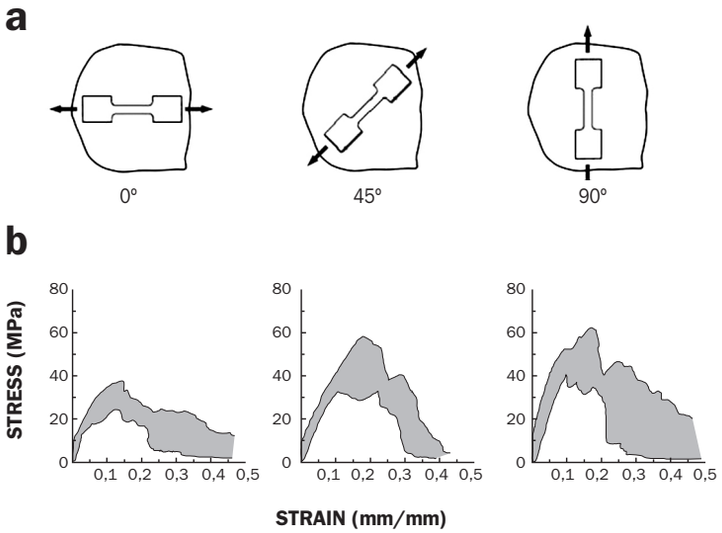

Fig. 77. *Tensile tests on scales of Morone saxatilis. Influence of anisotropy. (Zhu et al. 2012).*

A*nisotropy* has been investigated in a series of tests performed by Zhu *et al*. (2012) on scales of the striped bass (*Morone saxatilis*), an anadromous fish found along the Atlantic coast of North America, and which, though living in the sea, enters freshwater to reproduce. This fish can reach a length of 150 cm and a weight of 30 kg. The shape and disposition of the specimens, which were tested in tension, are shown in figure 77a and the results of these tests presented in figure 77b, in which a large dispersion of the results is apparent (shaded zones). The average values of the initial elastic modulus ranged from 600 MPa, for specimens with an orientation of 45°, up to 850 MPa, for specimens orientated in the longitudinal direction of the fish, 0°. Specimens with a 90° orientation yielded intermediate values. As for the tensile strength, the values obtained were; 30 MPa for 0° and 50 MPa for 90°, with intermediate values when the orientation was 45°.

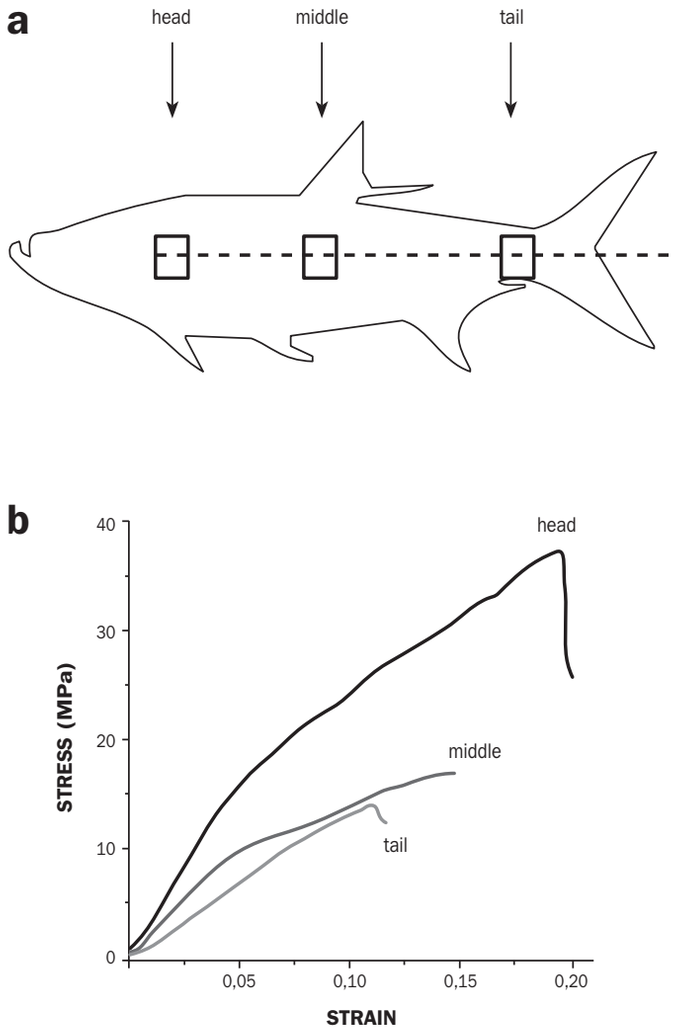

Fig. 78. *Tensile tests on scales of* Megalops atlanticus. *Influence of position. (Murcia et al. 2018).*

The *heterogeneity* of the scales varies according to their position, that is to say, whether they are in the head, middle of the body or tail, as is also apparent. For example, in the tests performed by Murcia *et al*. (2018) on shad scales (*Megalops atlanticus*), mentioned above, the heterogeneity can be appreciated. The locations from which the specimens were taken are identified in figure 78a and in this experiment the orientation was always the same, in the longitudinal direction of the fish (0°, following the previous notation). Engineering stress-strain curves which represent the average values of the results are shown in figure 78b. In summary, the values obtained, which confirm the heterogeneity of the material, are as follows: The initial elastic modulus diminishes from head to tail; from 300 MPa for scales taken from the head to 150 MPa for those from the tail. The tensile strength data have a large spread in values, the average strength of specimens taken from the head was greater than those of specimens taken from the other locations, reaching 35 MPa. The average value for specimens from the middle was about18 MPa, while that for those taken from the tail was about 15 MPa.

In order to substantiate these results, Murcia *et al*. (2018) proposed a semi-empirical model –valid only for elastic behaviour– in which account is taken of the contribution of the three regions of the *elasmoid* scales (figure 79a), discussed in the previous section; the hard external layer, surface layer (SL) and the internal and external layers of the elasmoidine layer, (IE) and (EE) respectively. (Later, a brief summary of how to develop this type of model will be provided, only for information purposes. The reader interested in the detail of the derivation should consult the cited reference).

The model assumes that each layer behaves as a Hookean spring and that the three layer act in parallel, so that the relationship between the applied force F, (in a direction parallel to the layers) and the displacement, Δ is given by

$$F = (\Delta/L)\ \Sigma\ (A_i\ E_i)$$

where E_i and A_i (i = 1, 2, 3) are the area and elastic modulus of each layer, so that

$$\sigma = F/A = (\Delta/L)\ \Sigma\ (A_i\ E_i\ /\ A)$$

in which $A = A_1 + A_2 + A_3$ is the total area.

Since the width of the three layers is the same, the ratios of the areas are the same as those of the thicknesses (t_1, t_2, t_3 and the total thickness t) which are known values (from microscopic observation of the cross-sections). The above expression can then be written as

$$\sigma = E\ \varepsilon = (t_1E_1/t + t_2E_2/t + t_3E_3/t)\ \varepsilon = (\alpha_1E_1 + \alpha_2E_2 + \alpha_3E_3)\ \varepsilon$$

where $\varepsilon = \Delta/L$ is the total strain. Approximately, α_1 = 0.12, α_2 = 0.30 and α_3 = 0.58. It then remains to evaluate E_1, E_2, and E_3.

The elastic modulus of the hard layer, E_1, is calculated by discretising the layer in to six slices, as shown in figure 79c, bearing in mind that the percentage of mineralisation of the layer varies from70% to 17%, as shown in figure 79b. The average value of each slice is calculated from values of the moduli of the matrix and collagen fibres, using data from the literature, and employing Nielsen and Chen's (1968) model for composite materials with short, randomly distributed, fibres.

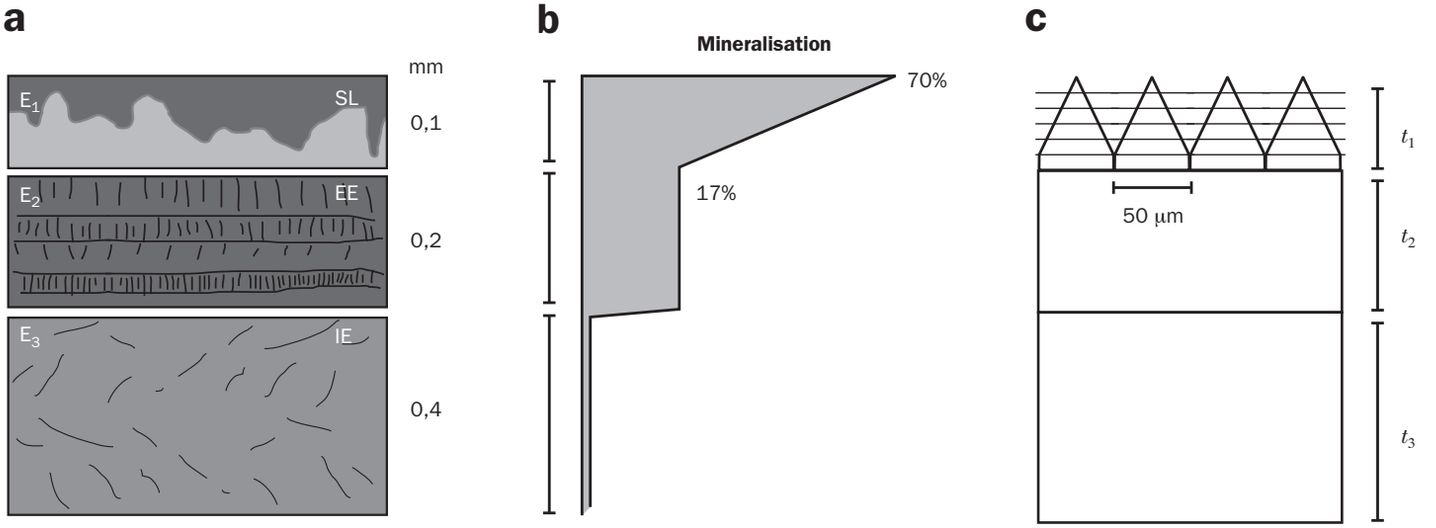

Fig. 79. *a) Cross-section of a carp scale. b) Distribution of the mineralisation across the three layers. c) Scheme used for the calculation. Area A_i of each layer is the product of its thickness t_i i and the width of each scale (in the direction perpendicular to the plane of the drawing)*

Calculation of the elastic modulus of the external elasmoidine layer, E_2, is more complicated, because this region has a laminar structure, with the sheets helically stacked. The sheets are formed of mineralised collagen fibres. Several, quite sophisticated, models were suggested for the calculation of the elastic modulus of these structures, but the authors **(**Nielsen and Chen**)** proposed an average value, given by

$$E_2 = \Sigma\ (t_i / t_T)\ E(\theta_i)$$

where t_i is, now, the thickness of each lamina, t_T the thickness of the layer, and θ_i the angle the two sheets form between each other. $E(\theta_i)$ is calculated using the above cited Nielsen and Chen model.

Finally, since the internal elasmoidine layer is hardly mineralised (figure 79) it is assumed that the elastic modulus, E_3, will be of the order of that of hydrated collagen fibres, at about 0.15 GPa.

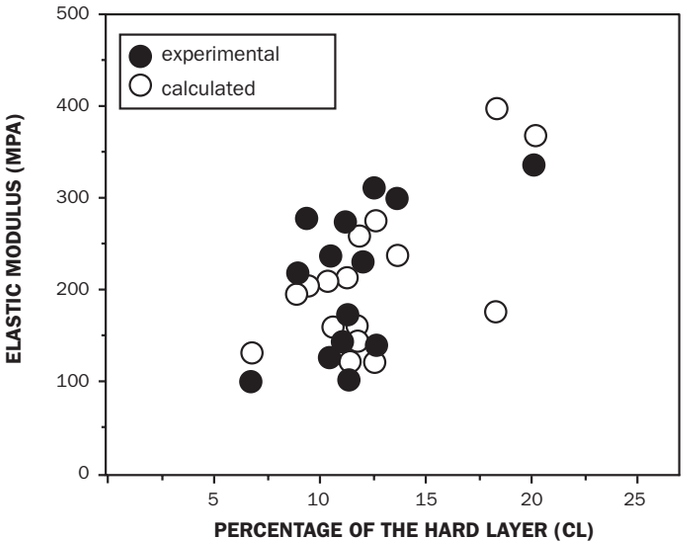

Fig. 80. *Elastic modulus values as a function of the percentage of the hard layer (CL). Comparison between experimental and calculated results.*

Experimental values of the initial elastic modulus are compared in figure 80 to those calculated from this model. The average error between the predictions and experiment is about 7%, a reasonable value bearing in mind the nature of this type of material. From the results obtained it can be seen that the elastic modulus depends greatly upon the contribution of the hard layer, CL, which is preponderant in the head region of the fish. The predictions of this model are largely based upon the mineralisation of its components, the model could be improved if account were taken of the interactions between the collagen fibres in the elasmoidine regions, EE and IE. Anyway, the models put into relief the various roles –percentage and distribution– of some of the components which allow the design of better armours.

A further step in modelling is to resort to smaller levels; to model the collagen fibres, their distribution in the sheets, and the effectiveness of different forms of stacking. For such a proposition, numerical analysis is a very useful tool and, in particular, in models based on molecular dynamics.

Yang *et al*. (2018) have used these techniques in order to understand how the collagen fibres behave in tensile test on arapaima scales. The structure of the elasmoidine was modelled as a superposition of *bundles* of collagen fibres. Each bundle was composed of three superposed *laminas* which form angles of 42°, 78°, and 18° between each other. And each lamina was composed of parallel collagen fibres. Each fibre was, in turn, modelled like a string of rosary beads in which the beads are connected by springs, (here, lower levels were not considered, and the fact that the collagen fibres were formed of fibrils was ignored). This model allowed an investigation of how the angle between two sheets, the interaction between fibres, and the stiffness of the fibres, influence the mechanical response of the scales.

In the tensile tests, calculation of the stress as a function of the strain was performed assuming a hyper-elastic material, with a potential function which took into account the interaction between two beads, between three beads, and that between fibres. Not all of the parameters needed for this calculation were known, so it was necessary to pick the unknown parameters which gave the best fit to the experimental results, such as in the case of the interaction energy between the fibres (this value can vary between 0.05 and 3.0 J/m^2, and the best fit in this case was about 1.0 J/m^2). If it is assumed that failure of the scale is initiated with the first separation of the collagen sheets, the calculated value was about 26.4 MPa, which fits quite well with the experimental data, between 30 and 40 MPa. Once again, the model can be refined to provide a further step toward evaluation of the contribution of each element, and of the microstructure in detail, which would permit a better understanding of the mechanical behaviour of this very hierarchical material.

Rupture by tearing tests

The greatest threat met by a fish is the teeth of an adversary, an attack can cause tearing of the scales. From this perspective, in an analysis of the tear resistance of the scales it is useful to know how the distinct components of this hierarchical structure stand up in against the cited threat.

S. Murca *et al*. (2015) investigated the tear resistance of carp (*Cyprinus carpio*) scales and demonstrated that the specific tear strength R (see section 2.3.3) depends, to a large extent, on the mineralised external layer and the external elasmoidine layer, such that the tear resistance increases with the thicknesses of these layers.

In these tests the *anisotropy* and heterogeneity of the scales were taken into account, depending upon their position. Figure 81a outlines how the anisotropy was studied; by testing specimens prepared with different orientations; 0º, 45º, and 90º. The *heterogeneity* was also examined by testing scales near the head, from the middle region of the body and the tail, as indicated in figure 81b.

The average specific tearing resistance, R, was determined following the process outlined in section 2.3.3. The dimensions of the specimens are shown in figure 81c, together with a sketch of the test configuration.

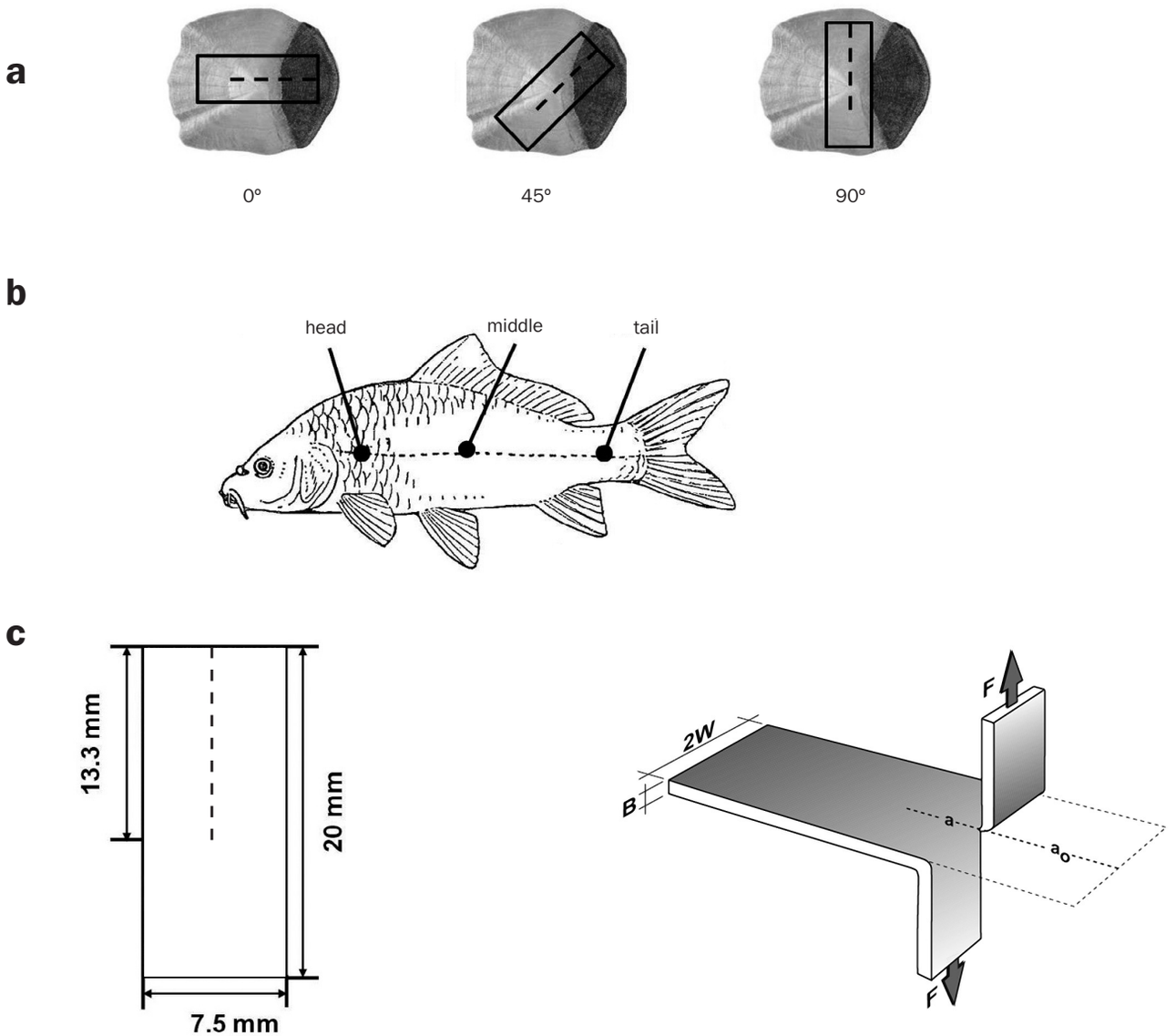

Fig. 81. T*ear test on the scales of* Cyprinus carpio. *a) Position of the samples to investigate the anisotropy. b) Position of the samples to investigate the heterogeneity. c) Dimensions of the samples and schematic arrangement of the test.*

Since the scales have a nonlinear behaviour in the tensile tests, it was assumed that they could be treated as an *elastomeric* material, and that equation (93) could be used to calculate R, that is to say

$$R = \frac{2F_R\lambda_R}{B} - 2W\mathcal{W}_R$$

Where F, B and W are defined in figure 81c, $\lambda = l/l_0 = 1 + \varepsilon$, and ε is the engineering strain remote from the tear, and $\mathcal{W}$ is the elastic strain energy density referred to the undeformed volume of configuration, also far from the tear.

The cited authors argue that, in this case, the strain, ε, far from the tear is negligible compared to 1, and that the elastic strain energy density $\mathcal{W}$ is also small. Consequently, the previous expression can be approximated by

$$R = 2\,F_{\mathrm{R}}/B$$

The authors performed tear tests at ambient temperature (21ºC) and at low temperatures; 0 ºC, - 30 ºC and - 150 ºC. The results of an experiment at ambient temperature, on a scale near the head and with an orientation of 0º, are presented in figure 82.

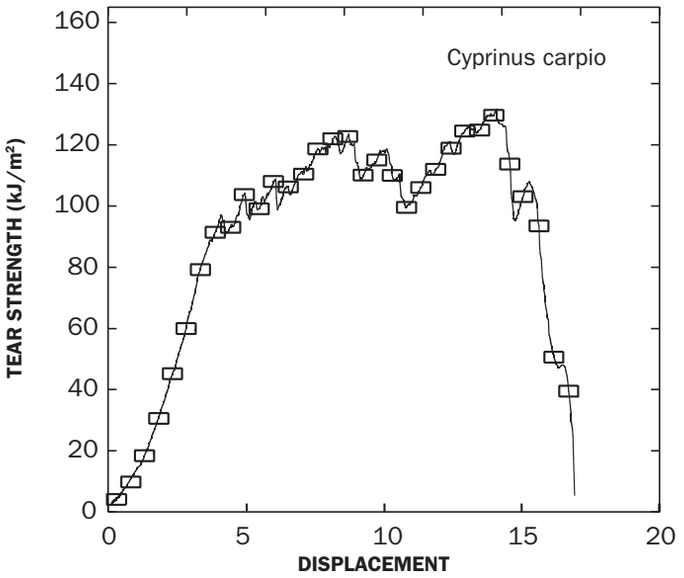

Fig. 82. *Tear test on scales from* Cyprinus carpio, *at ambient temperature, with a scale taken from a region near the head, and an orientation of 0º.*

The scales near the head showed a marked *anisotropy* in the tests at ambient temperature. The average values were: 120 kJ/m^2 with scales orientated at 0º, 100 kJ/m^2 for a 45º orientation, and 90 kJ/m^2 for those at 90º. For scales taken from the middle region of the body and tail anisotropy was not so apparent and, in both cases, the average value, for the different orientations, was about 90 kJ/m^2.

Heterogeneity was also observed in tests performed on scales taken from different locations on the body. At ambient temperature, scales located near the head gave higher values than those from the middle and tail, these last two gave similar values.

The authors of this study concluded that the specific tear resistance depended primarily on the thickness of the mineralised external layer, and the number of laminas in the external elasmoidine layer. These two microstructural features are functions of the anatomical position of the scales and are, possibly, related to the functional needs of the fish.

Puncture tests

The principal function of scales is in the mechanical protection against aggressors, particularly from the teeth of predators. The tensile strength and tear resistance, although important properties, are not sufficient for the evaluation of the resistance to sharp puncture. Indentation tests (see section 2.2.3 in *Biological Materials*–three-dimensional) provides more information on the ability of scales to resist the action of pointed objects, capable of perforating the skin and damaging the softer, weaker internal tissue.

D. Zhu *et al*. (2012, 2013) studied the resistance of the elasmoid scales of the Atlantic sea bass (*Morone saxatilis*), whose characteristics were outlined above, in section 3.4.2. For this, they first investigated the behaviour of a single scale under shear punching and then, the more representative, case of three overlapping scales.

The penetration resistance of a scale was investigated using a device –shown in simplified form in figure 83a– which was designed to simulate the tooth of a predator. The indenter terminates in a rounded point of radius 25 μm. The scale rests on a silicon substrate which is meant to simulate the skin protected by the scale. Typical output data from these tests is the force as a function of the displacement of the indenter, which are shown in figure 83b. In all cases, a small step was detected, at about 2 N, and the maximum values of the force lay between 3.0 and 3.5 N.

Theses authors distinguished three stages in the tests (figure 83b): The first, associated with the initial linear part of the force-displacement curve, corresponds to the bending of the scale. At the end of this stage –at a load of about 2 N– cracking of the hard layer of the scale, and sliding and separation of the most mineralised layers of the elasmoidine, are initiated. Finally, the indenter perforates the scale and causes a sudden drop in the load, giving rise to the third stage.

In a more detailed analysis of this process, D. Zhu *et al*. 2012 showed that during sharp puncture, the scale –in the second stage– goes through two phases: First, the hard external layer cracks, following the pattern shown in figure 83c, and creates four plates of hard material. In a second phase, the deformation of these plates is impeded by the fibrous elasmoidine layer which acts as like a resisting membrane due to the elasticity of the collagen fibres. Thanks to these two processes, the strength of the scale increases about 50% rising from 2 to 3 N. The combination of the hard layer, which can crack in a controlled manner, and the soft elastic substrate, results in an effective design to defend it against puncture.

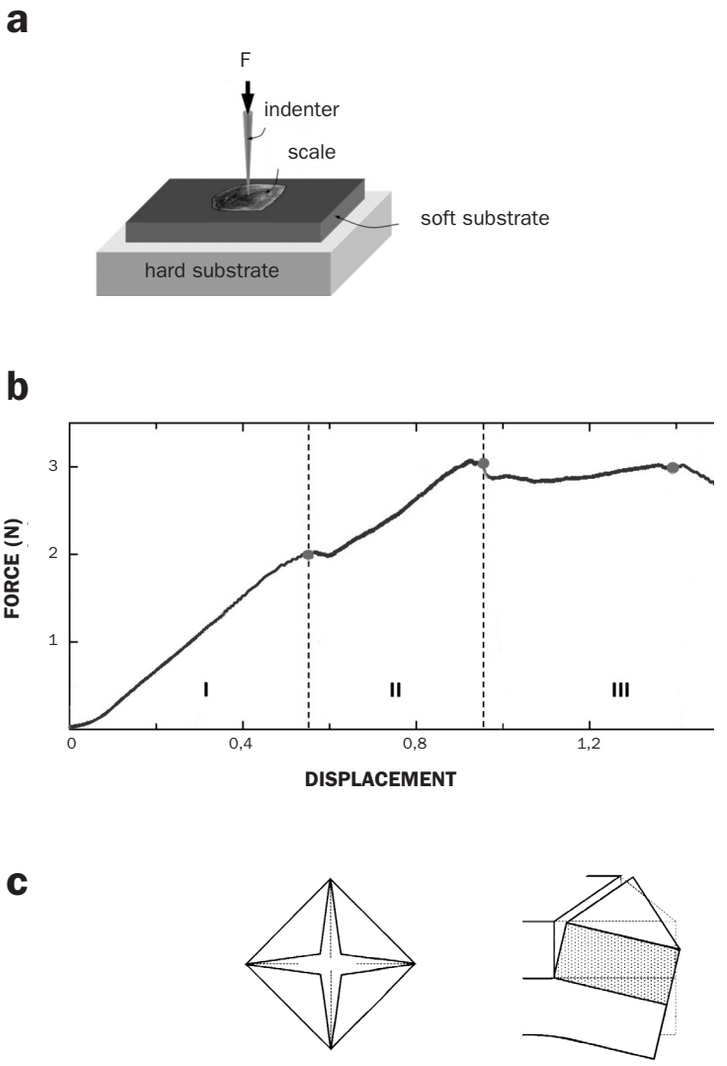

Fig. 83. *a) Schematic representation of a device for the puncture test.*
b) Distinct stages in the test.
c) Schematic representation of the rupture of the hard layer.

In reality, a sharp puncture attack is not resisted by just one scale, the scales overlap and share the load among themselves. D. Zhu *et al*. (2013) investigated this phenomenon in striped bass, in which the scales are arranged in overlapping rows so that each scale overlaps with another six –three on the front and another three on the back– in this arrangement, every point on the surface is covered with three scales. For these test, the authors used a device similar to that described above, and studied in influence of the stiffness of the substrate, the number of scales, the friction between them, and the way they overlap.

The stiffness of the *overlap* influences the results. Three substrates were tried; a rigid one, an elastomer, and the other simulating the natural substrate of the fish. The force-displacement curves had similar values for the maximum force, but very different values of the displacement under the maximum load; small values for the rigid substrate, large values for the elastomeric and even larger for the natural.

The experiments on different superposed scales showed, as might be expected, that the puncture force increased with the number of scales. The most striking result was that the perforation mechanism was similar to that observed in experiments on a single scale, which was replicated in passing from one scale to another.

The influence of friction between the scales was investigated by means of a puncture experiment with two scales and numerical simulation of two extreme situations; two scales bonded together, and two in contact, without friction between them. The experimental results showed that the influence of friction was, at least in this test, negligible.

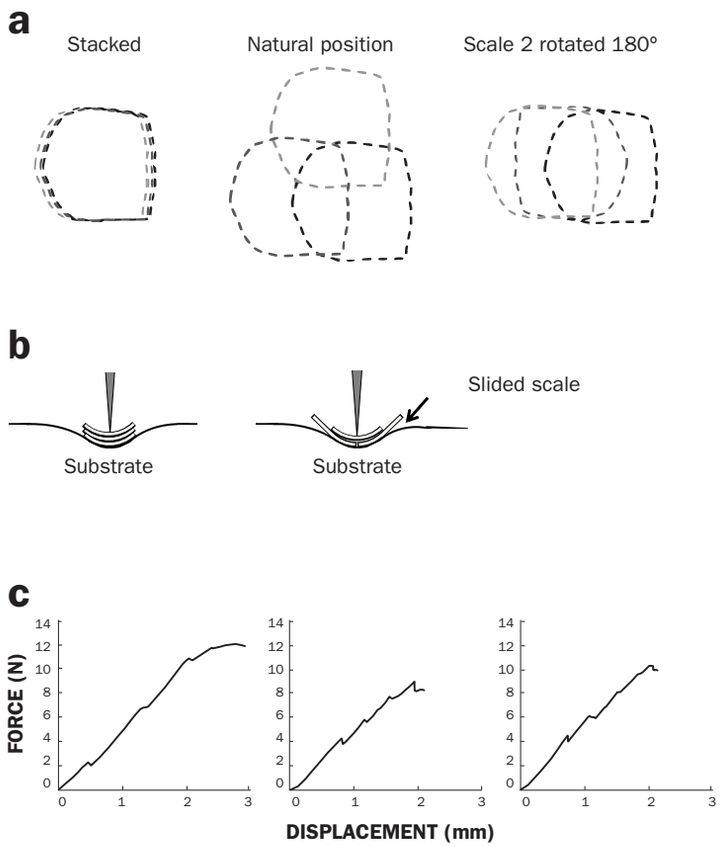

Fig. 84. *a) Different arrangements of the three overlapping scales.*
b) Different behaviours of the scales and substrate.
c) Force-displacement curves,

Finally, the effect of the arrangement of the overlap between the scales was investigated using the three configurations shown in figure 84a; in one of these the three scales are stacked on top of each other, in the second they are in the natural position and in the third, the second of the three scale has been rotated through 180° (as shown in the figure). The force displacement curves indicated that the initial stiffness is practically the same in all three cases, and that maximum load was greater when the scales were stacked on top of each other and somewhat less in the other two cases (figure 84c). The most interesting result lay in the difference between the deformation mechanisms of the scales and substrate, illustrated, in a simplified form, in figure 84b. When the scales overlapped in the natural position, they slid over each other, the area of contact with the substrate increased, and the load was spread over a larger area and the damage decreased.

Summarising; the stiffness of the substrate does not affect the value of the puncture force for the range of stiffnesses studied, which were representative of the stiffnesses of fish substrate and of materials used in the artificial armours inspired by biomimetics. Stacking three scale tripled the protection against puncture, compared to a single scale. Possible friction between the scales did not appear to increase the puncture resistance. Finally, the experiments demonstrated that, even though the scales could resist puncture, sliding between the scales and soft substrate redistributed the stresses caused by the indenter over a larger volume, and soothed the damage.

Similar studies have been carried out by other scientists. M Meyers and co-workers (W Yang *et al*. 2014) performed detailed investigations into the strength of the elasmoid scales of the *Arapaima gigas* using indentation tests, X-ray diffraction analysis, and molecular dynamics calculations, and achieved similar results to those already discussed: When a predator's teeth bite into the scales, the hard external layer breaks first and the soft elasmoidine layer is left exposed. If the teeth continue penetrating, the mineralised collagen fibres dispersed in sheets with different orientations must be separated, reorienting the collagen fibres and stressing them. All this consumes energy, facilitates crack branching and, ultimately, the damage is less.

P Y Chen *et al*. (2012) also studied the behaviour of arapaima scales under the action of piranha and shark teeth, using nanoindentation techniques, and obtained similar results.

3.4.3. Biomimetics: Flexible artificial armour

Elasmoid scales are a source of inspiration for the design of armours; the *hardness* of the scales protecting the fish against the teeth of its predators, and being *imbricated* and anchored to a soft substrate, to provide sufficient flexibility to the skin so as not to impede movement.

A very simple design, based upon these two concepts, is to fabricate armour which protects the front against penetration while being flexible has been suggested by several authors (S Rudykh *et al*. 2015). The architecture of the armour shown, schematically, in figure 85a consists of two layers bonded together: The upper layer is formed of thin hard acrylic polymer sheets (0.5 mm thick) and the lower layer is a soft elastomeric material.pa inferior por un material blando, un elastómero.

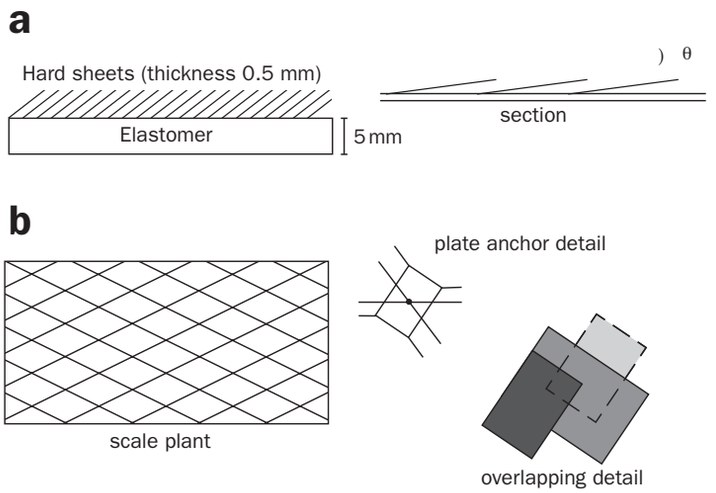

Fig. 85. *a) Schematic representation of the armour proposed by S. Rudykh et al. (2015).*
b) Schematic representation of the armour proposed by N. Funk et al. (2015).

The resistance to penetration was measured by three-point flexure tests. The resistive capacity can be controlled by altering the percentage of the hard layer, and the flexibility by means of the angle θ, which the sheets form with the soft layer (figure 85a). Increasing the resistive capacity reduces the flexibility, and increasing the inclination of the sheets (between 10 ° and 45°) increases the flexibility. With a judicious combination if the percentage of the hard layer and the angle θ, it is possible to optimise the design of the armour. The authors suggest that the resistance can be increased by a factor of 40, at the cost of reducing the flexibility by a factor of 5. Playing with these two factors, an armour can be designed with *locally* different properties; providing more resistance to the more delicate zones and greater flexibility where needed.

Another simple design, taking into account the hierarchical structures that nature has to offer, is also based upon covering a soft substrate with hard scales. In this case the soft base is a mesh of flexible polypropylene fibres (rather than an elastomer) and the scales are, now, thin acetate sheets (N Funk *et al*. 2015).

The mesh, primarily, provides a flexible support to the *scales* –the average value of its elastic modulus is seven orders of magnitude less than that of the scales– and, moreover, it serves to anchor the plates at the nodes (figure 85b). The anchor is made such that the plates can overlap and rotate a little, very much like the way elasmoid scales behave. The cited authors performed several tests –on what they called *synthetic skin*– tensile, flexure and puncture, with specimens measuring 180 mm by 150 mm, and which contained 690 *scales*, with satisfactory results. The overlapping of the scales (between two and three) allowed a better redistribution of the forces and a reduction in the damage produced by the punching. They also developed a simple model of the architecture –mesh and plates– which was able to reproduce their experiments. The advantage of a model which replicates the experimental results, is that it allows modification of the parameters (shape and properties of the mesh, and dimensions and properties of the plates) in order to optimise the performance of the armour; perhaps by using stronger fibres to resist rupture of the mesh, modifying the shape of the scales or increasing their flexural stiffness.

Based on these two ideas –hard overlapping plate and a soft substrate– several examples of light, flexible armour have been designed. Biomimetics has attempted to provide a further step towards integrating both properties in the same material, by means of the concept of *flexible ceramics* (M A Meyers *et al*. 2012). The concept, was inspired by the elasmoid scales of the *Arapaima gigas*, whose corrugations on the hard external layer play an important structural role. If the thickness of this layer were homogeneous (always the same) the flexibility of the scale would be more restricted and more likely to crack on bending because the material is brittle. However, if it were corrugated it becomes more flexible, as indicated in figure 85c. In the referenced article, the authors confirm this advantage by means of an elastic calculation. Consequently, cracking is localised at the bottom of the valleys of the corrugations and is less serious. S Rudykh et al. (2015) have demonstrated that it is possible to fabricate very flexible armours with these concepts.

4 CHAPTER References

Agianniotis A, Rachev A, Stergiopulos N. (2012)
Active Axial Stress in Mouse Aorta
J of Biomechanics **45** 1924-1927

Alexander R. (1962)
Visco-Elastic Properties of the Body-Wall of Sea Anemones
J Exp Biol **39**, 373-386

Armentano R L, Levenson, J G, Barra J et al. (1991)
Assessment of elastin and collagen contribution to aortic elasticity in conscious dogs
Am. J. Physiol., **260** H1870–H1877

Atkins A G, Mai Y W (1985)
Elastic and Plastic Fracture
John Wiley & Sons

Bäck, M, Gasser T C, Michel J B, Caligiuri G (2013)
Review. Biomechanical factors in the biology of aortic wall and aortic valve diseases. Cardiovascular Research **99** 232–241

Billiar KL, Sacks MS. (2000)
Biaxial mechanical properties of the natural and glutaraldehyde treated aortic valve cusp–Part II: A Structural Constitutive Models.
J Biomech Eng **122** 327–335

Bishop MC, Coulston CN. (1989)
Roman Military Equipment
Shire Publications

Bishop J E, Lindahl G (1999)
Regulation of cardiovascular collagen synthesis by mechanical load
Cardiovasc. Res., **42** 27–44

Bouligand Y (1972)
Twisted fibrous arrangements in biological materials and cholesteric mesophases
Tissue & Cell **4** (2) 189-217

Burton AC (1954)
Relation of structure to function of the tissues of the wall of blood vessels.
Physiol Rev **34** 619-642

Capaldi F M. (2012)
Continuum Mechanics
Cambridge U.P.

Carrera A, García Páez, et al. (2001)
Pretensado y comportamiento mecánico del pericardio de ternera utilizado en la construcción de bioprótesis cardíacas.
Biomecánica **9**, 1, 3–11

Chapman G. (1953)
Studies on the Mesogloea of Coelenterates: II. Physical Properties
J Exp Biol **30**, 440-451

Chen P et al. (2012)
Predation versus protection: Fish teeth and scales evaluated by nanoidentation
J. Mater. Res. **27** 100-112

Chen, X L,Varner S E et al. (2003)
Laminar flow induction of antioxidant response element-mediated genes in endothelial cells. a novel anti-inflammatory mechanism.
J. Bio. Chem. **278** 703–711

Chitapalli R K et al. (2014)
Fabrication, testing and modeling of a new flexible armor inspired from natural fish scales and osteoderms
Bioinspir. Biomim. **9** 036005

Choi H S, Vito R P, (1990)
Two dimensional stress-strain relationship for canine pericardium.
J. Biomech. Eng. **112** 153–159

Choung C J, Fung Y C. (1986)
Residual stress in arteries
In *Frontiers in Biomechanics.* G. W. Schmid-Schoenbein, et al. (Eds.), (pp. 117–129).
New York: Springer

Claes E. (2010)
Estudio mecánico de las arterias coronarias humanas y sus sustitutos vasculares
Tesis Doctoral, Universidad Politécnica de Madrid

Claramunt R, García Páez J M, Alvarez L, Ros A, Casado M C. (2012)
Fatigue behaviour of young ostrich pericardium
Material Sciences and Engineering C, **32** 6 1415-1420

Claramunt R, García Páez J M, Alvarez L, Spottorno J, Ros A, Casado M C. (2011)
Short-term fatigue testing can predict medium-term pericardium behaviour
JMBBM

Courtman DW, Pereira CA, Kashef V, McComb D, Lee JM, Wilson GJ. (1994).
Development of a pericardial acellular matrix biomaterial: biochemical and mechanical effects of cell extraction.
J Biomed Mater Res **28** (6) 655–666

Clark J M, Glagov S. (1985)
Transmural organization of the arterial media: The lamellar unit revisited
Arterioscler. Thromb. Vasc. Biol. **5** 19-34.

Cubo N, Garcia M, Del Cañizo J F, Velasco D, Jorcano J L. (2016)
3D bioprinting of functional human skin: production and in vivo analysis.
Biofabrication. Dec 5;9(1):015006.

Cugno A M et al. (2012)
On the mechanical behaviour of scales from *Cyprinus carpio*
JMBBM **7** 17-29

Dannenberg H. (1961)
Measurement of adhesión by a blister method
J Appl Polym Sci **5**, 125-134

Demiray H. (1981)
Large deformation analysis of some soft biological tissues
J. Biomech. Eng., **103**, 73–78.

Elices M. (1998)
Mecánica de la Fractura
ETSICCP, Universidad Politécnica de Madrid

Escofflier C et al. (1989)
Age-related mechanical properties of human skin: an in vivo study
J Invest Dermatol **93**, 353-357

Fronek K, Schmid-Schoenbein G, Fung Y C. (1976)
A noncontact method for three-dimensional analysis of vascular elasticity in vivo and in vitro
J Appl Physiol **40**, 634-637

Fung Y C. (1993)
Biomechanics Mechanical Properties of Living Tissues, 2nd Ed.
Springer

Fung Y C. (1975)
Stress, deformation, and atelectasis of the lung
Circulation Res **37**, 481-496

Fung Y C, Lin S. (1991)
Changes of zero-stress state of rat pulmonary arteries in hypoxic hypertension
J Appl Physiol **70** 2455-2470

Fung Y C, Liu S Q. (1989)
Change of residual strains in arteries due to hypertrophy caused by aortic constriction
Circulation Res. **65** 1340-1349.

Fung Y C, Fronek K, Patitucci P. (1979)
Pseudoelasticity of arteries and the choice of its mathematical expression
Am J Physiol **237** H620-H631

Fung Y C, Tong P, Palitucci P. (1978)
Stress and strain in the lung
J Eng Mech Div Am Soc Civil Eng **104** 201-224

Funk N et al. (2015)
Bioinspired Fabrication and Characterization of a Synthetic Fish Skin for the Protection of Soft Materials.
Appl. Mater. Interfaces **7** 5972-5983

García-Herrera C. (2008)
Comportamiento Mecánico de la Aorta Ascendente: Caracterización Experimental y Simulación Numérica
Tesis Doctoral, Universidad Politécnica de Madrid

García-Páez J M, Carrera A, Herrero J, et al. (2006)
Determination of the force necessary for the propagation of tears in ostrich and calf pericardium.
J Biomedical Materials Research: Part B Applied Biomaterials. **79** (2) 229-235

García-Páez J M, Carrera A, Herrero J et al. (2004)
Resistance to tearing of calf and ostrich pericardium: influence of the type of suture material and the direction of the suture line
J Biomedical Materials Research: Part B Applied Biomaterials. **69** (2) 125-34

García-Páez J M, Claramunt R, Herrero J et al. (2009)
Energy consumption as a predictor test of the durability of a biological tissue employed in cardiac bioprosthesis
J Biomedical Materials Research Part A. **89A** 336–344

García-Páez J M, Herrero J, Carrera A et al. (2001)
Ostrich pericardium, a biomaterial for the construction of valve leaflets for cardiac bioprostheses: mechanical behaviour, selection and interaction with suture materials.
Biomaterials **22** 20 2731–2740

García-Páez J M, Jorge E, Claramunt R et al. (2010)
Propagation of tears in pericardium from young bulls: influence of the suture.
Artificial Organs **34**, (3) 65-71

García-Paéz J M, Herrero J, Carrera et al. (2000).
The influence of chemical treatment and suture on the elastic behavior of calf pericardium utilized in the construction of cardiac bioprostheses.
J Mater Sci Mater Med. **11** (5) 273–277

Gasser T C, Gallinetti S, Xing X, Forsell C, Swedenborg J, Roy J. (2012)
Spatial orientation of collagen fibers in the Abdominal Aortic Aneurysm wall and its relation to wall mechanics
Acta Biomaterialia, **83** 091–3103, 201

Gil-Duran S, Arola D, Ossa E A. (2016)
Effect of chemical composition and microstructure on the mechanical behaviour of fish scales from *Megalops atlanticus*.
JMBBM **56** 134-145

Gosline J M. (1971)
Connective Tissue Mechanics of *Metridium Senile* : I. Structural and Compositional Aspects
J Exp Biol **55**, 763-774

Gosline J M. (1971)
Connective Tissue Mechanics of *Metridium Senile* : II. Visco-Elastic Properties and Macromolecular Model
J Exp Biol **55**, 775-795

Grytsan A, Eriksson T, Watton PN, Gasser T C. (2017)
Growth Description for Vessel Wall Adaptation: A Thick-Walled Mixture Model of Abdominal Aortic Aneurysm Evolution
doi: 10.3390/ma10090994.

Guinea G V, Atienza J M Elices M, Aragoncillo P, Hayashi K. (2005)
Thermomechanical behaviour of human carotid arteries in the passive state.
AJP- Heart and Circulatory Physiology **288**, 2940-2945

Harding C. (2004)
The stratum corneum: Structure and function in health and disease
Dermatologic Therapy **17**, 6-15

Holzapfel G A. (2006)
Nonlinear Solid Mechanics
John Wiley & Sons.

Holzapfel G A, Gasser T C (2001)
A viscoelastic model for fiber-reinforced composites at finite strains: Continuum basis, computational aspects and applications
Computer Methods in Applied Mechanics and Engineering. **190**, 4379–4403.

Hoppmann W H, Wan L. (1970)
Large deformation of elastic tubes
J Biomech **3**, 593-600

Horný L, Adamek T, Kulvajtova M. (2014)
Analysis of axial prestretch in the abdominal aorta with reference to post mortem interval and degree of atherosclerosis.
JMBBM. **33**:93-98.

Horný L, Gultová E, Chlup H et al. (2010)
Mullins Effect in Aorta and Limiting Extensibility Evolution
Bulletin of Applied Mechanics**, 6** 21 1-5

Humphrey J D, Yin F C P. (1988)
Biaxial mechanical behavior of excised epicardium.
J. Biomech. Eng. **110**, 349-351

Humphrey J D. (2002)
Cardiovascular Solid Mechanics: Cells, Tissues, and Organs, Springer.

Ikoma T et al. (2003)
Microstructure, mechanical, and biomimetic properties of fish scale from *Pagrus major*.
J. Structural Biology **142** 327-333

Kita M, Negi A, Kawano S. Honda Y, Maegawa S. (1990)
Measurement of Retinal Adhesive Force in the in Vivo Rabbit Eye
Investigative Opthalmology and Visual Science, **31**, 4, 624-628

Kwan M K, Woo S LY. (1989)
A structural model to describe the nonlinear stress-strain behavior for parallel-fibered collagenous tissues
J Biomech Eng **111**, 361-363

Landau L D, Lifshitz E M. (1986)
Theory of Elasticity (3ª Ed.)
Pergamon Press

Lanir Y. (1979)
A structural theory for the homogeneous biaxial stres strain relationships in flat collagenoust issues
J Biomech **12**, 423-436

Lanir Y, Fung Y C. (1974)
Two-dimensional mechanical properties of rabbit skin. I. Experimental system
J Biomech **7** 1 29-34

Lanir Y, Fung Y C. (1974)
Two-dimensional mechanical properties of rabbit skin. II. Experimental results
J Biomech **7** 2 171-182

Lanne T, Sonesson B, Bergqvist D, Bengtsson H, Gustafsson D (1992)
Diameter and compliance in the male human abdominal aorta: influence of age and aortic aneurysm.
Eur J Vasc Surg **6** 178-184.

Lindley P. B. (1972)
Energy for crack growth in model rubber components
J. Strain Analysis **7**, 2, 132-140

Lyman M. (2019)
The remarkable life of the skin
Bantom Press

McDonald D A (1974)
Blood Flow in Arteries
Edward Arnold, London

Martin C, Sun W. (2014)
Modeling of long-term fatigue damage of soft tissue with stress softening and permanent set effects
Biomechanics and modeling in mechanobiology. **12** 4 645–655

Matsumoto T, Hayashi K (1994)
Mechanical and dimensional adaptation of rat aorta to hypertension
J. Biomech Eng **116** 278-283.

Matsumoto T, Hayashi K (1996)
Stress and strain distribution in hypertensive and normotensive rat aorta considering residual strain.
J Biomech Eng **118** 62-73

Mendoza-Novelo B, Avila E E, Cauich-Rodríguez J V, Guinea G V, et al. (2011).
Decellularization of pericardial tissue and its impact on tensile viscoelasticity and glycosaminoglycan content.
Acta Biomater, **7**, 3 1241-1248

Mendoza-Novelo B, Cauich-Rodriguez J V. (2009).
The effect of surfactants, crosslinking agents and L-cysteine on the stabilization and mechanical properties of bovine pericardium.
J Appl Biomater Biomech. **7** 2 123–131

Mendoza-Novelo B, Alvarado-Castro D I, Guinea G V et al. (2013)
Stability and mechanical evaluation of bovine pericardium cross-linked with polyurethane prepolymer in aqueous medium.
Materials Science and Engineering C33 2392-2398.;
DOI:10.1016/j.msec.2013.02.001

Meyers MA et al. (2012)
Battle in the Amazon: Arapaima versus Piranha
Adv. Eng. Mater. **14** 279-288

Mirnajafi, Raymer J, Scott M J, Sacks M S. (2005)
The effects of collagen fiber orientation on the flexural properties of pericardial heterograft biomaterials
Biomaterials, **26**, 7 795–804

Murcia S et al. (2015)
Temperature effects on the fracture resistance of scales from *Cyprinus carpio*
Acta Biomaterialia **14** 154-163

Murcia S et al. (2017)
The natural armors of fish: A comparison of the lamination pattern and structure scales
JMBBM **73** 17-27

Murcia S et al. (2018)
Contributions of the layer topology and mineral content to the elastic modulus and strength of fish scales.
JMBBM **78** 56-64

Nawroth J et al. (2012)
A tissue-engineered jellyfish with biomimetic propulsión
Nature Biotechnology **30** 8 792-797

Nielsen L, Chen P (1968)
Young´s modulus of composites filled with randomly oriented fibers
J. Mater. **3** 352-358

O'Connell M K, Murthy S, Phan S et al. (2008)
The three-dimensional micro- and nanostructure of the aortic medial lamellar unit measured using 3d confocal and electron microscopy imaging
Matrix Biol. **27** 171–181

Pashneh-Tala et al. (2016)
The Tissue-Engineered Vascular Graft–Past, Present, and Future
Tissue Engineering B, **22** 1, 68-100

Purslow P P. (1983)
Measurement of the fracture toughness of extensible connective tissues
J Materials Sci **18**, 3591-3598

Polzer S, Bursa J, Gasser T C, Staffa R, Vlachovsky R. (2013)
Numerical implementation to predict residual strains from the homogeneous stress hypothesis with application to abdominal aortic aneurysms
Annals of Biomedical Engineering, **41** 1516–1527.

Qu Q et al. (2015)
New genomic and fossil data illuminate the origin of enamel
Nature DOI 10:1030/nature 15259

Rachev A, Stergiopulos N, Meister J J. (1998)
A model for geometric and mechanical adaptation of arteries to sustained hypertension. ASME J Biomech Eng **120** 9-17

Raghavan M L, Vorp D A (2000)
Toward a biomechanical tool to evaluate rupture potential of abdominal aortic aneurysm: Identification of a finite strain constitutive model and evaluation of its applicability
Journal of Biomechanics **33** 475–482.

Rémi E, Khelil N, Di Centa I, et al. (2011)
Pericardial Processing: Challenges, Outcomes and Future Prospects; Chapter 22,
Biomaterials Science and Engineering. R. Pignatello, ed. DOI: 10.5772/24949

Riveros F, Chandra S, Finol E A, Gasser T C, Rodriguez J F. (2013)
A pull-back algorithm to determine the unloaded vascular geometry in anisotropic hyperelastic AAA passive mechanics
Annals of Biomedical Engineering, **41** 694–708

Rivlin R.S., Thomas A.D. (1953)
Rupture of rubber: I. Characteristic energy for tearing
J Polym Sci **10**, 291-318

Rojo F J, García Páez J M, Guinea G V, et al. (2010)
Optimal selection of biological tissue using the energy dissipated in the first loading cycle.
J. of biomedical materials. Part B, Applied biomaterials, **95B**, 2, 414-20

Roach M R, Burton A C (1957)
The reason for the shape of the distensibility curves of arteries
Can J Biochem Physiol **35** 8 681-690

Roy C S. (1881)
The elastic properties of the arterial wall
J. Physiol. **3** 125–159

Rudykh S, Ortiz C, Boyce M C. (2015)
Flexibility and protection by design: imbricated hybrid microstructures of bio-inspired armor
Soft Matter **11** 2547-2554

Sacks M S, Smith D B, Hiester ED. (1997)
A Small Angle Light Scattering Device for Planar Connective Tissue Microstructural Analysis
Annals of Biomedical Engineering, **25** 678-589

Sacks M S, Chuong C J. (1998)
Orthotropic Mechanical Properties of Chemically Treated Bovine Pericardium
Annals of Biomedical Engineering. **26** 892–902

Sacks M S. (1999)
A method for planar biaxial mechanical testing that includes in-plane shear
J Biomech Eng **121**, 551-555

Sacks M S, Sun W. (2003)
Multiaxial mechanical behavior of biological materials
Annu Rev Biomed Eng **5**, 251-284

Sellaro T L, Hildebrand D, Lu Q J. et al. (2007)
Effects of collagen fiber orientation on the response of biologically derived soft tissue biomaterials to cyclic loading.
Journal of Biomedical Materials Research Part A, **80A** 194–205

Shadwick R E, Russell A P, Lauff R F. (1992)
The structure and mechanical design of rhinocerus dermal armour
Phil Trans R Soc Lond B. **337** 419-428

Sherman V R et al. (2018)
A comparative study of piscine defense: The scales of *Arapaina gigas*, *Latimera chalumnae* and *Atractosteus spatula*.
JMBBM **73** 1-16

Shoemaker P A et al. (1986)
A constitutive model for two-dimensional soft tissues and its application to experimental data
J Biomech **19** 695-702

Sire J Y et al. (2009)
Origin and evolution of the integumentary skeleton in non-tetrapod vertebrates
J. Anat. **214** 409-440

Sokolis D P. (2007)
Passive mechanical properties and structure of the aorta: segmental analysis
Acta Physiol. , **190** 277–289

Sun W, Sacks M, Fulchiero G et al., (2004)
Response of heterograft heart valve biomaterials to moderate cyclic loading
Journal of Biomedical Materials Research Part A **69A**, 658–669

Tanaka T, Fung Y C. (1974)
Elastic and inelastic properties of the canine aorta and their variation along the aortic tree
J Biomechanics **7**, 357-370

Timoshenko S, Woinowsky-Krieger S. (1959)
Theory of plates and shells
McGraw-Hill

Tong P, Fung Y. (1976)
The stress-strain relationship for the skin
J Biomechanics **9**, 649-657

Tonge T K, Atlan L S, Voo L M, Nguyen T D. (2013a)
Full-field bulge test for planar anisotropic tissues: Part I – Experimental methods applied to human skin tissue
Acta Biomaterialia **9** 5913–5925

Tonge T K, Voo L M, Nguyen T D. (2013b)
Full-field bulge test for planar anisotropic tissues: Part II – A thin Shell method for determining material parameters and comparison of two distributed fiber modeling approaches
Acta Biomaterialia **9** 5926–5942

Tobaruela A. (2016)
Caracterización mecánica de materiales de base colágeno para aplicaciones cardiovasculares, Tesis Doctoral, Universidad Politécnica de Madrid

Tobaruela A, Elices M, Bourges J Y, Rojo F J, Atienza J M, Guinea G V. (2016)
Tear and decohesion of bovine pericardial tissue.
JMBBM 1–9

Trowbridge E A, Crofts C E, Lawford P, Black M M. (1989)
The mechanical properties of natural and chemically modified bovine pericardium for use with heart valve substitutes.
In *Material properties and stress analysis in biomechanics* Chapter 2. Manchester University Press

Trowbridge E A, Crofts C.E (1989)
The tearing strength of glutaraldehyde fixed bovine pericardium
Biomaterials, artificial cells and artificial organs. **17**, 3, 315-328

Van der Geest J P, Sacks M S, Vorp D A (2006)
The effects of aneurysm on the biaxial mechanical behavior of human abdominal aorta.
J Biomechanics, **39** 1324–1334

Vawter D, Fung Y C, West J B. (1979)
Constitutive equation of lung tissue elasticity
J Biomech Eng Trans ASME **101**, 38-45

Veronda D R, Westmann R A. (1970)
Mechanical characterization of skin-finite deformations
J Biomechanics **3**, 111-124

Viidik A. (1990)
Structure and function of normal and healing tendons and ligaments
In *Biomechanics of Diarthrodial Joints*, Mow, Ratcliffe and Woo (eds.) 3-38
Springer. New York.

Viidik A. (1968)
A rheological model for unaclcified parallel-fibered collagenous tissue
J Biomechanics **1**, 3-11

Vogel H G. (1972)
Influence of age, treatment with corticosteroids and strain rate on mechanical properties of rat skin
Biochim Biophys Acta **286**, 79-83

Wan K T, Mai Y M. (1995)
Fracture mechanics of a new blister test with stable crack growth
Acta Metall Mater **143**, 4109-4115

Williams J G. (1997)
Energy release rates for the peeling of flexible membranes and the analysis of blister tests
Int J of Fracture **87**, 265-288

Wollnsky H, Glagov S. (1967)
A lamellar unit of aortic medial structure and function in mammals
Circ Res **20** 99-111

Wu K S, Osdol W, Dauskart R. (2006)
Mechanical properties of human stratum corneum: Effects of temperature, hydration, and chemical treatment
Biomaterials **27** 785-795

Yang W et al. (2013a)
Natural flexible dermal armor
Adv. Mater. **25** 31-48

Yang W et al. (2013b)
Structure and fracture resistance of alligator gar (*Atractosteus spatula)* armored fish scales.
Acta Biomaterialia **9** 5876-5889

Yang W et al. (2014)
Protective role of *Arapaima gigas* fish scales: Structure and mechanical behaviour.
Acta Biomaterialia **10** 3599-3614

Yeoh O. H. (1993)
Some forms of the strain energy function for rubber
Rubber Chem.Technol. **66**, 754-771

Zhu D et al. (2012)
Structure and mechanical performance of a modern fish scale
Adv. Eng. Mater. **4** B185-B194

Zhu D et al. (2013)
Puncture resistance of the scaled skin from stripped bass: Collective mechanisms and inspiration for new flexible armor designs.
JMBBM **24** 30-40

Zhu J, Wang X, He C, Wang H. (2012)
Mechanical properties, anisotropic swelling behaviours and structures of jellyfish mesogloea
JMBBM **6**, 63-73

SUBJECT INDEX